Floods, Droughts, and Tropical Cyclones: Investigating Climate Extremes through Variations in Lacustrine Sedimentology

By

Jessica Rose Rodysill

B.S., University of Minnesota, 2008

Sc.M., Brown University, 2010

A dissertation submitted in partial fulfillment of the requirements for the degree of Doctor of Philosophy in The Department of Geological Sciences at Brown University

PROVIDENCE, RHODE ISLAND

MAY 2014

This dissertation by Jessica R. Rodysill is accepted in its present form
by the Department of Geological Sciences as satisfying the
dissertation requirement for the degree of Doctor of Philosophy.

Date__________ ______________________________
James Russell, Advisor

Date__________ ______________________________
Jeffrey Donnelly, Advisor

Recommended to the Graduate Council

Date__________ ______________________________
Timothy Herbert, Reader

Date__________ ______________________________
Warren Prell, Reader

Date__________ ______________________________
Jan Tullis, Reader

Date__________ ______________________________
Donald Rodbell, Reader

Approved by the Graduate Council

Date__________ ______________________________
Peter Weber, Dean of the Graduate School

Curriculum Vitae

Jessica R. Rodysill

Born on March 5, 1985 in Duluth Minnesota to Steven and Patricia Rodysill

EDUCATION

Ph.D. Geological Sciences — expected July 2013

Brown University, Providence, RI

Sc.M. Geological Sciences — May 2010

Brown University, Providence, RI
Thesis Title: A paleolimnological record of drought from East Java, Indonesia during the last 1,400 years

B.S. Geology — May 2008

University of Minnesota, Minneapolis, MN

Proficiency in Spanish

PROFESSIONAL APPOINTMENTS

Brown University	Graduate Student	Sept. 2008-present
Limnological Research Center University of Minnesota	Research Assistant	June 2007- Aug. 2008
Laboratory of Paleontology University of Minnesota	Research Assistant	Oct. 2006-May 2008
University of Minnesota	Distance Learning Course Editor Introductory Geology	March – May 2007
Moose Lake Community Schools	Tutor All subject areas, K-12	May – June 2005

PUBLICATIONS

Peer-Reviewed Journal Articles

J.R. Rodysill, J.M. Russell, S.D. Crausbay, S. Bijaksana, M. Vuille, R.L. Edwards, H. Cheng (In Review) A severe drought during the last millennium in East Java, Indonesia. *In review for Quaternary Science Reviews*.

B.L. Konecky; J.M. Russell; **J.R. Rodysill**; M. Vuille; S. Bijaksana; Y. Huang (2013) Intensification of southwestern Indonesian rainfall over the past millennium. *Geophysical Research Letters.* Vol.40, Issue 2. Pp. 386-391. DOI: 10.1029/2012GL054331

J.R. Rodysill; J.M. Russell; S. Bijaksana; E. T. Brown; L. Saffiuddin; H. Eggermont (2012). A paleolimnological record of drought from East Java, Indonesia during the last 1,400 years. *Journal of Paleolimnology.* Vol. 47. No. 1. Pp. 125-139. DOI 10.1007/s10933-011-9564-3

J.R. Rodysill; J. Russell; B. Lunghino; S. Bijaksana. Heavy rainfall in East Java, Indonesia over the last millennium: Connections to the El Niño-Southern Oscillation. *In prep to be submitted to Nature Geoscience.*

J.R. Rodysill; J.P. Donnelly; R. Evans; A. Ashton; M.R. Toomey. Extreme floods during the Holocene preserved in floodplain lake sediments. *In prep to be submitted to Quaternary Science Reviews*.

J.R. Rodysill; J.P. Donnelly; R. Evans; A. Ashton. Northern Gulf of Mexico tropical cyclone activity over the past 4500 years from sediment archives. *In prep.*

Abstracts (National and International Meetings)

J.R. Rodysill; J.P. Donnelly; M.R. Toomey; R. Sullivan; D. MacDonald; R. Evans; A. Ashton (2012) Late Holocene hurricane activity in the Gulf of Mexico from a bayou sediment archive. American Geophysical Union Fall Meeting, San Francisco, CA, 3-7 Dec. (poster)

J.R. Rodysill; J. Russell; B. Lunghino; S. Bijaksana (2012) La Niña-induced Rainfall events in East Java, Indonesia during the past millennium. American Geophysical Union Fall Meeting, San Francisco, CA, 3-7 Dec. (oral)

J.P. Donnelly; P. Lane; P.J. van Hengstum; A.D. Hawkes; M.R. Toomey; **J.R. Rodysill**; P. Ranasinghe (2012) Late Holocene North Atlantic hurricane activity. Geological Society of America Abstracts with Programs, Vol. 44, No. 7, p. 618 (oral).

B.L. Konecky; J.M. Russell; **J.R. Rodysill**; M. Vuille; S. Bijaksana; Y. Huang (2012) Intensification of Western Indonesian Rainfall over the Past Millennium: Isotopes, Observations, and Teleconnections. Graduate Climate Conference, Pack Forest, WA, 26-28 Oct. (oral)

B.L. Konecky; J.M. Russell; **J.R. Rodysill**; M. Vuille; S. Bijaksana; Y. Huang (2012) Intensification of the Australasian Monsoon over Java, Indonesia, during the past millennium. International Paleolimnology Symposium Glasgow, Scotland, 21-24 Aug. (oral)

J.R. Rodysill; J.P. Donnelly (2011) Major hydrologic shifts in northwest Florida during the Holocene from a lacustrine sediment record. American Geophysical Union Fall Meeting, San Francisco, CA, 5-9 Dec. GC51H-1120 (poster).

B.L. Konecky; J.M. Russell; M. Vuille; **J.R. Rodysill**; L.R. Cohen; A.F. Chuman; Y. Huang (2011) "A Zonal Mode in the Indian Ocean over the Past Millennium? Isotopic Evidence from Continental Climate Archives and Model Simulations." American Geophysical Union Fall Meeting, San Francisco, CA, 5-9 Dec. PP24B-07 (oral).

J.R. Rodysill; J.P. Donnelly (2011) A new record of extreme climate events using an innovative approach to reconstruct floods in northwest Florida. Geological Society of America Annual Meeting, Minneapolis, 189-34. Geological Society of America Abstracts with Programs, Vol. 43, No. 5, p. 468 (poster).

J.R. Rodysill; J.M. Russell; S. Bijaksana; L. Saffiuddin; H. Eggermont (2010) Centennial-scale hydrological variations in East Java, Indonesia during the past 1400 years from paleolimnological records. American Geophysical Union Fall Meeting, San Francisco, CA, 13-17 Dec. PP51B-04 (oral).

J.R. Rodysill; J.M. Russell; S. Bijaksana; L. Saffiuddin; H. Eggermont (2010) A multi-proxy record of climate variability and anthropogenic activity from maar lake sediments in East Java, Indonesia. Geoloical Society of America Annual Meeting, Denver, 115-2. Geological Society of America *Abstracts with Programs*, Vol. 42, No. 5, p. 303 (poster).

J.R. Rodysill; J. M. Russell; S. Bijaksana; E. T. Brown; C. Bousquet; L. Saffiuddin (2009) Paleolimnological records of decade- to century-scale rainfall variability in East Java, Indonesia during the past millennium. American Geophysical Union Fall Meeting, San Francisco, CA, 14-18 Dec. PP13D-1435 (poster).

TEACHING EXPERIENCE

Teaching Assistant, Brown University (led lab exercises, guest lecturer, designed and graded exams)

Utah Geology Field Course	March 2013
Limnology: The Study of Lakes	Spring 2012
Physical Processes in Geology	Fall 2011
Earth: Evolution of a Habitable Planet	Spring 2011
Physical Processes in Geology	Fall 2010
Arizona Geology Field Course	March 2010
Sedimentology and Stratigraphy	Fall 2009

SPARK Science for Middle School Summer Program Co-Teacher July 2010

Sheridan Center for Teaching and Learning Certificate 1 Program 2009

Volunteer science educator, Vartan Gregorian Elementary School 2008 to present

Lab Instructor for Introductory Geology, University of Minnesota 2007 to 2008

HONORS AND AWARDS

Dissertation Fellowship, Brown University	2012-2013
Dr. Roscoe G. Jackson II award	2012
GSA graduate research grant	2012
GSA graduate research grant	2009
First Year Graduate Student Fellowship, Brown University	2008-2009
Outstanding Teaching Award	2007-2008
University of Minnesota Women's Club Scholarship	2007-2008
Ralph and Jayne McMillen Scholarship	2007-2008
Richard Clarence Dennis Scholarship	2006-2007

Dean's List (Fall 2003, Fall 2005, Spring 2006, Fall 2006, Spring 2007, Fall 2007, Spring 2008)

SERVICE

Graduate Mentoring Program Representative April 2012 to present
Brown University Department of Geological Sciences

- Responsibilities include designing a network of mentors for incoming graduate students, organizing social events for mentees and mentors, and supervising mentoring relationships

Graduate Student Teaching Committee May 2011 to present
Brown University Department of Geological Sciences

- Responsibilities include developing a structured support system for future teaching assistants, identifying methods for improving graduate student teaching in the geologic sciences, and organizing and participating in outreach programs designed to educate the community on current science issues and research developments.

Faculty and Graduate Student Club Vice President May 2011 to present
Brown University, elected position

- Responsibilities include decision-making on future club policies, allotting funds for the non-profit organization, promoting and participating in club events, and identifying misuse of club facilities.

Undergraduate Research Co-advisor to Brent Lunghino Sept. 2011 to Aug. 2012
Brown University Department of Geological Sciences

- Responsibilities included teaching and supervising laboratory procedures, assistance with developing data interpretations, and revising and editing the written thesis.

Paleoclimate research group Sept. 2006 to May 2008
University of Minnesota Department of Geology and Geophysics

- Responsibilities included attending weekly meetings to read and discuss recently published paleoclimate papers.

University of Minnesota Geological Society Vice President May 2007 to Aug. 2008
University of Minnesota Department of Geology and Geophysics, elected position

- Responsibilities included organization of fundraising events, coordinating social events, managing organization funds, and planning and preparation for Colorado Plateau Geology Field Short Course.

University of Minnesota Geological Society Treasurer Sept. 2006 to May 2007
University of Minnesota Department of Geology and Geophysics, elected position

- Responsibilities included organization of fundraising events, coordinating social events, managing organization funds, and planning and preparation for Scotland Geology Field Trip

Undergraduate Committee Representative Mar. 2007 to Aug. 2008
University of Minnesota Department of Geology and Geophysics

FIELD EXPERIENCE

Participant, organizer, leader - five multi-week field work expeditions Jan. 2011 to Aug. 2013
Focus: Collection of sediment cores, surface sediment samples, CHIRP seismic and GPR survey data and water column temperature and conductivity data in the Florida panhandle, across the northeast and mid-western United States, and in coastal South Carolina.

Archaean Geology Field Short Course July 2010
Focus: Sudbury crater impact structures and using Archaean bedrock exposures in the Canadian Shield to infer early Earth processes.

Colorado Plateau Field Short Course May 2008
Focus: The geology surrounding the Colorado Plateau including Grand Canyon formation and evolution, Meteor Crater, and evidence for volcanism in New Mexico.

Scotland Field Short Course May 2007
Focus: An overview of the complex geologic history of Scotland through observations of a wide variety of geologic features including the fossil record, sedimentary structures, and igneous and metamorphic deformation.

Advanced Field Camp July-Aug. 2006
Focus: Demonstrating knowledge and understanding of mapping and interpreting complex igneous and metamorphic structural geology.

Introductory Field Camp June-July 2006
Focus: Applying basic geologic mapping techniques to interpret the regional geologic history with a particular interest in sedimentary basins.

Hawaii Field Short Course May 2006
Focus: Observing geologic evidence for hot spot volcanism, tsunamis, and tropical soil weathering and beach processes.

Acknowledgements

I would like to dedicate this thesis to my parents, Trish and Steve Rodysill. Without their endless love and support, I would not be here today. I am incredibly lucky to have such wonderful, selfless, kind, and brilliant parents who have always been excited about my interests and accomplishments and know just what to say at just the right times. Mom and Dad, thank you so much for everything! I also am grateful for my little brother Paul, his sense of humor, and our late night deep conversations about how we can make the world a better place. Paul you are so bright and have so much to bring to this world; I am in awe of you. Thank you for being the best big-little brother I could ever ask for!

I owe many thanks to my dissertation advisors, Jim Russell and Jeff Donnelly. Thank you for your time, patience, guidance, and support over these last several years. I have learned so much from the two of you and have thoroughly enjoyed doing it. I also want to thank the rest of my advisory committee, Jan, Tim, and Warren, for guiding me through my research, keeping me focused on the important things, and reminding me to always focus my efforts on putting my work in the context of the bigger picture.

I was fortunate to have a wonderful and hilarious lab group during my stay at Brown: the JMR lab group. Thanks to the booming laughs of Shannon and Jim, every meeting sounded like a party to everyone else down the hall. Shannon and Bronwen, I am so fortunate to have gotten to know you over the last 5 years, both in the research world and as friends outside of work. Io and Willy D., carry on the awesomeness of the JMR lab group that Shannon, Bronwen, and I have to leave behind.

Some of the best experiences of my grad school career took place at WHOI and with the awesome people in CRL. Every time I came back to Brown after a day at WHOI, I was so cheerful and giddy that everyone knew "it must have been a WHOI day." Steph and Richard are such amazing people. They are truly a gift to the CRL and were a gift to me during the last three years. Brent, Christy, Kelsey, Aaron, and Leah: you turned my hardest spring into my best summer EVER. Your collective energy, excitement, and kindness were exactly what I needed, thank you! Natalia, you were such a joy to have around. Your uplifting spirit always brightens the day of those around you, including me. Toomey! Thanks for being cool. You have a way of breaking people out of their shell and making sure everyone is having a good time. I have appreciated our time together!! Good luck finishing your thesis "Things about stuff." Jess and Kevin, thank you for being great mentors and for believing in me.

Joe Orchardo and Davy Murray, you were such excellent mentors and teachers. I have always raved about you and will continue to do so. Thanks for teaching me how to be a great lab scientist and for your support over the years! Thank you, Bill Collins, for always taking care of my need. From giving me softball pointers to printing my AGU poster at 8 pm on Friday night, you always go above and beyond, and your efforts do not go unappreciated.

Bill France, you are the best bartender at the GCB. Thanks for always making sure I'm having a good time. I want to thank the geo grad students, and in particular the group I started with (Kerri, Leah, Mark, Rocio, Bronwen, Shannon, Chen, David, Jeff, and Tina) for all the good times and awesome experiences we shared. I have enjoyed our time together! Susie, thank you for being an awesome Cape roommate. You are a super great motivator, workout buddy, and friend.

Leah Cheek, words can not express how grateful I am for our friendship and for having you in my life. You have changed my world. Your unending kindness, hope, support, and compassion are gifts that are hard to come by, and through them you have supported me in ways you can not even imagine. I have cherished our time together and will continue to do so, because we will find a way to be close friends forever. <3

I owe special thanks to my accountability group, Leah and Kerri, for encouraging me and setting me straight over the last year. I've really enjoyed growing closer during our weekly meetings.

Brendan, thank you for being my rock. It's not a geology joke. You have been my strength, my friend, my life coach, and my endless source of entertainment. I am grateful to have you in my life. Thank you for spending yours with me.

Table of Contents

List of Tables

List of Figures

CHAPTER 1

Introduction

Jessica R. Rodysill

Department of Geological Sciences, Brown University

1.1 Modern climate extremes in Indonesia and the United States

Climate extremes, such as flooding and drought, often have devastating effects, resulting in loss of life and property, enormous damage costs, and threatening drinking water and food supply for entire nations. Understanding the underlying causes of abrupt climate changes is vital to the improving the prediction of and preparation for future extreme climate events.

Recent catastrophic flooding in Indonesia between January and March, 2013 resulted in over 220 deaths, displacement of 300,000 people from their homes, and destruction of 27,000 homes, medical facilities, and schools (Indonesia National Disaster Management and Mitigation Agency Disaster Bulletin, March 2013). This flooding came only five years after Indonesia received over 250 mm (10 inches) of rain in 10 days in December 2007 and January 2008 that resulted in devastating floods and mudslides, killing over 110 people, damaging 8,000 homes, and removing over 350 km of roadway (Lang and Lindsey, 2008; Indonesia National Disaster Management Agency). Drought occurring in July, August, and September of 2012 separated these flood years, leaving over 10,000 of people without water and destroying over 300,000 acres of crops (United Press International, 2012).

In the United States, the number of disasters related to extreme climate events exceeding $1 billion in damage costs has been steadily increasing since 1980, and these events are becoming more expensive (NOAA, 2012). These trends have been attributed to population increase and development in areas that are vulnerable to damages during climate extremes (Downton and Pielke, 2005; Pielke et al., 2008). The top four types of climate events resulting in over $1 billion in damages in the United States from 1980 to 2011 are tropical cyclones, droughts, severe local storms, and non-tropical cyclone-related flooding (Table 1.1; Smith and Katz, 2013). Loss of life, destruction of homes and infrastructure, and billions of dollars of crop loss in the U.S. during extreme climate events that result in exceedingly more expensive and more frequent catastrophes costing over $1 billion highlight the importance of understanding the mechanisms controlling event frequency and strength to better anticipate future threats.

This thesis focuses on flooding and drought in East Java, Indonesia and tropical cyclones and flooding in northwest Florida, United States. Indonesian precipitation is controlled by the seasonal monsoons, which deliver heavy rainfall to East Java during Austral summer, when wind direction is northwesterly, and drive a reduction in rainfall during Austral winter, when wind direction is southeasterly. These monsoonal changes are associated with the migration of the Inter-Tropical Convergence Zone (ITCZ), a zonal band of low pressure and converging winds that produces heavy rainfall and moves northward during Austral winter and southward, reaching Java, during Austral summer. East Java is situated in a region of deep atmospheric convection over the Indo-Pacific Warm Pool, on the western limb of the Pacific Walker Cell, a zonal overturning atmospheric circulation pattern spanning the tropical Pacific Ocean, and on the eastern limb of the Indian Ocean Walker Cell, a similar zonal circulation pattern over the tropical Indian Ocean. Perturbations to the Walker cells associated with the interannual variations in the El Niño-Southern Oscillation (ENSO) and the Indian Ocean Zonal Mode (IOZM) influence the convective intensity over East Java, producing precipitation anomalies there. During El Niño (La Niña) events, the weakening (strengthening) of the

Pacific Walker Circulation reduces (enhances) local convection and produces anomalous easterlies (westerlies) that tend to correlate with negative (positive) rainfall anomalies in Indonesia (Figure 1.1; Hendon, 2003). Similarly, positive (negative) IOZM events weaken (strengthen) the Indian Ocean Walker Circulation and locally reduce (enhance) convection in East Java, producing negative (positive) rainfall anomalies in East Java (Saji et al., 1999) sometimes independently from ENSO (Ashok et al., 2003).

Similarly, precipitation in Florida is influenced by the interannual variations in ENSO through atmospheric teleconnections: El Niño events tend to be associated with excess rainfall and La Niña events tend to be associated with drought from January to March (Figure 1.1; IPCC, 2007; Climate Prediction Center). Precipitation in Florida is highest during summer when the wind direction changes from northeasterly to southeasterly as the ITCZ migrates northward, toward Florida, delivering warm, moist air from the Gulf of Mexico onto the continent (Watts and Hansen, 1994; Poore, 2008; Climate Prediction Center). Warming of Gulf of Mexico sea surface temperatures (SSTs), tropical cyclones, and winter storms, in addition to ENSO variability, lead to anomalous precipitation capable of causing floods in Florida (Watts and Hansen, 1994; Climate Prediction Center).

To best predict when and where extreme climate events are likely to occur, it is essential to have the ability to predict how the climate variables that produce such events, such as monsoon strength, ENSO, IOZM, ITCZ, and SSTs, will behave in the future.

1.2 The future of climate extremes from models

The models included in the most recent IPCC report predict that on a global scale, the intensity of precipitation events will increase over the next century, particularly in the tropics, as the globally-averaged mean water vapor increases and greater amounts of moisture are available for rapid rainout (IPCC, 2007). Further, the models predict that mean precipitation will decrease in the subtropics, causing dry extremes to become drier over the next century (IPCC, 2007).

Climate models predict that the tropical Pacific Ocean will transition to a more El Niño-like mean state that would result in an eastward precipitation shift, away from Java (IPCC, 2007). The model predictions are inconsistent on future ENSO event frequency and intensity, suggesting there may not be a significant change in ENSO event trends in the coming century (IPCC, 2007). Modeling results suggest that on millennial timescales, periods characteristic of an El Niño-like mean state are associated with more frequent El Niño events (Clement et al., 1996; Emile-Geay et al., 2007), which could suggest that Java will experience more frequent droughts and Florida will experience more frequent flooding, based on observed flood, drought, and ENSO relationships.

Climate models predict that during the next century, the peak wind intensities and the near-storm precipitation from tropical cyclones will increase and the overall frequency of storms will decrease (IPCC, 2007). Rising storm intensity could cause more intense flooding and greater destruction in Florida, and elsewhere along the U.S. coastline, in the coming century.

These projections from the 2007 IPCC report indicate that, based on the current knowledge within the climate science community, climate extremes, particularly floods, droughts, and hurricanes, are expected to rise in intensity. Crucial to this prediction is our ability to relate forcing mechanisms to climate system behavior on a range of timescales, such that the physics included in the models is accurate and the model output can be verified with observational and reconstructed data. Instrumental and observational data are too short to resolve climate variability on centennial and longer timescales. Paleoclimate reconstructions are the best information available to us for reconstructing the histories of extreme climate event frequency and intensity and testing how their occurrence and strength relate to mean-state climate. The work presented in this thesis adds to the growing network of paleoclimate reconstructions and contributes to our understanding of extreme climate events and the conditions under which they occur.

1.3 Paleoclimate overview and outstanding questions

The global climate of the last millennium has been divided into two periods based on global temperature patterns: the Medieval Climate Anomaly (MCA; ~950-1250 CE), defined by a period of northern hemisphere warming, and the Little Ice Age (LIA; ~1350-1800 CE), defined by a period of northern hemisphere cooling (Mann et al., 2009). Tropical coral and northern hemisphere temperature reconstruction data suggest that the MCA was characterized by a more La Niña-like state in the tropical Pacific (Cobb et al., 2003; Mann et al., 2009) and modeling suggests a La Niña-like state is the expected response to increased radiative forcing via the ocean dynamical thermostat mechanism (Clement et al., 1996; Karnauskas et al., 2009), whereby an imposed heating on the tropical Pacific warms SSTs in the west more than in the east, where SSTs are modulated by upwelling. The resultant enhanced zonal SST gradient strengthens the easterly trade winds, which further strengthens the zonal SST gradient via the Bjerknes feedback (Clement et al., 1996).

High-resolution records in the Indo-Pacific Warm Pool region are generally short and sparse, and those that exist reveal a complex hydrologic history over the last millennium. Isotopic records from Makassar Strait sediments and Liang Luar cave speleothems suggest the wettest conditions of the last millennium occurred from 1500 to 1700 CE (Oppo et al., 2009; Tierney et al., 2010; Griffiths et al., 2009), whereas lake sediment records from East Java and Palau indicate drought from 1520 to 1795 CE and 1450 to 1650 CE (Sachs et al., 2009; Crausbay et al., 2006).

On longer, millennial timescales, proxy reconstructions and modeling studies show solar heating and a La Niña-like mean state resulted in reduced ENSO activity during the Holocene (Rodbell et al., 1999; Moy et al., 2002; Koutavas et al., 2006; Emile-Geay et al., 2007), which has been attributed to a change in the seasonal cycle and a northward-displaced ITCZ (Clement et al., 2000; Cane, 2005; Koutavas et al., 2006). However, the way in which ENSO responds to changes in radiative heating and the tropical Pacific SST gradient on shorter, centennial timescales is less certain; a coral-based temperature reconstruction from the Line Islands in the central equatorial Pacific suggests that there has been no change in ENSO variance over the last millennium (Cobb et al., 2013), whereas records of rainfall-driven runoff in lake sediments from Ecuador and the Galápagos in the eastern tropical Pacific are indicative of greater El Niño activity during the MCA relative to the LIA (Moy et al., 2002; Conroy et al., 2008). No continuous ENSO reconstructions exist from the western side of the ENSO system, so it is yet unknown how La Niña activity has varied during the last millennium or whether it co-varied with El Niño activity, as is suggested during the early part of the last millennium from biomarker concentrations in eastern equatorial Pacific sediments (Makou et al., 2010).

Historical data show that the frequency and intensity of tropical cyclones have exhibited substantial decadal variability over the last several decades (Knapp et al., 2010), which is thought to be controlled by factors that influence storm formation and convection strength, including SST variations, wind shear, and lower troposphere temperatures (DeMaria, 1996; Emanuel, 1999; Emanuel, 2003; Jaggar and Elsner, 2006; Mann et al., 2009). Large differences in the trends of reconstructed tropical cyclone activity in the northern Gulf of Mexico from multiple sites leave an unclear picture of Late Holocene intense hurricane variability (Liu and Fearn ,1993; Liu and Fearn, 2000; Lambert et al., 2008; Lane et al., 2011). Additional records are needed from the northern Gulf of Mexico region to elucidate the variability in tropical cyclone activity and assess the relationships between hurricane history and potential forcing mechanisms.

Several major river floods in Florida during the last century correlate in timing with some ENSO events and tropical cyclones (Chapter 6), yet the relationship between flooding and these phenomena is not straightforward. Little research has been done in Florida to better understand the underlying causes of major floods or to reconstruct the patterns of river floods during the Holocene. Pollen studies in Florida, southern Georgia, and southern Alabama reveal gradual moisture trends toward wetter conditions throughout the Holocene (Watts, 1969; Watts, 1971; Watts, 1975; Grimm et al., 1993; Watts and Hansen, 1994), but it remains unclear what controls the devastating river flooding that historically occurs under a wide variety of conditions (e.g. hurricanes and El Niño events; Advanced Hydrologic Prediction Service; Chapter 6).

In light of these uncertainties, the outstanding questions addressed in this thesis are:

> How have the Indonesian monsoons responded to variations in radiative forcing and ITCZ mean position over the past millennium?
>
> What is the history of decadal to centennial-scale drought in East Java over the last millennium, and how do droughts relate to mean climate?
>
> What factors caused intense multi-decadal drought to occur in East Java in the past millennium?
>
> What is the history of flooding in East Java over the last millennium, and how does flooding relate to monsoon strength, ITCZ mean position, and long-term variability in ENSO and the IOZM?
>
> How has La Niña activity varied over the last millennium and how does that relate to El Niño activity and mean climate?
>
> How has Gulf of Mexico tropical cyclone activity varied at the centennial timescale during the late Holocene, and how do these variations relate to previous

tropical cyclone reconstructions and changes in mean climate? What drives centennial variability in intense tropical cyclones in the Gulf of Mexico?

What is the history of flooding in northwest Florida during the Holocene, and what drives flood frequency on centennial to millennial timescales? How does the flood history of northwest Florida relate to local tropical cyclone activity, ENSO variability, local SSTs, and mean hydrologic conditions?

1.4 Lacustrine sedimentologic approach

Lakes are globally distributed, allowing for sediment-based reconstructions to be strategically located for studying specific components of climate change (e.g. tropical cyclone overwash deposition in coastal lakes or variations in monsoonal rainfall in East Java). Furthermore, lakes are extremely sensitive to climate and the environment; in-lake processes and the delivery of exogenic materials to the lake respond to changes in local climate and alter the character of the sediment that ultimately accumulates in the basin. Each of these processes responds uniquely to different components of the local environment with varying sensitivities to local environmental change, making lakes ideal archives for reconstructing multiple aspects of local climate changes at a variety of timescales.

Collection of sediment cores that capture a vertical profile of sediment, often in conjunction with historical observations that overlap the most recent century of the sediment record, are used to develop a multi-proxy record of paleoclimate extending back several millennia. Rapid accumulation of sediments through time promotes the preservation of the sediment record such that climate reconstructions in these archives are often continuous and high-resolution. Through a variety of dating methods, we are able to determine the timing of the environmental changes we observe. Holocene-aged sediments are typically dated with ^{14}C methods that identify ages with uncertainties on the order of a few decades, while sediment from the last 150 years can be more precisely dated with ^{210}Pb-dating methods, providing ages with sub-annual to interannual uncertainties.

My approach to investigating past climate in Indonesia and Florida is to reconstruct paleoclimate using variations in sediment lithology and geochemistry from lake cores. The data I include in my paleoclimate interpretations at each site differ based on the local environment, however in many cases I use the same measurements from site to site that inform about different aspects of the local environment. For example, I use the sand content in sediment cores, in conjunction with several additional observations and proxy data, to infer changes in depositional energy associated with rainfall-driven runoff in a lake in Indonesia (Chapter 4), tropical cyclone-induced overwash and sediment transport into a coastal bayou in Florida (Chapter 5), and riverine floods in a lake in Florida (Chapter 6).

Despite the wealth of information that can be gained from this approach, few climate records using this methodology exist on the global scale. Finding a site that is well-positioned and sensitive to the appropriate components of climate can be challenging, and the sensitivity of the site and resolution of the record can limit the scope of the research. Each site responds in unique ways to environmental changes, and each proxy utilized in this thesis can be affected by multiple components of the local climate, making it difficult to tease apart variations in a specific component of the regional climate. Through the measurement of many proxies and cross-proxy validation, the methods used in this thesis allow for elimination of some scenarios of past climate and environmental changes, while supporting others.

Lakes are geographically stationary in space, and thus are best used for understanding past climate and environmental changes of one specific site. For example, in Chapter 5 I introduce a new record of overwash deposits that represents local hurricane activity in the Gulf of Mexico. These deposits are formed when a hurricane comes within close proximity of the site, however a single lake record from the Gulf of Mexico does not represent the storm climatology of the entire Gulf because of the stochastic nature of hurricanes and the stationarity of the site. Hurricanes may randomly make landfall at a particular site more frequently, causing a sediment record there to have more overwash deposits than a record from proximal site. Regional climate histories can be more confidently reconstructed through the addition of multiple sites in a given region that tell the same story as one another, as is done for Chapter 3 of this thesis.

An additional caveat to this approach is that the climate reconstruction is often only representative of a fraction of the climate events in that specific site. For example, only a subset of hurricanes that come within close proximity of the site is recorded in the sediment cores due to certain characteristics of the storms (e.g. wind direction and speed) and the sensitivity of the site, as is discussed in Chapter 5. Similarly, the temporal resolution of these types of records is typically too low to successfully reconstruct sub-annual changes in climate, which does not allow for all floods or hurricanes to be easily distinguishable from seasonal-scale rainfall changes. While the ideal climate reconstruction can tell us precisely how many climate events occurred, what the magnitude each event was, and what the exact timings of these events were such that we can accurately predict when the next event will occur, there is currently no archive that is capable of providing that level of detail in the paleorecord. However, the methodology used in this thesis does present the science community with new datasets that display strong relationships between the events identified in each record and aspects of historical climate, providing a sampling of extreme climate events across many regions. The types of datasets used in this thesis are best used to gain an understanding of how the climate systems that produce extreme climate events that we experience today, such as hurricanes, floods, El Niño or La Niña events, behaved during changes in mean climate. The knowledge we can extract from lake sediment-based climate reconstructions, including those produced in this thesis, provides a fundamental basis for predicting what we as people can expect in terms of broad-scale changes in the amplitudes and numbers of extreme climate events as the mean climate changes in the future.

1.5 Outline of chapters in this thesis

In this thesis, I use multiple sedimentological, geochemical and geophysical proxies to reconstruct different aspects of paleohydrology from lake sediment cores. The perspective gained by obtaining several datasets from a single sediment record provides further insights into the nature of local environmental changes that are vital for accurately interpreting the observed trends of a single proxy.

In Chapter 2, I identify both millennial and decadal-scale modes of hydroclimate variability in East Java using from sediments from Lake Logung. The long-term variations are consistent with a strengthening of the Indonesian monsoon and southward migration of the ITCZ during the past millennium. I demonstrate that the decadal scale droughts superimposed on the long-term moistening trend are not related to ITCZ mean position, but rather reflect multi-decadal weakening of the Walker Circulation. With the addition of a sediment core from a nearby lake and an updated age model on a third nearby lake, I show in Chapter 3 that the strongest drought of the last millennium in East Java occurred between 1790 and 1860 CE. In this chapter, I use an in-depth analysis of global climate records to demonstrate that this extreme drought was the result of several closely-spaced strong El Niño events followed by several large volcanic eruptions.

In Chapter 4, I introduce the first record of runoff from the Indo-Pacific Warm Pool region, which I attribute to heavy rainfall-induced flooding during strong La Niña events. I compare my new record from East Java with runoff records in the eastern equatorial Pacific to argue that El Niño and La Niña activity co-vary on centennial timescales over the last millennium and were high during the MCA relative to the LIA. These findings support modeling efforts that show the probability of stronger ENSO events is higher during a La Niña-like mean state in the tropical Pacific Ocean.

In Chapter 5, I present a new record of intense hurricane landfalls in northwest Florida that exhibits good agreement with other northern Gulf Coast storm reconstructions. I argue that these records reflect northern Gulf of Mexico intense hurricane activity. This record supports the idea that heightened strong hurricane activity is controlled in part by Loop Current penetration. Additionally, I argue that ENSO contributes to tropical cyclone strength in the Gulf of Mexico during the late Holocene.

In Chapter 6, I show that lake sediments situated in river floodplains are exceptional environments for preserving flood deposits, and multiple sites within the same floodplain can be used to constrain flood magnitude. These northern Florida lake-level histories are consistent with pollen-inferred hydrologic histories throughout the Holocene, including a prolonged drought beginning in the mid-Holocene. I show that major flooding in northwest Florida is most sensitive to regional water balance; heavy rainfall during hurricanes, El Niño events, and periods of warm SSTs are more likely to induce major flooding when mean state regional hydrology is wet and sea level is high.

This thesis contributes several new insights on climate extremes in East Java and Florida during the last few millennia. Chapters 2, 3, and 4 improve our overall understanding of the controls on decadal to millennial-scale variations in Indo-Pacific Warm Pool hydrology by elucidating the relative controls of ITCZ and Walker Circulation on drought and flooding in East Java. Chapter 4 advances our understanding of centennial-scale variations in ENSO over the last millennium and supports the use of runoff records in the tropical Pacific for inferring ENSO variability, which is crucial for testing the role of ENSO on tropical cyclone activity (Chapter 5) and rainfall-induced river floods in ENSO-teleconnected regions (Chapter 6). Chapters 5 and 6 provide a unique direct comparison between local flooding history (Chapter 6) in northwest Florida and late Holocene local tropical cyclone landfalls (Chapter 5).

1.6 References

"Advanced Hydrologic Prediction Service." National Oceanic and Atmospheric Administration. 30 May 2013. Web. 30 May 2013. <http://water.weather.gov/ahps/>.

Ashok, K., Guan, Z., Yamagata, T., 2003. A look at the relationship between the ENSO and the Indian Ocean Dipole. J. Meteor. Soc. Japan 81, 41-56.

Cane, M.A. 2005. The evolution of El Niño, past and future. Earth Plan. Sci. Lett. 230, 227-240.

Clement, A.C., Seager, R., Cane, M.A., 2000. Suppression of El Niño during the mid-Holocene by changes in Earth's orbit. Paleoceanography. 15, 731-737.

Clement, A.C., Seager, R., Cane, M.A., Zebiak, S.E., 1996. An ocean dynamical thermostat. J. Climate 9, 2190-2196.

Climate Prediction Center. National Centers for Environmental Prediction. National Oceanic and Atmospheric Administration. 24 January 2005. Web. 4 July 2013. <http://www.cpc.ncep.noaa.gov/>

Cobb, K.M., Westphal, N., Sayani, H.R., Watson,J.T., Di Lorenzo,E., Cheng, H., Edwards, R.L., Charles, C.D., 2013. Highly variable El Niño-Southern Oscillation throughout the Holocene. Science. 339, 67-70.

Conroy, J.L., Overpeck, J.T., Cole, J.E., Shanahan, T.M., Steinitz-Kannan, M., 2008. Holocene changes in eastern tropical Pacific climate inferred from a Galápagos lake sediment record. Quat. Sci. Rev. 27, 1166-1180.

Crausbay, S.D., Russell, J.M., Schnurrenberger, D.W., 2006. A ca. 800-year lithological record of drought from sub-annually laminated lake sediment, East Java. J. Paleolimnol. 35, 641-659.

DeMaria, M., 1996. The effect of vertical shear on tropical cyclone intensity change. J. Atmos. Sci. 53, 2076-2087.

Downton, M.W., Pielke, Jr., R.A., 2005. How accurate are disaster flood loss data? The case of U.S. flood damage. Nat. Haz. 35, 211-228.

Emanuel, K.A., 1999. Thermodynamic control of hurricane intensity. Nature. 401, 665-669.

Emanuel, K., 2003. Tropical Cyclones. Annu. Rev. Earth Planet. Sci. 31, 75–104.

Emile-Geay, J., Cane, M., Seager, R., Kaplan, A., Almasi, P., 2007. El Niño as a mediator of the solar influence on climate. Paleoceanography. 22, doi:10.1029/2006PA001304.

Griffiths, M.L., Drysdale, R.N., Gagan, M.K., Zhao, J.-x., Ayliffe, L.K., Hellstrom, J.C., Hantoro, W.S., Frisia, S., Feng, Y.-x., Cartwright, I., St. Pierre, E., Fischer, M.J., Suwargadi, B.W., 2009. Increasing Australian-Indonesian monsoon rainfall linked to early Holocene sea-level rise. Nat. Geosci. 2, 636-639.

Grimm, E.C., Jacobson, Jr., G.L., Watts, W.A., Hansen, B.C.S., Maasch, K.A., 1993. A 50,000-year record of climate oscillations from Florida and its temporal correlation with the Heinrich Events. Science. 261, 198-200.

Hendon, H.H., 2003. Indonesian rainfall variability: Impacts of ENSO and local air-sea interaction. J. Climate 16, 1775-1790.

Indonesia National Disaster Management and Mitigation Agency Disaster Bulletin, March, 2013. Web. 10 July 2013. <http://www.bnpb.go.id/>

IPCC (Intergovnermental Panel on Climate Change). Contribution of Working Group I to the Fourth Assessment Report of the Intergovernmental Panel on Climate Change, 2007. Solomon, S., D. Qin, M. Manning, Z. Chen, M. Marquis, K.B. Averyt, M. Tignor and H.L. Miller (eds.) Cambridge University Press, Cambridge, United Kingdom and New York, NY, USA.

Jaggar, T.H., Elsner, J.B., 2006. Climatology models for extreme hurricane winds near the United States. J. Clim. 19, 3220-3236.

Karnouskas, K.B., Seager, R., Kaplan, A., Kushnir, Y., Cane, M.A., 2009. Observed strengthening of the zonal sea surface temperature gradient across the equatorial Pacific Ocean. J. Climate 22, 4316-4321.

Knapp, K.R., Kruk, M.C., Levinson, D.H., Diamond, H.J., Neumann, C.J., 2010. The International Best Track Archive for Climate Stewardship (IBTrACS): Unifying tropical cyclone best track data. Bull. Amer. Meteor. Soc. 91, 363-376.

Koutavas, A., deMenocal, P.B., Olive, G.C., Lynch-Stieglitz, J., 2006. Mid-Holocene El Niño–Southern Oscillation (ENSO) attenuation revealed by individual foraminifera in eastern tropical Pacific sediments. Geology. 34, 993-996.

Lambert, J.W., Aharon, P., Rodriguez, A.B., 2008. Catastrophic hurricane history revealed by organic geochemical proxies in a coastal lake sediments: a case study of Lake Shelby, Alabama (USA). J. Paleolimnol. 39, 117-131.

Lane, P., Donnelly, J.P., Woodruff, J.D., Hawkes, A.D., 2011. A decadally-resolved paleohurricane record archived in the late Holocene sediments of a Florida sinkhole. Mar. Geo. 287, 14-30.

Lang, S., Lindsey, R. "Flooding and Landslides in Indonesia." *Natural Hazards: Floods.* National Atmospheric and Space Administration Earth Observatory. 2008. Web. 26 June 2013. <http://earthobservatory.nasa.gov/NaturalHazards/ >

Liu, K., Fearn, M.L., 1993. Lake-sediment record of late Holocene hurricane activities from coastal Alabama. Geology 21, 793-796.

Liu, K., Fearn, M.L., 2000. Reconstruction of prehistoric landfall frequencies of catastrophic hurricanes in northwestern Florida from lake sediment records. Quat. Res. 54, 238-245.

Makou, M.C., Eglinton, T.I., Oppo, D.W., Hughen, K.A., 2010. Postglacial changes in El Niño and La Niña behavior. Geology 38, 43-46.

Mann, M.E., Woodruff, J.D., Donnelly, J.P., Zhang, Z., 2009. Atlantic hurricanes and climate over the past 1,500 years. Nature 460, 880-885.

Mann, M.E., Zhang, Z., Rutherford, S., Bradley, R.S., Hughes, M.K., Shindell, D., Ammann, C., Faluvegi, G., Ni, F., 2009. Global signatures and dynamical origins of the Little Ice Age and Medieval Climate Anomaly. Science 326, 1256-1260.

Moy, C.M., Seltzer, G.O., Rodbell, D.T., Anderson, D.M., 2002. Variability of El Niño/Southern Oscillation activity at millennial timescales during the Holocene epoch. Nature 420, 162-165.

National Oceanic and Atmospheric Administration (NOAA), 2012. Spatial Trends in Coastal Socioeconomics Demographic Trends Database: 1970-2010. 17 June 2013. Web. 10 July 2013. <http://coastalsocioeconomics.noaa.gov/ >

Oppo, D.W., Rosenthal, Y., Linsley, B.K., 2009. 2,000-year-long temperature and hydrology reconstructions from the Indo-Pacific warm pool. Nature 460, 1113-1116.

Pielke, Jr., R.A., Gratz, J., Landsea, C.W., Collins, D., Saunders, M.A., Musulin, R., 2008. Normalized hurricane damage in the United States: 1900-2005. Nat. Haz. Rev. 1, 29-42.

Poore, R.Z., 2008. Holocene climate and climate variability of the Northern Gulf of Mexico and Adjacent Northern Gulf Coast: A Review. Open Paleont. J. 1, 7-17.

Rodbell, D.T., Seltzer, G.O., Anderson, D.M., Abbott, M.B., Enfield, D.B., Newman, J.H., 1999. An ~15,000-year record of El Niño-driven alluviation in southwestern Ecuador. Science 283, 516-520.

Sachs, J.P., Sachse, D., Smittenberg, R.H., Zhang, Z., Battisti, D., Golubic, S., 2009. Southward movement of the Pacific intertropical convergence zone AD 1400-1850. Nat. Geosci. 2, 519-525.

Saji, N.H., Goswami, B.N., Vinayachandran, P.N., Yamagata, T., 1999. A dipole mode in the tropical Indian Ocean. Nature 401, 360-363.

Smith, A.B., Katz, R.W., 2013. U.S. billion-dollar weather and climate disasters: Data sources, trends, accuracy, and biases. Nat. Haz. 67. 387-410.

Tierney, J.E., Oppo, D.W., Rosenthal, Y., Russell, J.M., Linsley, B.K., 2010. Coordinated hydrological regimes in the Indo-Pacific region during the past two millennia. Paleoceanography 25, PA1102, doi: 10.1029/2009PA001871.

United Press International. "Drought has Indonesians thirsty for water." 13 September 2012. Web. 11 July 2013. < http://www.upi.com/Top_News/World-News/2012/09/13/Drought-has-Indonesians-thirsty-for-water/UPI-21361347552806/>

Watts, W.A., 1969. A pollen diagram from Mud Lake, Marion County, north-central Florida. Geol. Soc. Amer. Bull. 80, 631-642.

Watts, W.A., 1971. Postglacial and interglacial vegetation history of southern Georgia and central Florida. Ecology 52, 676-690.

Watts, W.A., 1975. A late Quaternary record of vegetation from Lake Annie, south-central Florida. Geology 3, 344-346.

Watts, W.A., Hansen, B.C.S., 1994. Pre-Holocene and Holocene pollen records of vegetation history from the Florida peninsula and their climatic implications. Palaeogeog. Palaeoclim. Palaeoecol. 109, 163-176.

	Cumulative damage costs (out of $881.2 billion)	Percent of all events >$1billion (133 events total)
Tropical Cyclones	$417.9 billion	23.3 %
Droughts	$210.1 billion	12 %
Severe Local Storms	$94.6 billion	32.2 %
Floods (non-tropical cyclone)	$85.1 billion	12 %

Table 1.1: Damage costs and percent of total events represented by each category for the top four most expensive types of extreme climate events resulting in damages exceeding $1 billion between 2008 and 2011 (Smith and Katz, 2013). Damage costs are adjusted for inflation and are reported in U.S. dollars in the year 2011.

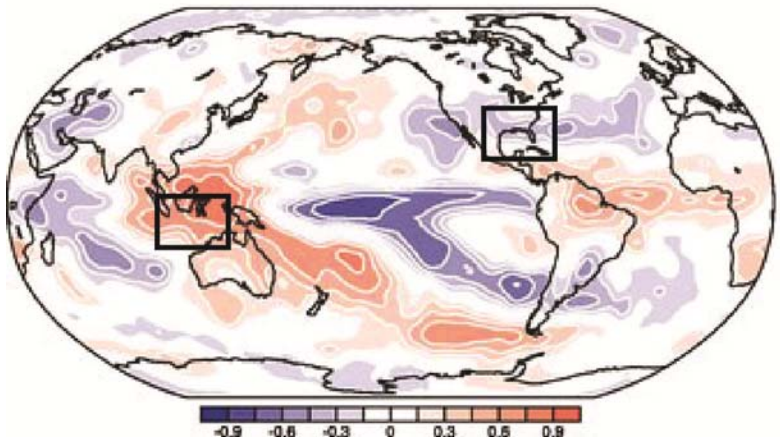

Figure 1.1: Correlation of the Southern Oscillation Index with GPCP precipitation from 1979-2003 (Adapted from IPCC, 2007). Areas in blue indicate a positive (negative) correlation between rainfall and El Niño (La Niña) conditions, and areas in red indicate a positive (negative) correlation between rainfall and La Niña (El Niño) conditions. The study regions relevant to this thesis are outlined in black rectangles.

CHAPTER 2

A paleolimnological record of rainfall and drought from East Java, Indonesia during the last 1,400 years

Jessica R. Rodysill[1]

James M. Russell[1], Satria Bijaksana[2], Erik T. Brown[3], La Ode Safiuddin[4], Hilde Eggermont[5]

[1]Department of Geological Sciences, Brown University

[2]Faculty of Mining and Petroleum Engineering, Institut Teknologi Bandung

[3]Large Lakes Observatory and Department of Geological Sciences, University of Minnesota Duluth

[4]Faculty of Mathematics and Natural Sciences, Institut Teknologi Bandung

[5]Freshwater Biology, Royal Belgian Institute of Natural Sciences

Published in: *Journal of Paleolimnology* 47: 125-139, Doi: 10.1007/s10933-011-9564-3

2.1 Abstract

Variations in the location and strength of convection in the Western Pacific Warm Pool (WPWP) have a profound impact on the distribution and amount of global rainfall. Much of the variability in WPWP convection is attributed to variations in the El Niño-Southern Oscillation (ENSO), for which the long-term trends and forcing mechanisms remain poorly understood. Despite the importance of WPWP convection to global climate change, we have very few paleohydrological reconstructions from the region. Here we present a new paleolimnologic and paleohydrologic record spanning the past 1,400 years using a multi-proxy dataset from Lake Logung, located in East Java, Indonesia that provides insights into centennial-scale trends in warm pool hydrology. Organic matter $\delta^{13}C$ data indicate that East Java became wetter over the last millennium until *ca*. 1800 Common Era (CE), consistent with evidence for the southward migration of the Intertropical Convergence Zone (ITCZ) during this time. Superimposed on this long-term trend are four decade- to century-scale droughts, inferred from organic matter $\delta^{13}C$ and calcite abundance data. They are centered at 1030, 1550, 1830, and 1996 CE. The three more recent droughts correlate with hydrologic anomalies documented in other proxy records from the WPWP region on both sides of the equator, and the two most recent droughts correlate in time with historically documented periods of multiple, intense El Niño events. Thus, our record provides strong evidence that century-scale hydrologic variability in this region relates to changes in the Walker Circulation. Human activity within the lake catchment is apparent since 1860 CE.

2.2 Introduction

The Western Pacific Warm Pool (WPWP) plays a critical role in global climate, influencing global rainfall patterns and the supply of water vapor to the atmosphere through reorganizations of oceanic and atmospheric circulation patterns (Pierrehumbert 2000). Variations in convective intensity in the WPWP region are controlled in part by anomalous sea surface temperatures (SSTs) associated with the El Niño-Southern Oscillation (ENSO) and coupled changes in the strength and position of the Intertropical Convergence Zone (ITCZ). Indonesia sits at the heart of the tropical western Pacific, and its population has suffered severe drought and food insecurity due to recent WPWP variations. For instance, the 1997/98 El Niño event is linked to extensive fires and respiratory health problems for over 20 million people (Byron and Shepherd 1998), as well as significant food insecurity due to reductions in rice production in Java (Naylor et al. 2001).

Indonesia hosts numerous lakes that record the region's hydrologic history, yet there are few continuous, high-resolution paleoclimate records from the WPWP region, and the few existing high-resolution records exhibit substantial disagreement about hydrological trends during the last millennium. For example, oxygen and deuterium isotopic records from the Makassar Strait and Liang Luar cave in Flores, Indonesia suggest that the wettest conditions in the last millennium occurred between 1500 and 1700 CE (Oppo et al. 2009; Tierney et al. 2010; Griffiths et al. 2009), while lake sediment records from Palau and East Java indicate that dry conditions prevailed from 1520 to 1795 CE and from 1450 to 1650 CE (Sachs et al. 2009; Crausbay et al. 2006). Given the paucity of records from the region, it is unclear whether these differences derive from uncertainties in the proxy records and their chronologies, or whether they represent real climate gradients that could elucidate variations in the complex interactions among ENSO, the Asian monsoons, and the position of the ITCZ. Additional high-resolution records are therefore needed to better understand the history and spatial relationships of rainfall and drought within the WPWP region.

Here we present a continuous, high-resolution record of drought in East Java, Indonesia based upon lithologic, geochemical, and stable isotopic analyses of a core from a maar crater lake, Lake Logung, in East Java, Indonesia. This new record augments previous studies of crater-lake sediments in East Java and highlights the complex controls on moisture balance variations in the Southeast Asian tropics.

2.2.1 Study region

Java is one of the Greater Sunda Islands in southern Indonesia, situated at the western edge of the WPWP between the Indian and Pacific oceans (Figure 2.1). The climate of East Java is controlled by the seasonal migration of the ITCZ over the southern tropics, concomitant changes in the monsoons, and inter-annual changes in the phase of the El Niño-Southern Oscillation. The northwest monsoon delivers humid air and heavy rainfall to Java in austral summer as the ITCZ migrates southward over the island, whereas during austral winter the southeast monsoon brings relatively cool, dry conditions while the ITCZ is positioned over mainland Asia (Figure 2.1). Annual rainfall near our study site averages ~2500 mm, with ~1800 mm falling during the wet season (December-May) and ~700 mm during the dry season (June-November; Vose et al.

1992). The phase of El Niño Southern Oscillation (ENSO) strongly correlates to both seasonal and inter-annual rainfall anomalies in this region (Hendon 2003). El Niño events are associated with cooler SSTs in the WPWP region and warmer SSTs in the central and eastern Pacific, which drive anomalous easterly winds across the equatorial Pacific and Indonesia and weaken the Walker Circulation and vertical convection over the WPWP. The anomalous easterlies prevail into austral summer, delaying the arrival of the northwest monsoon and prolonging the dry season in East Java (Hendon 2003). Over 90% of droughts in Indonesia between 1861 and 1976 are associated with El Niño events (Quinn et al. 1978).

Lake Logung (8°2.443'-8°2.609'S and 113°18.344'-113°18.54'E) is a small, ~250-m-diameter maar crater lake located in eastern Java, with a maximum depth of 7 m. The lake sits at an elevation of 215 m on the southwest side of Gunung Lamongan, one of 21 historically active volcanoes on the island of Java (Carn and Pyle 2001). The bedrock near our study site is composed of dominantly mafic volcanic material derived from Sunda arc volcanism (Carn and Pyle 2001). Lake Logung was weakly stratified with hypoxic bottom water in July 2008. Temperature and pH varied from 29.53 °C and 8.14, respectively at the surface to 28.49 °C and 7.4, respectively just above the sediment water interface. The conductivity increased from a minimum of 0.345 mS cm^{-1} at 1 m water depth to 0.358 mS cm^{-1} at the lake bottom and the lake chemistry is dominated by Ca^{2+}, Mg^{2+}, and HCO_3^-. Lake Logung is fed by two small springs that enter the lake from the northeast and northwest. An outlet on the southeast side of the lake allows for some surface outflow, but evaporation also strongly influences lake level and increases lake salinity. Water balances, salinities, and algal ecology of lakes in East Java have been shown to be sensitive to changes in climate, making them ideal sites for reconstructing drought history (Green et al. 1976; Crausbay et al. 2006).

2.3 Materials and methods

2.3.1 Core collection

Piston cores were recovered from Lake Logung at 6.8 m water depth in July 2008. The uppermost 35 cm of sediment was recovered using a hand-held Uwitec™ gravity corer and was extruded in the field in 2-cm slices using a modified Verschuren (1993) extruder to preserve sediment physical properties and water content. The upper 3.75 m were recovered in polycarbonate tubes in offset, overlapping cores, using a Bolivia corer. A Livingstone corer was used to recover an additional 3.81 m of sediment below a resistant ash layer that limited Bolivia core recovery. Livingstone sections were extruded in the field, wrapped and sealed in polyethylene plastic, and stored in PVC tubes for transport to Brown University.

2.3.2 Core chronology

Six ^{14}C dates were obtained on charcoal that was isolated from the sediment by sieving at 250 μm, then by manually separating the charcoal from other coarse particles under a dissecting microscope. Three ^{14}C dates were also derived from plant macrofossils, and five ^{14}C dates were obtained on bulk sediment samples. All ^{14}C

samples were chemically pretreated using standard techniques and analyzed at the Woods Hole Oceanographic Institution National Ocean Sciences AMS Facility. ^{14}C ages were calibrated to calendar years using the IntCal09 model from Calib 6.0 (Stuiver and Reimer 1993). In addition, sediment samples from the upper 2 m of the core were dated using ^{210}Pb via alpha spectroscopy at Flett Research Laboratories, and age modeling was accomplished using the constant rate of supply model (Appleby and Oldfield 1978; Appleby 1997).

2.3.3 Lithostratigraphic analysis

All core sections were split and macroscopically and microscopically described using the procedures outlined in Schnurrenberger et al. (2003). A GeoTek Multi-Sensor Core-Logger was used to measure point-sensor magnetic susceptibility of the sediment at 1-cm resolution. Trends in the bulk elemental composition of the core were determined using the ITRAX Corescanner at the University of Minnesota Duluth Large Lakes Observatory at 1-cm resolution using a Mo X-ray source with a 120-second dwell time. These data were supplemented by INNOV-X Systems Alpha 4000 Handheld XRF analyzer data measured on extruded gravity core samples with a 90-second dwell time. Trends in elemental counts from the handheld XRF analyzer were identical to those measured on the ITRAX corescanner, so we scaled the handheld XRF measurements to those made on the ITRAX corescanner for each element individually. Elements from mineral phases formed by in-lake processes were investigated by correcting XRF data for variability in the proportion of terrigenous inputs, as has been done previously, for instance, with data from Lake Malawi, by normalization to Ti, which is only incorporated into the sediments through terrestrial inputs of silicate minerals (Brown et al. 2007). Using these data, a 6.89-m-long composite section was constructed in the CoreWall environment (Rao et al. 2005). Data presented in this paper are from this composite stratigraphy.

Subsamples were taken from the cores every 5 cm immediately after core splitting and were freeze-dried, analyzed for water content, and homogenized using a mortar and pestle prior to geochemical analysis. Subsamples were analyzed for total inorganic carbon (TIC) content on a UIC CM5014 CO_2 Coulometer with a UIC CM5240 TIC Autoanalyzer. Precision, verified with 10% sample replication and pure $CaCO_3$ standards, is 0.237%. X-ray diffraction (XRD) was used to identify of carbonate minerals using a Rigaku MiniFlex X-ray Diffractometer at the University of Minnesota. Subsamples were analyzed for their total carbon (TC) and total nitrogen (TN) content using an NC2100 Elemental Analyzer. Precision on standards and 10% sample replication was 0.260% and 1.60% for N and C, respectively. The TIC content was subtracted from the TC content to determine total organic carbon (TOC) content, which was used to calculate the molar ratio of organic carbon to nitrogen ($C:N_{org}$), a measure commonly used to determine whether the source of bulk organic matter is of a dominantly terrestrial or lacustrine origin (Meyers and Lallier-Vergès 1999). Biogenic opal concentrations were measured in subsamples every 10 cm using hot alkaline digestions to extract opaline silica, followed by spectrophotometric analysis of Si concentrations as outlined in Russell and Johnson (2005, modified after DeMaster 1981). The carbon and nitrogen isotopic compositions of organic matter ($\delta^{13}C_{org}$ and $\delta^{15}N_{org}$)

were measured on a Costech Instruments elemental combustion system coupled to a Delta V Plus isotope ratio mass spectrometer via a Conflo II interface. For these analyses, sediment samples were pretreated by soaking in 1N HCl for 1 hour at room temperature to remove inorganic carbon. Precision on standards and 10% sample replication were 0.124‰ and 0.674‰ for $\delta^{13}C_{org}$ and $\delta^{15}N_{org}$, respectively. The $\delta^{15}N_{org}$ was measured on a subset of samples prior to and after the acid pretreatment; isotopic values on both types of sample lie within the precision without bias, so fractionation during acid pretreatment was considered negligible.

2.4 Results

2.4.1 Core chronology

Our age model was formed by linear interpolation between three plant macrofossil and two bulk sediment calibrated AMS ^{14}C dates as well as ten ^{210}Pb dates (Table 2.1, Figure 2.2). Six ^{14}C-dated charcoal samples were excluded from the age model because their ages are significantly older than those derived from plant macrofossils at similar depths in the core. We believe this discrepancy is due to reworking of charcoal within the lake or storage in surrounding soils prior to burial within the sediments, a process often observed in lakes (Björck and Håkansson 1982; O'Sullivan et al. 1973). Three bulk sediment samples have ages significantly older than the plant macrofossils at similar depths and were also excluded from our age model.

The large number of ^{14}C ages excluded from our age model contributes to uncertainty and therefore warrants discussion. We assumed that sediment reworking was the primary process causing erroneous ^{14}C ages, and therefore selected the youngest ages for inclusion in our age model. The opposite assumption, i.e. that the older charcoal and bulk sediment ^{14}C ages are correct, would require significant reworking of the plant macrofossils or root penetration through >1.5 m of sediment to achieve erroneously young ^{14}C dates on macrofossils. Well-preserved thin beds throughout the dated intervals, however, imply very minimal vertical sediment disturbance. The majority of the old ^{14}C ages fall within a 140-cm interval, where we infer significant hydrologic fluctuations (see later discussion) that could lead to erosion during transgressive and regressive lake level cycles.

We removed volcanic ash beds from the cumulative depth before applying the age model to the core and reinserted them as instantaneous events, so they are not included in sedimentation rate calculations. Sedimentation rates in the lower 2.5 m of the core average 0.3 cm yr^{-1}, while ^{210}Pb dates suggest an average sedimentation rate of 1.5 cm yr^{-1} in the upper meter of the core, implying a significant change in sedimentation rate between 435 and 116 cm depth (Figure 2.2). Several data described below suggest the transition to modern sedimentation patterns occurs at 232 cm depth, and we therefore extrapolated the sedimentation rate from the ^{210}Pb-dated portion of the core back to 232 cm in our age model. The slope in the age model between 232 cm depth and the youngest ^{14}C date indicates an additional increase in sedimentation rate occurs within this depth interval. The lack of age-control points between the ^{210}Pb-dated portion of the core and the ^{14}C-dated portion of the core results in considerable age uncertainty for this portion of our chronology, gradually rising from 15 years at 116 cm depth to 60 years at 435 cm depth. Age model error approximations were derived using the approach developed by Heegaard et al. (2005). The age model is more accurate below 435 cm depth, where ^{14}C dates are more closely spaced, and above 116 cm depth, where ^{210}Pb dates are closely spaced.

2.4.2 Sediment lithostratigraphy and geochemistry

The sediments from Lake Logung are generally dark olive-grey to brown, medium-bedded fine silt with varying amounts of diatoms, carbonate, and organic matter. Based upon variations in sediment lithology, we subdivided the core into two lithostratigraphic units: Unit 1 (640 to 1860 CE) and Unit 2 (1860 CE to present; Figures 2.3, 2.4). Several macroscopic features observed in the core are apparent in magnetic susceptibility and XRF geochemical data, including two volcanic ash beds at 1175 and 1690 CE, and five black fine-sand layers with angular contacts between 900 and 1820 CE.

The five black sand layers and two ashes correspond to prominent peaks in both magnetic susceptibility and XRF-derived Ti and Fe abundances in Unit 1 (Figure 2.3). Both magnetic susceptibility and abundances of Ti and Fe abruptly increase at the transition to Unit 2, followed by a gradual decline toward the present, confirming that this transition is associated with a large change in the abundance of ferromagnetic minerals (Figure 2.3).

Percent TIC and XRF-derived Ca:Ti data document four carbonate beds within our core from 930-1130, 1460-1640, 1790-1860, and 1985-2008 CE. The carbonate in these four intervals is fine-grained, low-Mg calcite, based on smear slide analyses and XRD measurements (Goldsmith and Graf 1958). Calcite comprises 5-43% of the sediment by mass in these intervals (Figure 2.3). Gastropod shells are present for a brief part of the 1460-1640 CE carbonate event, but the highest carbonate abundance within this period does not correspond with the shell bed. Using water chemistry data collected in 2008 and the calcite solubility of Plummer and Busenberg (1982), the lake was super-saturated with respect to $CaCO_3$ (**Ω** = 4.59) in 2008, consistent with elevated %TIC and Ca:Ti in the top centimeter of sediment.

Trends in XRF-derived Si:Ti and %biogenic opal generally compare well, allowing us to use Si:Ti to approximate biogenic silica concentrations (Figure 2.4). Si:Ti is generally high and quite variable throughout Unit 1 relative to Unit 2, then decreases dramatically at the transition from Unit 1 to Unit 2.

$C:N_{org}$ decreases abruptly from an average of 13.8 in Unit 1 to 9.69 in Unit 2 (Figure 2.4). Within Unit 1, $C:N_{org}$ is punctuated by seven extremely low values, each occurring in black fine-sand layers and ash beds. These beds have exceedingly low %TOC and %TN, suggesting these data points are inaccurate due to low organic matter content. $\delta^{15}N_{org}$ values average 0.65‰ in Unit 1 with little variability and show a rapid enrichment to an average of 3.82‰ in Unit 2 that is simultaneous with an increase in Ti and decreases in $C:N_{org}$ and %biogenic opal (Figures 2.3, 2.4). The average value of $\delta^{13}C_{org}$ is -27.1‰ and varies considerably throughout the record, ranging from -22.92 to -30.36‰. A long-term trend toward isotopically depleted $\delta^{13}C_{org}$ values begins ~1200 CE and ends ~1800 CE. Century-scale intervals of enriched $\delta^{13}C_{org}$ superimposed on the long-term trend in Unit 1 are concurrent with increases in %TIC and Ca:Ti, and the enrichment of $\delta^{13}C_{org}$ in Unit 2 coincides with $\delta^{15}N_{org}$ enrichment.

Average mass accumulation rates of terrigenous material, organic matter, biogenic silica, and carbonate to the sediments, calculated from these data between 440 and 690 cm and 0 and 116 cm, where sediment accumulation rates are well constrained by ^{14}C dates and ^{210}Pb dates, respectively, indicate an enormous increase in mass flux of all sediment components in the younger sediments. Accumulation rates of terrigenous material, organic matter, and biogenic silica increased from 10 to 213 mg cm^{-2} yr^{-1}, 6 to 22 mg cm^{-2} yr^{-1}, and 9 to 52 mg cm^{-2} yr^{-1}, respectively.

2.5 Discussion

2.5.1 Evidence for anthropogenic impacts ca. 1860 CE

Ti is incorporated into the sediments only through terrestrial inputs; consequently increases in magnetic susceptibility and Ti are interpreted to indicate an increase in terrestrial runoff, except in tephra beds. Therefore, increased Ti, Fe, magnetic susceptibility, and a nearly order of magnitude increase in sedimentation rates indicate a large, abrupt increase in terrigenous inputs to Lake Logung at the transition from Unit 1 to 2 at 1860 CE (Figures 2.2, 2.3). Indeed, virtually all data in Lake Logung exhibit drastically different behavior in Unit 2 compared to Unit 1, documenting a profound environmental shift during the mid-1800s. The rise in terrigenous inputs occurred amidst a period of extensive land clearance during the Cultuurstelsel, a widespread forced cultivation program in Java that began in 1830 and intensified until it was brought to an end in 1870 (Poesponegoro and Notosusanto 1984). We suggest that the changes in our data at 1860 CE document anthropogenic land clearance, erosion, and the beginning of agricultural practices within the Logung catchment, triggering the dramatic increase in clastic sedimentation as well as increased nutrient loading and aquatic primary productivity.

Numerous bulk organic geochemical indicators in our core suggest increased productivity associated with land clearance, including changes in $C:N_{org}$, as well as %TOC, %TN, and %BSi. While magnetic susceptibility and Ti data document a clear increase in clastic sediment supply to Logung, the simultaneous decrease in $C:N_{org}$ suggests a shift in organic matter source from a mix of aquatic and terrestrial organic matter during Unit 1 to dominantly aquatic organic matter deposited in the last 150 yrs (Meyers and Lallier-Vergès 1999; Figure 2.4). This occurs despite evidence for increased delivery of soil-derived clastic minerals to the lake, suggesting an increase in aquatic primary productivity accompanied the increase in terrigenous sediment supply. While %TOC and Si:Ti decrease at the beginning of Unit 2, these declines reflect dilution of organic matter and biogenic opal due to the massive influx of terrestrial material (Figure 2.4). Increased aquatic productivity in Unit 2 is strongly supported by the 4-fold and 6-fold increases in the mass accumulation rates of organic matter and biogenic opal, respectively, relative to Unit 1. Interestingly, $C:N_{org}$ is low throughout Unit 2 despite the gradual decline in Ti and magnetic susceptibility, indicating high aquatic primary productivity continued despite changes in the extent of anthropogenic soil erosion, potentially due to recycling of nutrients within the lake or continued delivery of nutrients to the lake during the last 150 years.

These changes are accompanied by isotopic enrichment in the $\delta^{13}C$ and $\delta^{15}N$ of organic matter in Lake Logung. Numerous factors influence lacustrine $\delta^{15}N_{org}$ and $\delta^{13}C_{org}$, including both lacustrine and terrestrial processes. Aquatic photosynthetic organisms preferentially utilize ^{14}N and ^{12}C, thus an increase in productivity enriches the $\delta^{15}N$ and $\delta^{13}C$ of the water and algal organic matter (Fogel and Cifuentes 1993; Hollander and McKenzie 1991). Enrichments in $\delta^{15}N_{org}$ and $\delta^{13}C_{org}$ in Unit 2 therefore likely result, at least partly, from enhanced productivity, stimulated by an increase in nutrient flux from the landscape (Figure 2.4). Although $\delta^{13}C_{org}$ enrichment in tropical lake sediment can indicate an increase in the ratio of C_4 versus C_3 plants (O'Leary 1988; Russell et al. 2009), this seems unlikely in Unit 2, as the $C:N_{org}$ values, along with clear evidence for an increase in aquatic productivity, imply aquatic sources dominate the sediment organic matter. Moreover, the Cultuurstelsel drove extensive cultivation of coffee in east Java, which is not a C_4 plant.

Isotopic enrichment of the DIN reservoir in the lake due to the sudden addition of anthropogenic materials is commonly observed in the $\delta^{15}N_{org}$ preserved in the sediments in lakes such as Lake Ontario (Hodell and Schelske 1998) and in tropical lakes such as Lake Wandakara (Russell et al. 2009), although the processes are unclear. The consistently low $\delta^{15}N_{org}$ prior to the rise in terrestrial inputs, averaging 0.65‰, is characteristic of nitrogen derived from cyanobacterial nitrogen fixation, which involves minimal fractionation of gaseous atmospheric N_2 (Talbot 2001). In Unit 2, increased fluxes of terrestrial plant material to the lake, which typically have $\delta^{15}N$ values between 2 and 10‰ (Talbot 2001), could cause or contribute to the ~5‰ enrichment observed in $\delta^{15}N_{org}$ at the beginning of Unit 2; however, $\delta^{15}N_{org}$ does not decline during the subsequent decrease in terrigenous inputs documented by magnetic susceptibility and Ti counts. The ~5‰ enrichment in $\delta^{15}N_{org}$ is also characteristic of the addition of fertilizers and manure, which typically contain enriched $\delta^{15}N$ values ranging from 5 to 25‰ (Heaton 1986; Kendall 1998). Moreover, $\delta^{15}N_{org}$ data could provide evidence for changes in lacustrine nitrogen cycling, as enriched $\delta^{15}N_{org}$ coupled with evidence for hypolimnetic anoxia in Unit 2 could imply increased rates of denitrification in hypoxic to anoxic bottom waters (Hodell and Schelske 1998).

Indeed, smear slide analyses reveal the presence of siderite in sediments in Unit 1. Siderite has been observed in sediments deposited under stratified, wet conditions in deep lakes in Eastern Java (Crausbay et al. 2006), and its presence is typically associated with anoxic hypolimnetic conditions. Siderite precipitated in the water column requires anoxic bottom water, whereas diagenetic siderite requires anoxia only in the sediments (Kelts and Hsü 1978; Faure 1998). Although it is unclear whether the siderite in Lake Logung formed within the water column or sediments, we observe siderite only in the sediments of Unit 1. These data suggest the development of anoxic conditions during the main phase of human impacts on Lake Logung, consistent with numerous studies of hypolimnetic anoxia during cultural eutrophication in many lake systems (Myrbo 2008; Stoermer et al. 1996).

Although the increase in terrigenous sediment flux could result from either anthropogenic land clearance or increased precipitation and runoff, its magnitude, coupled with clear biological changes in the lake marked by increased primary productivity and $\delta^{15}N_{org}$ and $\delta^{13}C_{org}$ enrichment, indicate that human activity is at least partially, if not largely responsible for this transition. In this context, it is important to note that nearby station data do not display a dramatic increase in rainfall circa 1860 CE (Vose et al. 1992). Therefore, we conclude that anthropogenic activity occurred in the catchment of Lake Logung circa 1860 CE.

2.5.2 Paleoclimate changes during the past 1,400 years

Variations in lacustrine sedimentation in Lake Logung, and particularly variations in calcium carbonate content, record clear evidence for decade- to century-scale changes in moisture balance in East Java during the past millennium. Carbonate presence and mineralogy in tropical lake sediments has been commonly used in conjunction with other proxy data to interpret paleohydrological histories, where the ratio of precipitation to evaporation, often accompanied by shifts between open-basin and closed-basin conditions, is the dominant control on carbonate precipitation, such as in Lake Malawi (Brown et al. 2007), Edward (Russell et al. 2003), Bosumtwi (Talbot and Kelts 1986), and Lamongan (Crausbay et al. 2006). Calcite mineral grains observed in smear slides consist primarily of euhedral crystals, indicating an authigenic origin and documenting substantial changes in lake water chemistry and salinity through time. In low-salinity lakes like Logung, decreased regional precipitation:evaporation results in evaporatively driven increases in salinity, driving Ca^{2+} and CO_3^{2-} concentrations to calcite saturation (Müller et al. 1972; Kelts and Hsü 1978). Lacustrine calcite precipitation can also be initiated through an increase in pH driven by CO_2 consumption during periods of heightened aquatic primary productivity (Kelts and Hsü 1978). There is, however, no correlation between %TIC and indicators of primary productivity such as $C:N_{org}$ values or %biogenic opal in Unit 1 (Figure 2.4). In lakes that are supersaturated with respect to calcite, positive shifts in lake water balance that deliver excess Ca^{2+} and HCO_3^- to the lake result in enhanced calcite accumulation in the sediments. In groundwater-fed systems, this can result in a positive correlation between calcite flux to sediments and lake hydrologic balance (Shapley et al. 2005; 2010). We do not, however, expect the groundwater from the mafic volcanic landscape to be a significant source of Ca^{2+} and HCO_3^- to the lake.

Several additional lines of evidence point to drought during calcite events, including variations in $\delta^{13}C_{org}$. The occurrence of relatively enriched $\delta^{13}C_{org}$ in calcite beds (Figure 2.4) can be achieved by multiple mechanisms that influence the $\delta^{13}C$ of lake water, and hence $\delta^{13}C_{org}$. Increases in the residence time of lacustrine dissolved inorganic carbon in response to negative hydrologic balance and increased lake salinity can enrich $\delta^{13}C_{org}$ derived from aquatic sources (Kelts and Hsü 1978). Moreover, as lake alkalinity increases in response to drought, many algal taxa can shift to utilize dissolved bicarbonate rather than CO_2, further enriching $\delta^{13}C_{org}$. Finally, variations in the vegetation within the lake catchment can influence $\delta^{13}C_{org}$. The $\delta^{13}C$ of terrestrial vegetation typically ranges from -33 to -24‰ in C_3 plants and from -16 to -10‰ in C_4 plants (O'Leary 1988; Talbot 1990). Changes in the relative abundances of these plants in lake catchments can affect lacustrine $\delta^{13}C_{org}$, both through direct incorporation of terrestrial plant debris, as well as changes in the $\delta^{13}C$ of dissolved organic and inorganic carbon delivered to the lake from catchment soils. In some tropical lake sediments, bulk organic $\delta^{13}C$ values are equivalent to the $\delta^{13}C$ values of landscape vegetation (Huang et al. 1999; Russell et al. 2009). Therefore, shifts toward a greater abundance of C_4 plants, which are favored under dry conditions (Collatz et al. 1998), can partially account for $\delta^{13}C_{org}$ enrichment during drought. We do not believe variations in $\delta^{13}C_{org}$ are caused by organic matter degradation, since there is no systematic relationship between $\delta^{13}C_{org}$ and $C:N_{org}$ (Figure 2.4).

Given the numerous pathways by which $\delta^{13}C_{org}$ enrichment can occur in response to drought in tropical lakes, as well as the covariation between %TIC and $\delta^{13}C_{org}$, we interpret $\delta^{13}C_{org}$ enrichment to indicate relatively dry conditions. We take a conservative approach by defining drought intervals in our record only as intervals where enrichment in $\delta^{13}C_{org}$ is accompanied by an increase in %TIC, however additional periods of enriched $\delta^{13}C_{org}$ could also be indicative of drought, such as that centered at 1300 CE. Following these lines of reasoning, the long-term trend toward depleted $\delta^{13}C_{org}$ values during the last millennium signifies a gradual transition toward wetter conditions, while calcite deposition events, coupled with $\delta^{13}C_{org}$ enrichment, indicate periods of drought, with major events occurring from 930 to 1130, 1460 to 1640, 1790 to 1860, and 1985 to 2008 CE.

There are several important caveats to consider with the calcite drought proxy, including lags between onset of drought and onset of calcite precipitation, the lag time between the cessation of a drought and termination of the calcite precipitation, and the sensitivity of calcite precipitation to hydrologic conditions. The amount of time between the onset of drought and calcite precipitation depends on the state of the lake water chemistry prior to the onset of the drought; i.e. how much water must be evaporated from the lake to drive it to calcite saturation. For this reason, it is possible that not all droughts in East Java appear as calcite precipitation events in Lake Logung. Following a drought, calcite precipitation can continue for a period of time before increased rainfall reduces the salinity of the lake to below calcite saturation. For this reason, droughts documented in the Lake Logung record may appear to last significantly longer than they would in the historical record, and it is possible that a single calcite bed may represent multiple droughts rather than one prolonged period of drought. This is particularly the case in lakes such as Lake Logung that fluctuate around their outlet level, leading to shifts between closed- and open-basin conditions.

Additionally, the increased delivery of calcite to the sediments can temporarily increase linear sedimentation rates within calcite beds, causing errors in the duration of droughts calculated from a linearly interpolated age model. We explored the potential effects of carbonate accumulation on net sediment accumulation rates by creating a new age model that assumes all sediment components other than $CaCO_3$ accumulated in the sediment at a constant rate. In this model, addition of 5-43% $CaCO_3$ to lengths of sediment equivalent to the duration of our carbonate-inferred droughts can increase the duration of each carbonate precipitation event by merely six years due to short-lived, 2.6 to 4.9% increases in sedimentation rate associated with the rapid addition of $CaCO_3$. These small offsets are well within the error of our age model, implying that carbonate accumulation has an insignificant effect on the accuracy of the core chronology. Moreover, the timing of changes in %TIC and other drought indicators, such as $\delta^{13}C_{org}$, appears to be very similar in our core, suggesting that there is little time lag between the onset and termination of droughts and changes in %TIC.

Our data clearly elucidate the hydrology of Lake Logung during the past millennium. $\delta^{13}C_{org}$ data suggest a gradual transition from drier to wetter conditions during the last millennium. Dry intervals superimposed on this millennial-scale variability occur from 930 to 1130, 1460 to 1640, 1790 to 1860, and 1985 to 2008 CE, when calcite abundance in the sediments is high and $\delta^{13}C_{org}$ is more enriched. Prior to 930 CE, and from 1130 to 1460 and 1640 to 1790 CE, calcite abundances are low and $\delta^{13}C_{org}$ is more depleted, while periods of increased terrestrial runoff represented by Ti peaks are more frequent; we interpret these as relatively wet intervals.

2.5.3 Paleoclimate implications

Our data document considerable millennial- and centennial-scale hydrologic variability in East Java, Indonesia over the past ~1,400 yrs. To explore the potential climatic controls on the hydrologic history of East Java, we compare the timing of the droughts in our record with other Western Pacific paleohydrological records, as well as datasets that document changes in the mean position of the ITCZ and ENSO variability over the past ~2 millennia (Figure 2.1).

Cave $\delta^{18}O$ records in China, lake sediment records across the tropical Pacific, and Makassar Strait $\delta^{18}O$ and δD_{wax} records provide clear evidence for changes in monsoon strength and associated migration of the mean position of the ITCZ over the tropical western Pacific during the past millennium (Figure 2.5; Wang et al. 2005; Zhang et al. 2008; Sachs et al. 2009; Oppo et al. 2009; Tierney et al. 2010). These records suggest the ITCZ reached its northernmost extent between 900 and 1100 CE, shifted southward and reached its southernmost extent between 1420 and 1640 CE, and then began to shift northward between *ca*. 1700 and 1800 CE (Sachs et al. 2009; Zhang et al. 2008; Wang et al. 2005). Paleoclimate models and theory indicate that these shifts are a response to changes in the interhemispheric heat gradient over the past millennium (Broccoli et al. 2006); namely the warm conditions associated with the "Medieval Climate Anomaly" (MCA) in the 900s to the 1100s, and the cool "Little Ice Age" (LIA) from the 1300s to the 1800s. Assuming that southward migration of the ITCZ would increase precipitation at our site in East Java (~8°S), the trend toward a wetter climate over the last millennium observed in the Lake Logung $\delta^{13}C_{org}$ is evidence that the mean position of the ITCZ is a primary control on millennial-scale moisture balance variations in East Java (Figure 2.5). Moreover, we note that the millennial-scale patterns that we observe in East Java are highly coherent with sea surface salinity and leaf wax δD data from the Makassar Strait (Figure 2.5; Oppo et al. 2009; Tierney et al. 2010), suggesting coherent hydrologic variability over much of Indonesia at this time scale.

Two of the four multidecadal- to centennial-scale droughts in the Lake Logung record occurred when lake sediment records from across the tropical Pacific Ocean and oxygen and deuterium isotopic data from caves in China and sediment in the Makassar Strait suggest the ITCZ was displaced to the south (Sachs et al. 2009; Wang et al. 2005; Zhang et al. 2008; Oppo et al. 2009; Tierney et al. 2010), which suggests that at least some of the decade- to century-scale droughts in East Java are not primarily controlled by the mean position of the ITCZ (Figure 2.5). These droughts coincide with evidence for drought in paleohydrological reconstructions from the Makassar Strait, implying that our drought record is representative of regional hydrologic variations (Figure 2.5). Drought from 1460 to 1640 CE in the Lake Logung record is synchronous with the most prolonged drought recorded in Lake Lamongan (7°59'S, 113°23'E), another maar lake on the southwest side of the Gunung Lamongan volcano (Figure 2.5; Crausbay et al. 2006). The two recent droughts from our record are not concurrent with periods of prolonged drought in Lake Lamongan. The lack of a ^{210}Pb chronology from Lake Lamongan, however, coupled with gaps between core sections and errors in sediment radiocarbon dates, causes large age uncertainties in the upper sediments of the Lamongan sequence. The 1460 to 1640 CE drought in our record also coincides with dry conditions observed during the 16th and 17th centuries in a ~500-yr dinosterol δD record of hydrologic variability derived from sediments from Spooky Lake, Palau (7°09'N, 134°22'E; Sachs et al. 2009). The onset of the 1790 to 1860 CE drought in the Lake Logung record coincides with a historically documented, dramatic drought that resulted from a series of severe El Niño events and impacted much of southern Asia, including Java, in the late 1700s (Grove 1998). Late 1700s drought is also recorded in $\delta^{18}O$, dust, and chloride concentrations in Himalayan ice cores, which indicate drought conditions persisted until 1796 CE (Thompson et al. 2000).

Our most recent drought occurs at a time when in-lake processes are heavily influenced by anthropogenic activity; the presence of calcium carbonate and enriched $\delta^{13}C$ in the sediments during the last 25 years may result from human activity rather than a change in climate. There is, however, evidence for a reduction in convection beginning around 1970, in isotopic enrichments in the δD_{wax} record from the Makassar Strait (Figure 2.5; Tierney et al. 2010) and in the dinosterol δD record from Spooky Lake (Sachs et al. 2009). δD_{wax} enrichment in the Makassar Strait is attributed to the isotopic enrichment in rainfall due to either a reduction of tropical convective mass flux over Indonesia associated with a weakened Walker Circulation (Vecchi et al. 2006), or changes in evaporation rates and recycling occurring in the rainfall source region (Tierney et al. 2010). While these processes could affect δD_{wax}, dinosterol δD enrichment in Spooky Lake is attributed to drought in Palau during multiple strong El Niño events during recent decades (Sachs et al. 2009), such as the 1982/83 and 1997/98 El Niño events (Cane 1983; McPhaden 1999). Thus, multiple independent lines of evidence, ranging from these isotopic records to our Lake Logung record, indicate coherent patterns of climate variability, consistent with drought on both sides of the equator, and provide further evidence that the mechanism driving hydrologic variability at these time scales within the WPWP relates to changes in Walker Circulation dynamics. The spatial relationships of drought across the northern and southern tropics, consistent with El Niño event-driven drought, and the concurrence of historical El Niño events and increasing pressure over the WPWP during the most recent drought in Lake Logung, suggest decade- to century-scale drought in Lake Logung is controlled by variations in ENSO. If so, it is interesting to note that regional drought in the Lake Lamongan and Lake Logung records between 1450 and 1650 CE coincides with a period of Northern Hemispheric cooling when many data indicate the ITCZ was displaced to the south, as southward ITCZ displacement promotes the formation of El Niño events on an interannual time scale (Cane 2005). We also observe drought, however, from 930 to 1130 CE, during a period of Northern Hemisphere heating, thus our record does not reveal a clear relationship between interhemispheric heat gradients and century-scale ENSO variability.

2.6 Conclusions

We present a new, high-resolution drought record from the climatically important WPWP region. Our data suggest enhanced anthropogenic activity within the catchment of Lake Logung began circa 1860 CE. Prior to that time, variations in the lake sediment composition likely reflect the response of lacustrine sedimentation processes to climate forcing. Our record documents four droughts during the past 1400 years that occurred from 930 to 1130, 1460 to 1640, 1790 to 1860, and 1985 to 2008 CE, superimposed on a long-term trend toward wetter conditions in East Java throughout the past millennium. We suggest that while this long-term pattern likely results from ITCZ migration, the spatial relationships between the higher-frequency droughts documented in our record and the hydrological trends observed in reconstructions from other sites in the WPWP region are consistent with patterns in hydrology associated with ENSO dynamics. This interpretation is supported by the co-occurrence of drought with historically documented regional drought associated with a failure of the Southeast Asian monsoon during El Niño events.

2.7 Acknowledgments

We thank Dave Murray, Joe Orchardo, and Candice Bousquet for laboratory assistance. We also thank the Limnological Research Center for assistance with Corewall and x-ray diffraction. We thank the anonymous reviewers whose comments improved the quality of this manuscript. We thank the Government of Indonesia and

Indonesian Ministry of Research and Technology (RISTEK) for permission and assistance in conducting field research. This research was funded by NOAA award NA09OAR4310107 and a National Geographic Society research grant to J. Russell.

2.8 References

Appleby, P.G., 1997. Sediment records of fallout radionuclides and their application to studies of sediment-water interactions. Water Air Soil Pollut. 99, 573-586.

Appleby, P.G., Oldfield, F., 1978. The calculation of ^{210}Pb dates assuming a constant rate of supply of unsupported ^{210}Pb to the sediment. Catena 5, 1-8.

Björck, S., Håkansson, S., 1982. Radiocarbon dates from Late Weichselian lake sediments in South Sweden as a basis for chronostratigraphic subdivisions. Boreas 11, 141-150.

Broccoli, A.J., Dahl, K.A., Stouffer, R.J., 2006. Response of the ITCZ to Northern Hemispheric cooling. Geophys. Res. Lett. 33, L01702, doi: 10.1029/2005GL024546.

Brown, E.T., Johnson, T.C., Scholz, C.A., Cohen, A.S., King, J.W., 2007. Abrupt change in tropical African climate linked to the bipolar seesaw over the past 55,000 years. Geophys. Res. Lett. 34, L20702, doi: 10.1029/2007GL031240.

Byron, N., Shepherd, G., 1998. Indonesia and the 1997-98 El Niño: Fire problems and long-term solutions. Nat. Resour. Perspect. 28.

Cane, M.A., 1983. Oceanographic Events during El Niño. Science 222, 1189-1195.

Cane, M.A., 2005. The evolution of El Niño, past and future. Earth Planet. Sci. Lett. 230, 227-240.

Carn, S.A., Pyle, D.M., 2001. Petrology and geochemistry of the Lamongan Volcanic Field, East Java, Indonesia: primitive Sunda Arc magmas in an extensional tectonic setting? J. Petrology. 42, 1643-1683.

Collatz, G.J., Berry, J.A., Clark, J.S., 1998. Effects of climate and atmospheric CO_2 partial pressure on the global distribution of C_4 grasses: present, past, and future. Oecologia 114, 441-454.

Crausbay, S.D., Russell, J.M., Schnurrenberger, D.W., 2006. A ca. 800-year lithological record of drought from sub-annually laminated lake sediment, East Java. J. Paleolimnol. 35, 641-659.

DeMaster, D.J., 1981. The supply and accumulation of silica in the marine environment. Geochim. Cosmochim. Acta. 45, 1715–1732.

Faure, G., 1998. Principles and Applications of Geochemistry. Prentice Hall, Upper Saddle River, NJ, pp. 600.

Fogel, M.L., Cifuentes, L.A., 1993. Isotope fractionation during primary production. In: Engel MH, Macko SA (eds.) Organic Geochemistry: Principles and Applications. Plenum Press, New York, pp. 73-98.

Goldsmith, J.R., Graf, D.L., 1958. Relation between lattice constants and composition of the Ca-Mg carbonates. Am. Mineral. 43, 84-101.

Green, J., Corbet, S.A., Watts, E., Lan, O.B., 1976. Ecological studies on Indonesian lakes. Overturn and restratification of Lake Lamongan. J. Zool. 180, 315-354.

Griffiths, M.L., Drysdale, R.N., Gagan, M.K., Zhao, J-x., Ayliffe, L.K., Hellstrom, J.C., Hantoro, W.S., Frisia, S., Feng, Y-x., Cartwright, I., St. Pierre, E., Fischer, M.J., Suwargadi, B.W., 2009. Increasing Australian-Indonesian monsoon rainfall linked to early Holocene sea-level rise. Nat. Geosci. 2, 636-639.

Grove, R.H., 1998. Global impact of the 1789-93 El Niño. Nature 393, 318-319.

Heaton, T.H.E., 1986. Isotopic Studies of nitrogen pollution in the hydrosphere and atmosphere: A review. Chem. Geol. 59, 87-102.

Heegaard, E., Birks, H.J.B., Telford, R.J., 2005. Relationships between calibrated ages and depth in stratigraphical sequences: an estimation procedure by mixed-effect regression. The Holocene 15, 612-618.

Hendon, H.H., 2003. Indonesian Rainfall Variability: Impacts of ENSO and Local Air-Sea Interaction. J. Climate. 16, 1775-1790.

Hodell, D.A., Schelske, C.L., 1998. Production, sedimentation, and isotopic composition of organic matter in Lake Ontario. Limnol. Oceanogr. 43, 200-214.

Hollander, D.J., McKenzie, H.L., 1991. CO_2 control on carbon-isotope fractionation during aqueous photosynthesis: A paleo-$p$$CO_2$ barometer. Geology 19, 929-932.

Huang, Y., Street-Perrott, F.A., Perrott, R.A., Metzger, P., Eglinton, G., 1999. Glacial-interglacial environmental changes inferred from molecular and compound-specific $\delta^{13}C$ analyses of sediments from Sacred Lake, Mt. Kenya. Geochim. Cosmochim. Acta 63, 1383-1404.

Kelts, K., Hsü, K.J., 1978. Freshwater carbonate sedimentation. In: Lerman A (ed.) Lakes: Chemistry, Physics, Geology. Springer-Verlag, New York, pp. 295-323.

Kendall, C., 1998. Tracing nitrogen sources and cycling in catchments. In Kendall C, McDonnell JJ (eds.) Isotope Tracers in Catchment Hydrology. Elsevier, Amsterdam, 519-576.

Mackereth, F.J.H., 1966. Some chemical observations on post-glacial lake sediments. Philos. Trans. R. Soc. Lond. B250, 165-213.

McPhaden, M.J., 1999. Genesis and evolution of the 1997-98 El Niño. Science 283, 950-954.

Meyers, P.A., Lallier-Vergès, E., 1999. Lacustrine sedimentary organic matter records of Late Quaternary paleoclimates. J. Paleolimnol. 21, 345-372.

Müller, G., Irion, G., Förstner, U., 1972. Formation and diagenesis of inorganic Ca-Mg carbonates in the lacustrine environment. Naturwissenschaften 59, 158-164.

Myrbo, A., 2008. Sedimentary and historical context of eutrophication and remediation in urban Lake McCarrons (Roseville, Minnesota). Lake and Reservoir Management 24, 349-360.

Naylor, R.L., Falcon, W.P., Rochberg, D., Wada, N., 2001. Using El Niño/Southern Oscillation climate data to predict rice production in Indonesia. Clim. Change 50, 255-265.

O'Leary, M.H., 1988. Carbon Isotopes in Photosynthesis. Bioscience 38, 328-336.

Oppo, D.W., Rosenthal, Y., Linsley, B.K., 2009. 2,000-year-long temperature and hydrology reconstructions from the Indo-Pacific warm pool. Nature 460, 1113-1116.

O'Sullivan, P.E., Oldfield, F., Battarbee, R.W., 1973. Preliminary studies of Lough Neagh sediments I. Stratigraphy, chronology and pollen analysis. In: Birks HJB, West RG (eds.) Quaternary Plant Ecology. Blackwell Scientific Publications, Oxford, pp. 267-278.

Pierrehumbert, R.T., 2000. Climate change and the tropical Pacific: The sleeping dragon wakes. Proc. Natl. Acad. Sci. 97, 1355-1358.

Plummer, L.N., Busenberg, E., 1982. The solubilities of calcite, aragonite and vaterite in CO_2–H_2O solutions between 0 and 90°C, and an evaluation of the aqueous model for the system $CaCO_3$–CO_2–H_2O. Geochim. Cosmochim. Acta 46, 1011-1040.

Poesponegoro, M.D., Notosusanto, N., 1984. Sejarah Nasional Indonesia (Indonesian National History) Book IV. PN Balai Pustaka.

Quinn, W.H., Zopf, D.O., Short, K.S., Kuo, Yang, R.T.W., 1978. Historical trends and statistics of the Southern Oscillation, El Niño, and Indonesian droughts. Fish. Bull. 76, 663-678.

Rao, A., Rack, F., Kamp, B., Fils, D., Ito, E., Morin, P., Higgins, S., Leigh, J., Johnson, A., Renambot, L., 2005. CoreWall: A Scalable Interactive Tool for Visual Core Description, Data Visualization, and Stratigraphic Correlation. Eos Trans. AGU, 86(52), Fall Meet. Suppl., San Francisco, CA, 12/05/2005.

Russell, J.M., Johnson, T.C., 2005. A high-resolution geochemical record from Lake Edward, Uganda Congo and the timing and causes of tropical African drought during the late Holocene. Quat. Sci. Rev. 24, 1375-1389.

Russell, J.M., Johnson, T.C., Kelts, K.R., Laerdal, T., Talbot, M.R., 2003. An 11,000 year lithostratigraphic and paleohydrologic record from equatorial Africa: Lake Edward, Uganda-Congo. Palaeogeogr. Palaeoclimatol. Palaeoecol. 193, 25-49.

Russell, J.M., McCoy, S.J., Verschuren, D., Bessems, I., Huang, Y., 2009. Human impacts, climate change, and aquatic ecosystem response during the past 2000 yr at Lake Wandakara, Uganda. Quat. Res. 72, 315-324.

Sachs, J.P., Sachse, D., Smittenberg, R.H., Zhang, Z., Battisti, D., Golubic, S., 2009. Southward movement of the Pacific intertropical convergence zone AD 1400-1850. Nat. Geosci. 2, 519-525.

Schnurrenberger, D., Russell, J.M., Kelts, K., 2003. Classification of lacustrine sediments based on sedimentary components. J. Paleolimnol. 29, 141-154.

Shapley, M.D., Ito, E., Donovan, J.J., 2005. Authigenic calcium carbonate flux in groundwater-controlled lakes: Implications for lacustrine paleoclimate records. Geochim. Cosmochim. Acta 69, 2517-2533.

Shapley, M.D., Ito, E., Forester, R.M., 2010. Negative correlations between Mg:Ca and total dissolved solids in lakes: False aridity signals and decoupling mechanisms for paleohydrologic proxies. Geology 38, 427-430.

Stoermer, E.F., Emmert, G., Julius, M.L., Schelske, C.L., 1996. Paleolimnologic evidence of rapid recent change in Lake Erie’s trophic status. Can. J. Fish. Aquat. Sci. 53, 1451-1458.

Stuiver, M., Reimer, P.J., 1993. Extended ^{14}C data base and revised Calib 3.0 ^{14}C age calibration program. Radiocarbon 35, 215–230.

Talbot, M.R., 1990. A review of the palaeohydrological interpretation of carbon and oxygen isotopic ratios in primary lacustrine carbonates. Chem. Geol. 80, 261-279.

Talbot, M.R., 2001. Nitrogen Isotopes in Palaeolimnology. In: Last WM, Smol JP (eds) Tracking Environmental Change Using Lake Sediments 2, Kluwer Academic Publishers, Dordrecht, The Netherlands, pp. 401-439.

Talbot, M.R., Kelts, K., 1986. Primary and diagenetic carbonates in the anoxic sediments of Lake Bosumtwi, Ghana. Geology 14, 912-916.

Thompson, L.G., Yao, T., Mosley-Thompson, E., Davis, M.E., Henderson, K.A., Lin, P-N., 2000. A high-resolution millennial record of the south Asian monsoon from Himalaya Ice Cores. Science 289, 1916-1919.

Tierney, J.E., Oppo, D.W., Rosenthal, Y., Russell, J.M., Linsley, B.K., 2010. Coordinated hydrological regimes in the Indo-Pacific region during the past two millennia. Paleoceanography 25, PA1102, doi: 10.1029/2009PA001871.

Vecchi, G.A., Soden, B.J., Wittenberg, A.T., Held, I.M., Leetmaa, A., Harrison, M.J., 2006. Weakening of tropical Pacific atmospheric circulation due to anthropogenic forcing. Nature 441, 73-76.

Verschuren, D., 1993. A lightweight extruder for accurate sectioning of soft-bottom lake sediment cores in the field. Limnol. Oceanogr. 38, 1796-1802.

Vose, R.S., Schmoyer, R.L., Steurer, P.M., Peterson, T.C., Heim, R., Karl, T.R., Eischeid, J., 1992. The Global Historical Climatology Network: Long-term monthly temperature, precipitation, sea level pressure, and station pressure data. ORNL/CDIAC-53, NDP-041. Carbon Dioxide Information Analysis Center, Oak Ridge National Laboratory, Oak Ridge, Tennessee.

Wang, Y., Cheng, H., Edwards, R.L., He, Y., Kong, X., An, Z., Wu, J., Kelly, M.J., Dykoski, C.A., Li, X., 2005. The Holocene Asian monsoon: Links to solar changes and North Atlantic climate. Science 308, 854-857.

Zhang, P., Cheng, H., Edwards, R.L., Chen, F., Wang, Y., Yang, X., Liu, J., Tan, M., Wang, X., Liu, J., An, C., Dai, Z., Zhou, J., Zhang, D., Jia, J., Jin, L., Johnson, K.R., 2008. A test of climate, sun, and culture relationships from an 1810-yr Chinese cave record. Science 322, 940-942.

Cumulative Sediment Depth (cm)	NOSAMS accession number	Dated Material	14C age (years BP)	Calibrated Age (year CE)	2 Sigma Age Range 1 in years CE (probability)	2 Sigma Age Range 2 in years CE (probability)	2 Sigma Age Range 3 in years CE (probability)	2 Sigma Age Range 4 in years CE (probability)
251.1	77290	Charcoal	810 ± 40	1219	1160:1277 (1)			
299.3	77306	Charcoal	1000 ± 30	1018	983:1052 (0.740)	1081:1128 (0.200)	1135:1152 (0.060)	
315	79448	Bulk Sediment	815 ± 25	1223	1178:1267 (1)			
331.6	77291	Charcoal	1030 ± 40	993	938:1047 (0.835)	895:924 (0.087)	1088:1122 (0.061)	1138:1150 (0.017)
371.9	79541	Bulk Sediment	800 ± 35	1226	1176:1276 (1)			
389.3	77307	Charcoal	940 ± 30	1092	1025:1159 (1)			
435.3*	77308	Bulk Sediment	330 ± 25	1562	1483:1641 (1)			
488.3*	77309	Wood	720 ± 25	1278	1257:1298 (0.983)	1371:1378 (0.017)		
555	77320	Charcoal	1450 ± 40	601	547:655 (1)			
600.4	77319	Charcoal	1440 ± 35	609	561:656 (1)			
602.9*	77310	Plant	1130 ± 25	925	863:987 (0.982)	826:841 (0.017)	784:786 (0.001)	
602.9	79449	Bulk Sediment	1310 ± 30	692	656:728 (0.700)	736:772 (0.300)		
660*	77311	Plant	1390 ± 30	638	603:672 (1)			
681*	79450	Bulk Sediment	1410 ± 25	631	601:661 (1)			

Table 2.1: AMS ^{14}C dates are listed in order of increasing cumulative depth with NOSAMS accession number, type of material submitted for dating (charcoal, wood, plant material, and bulk sediment), radiocarbon age (years BP), calibrated age (year in the common era (CE)), and two sigma calibrated age ranges in years CE with their associated probabilities. Samples marked with an asterisk were included in the age model. Ash beds were removed from composite depth for application of the age model and were then reinserted. Listed depths are the composite depth after removal of ash beds

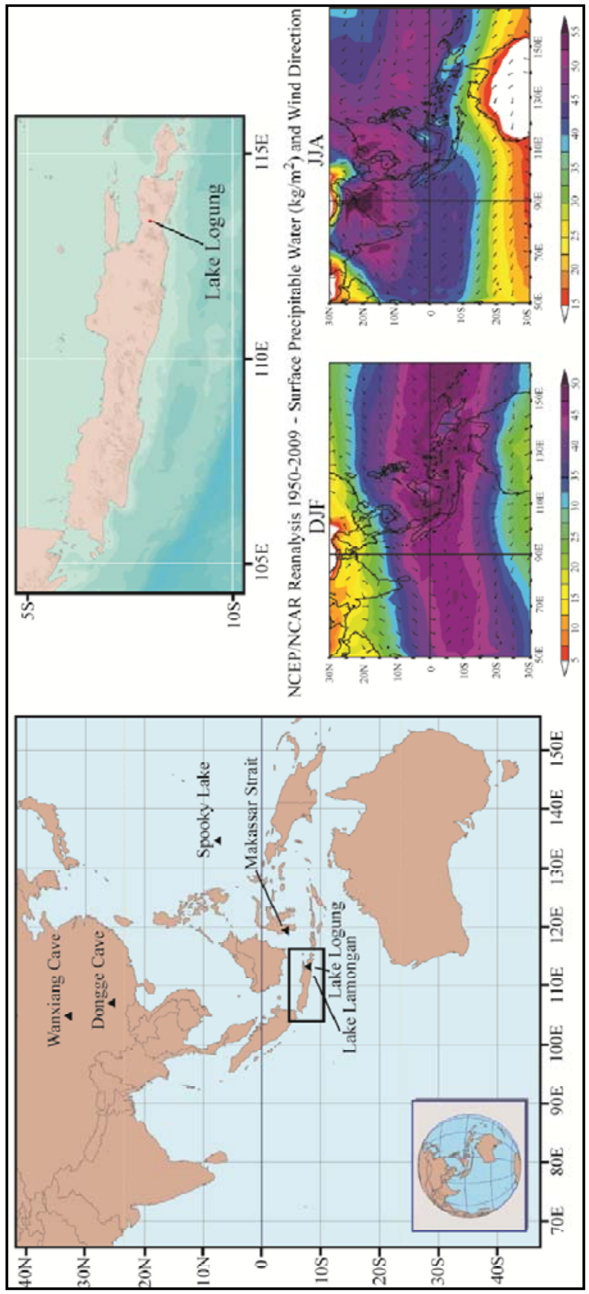

Figure 2.1: Left: Map of Southeast Asia and Australia with Java, Indonesia outlined in the rectangle. Triangles mark climate records that are included in the discussion section. Top Right: Map of Java, Indonesia, highlighting our study site. Bottom right: contour maps of NCEP/NCAR Reanalysis composite means of surface precipitable water in kg m^{-2} with arrows denoting wind direction for the period 1950 to 2009 for wet season (DJF, left) and dry season (JJA, right).

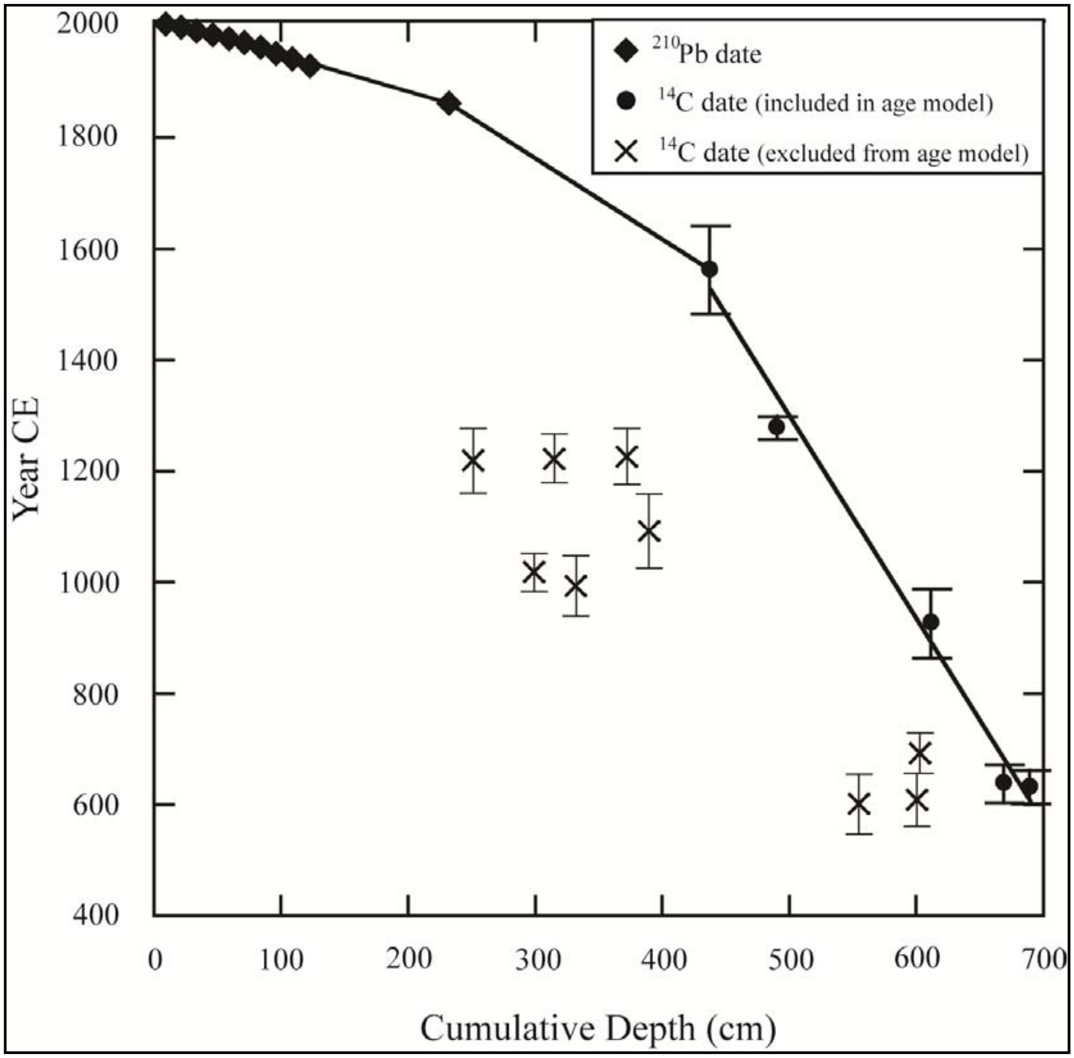

Figure 2.2: Age model for Lake Logung. Circles represent ^{14}C dates included in the age model, diamonds are ^{210}Pb dates, and Xs are ^{14}C dates that were excluded from the age model. Error bars on ^{14}C dates indicate 2-sigma calibrated age ranges. Solid lines indicate relative changes in sedimentation rate. Note the increase in sedimentation rate at 232 cm (1860 CE). Average sedimentation rates are 0.3 cm yr^{-1}, 0.9 cm yr^{-1}, and 1.5 cm yr^{-1} between 435-690 cm, 116-435 cm, and 0-116 cm, respectively.

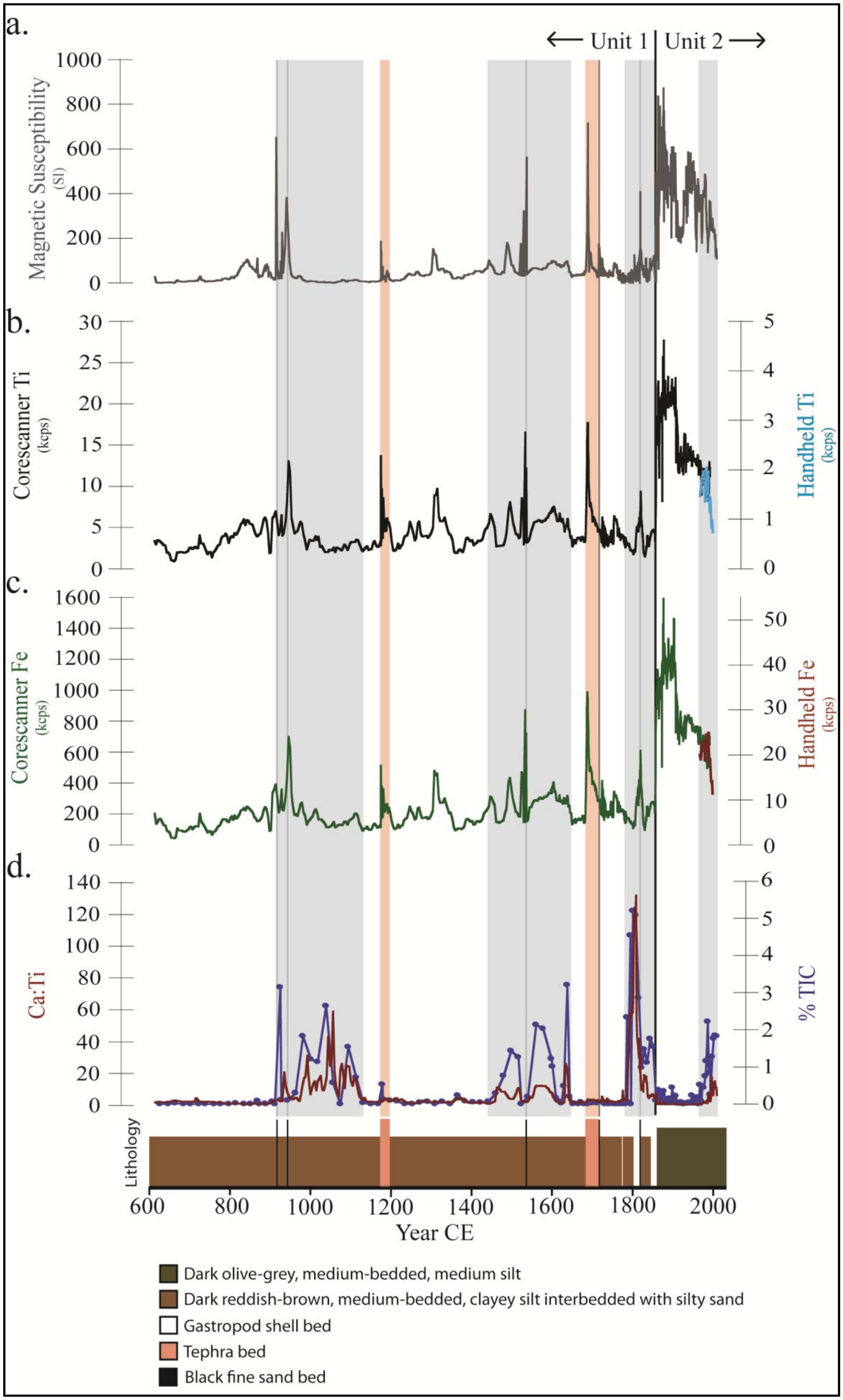

a.
← Unit 1
Unit 2 →
Magnetic Susceptibility (SI)
1000
800
600
400
200
0
b.
Corescanner Ti (kcps)
30
25
20
15
10
5
0
Handheld Ti (kcps)
5
4
3
2
1
0
c.
Corescanner Fe (kcps)
1600
1400
1200
1000
800
600
400
200
0
Handheld Fe (kcps)
50
40
30
20
10
0
d.
Ca:Ti
140
120
100
80
60
40
20
0
% TIC
6
5
4
3
2
1
0
Lithology
600
800
1000
1200
1400
1600
1800
2000
Year CE
Dark olive-grey, medium-bedded, medium silt
Dark reddish-brown, medium-bedded, clayey silt interbedded with silty sand
Gastropod shell bed
Tephra bed
Black fine sand bed

Figure 2.3: Comparison of Lake Logung magnetic susceptibility, x-ray fluorescence (XRF), total inorganic carbon (TIC) data, and sediment lithology plotted versus age (at bottom). The black vertical line marks the transition from Unit 1 to Unit 2 (1860 CE). Gray vertical bars highlight intervals of high carbonate abundance interpreted as drought. Data plotted are: (a) Magnetic Susceptibility (gray), (b) Ti abundance from ITRAX corescanner (black) and from handheld XRF analyzer blue), (c) Fe abundance from ITRAX corescanner (green) and from handheld XRF analyzer (maroon) and (d) Ca:Ti (maroon) and %TIC (dark blue). Dark blue closed circles are individual %TIC data points. The stratigraphic log at the bottom highlights major lithologic variations defined using the classification scheme from Schnurrenberger et al. (2003).

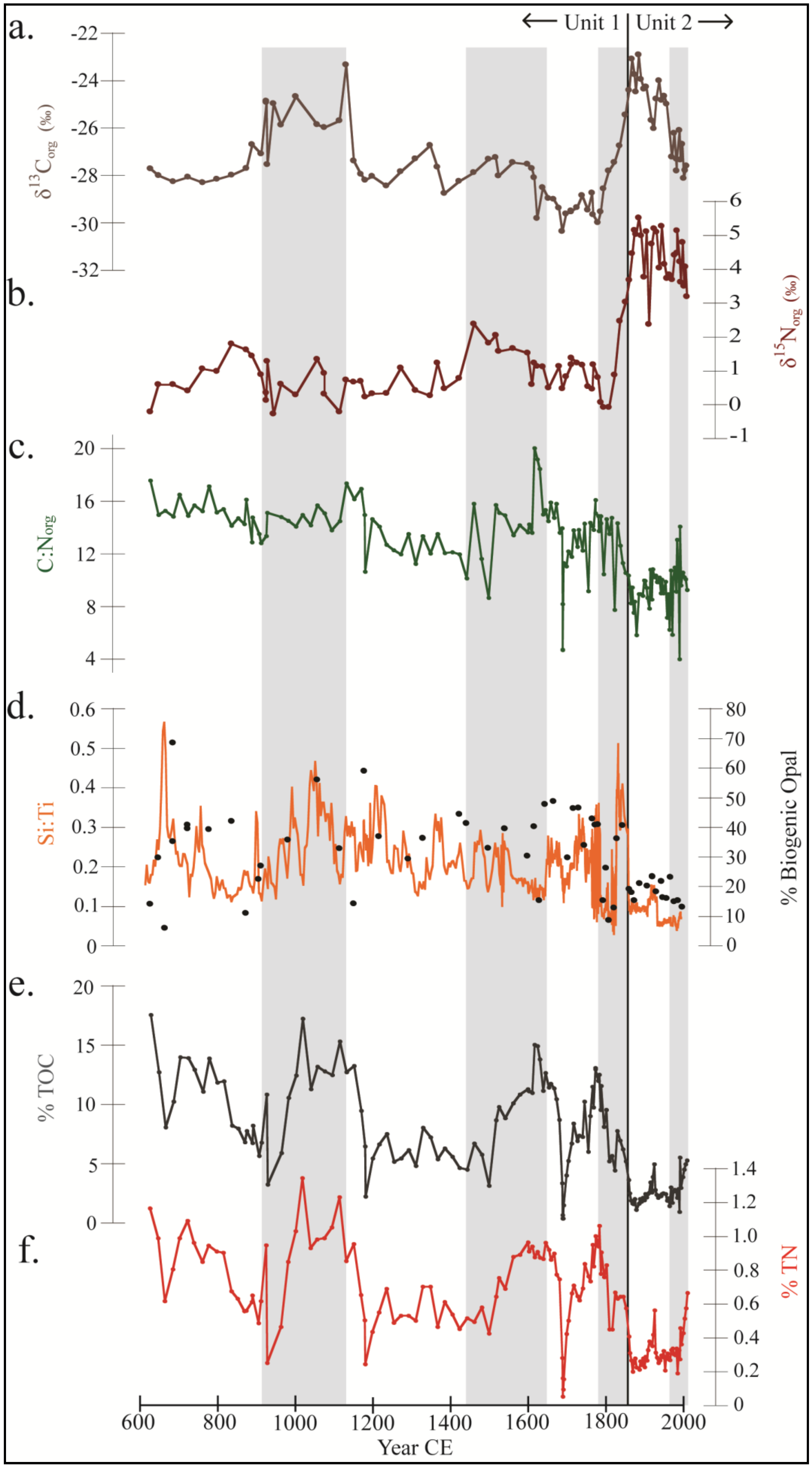

a.
b.
c.
d.
e.
f.
← Unit 1 | Unit 2 →
δ13Corg (‰)
δ15Norg (‰)
C:Norg
Si:Ti
% Biogenic Opal
% TOC
% TN
Year CE

Figure 2.4: Comparison of Lake Logung biogenic opal abundance and bulk organic C and N abundance and isotopic data plotted versus age (at bottom). The black vertical line marks the transition from Unit 1 to Unit 2 (1860 CE). Gray vertical bars highlight intervals of high carbonate abundance interpreted as drought. All circles are individual measurements. Data plotted are: (a) $\delta^{13}C_{org}$ (brown), (b) $\delta^{15}N_{org}$ (maroon), (c) $C:N_{org}$ (green), (d) XRF-derived Si:Ti (orange) and %biogenic opal (black circles), (e) %TOC (dark gray), and (f) %TN (red).

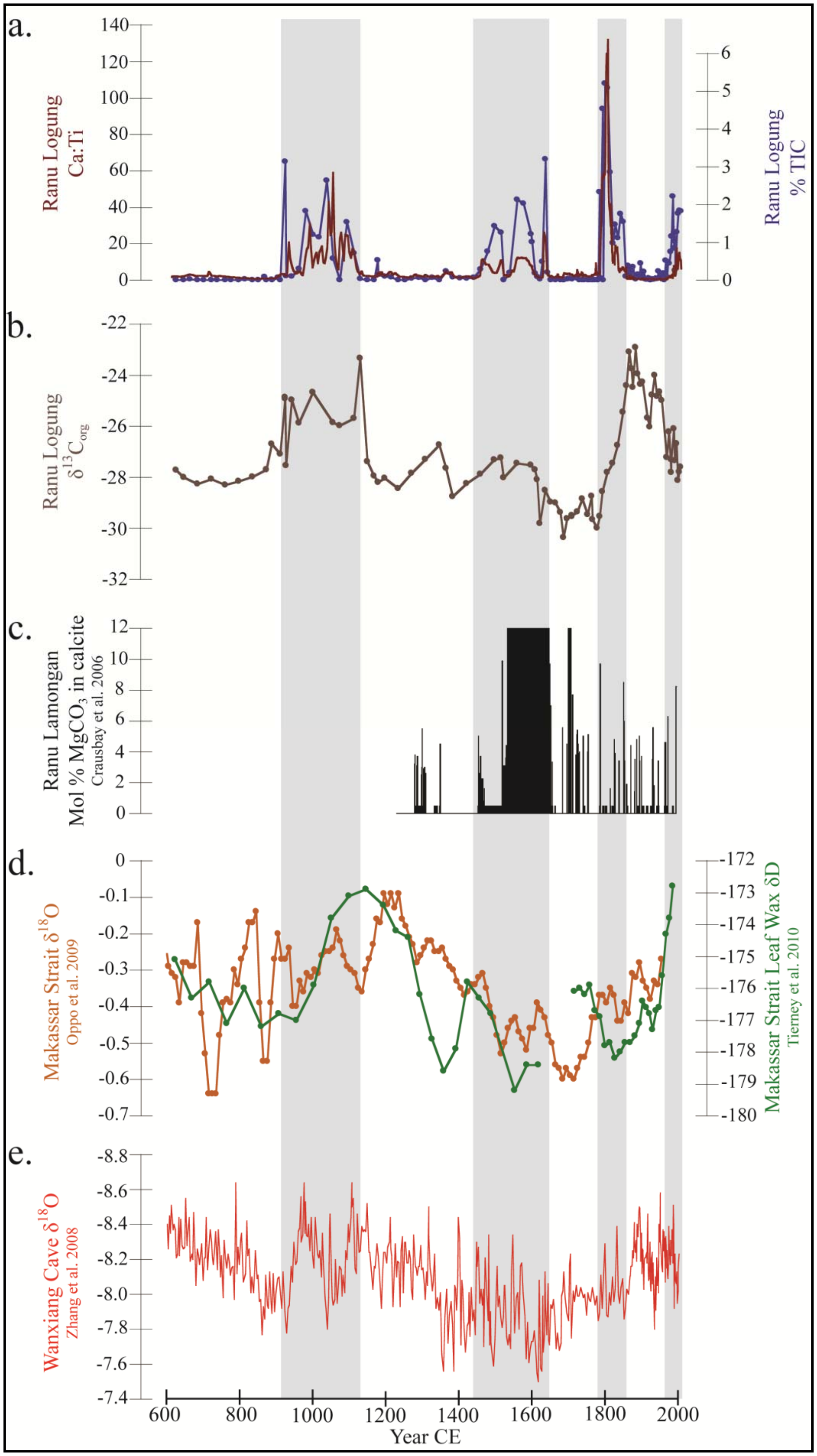
a.
Ranu Logung Ca:Ti
Ranu Logung % TIC
b.
Ranu Logung $\delta^{13}C_{org}$
c.
Ranu Lamongan Mol % $MgCO_3$ in calcite
Crausbay et al. 2006
d.
Makassar Strait $\delta^{18}O$
Oppo et al. 2009
Makassar Strait Leaf Wax δD
Tierney et al. 2010
e.
Wanxiang Cave $\delta^{18}O$
Zhang et al. 2008
Year CE

Figure 2.5: Comparison of Lake Logung Ca:Ti, %TIC, and organic matter $\delta^{13}C$ with other proxy data. (a) Lake Logung Ca:Ti (maroon), %TIC (blue) are plotted with Ca:Ti axis on the left and %TIC axis on the right. Blue circles are individual %TIC data points. (b) Lake Logung $\delta^{13}C_{org}$ is plotted in brown. Brown circles are individual $\delta^{13}C_{org}$ measurements. (c) Mol %$MgCO_3$ in calcite in Lake Lamongan lake sediments (black, Crausbay et al. 2006). (d) Makassar Strait $\delta^{18}O$ (orange; Oppo et al. 2009) and δD_{wax} (green, Tierney et al. 2010) are plotted with $\delta^{18}O$ axis on the left and δD axis on the right. More depleted isotopic values are interpreted as increased moisture. (e) Wanxiang Cave stalagmite $\delta^{18}O$ (Zhang et al. 2008). More enriched isotopic values are interpreted as decreased moisture associated with a southward-displaced Intertropical Convergence Zone. All figures are plotted such that, according to our interpretations, upward movement on the y-axis corresponds to northward ITCZ excursions.

CHAPTER 3

A severe drought during the last millennium in East Java, Indonesia

Jessica R. Rodysill[1]

James M. Russell[1], Shelley D. Crausbay[2], Satria Bijaksana[3], Mathias Vuille[4], R. Lawrence Edwards[5], Hai Cheng[5,6]

[1]Department of Geological Sciences, Brown University

[2]Horticulture and Landscape Architecture, Colorado State University

[3]Faculty of Mining and Petroleum Engineering, Institut Teknologi Bandung

[4]Department of Atmospheric and Environmental Sciences, University at Albany

[5]Department of Earth Sciences, University of Minnesota

[6]Institute of Global Environmental Change, Xi'an Jiaotong University

In Press in: *Quaternary Science Reviews*

3.1 Abstract

The Little Ice Age (LIA) is characterized by widespread northern hemisphere cooling during a period of reduced radiative forcing. Sediment records from three crater lakes indicate that the most severe drought of the last 1200 years struck East Java at the end of the LIA. We use ^{14}C and U-series dating applied to carbonate geochemical records from Lakes Lading, Logung, and Lamongan to demonstrate this drought occurred at 1790 Common Era (CE) +/- 20 years. Drought occurred during a period of strong El Niño events and Asian monsoon failures in the late 1790s, yet our records indicate that drought conditions persisted well beyond this decade and reached peak intensity in East Java ca. 1810 CE +/- 30 years. The continuation of severe drought into the 1800s may have resulted from the large volcanic eruptions that occurred in 1809, 1815 and 1835 CE, which likely caused brief, abrupt decreases in Indo-Pacific Warm Pool (IPWP) sea surface temperatures (SSTs), reducing local convection in East Java. Alternatively, broad changes in atmospheric circulation, such as a slowing of the Pacific Walker Circulation in response to decreased solar radiation during the LIA, could have produced several decades of drought in East Java. However, there is a lack of clear supporting evidence for such a change based upon paleohydrological records from the opposite ends of both the Indian and Pacific ocean zonal circulation systems. Based on the available evidence, we suggest severe multidecadal drought in East Java throughout the turn of the 19th century was driven by locally reduced convection resulting from a combination of heightened El Niño activity and volcanic eruptions.

3.2 Introduction

3.2.1 Background

Convection over the Indo-Pacific Warm Pool (IPWP) is a major source of atmospheric water vapor and is a vitally important component of the global hydrological cycle (Pierrehumbert, 2000). Emerging records from the IPWP indicate significant hydroclimate changes over the past millennium, which could have important consequences for tropical precipitation and global climate (Crausbay et al., 2006; Griffiths et al., 2009; Oppo et al., 2009; Sachs et al., 2009; Tierney et al., 2010; Rodysill et al., 2012; Konecky et al., 2013). Conflicting trends in reconstructed IPWP hydrology during the Little Ice Age (LIA) call into question how patterns of rainfall and drought respond to extended decadal to millennial-scale periods of warming and cooling. For example, isotopic records from the Makassar Strait and East Java indicate convective activity increased over southern Indonesia through much of the past millennium, yet decadal variations in these records exhibit significant temporal differences in hydrologic extremes (Oppo et al., 2009; Tierney et al., 2010; Rodysill et al., 2012; Konecky et al., 2013).

The Makassar Strait experienced the coldest temperatures of the past millennium circa 1700 CE (Oppo et al., 2009). While cool sea surface temperatures should reduce regional convective activity, lake sediments in East Java record the most severe droughts during the LIA from 1450 to 1650 Common Era (CE) and from 1790 to 1860 CE (Crausbay et al., 2006; Rodysill et al., 2012). These differences could arise from the diverse controls on the intensity of convection in the IPWP, which include changes in the mean position of the Inter-tropical Convergence Zone (ITCZ), changes in IPWP SSTs, and Walker Circulation strength associated with the El Niño-Southern Oscillation (ENSO) or the Indian Ocean Dipole (IOD). Understanding the regional hydrology in the IPWP during the LIA could illuminate how convective intensity responds to changes in the global climate system, and how IPWP variations in turn affect global-scale climate processes. Here we present a new record of drought from crater lake sediments in East Java and synthesize ages of droughts in nearby crater lakes that provide strong evidence for a major drought in East Java during the LIA.

3.2.2 Regional Setting

Our study site is located between the tropical Indian and Pacific Oceans on the island of Java, Indonesia, just south of the IPWP (Figure 3.1a). Seasonal rainfall variations in Java are controlled by the Austral summer monsoon, which brings heavy precipitation from the northwest, and the dry southeasterlies of the Austral winter monsoon (Figure 3.1c). Interannual variations in rainfall are influenced by the strength of the monsoons and the phase of ENSO, where anomalous cold SSTs, weaker Walker Circulation, and decreased vertical convection over the IPWP during El Niño events prolong southeasterly flow over Java, lengthening the dry season and causing drought (Hendon, 2003).

Lake Lading (8˚0.53’S, 113˚18.75’E) is a closed basin lake situated on the southwest side of Gunung Lamongan, a historically active volcano in Eastern Java (Carn and Pyle, 2001; Figure 3.1b). This ~200-m-diameter maar crater-lake is 8.6 m deep and sits at an elevation of 324 m in mafic volcanic bedrock (Carn and Pyle, 2001). Observations of water balance and salinity of East Java lakes have shown that lakes in this region are sensitive to seasonal changes in climate (Green et al., 1976), and sediment records from nearby crater lakes have demonstrated that these lakes can preserve a record of climate-driven salinity variations in their lithology and geochemistry covering at least the past 1,400 years (Crausbay et al., 2006; Rodysill et al., 2012).

3.3 Materials and Methods

We recovered two cores from the deepest part of Lake Lading using a Bolivia corer in July 2008 in offset, overlapping drives to minimize coring hiatuses. Resistant beds (tephras) below 2.5 m prevented penetration with the Bolivia corer, so a Livingstone coring system was used to recover an additional 3.6 m of sediment. The upper 42 cm of surface sediment was collected with a hand-held Uwitec™ gravity corer and extruded in the field in 1-cm increments with a modified Verschuren (1993) extruder to preserve chemical and physical sediment properties. The cores were split and macroscopically described at Brown University using the methods of Schnurrenberger et al. (2003). These cores were spliced into one composite section by visually correlating distinctive laminae and beds and distinctive geochemical variations.

The core chronology was assembled using ^{210}Pb dating methods to constrain ages in the upper meter of core, and ^{14}C ages on six plant macrofossils and one bulk sediment sample in the lower sections. ^{210}Pb activity was measured using alpha spectroscopy at

Flett Research Laboratories, and a constant rate of supply model was used to determine ^{210}Pb ages (Appleby and Oldfield, 1978; Appleby, 1997). Four ^{14}C dates were measured on plant material from cores that were collected from Lading in 1998 (Crausbay, 2000); sample depths corresponding to these dates were correlated to our cores using a combination of visual correlation of distinctive laminae and magnetic susceptibility profiles. An additional three ^{14}C dates were sampled directly from our cores to constrain correlation of the previously measured ^{14}C dates and to fill in gaps in the age model. These samples were analyzed at the Woods Hole Oceanographic Institution's National Ocean Sciences AMS Facility. All of the ^{14}C ages were calibrated to calendar years using the IntCal09 model from Calib 6.0 (Table 3.1; Stuiver and Reimer, 1993). Two ~20-cm-thick volcanic ash beds were treated as instantaneous events, so we removed them from the composite depth before calculating the age model. The age model and model error approximations were derived using a mixed-effect regression model applied to both ^{210}Pb and calibrated ^{14}C ages (Heegaard et al., 2005).

We developed continuous profiles of the elemental chemistry of our cores using an ITRAX corescanner with a Mo X-ray source at 1-cm resolution with a 120-s dwell time at the University of Minnesota Duluth's Large Lakes Observatory. We also measured the elemental chemistry of the uppermost, extruded sediment using an Innov-X Systems Alpha 4000 XRF. Overlapping measurements of Itrax and Innov-X XRF data have identical trends and were used to scale elemental counts from the Innov-X XRF to those made with the Itrax. Using these data, we estimated calcium carbonate content by normalizing counts of Ca to Ti, assuming that changes in Ti solely reflect terrigenous sources (e.g. Brown et al., 2007; Rodysill et al., 2012). We measured total inorganic carbon (TIC) concentrations on freeze-dried and homogenized subsamples at 10-cm resolution using a UIC CM5014 CO_2 Coulometer with a UIC CM5240 TIC Autoanalyzer to test whether downcore TIC abundance, another measurement that is used to approximate carbonate abundance, shared the same trends as Ca:Ti. Precision on these measurements of 0.237% TIC was verified with pure $CaCO_3$ standards and replication of 10% of the sample measurements. Samples containing greater than 2% TIC were analyzed on a Rigaku MiniFlex X-ray Diffractometer at the University of Minnesota to identify carbonate minerals and estimate percent Mg in calcite using X-ray diffraction (XRD) techniques (Goldsmith and Graf, 1958). We also conducted smear slide analyses across the interval where carbonate is present to characterize the relative abundance and phase of carbonate. Total contents of carbon and nitrogen (TC and TN) were measured, using an NC2100 Elemental Analyzer, on the same set of subsamples on which TIC was measured. Precision of TC and TN analyses is 1.60% and 0.26%, respectively, as determined from standards and replication of 10% of the samples. TIC values were subtracted from TC values to determine the % total organic carbon (TOC), for which the pooled uncertainty is 1.62%. TOC values were then divided by TN values to calculate $C:N_{org}$. Total organic matter content (% OM) was determined at 1-cm resolution by drying sediment samples in a drying oven overnight at 100˚C, burning the samples for 4 hours at 550˚C, and dividing the mass of sample lost by ignition at 550˚C by the dry sediment mass.

We provide additional chronological control on the timing of a drought event documented by carbonate-rich sediment in a core from nearby Lake Lamongan (Crausbay et al., 2006) through absolute dating of lacustrine aragonite with ^{234}U-^{230}Th

dating methods (Edwards et al., 1987). Two samples, labeled A and B, from a single bed composed of pure aragonite, as determined by a combination of smear slide analyses and XRD measurements, were analyzed using standard techniques in the Minnesota Isotope Laboratory at the University of Minnesota and are compared to previous ^{14}C-based chronologies from this core.

3.4 Results

3.4.1 Core Chronology—Lake Lading age model

^{210}Pb and ^{14}C ages indicate that our core from Lake Lading continuously spans the interval from ~ 800 CE to the present. A ^{14}C date at 371.1 cm from our sediment core is nearly identical to a date from Crausbay's (2000) core taken in 1998, at 375.6 cm in our composite section (Table 3.1; Figure 3.2), demonstrating that the ages obtained in older cores are reproducible and that our correlation of ^{14}C sample depths between cores is accurate. A ^{14}C date at 178.4 cm had multiple possible age ranges with comparable probabilities; we use the age range with the second highest probability, which fit best with sedimentation rates determined from the rest of the ^{14}C ages (Table 3.1). Using the age range with the highest probability would require a 4-fold increase and decrease in sedimentation rates prior to and during the ^{210}Pb-dated portion of our cores. We do not see evidence in any of our geochemical and lithological data to support such variation in sedimentation, and such changes would be in direct contradiction with the ^{210}Pb age model. The bulk sediment ^{14}C date at 252.2 cm is much older than the rest of the plant macrofossil ^{14}C ages above and below it. Given that there is evidence for reworking of material that resulted in old ^{14}C ages on charcoal and bulk sediment samples from nearby Lake Logung (Rodysill et al., 2012), and the possibility of ^{14}C reservoirs in these systems, we remove this age from the age model. After these adjustments, our mixed-effect regression through six ^{14}C ages between ~800 and 1800 CE indicates roughly linear sedimentation averaging 0.4 cm yr^{-1}, similar to pre-industrial sedimentation rates at nearby Lake Logung (Rodysill et al., 2012). ^{210}Pb data indicate sedimentation rates increase to 1.14 cm yr^{-1} toward the present (Figure 3.2), slightly lower than sedimentation rates during the historical period at Logung (Rodysill et al., 2012).

3.4.2 Sediment lithology and geochemistry of Lake Lading

Calcium carbonate, estimated from Ca:Ti and % TIC, is nearly absent from Lake Lading sediment except between the late 1700's and early 1800's, when %TIC increases to 6.3% (~50% $CaCO_3$) in a set of well-defined lamina (Figure 3.3). Our smear slide and XRD-analyses indicate this carbonate is composed of euhedral crystals of calcite, high-Mg calcite (7-8% Mg) and aragonite. Organic matter content ranges between 2 and 25% during the past 1200 years and lacks a clear long-term trend (Figure 3.3). $C:N_{org}$ exhibits substantial decadal-scale variability throughout the record, ranging between 10.5 and 19 and gradually decreasing from 1400 CE to the present. There is no clear relationship between either % OM or $C:N_{org}$ and %TIC.

3.4.3 Lake Lamongan U-Series Dating

The $^{230}Th/^{238}U$ activity ratio in two aragonite samples from the same depth in Lake Lamongan sediments is very low (0.00256 +/- 0.00015 in sample A and 0.00241 +/- 0.0005 in sample B), which indicates consistent incorporation of U into the aragonite as it precipitated (Lazar et al., 2004; Table 3.2). A common problem with using ^{234}U-^{230}Th dating methods in sediment samples is the presence of detrital U and Th, which are sources of error in the U-Th date determination (Stein and Goldstein, 2006). Pristine coral aragonite typically has $^{238}U/^{232}Th$ values between 10^4 and 10^5, as compared to aragonite samples from Lake Lisan sediments that contained detrital ^{232}Th and had $^{238}U/^{232}Th$ of $<10^2$ (Stein and Goldstein, 2006). Measured $^{238}U/^{232}Th$ for the two aragonite samples from Lake Lamongan sediments were on the order of 10^3 in sample A and 10^2 in sample B, indicating that sample A had low detrital ^{232}Th relative to sample B. The low $^{238}U/^{232}Th$ likely indicates that the aragonite in that sample contains some detrital ^{232}Th. Maximum ages for samples A and B from the uncorrected ^{230}Th dates are 1732 CE +/- 16 years and 1746 CE +/- 53 years, respectively (Table 3.2). Assuming an initial $^{230}Th/^{232}Th$ of (4.4 +/- 2.2) $*10^{-6}$ to correct for the initial ^{230}Th, we calculate an age for sample A of 1774 CE +/- 26 years and for sample B of 1791 CE +/- 57 years (Table 3.2). The U-series ages on the aragonite bed from Lake Lamongan give similar ages for the timing of the most severe drought in that reconstruction.

3.5 Discussion

3.5.1 Drought in Lake Lading record

Carbonate is present in the sediments of Lake Lading only during a brief, 60-year period within the 1160-year long record, from 1790 to 1850 CE (Figure 3.3). The euhedral shape of the calcite and aragonite grains in this bed suggests they are authigenic, indicating that shifts in lake water chemistry and salinity drove carbonate precipitation and preservation. Calcite saturation was most likely achieved by a rise in salinity in response to a decrease in regional precipitation:evaporation (Müller et al., 1972; Kelts and Hsü, 1978). It is unlikely that calcite precipitation was driven by enhanced runoff or groundwater supplying excess Ca^{2+} and HCO_3^-. Carbonate precipitation caused by enhanced runoff and groundwater supply generally occurs as the result of a positive shift in lake water balance in settings where the landscape is a significant source of these ions (Shapley et al., 2005, 2010), but Lake Lading is surrounded by a mafic landscape. Calcite precipitation can also be caused by greater primary productivity that drives CO_2 consumption, which increases the pH and drives the water chemistry to calcite saturation (Kelts and Hsü, 1978). Intensified productivity should increase the delivery of organic matter to the sediments and decrease the $C:N_{org}$, however % OM declines and $C:N_{org}$ is high during the late 1700's-early 1800's when carbonate is present (Meyers and Lallier-Vergès, 1999; Figure 3.3). Moreover, XRD and smear slide analyses show that the phase of carbonate throughout this event changes from pure calcite, to a mixture of high Mg-calcite and aragonite, to pure aragonite, then back to a mixture of high Mg-calcite and aragonite, and finally back to pure calcite. The transition from calcite to aragonite is common in lakes undergoing increasingly evaporative conditions (Müller et al., 1972). Finally, this event is precisely concurrent with the most pronounced enrichment in δD_{wax}

data from Lake Lading sediments (Konecky et al., 2013), a completely independent proxy for dry conditions. All of these observations are strong evidence for an evaporatively-driven rise in salinity due to decreased precipitation:evaporation as the primary control on carbonate precipitation in Lake Lading. Our estimate of the age range of this event, 1790-1850 CE, is based upon a mixed-effect regression model (Heegaard et al., 2005) through our ^{14}C and ^{210}Pb ages. Other age modeling techniques provide nearly identical ages; Bacon, for example, gave an age range of 1780 to 1840 CE (Blaauw and Christen, 2011). Together these data provide robust evidence for drought in East Java between 1790 and 1850 CE.

3.5.2 Drought in East Java lake records

Lake Lading is one of eleven crater lakes situated near the base of Gunung Lamongan. Among these lakes, Lading, Logung and Lamongan exhibit a clear gradient in calcium carbonate production and preservation. Calcium carbonate is present in the record from Lake Lading between 1790 and 1860 CE and is otherwise absent from the sediments. Four multidecadal periods of carbonate precipitation are present in a sediment core from Lake Logung, and carbonate precipitation was nearly continuous in a core from Lake Lamongan. Despite these geochemical differences, all three records point to the strongest drought conditions of the past millennium during the late 1700s and early 1800s. Drought in Lake Lading lasted from 1790 to 1850, culminating around 1810 CE when calcite was completely replaced by aragonite (Figure 3.4a). Our maximum age error during this event is 30 years, so the drought could have occurred between 1760 and 1880 CE.

The timing of drought in Lake Lading is nearly identical to the timing of a major drought documented in the sediments of Lake Logung, a maar lake 3.5 km south of Lading (Figures 3.1b, 3.4b). Droughts are recorded in Lake Logung by calcium carbonate mineral abundance interpreted from XRF-derived Ca:Ti and % TIC data (Rodysill et al., 2012). The most pronounced rise in calcite abundance in Lake Logung lasts from 1790 to 1860 and reaches maximum abundance between 1800 and 1810 CE (Figure 3.4b). The error on this portion of the Lake Logung age model is approximately 70 years, placing the drought between 1720 and 1920 CE. However, the timing of peak carbonate content coincides almost perfectly in the two lakes, suggesting strong drought just after the turn of the 19th century.

Further evidence of drought at this time comes from Lake Lamongan, 5 km northwest of Lake Lading (Figure 3.1). Carbonate is more continuously preserved in the sediments of Lake Lamongan, compared with Lakes Lading and Logung, and Crausbay et al. (2006) reconstructed moisture balance in this record from changes in carbonate mineralogy measured by the mol % Mg in calcite from XRD analyses and the phase of carbonate observed in smear slides (Figure 3.4c). They estimated that the strongest drought recorded in Lake Lamongan, marked by a prolonged interval of aragonite deposition, occurred at about 1550 CE based upon ^{14}C ages on plant macrofossils. However, lack of ^{210}Pb data, ^{14}C age reversals, plateaus in the ^{14}C age calibration curve during the LIA, and possible stratigraphic discontinuities made the original chronology of the Lamongan record problematic, particularly in the aragonitic section of core indicating drought. Our new U-Th dates obtained near the base of this aragonite bed yielded ages of 1774 CE +/- 26 and 1791 CE +/- 57 yrs for this interval (Figure 3.4c).. This implies a much more recent age than was determined through ^{14}C dating at Lamongan, and places the onset of severe drought very close to that observed in nearby Lakes Lading and Logung (~1790 CE +/- 30 yrs).

The U-Th ages were sampled from near the base of the aragonite-bearing sediment and therefore mark the beginning of the most severe drought in Lamongan. Interpolating between the U-Th date (1774 CE) and the core top (1998), an additional 80 cm of aragonite above the U-Th dates represents approximately 40 years of drought after 1774 with a mid-point in the 1790's, roughly in agreement with the length of carbonate-defined droughts in Lakes Lading and Logung. This is a conservative estimate of the duration of the drought in Lamongan; a purely linear sedimentation rate over the last few centuries in this lake is unlikely based on the 3-to-4-fold increases in sedimentation rates in the Lading and Logung basins during the last century (Rodysill et al., 2012; this study). More realistically, aragonite deposition probably persisted well into the 19^{th} century, which would push the middle of the aragonite bed closer to the peak intensity of drought recorded in Lading and Logung ca. 1810.

We estimated the timing of peak drought conditions in East Java by calculating a weighted mean age based upon the three records. To do this, we used the U-series age from sample A, which was sampled from the center of the aragonite bed in the Lake Lamongan core, and the ages and associated 95% confidence interval errors at the maximum carbonate concentration in Lakes Lading and Logung predicted from each cores' age model (Figure 3.5). The weight assigned to the age from each site is the reciprocal of the variance of each individual age at the 95% confidence level. The weighted mean was calculated by summing the products of the age from each site and their associated weights, then by dividing that value by the sum of the weights. The variance of the weighted mean is the reciprocal of the sum of weights. We determined that the maximum drought intensity in East Java occurred in 1790 CE +/- 20 yrs.

In sum, the carbonate content and mineralogy of three crater lakes in eastern Java indicate strong, coherent drought in the late 18^{th}-early 19^{th} century, reaching peak aridity at 1790 CE +/- 20 yrs. While Lamongan and Logung show evidence for multiple drought episodes during the past millennium, late 18^{th}-early 19^{th} century is the only event present in the Lake Lading record. The uniqueness of this event in our reconstruction from Lake Lading and its co-occurrence in three separate sites suggests that it was the strongest event to occur in this region during the last millennium.

3.5.3 Regional climate patterns and mechanisms of late LIA Drought in East Java

Drought in East Java can be induced by numerous mechanisms, including a weakening of the Pacific Walker Circulation associated with changes in ENSO and/or the Indian Ocean dipole, a decrease in local convection due to anomalous a cooling of IPWP SSTs, and changes in the strength of the Austral-Asian monsoon. Many of these mechanisms operate on seasonal to interannual timescales and their effects are short-lived, such as El Niño and Indian Ocean Dipole (IOD) events. At multidecadal timescales, changes in radiative forcing from volcanism, solar output, and greenhouse gases as well as natural variability in the ocean-atmosphere system might change the nature or frequency of these events and bias their variability toward phases that induce drought in Java. Multidecadal changes in these systems might also arise from changes internal to the Pacific Ocean and/or Indian Ocean circulation and dynamics, of which the long-term patterns and underlying causes are still unclear. Evaluating these forcings and processes and their relationship to late 1700s/early 1800s drought in East Java requires an extremely dense network of high resolution climate proxies. Recent tree ring, lake, and coral records have begun to provide such a framework, and are discussed below.

The East Java Drought peaks in intensity in 1790 CE and lasts approximately six decades. All three of the Indonesian lake records are based upon changes in lake salinity, which exhibits a threshold response to climate changes. Carbonate precipitation does not occur until the lake reaches saturation with respect to calcite, and a particular phase of carbonate does not stop precipitating until the salinity returns to below that threshold. The prolonged drought in East Java may either represent ~60 years of continually severe drought conditions, or several short-lived extreme droughts occurring in close temporal proximity such that neither the abundance nor phase of carbonate is changed between the termination of one single drought and the start of the next. Arid conditions between short-lived, extreme drought events might have been sustained by soil moisture feedbacks, producing a continuous response to individual stochastic forcing events. While the continuity of drought in East Java during this time is unclear, lake salinity rose to higher levels over the course of the ~60-year arid interval, culminating in a peak in arid conditions between 1775 and 1810 CE. Whether or not there was a continuous or punctuated decrease in precipitation:evaporation remains unclear. Thus, either a cluster of short-lived droughts during the late 1700s/early 1800s, or a single prolonged drought is capable of producing the signal recorded in the East Java crater lakes.

Tree ring, speleothem, and ice core records from Southeast Asia, India, and Southern Oman have documented numerous droughts in the late 1700s and early 1800s (Thompson et al., 2000; Duan et al., 2004; Fleitmann et al., 2004; Cook et al., 2010). The Strange Parallels Drought lasted from 1756 to 1768 and is associated with a major monsoon failure across India and Southeast Asia (Lieberman, 2003; Cook et al., 2010). The age of the Strange Parallels drought is approximately when prolonged drought began in Lake Lamongan, and is the earliest possible timing of the onset of drought in Lakes Logung and Lading; however, all three lakes indicate that the peak intensity of East Javan drought occurs a few decades after the Strange Parallels drought (Figure 3.4). Peak drought conditions in East Java overlap best in timing with the East India Drought, which resulted in widespread aridity in Southeast Asia and India from 1790 to 1796 (Cook et al., 2010). An associated drought in East Java could suggest linkages between Asian Summer Monsoon failure and changes in the Austral-Asian winter monsoon. However, the East India drought was very short-lived relative to the event that we document in East Javan lakes, similar to most droughts documented in Southeast Asian tree-ring archives. Moreover, droughts occurring in Southeast Asia and India were stronger from 1756-1768 and 1876-1878 (Thompson et al., 2000; Cook et al., 2010) and do not clearly align with peak drought conditions in East Java in the 1790s. Together, these relationships imply that droughts in mainland Asia do not directly correspond to droughts in East Java, so a climatic influence from outside the Asian Monsoon system played a role in creating anomalously dry conditions in East Java from 1790 to 1850 CE (Duan et al., 2004; Cook et al., 2010; Figures 3.1, 3.5a).

The drought in East Java has perhaps the best temporal association to the "Great El Niño event" between 1789 and 1797, of which the consequences have been documented across much of the tropics (Grove, 2007). This event is thought to include several very strong El Niño years between 1790 and 1796. Historically documented effects include prolonged and severe drought across Australia, the Caribbean islands, Mexico, Egypt, southern Africa, early snowmelt and excessive flooding on the Peruvian coast, and abnormally high temperatures and rainfall in North America (Grove, 1998; Ortlieb, 2000; Grove, 2007; Gergis et al., 2010). The earliest of these severe El Niño events coincides with an exceptionally severe drought documented by chloride and dust concentrations and $\delta^{18}O$ in the 560-year-long Himalayan ice core record (Figure 3.6a; Thompson et al., 2000). Historical archives of heavy rainfall and fishery failures from Peru document a period of several El Niño events beginning in the late 1700s and persisting into the mid-1800s, making these decades the most active interval of El Niño activity since 1550 in historical records (Garcia-Herrera et al., 2008). It is important to note that there have been individual El Niño events of equal or greater severity between 1525 and 2010 CE documented in historical archives (Ortlieb, 2000) and in the Niño3.4 SST index that do not produce drought in the Lake Lading record. If the Great El Niño caused the drought in East Java, then these data imply that the concentration of several severe El Niño events occurring over a short period of time is capable of producing prolonged East Javan drought, rather than a single, extremely severe El Niño event.

Following the late 1700s Great El Niño Event, a series of several massive volcanic eruptions occurring in 1809, 1815, and 1835 may have acted to prolong the drought in East Java into the early 1800s (Stothers, 1984; D'Arrigo et al., 2006; Cole-Dai et al., 2009). Volcanic eruptions are capable of directly causing drought in the IPWP region by temporarily decreasing IPWP SSTs and locally reducing atmospheric convection. El Niño events also correlate to large volcanic eruptions both in historical and model data (Adams et al., 2003; Mann et al., 2005), and could force drought in East Java through both local and remote ocean-atmosphere interactions. Large eruptions have been previously invoked to explain extreme declines in western Pacific warm pool SSTs between 1808 and 1818 CE and between 1836 and 1838 CE (D'Arrigo et al., 2006; Figure 3.6b). Peak carbonate abundance in the Lake Lading and Logung records occurs from 1800-1820 CE, slightly later than peak aridity in the Lake Lamongan record. Differences in the timing of peak aridity between the three crater lakes may result from age model uncertainties or differing sensitivities of the geochemistry at each site to changes in local aridity, as discussed in Section 4.2. The latter could imply aridity in East Java continued into the early 1800s, overlapping with the two large volcanic eruptions and the coldest IPWP SSTs in the early 1800s. Another volcanic eruption in 1835 CE occurred at the same time as another sharp drop in reconstructed IPWP SSTs, and may have contributed to drought after 1815 CE (Figure 6b; D'Arrigo et al., 2006).

Interannual drought in east Java is influenced not only by ENSO and volcanic activity but also zonal circulation changes in the Indian Ocean associated with the Indian Ocean Dipole mode. Positive IOD events are associated with reduced convection and drought in the IPWP region and enhanced convection and precipitation over the western

Indian Ocean and East Africa (Ashok et al., 2004). A recent modeling study demonstrated that, on multi-decadal timescales, Indian Ocean SSTs alter the Indian Ocean Walker Circulation and drive multi-decadal precipitation anomalies in East Africa in the absence of a Pacific Ocean influence (Tierney et al., 2013; Figure 3.6c). If either IOD activity or multidecadal "IOD-like" SST anomalies in the Indian Ocean caused East Javan drought, we would expect drought in East Java to correlate to positive rainfall anomalies along the east coast of tropical Africa. Based on our reconstruction, however, drought in East Java coincides with declining precipitation in East Africa (Tierney et al., 2013; Figure 3.6c). Similar evidence for drought in East Africa during this time period comes from Lake Naivasha (Verschuren et al., 2000) and Challa (Wolff et al., 2011). These records strongly suggest that East Africa was dry during drought in East Java, suggesting these events do not arise from IOD-like mechanisms. Our study sites in East Java are influenced by both Indian and Pacific ocean-atmosphere systems, and it is possible that changes in convection over the Indian Ocean may not have a significant impact on east Javan precipitation if the Pacific ocean-atmosphere system is unchanged. Whatever the case may be, this evidence suggests that neither prolonged positive IOD-like conditions persisting for several decades nor an increase in the frequency or intensity of interannual IOD events throughout the late 1700s/early 1800s were responsible for drought in East Java.

The association between drought in East Java, the Great El Niño Event, and volcanic eruption-induced cooling of warm pool SSTs strongly implicates changes in the tropical Pacific Walker Circulation as the forcing behind East Javan drought. If so, we would expect to find evidence for enhanced runoff in climate reconstructions on the eastern limb of the Pacific Walker Circulation. However, lake sediment runoff records from the Galápagos and Ecuador, a record of $\delta^{18}O$ from Galápagos corals, and South American ice core records in the Eastern Equatorial Pacific (EEP) region, which is climatically sensitive to historical ENSO activity, do not provide evidence for heightened El Niño activity or wet conditions at multi-decadal timescales during the late 1700s/early 1800s (Figure 3.6a; Dunbar et al., 1994; Moy et al., 2002; Thompson et al., 2003; Conroy et al., 2008). In fact, lake sediment records from the Galápagos exhibit the lowest frequency of runoff events in the last four centuries in the early 1800s, and Ecuadorian lake sediment records indicate very few runoff events throughout the drought in East Java. Given the extensive historical documentation of multiple intense El Niño events during the 1790s, it is possible that the spatial distribution of El Niño-driven precipitation anomalies may have been different during the 1790s relative to the present, such that the decade of severe El Niño events was not documented in these paleoreconstructions.

Drought in East Java was not driven by the multi-century decrease in western Pacific SST that occurred in the context of the LIA because the coldest SSTs occurred in the early 1700s, nearly a century before drought in our record (Oppo et al., 2009). It is possible that the East Java drought is a manifestation of random local variability, perhaps associated with cool SSTs and generally weakened atmospheric convection over the IPWP during the LIA. We find this explanation unlikely given that an internal random variable would need to coincide, by chance, with a series of extraordinarily strong volcanic eruptions and high frequency of El Niño events. This drought may then more likely be the result of several short-lived events (e.g. El Niño events, volcanic eruptions) that, while common throughout the last millennium, happened to occur in close timing during the late 1700’s and early 1800’s to produce a uniquely long and severe drought in an ENSO, IOD, and monsoon sensitive region such as East Java.

3.6 Conclusions

The strongest drought in East Java of the past millennium occurred at ~1790 CE +/- 20 yrs, during a prolonged period of cool IPWP SSTs during the late Little Ice Age. New U-Th dates pin the peak intensity of the drought to the late 1700s, and evidence for dry conditions from three crater-lake records suggests the drought was regionally coherent and severe, persisting well into the mid-1800s. It is clear from the synchronous onset of the drought in lakes Lading, Lamongan and Logung, within age model uncertainties, that dry conditions began in East Java in the late 1700s and peaked in intensity at 1790 CE +/- 20 years, coinciding with a series of globally-documented severe El Niño events between 1789 and 1797 termed the “Great El Niño event.” The persistence of the East Java drought until 1850 CE +/- 30 years, and peak drought intensity lasting through 1810 CE, may have been driven by three large volcanic eruptions at 1809, 1815, and 1835 CE, which set up conditions for drought through short-lived cooling of IPWP SSTs. While each of these climate drivers tends to produce drought on seasonal to interannual timescales, we suggest a combination of many short-lived drought-inducing events occurring in close temporal proximity to one another produced many decades of severe drought in East Java.

3.7 Acknowledgements

We thank the Government of Indonesia and Indonesian Ministry of Research and Technology (RISTEK) for permission and assistance in conducting field research. We thank Ed Cushing for providing ^{14}C ages from Lake Lading. We also thank Dave Murray, Joe Orchardo, and Candice Bousquet for laboratory assistance, Jessica Tierney, Kevin Anchukaitis, and Bronwen Konecky for improving the quality of this project, and the Limnological Research Center. This research was supported by a NOAA-CCDD grant to J. Russell and M. Vuille.

3.8 References

Adams, J.B., Mann, M.E., Ammann, C.M., 2003. Proxy evidence for an El Niño-like response to volcanic forcing. Nature 426, 274-278.

Appleby, P.G., 1997. Sediment records of fallout radionuclides and their application to studies of sediment-water interactions. Water Air Soil Pollut. 99, 573-586.

Appleby, P.G. and Oldfield, F., 1978. The calculation of ^{210}Pb dates assuming a constant rate of supply of unsupported ^{210}Pb to the sediment. Catena 5, 1-8.

Ashok, K., Guan, Z., Saji, N.H., Yamagata, T., 2004. Individual and combined influences of ENSO and the Indian Ocean Dipole on the Indian Summer Monsoon. J. Climate 17, 3141-3155.

Ashok, K., Behera, S.K., Rao, S.A., Weng, H., Yamagata, T., 2007. El Niño Modoki and its possible teleconnection. J. Geophys. Res. 112, C11007, doi:10.1029/2006JC003798.

Blaauw, M., Christen, J.A., 2011. Flexible paleoclimate age-depth models using an autoregressive gamma process. Bayesian Analysis 6, 457-474.

Brown, E.T., Johnson, T.C., Scholz, C.A., Cohen, A.S., King, J.W., 2007. Abrupt change in tropical African climate linked to the bipolar seesaw over the past 55,000 years. Geophys. Res. Lett. 34, L20702, DOI: 10.1029/2007GL031240.

Carn, S.A. and Pyle, D.M., 2001. Petrology and geochemistry of the Lamongan Volcanic Field, East Java, Indonesia: primitive Sunda Arc magmas in an extensional tectonic setting? J. Petrology 42, 1643-1683.

Cole-Dai, J., Ferris, D., Lanciki, A., Savarino, J., Baroni, M., Thiemens, M.H., 2009. Cold decade (AD 1810-1819) caused by Tambora (1815) and another (1809) stratospheric volcanic eruption. Geophys. Res. Lett. 36, L22703, doi:10.1029/2009GL040882.

Conroy, J.L., Overpeck, J.T., Cole, J.E., Shanahan, T.M., Steinitz-Kannan, M., 2008. Holocene changes in eastern tropical Pacific climate inferred from a Galápagos lake sediment record. Quat. Sci. Rev. 27, 1166-1180.

Cook, E.R., Anchukaitis, K.J, Buckley, B.M., D'Arrigo, R.D., Jacoby, G.C., Wright, W.E., 2010. Asian monsoon failure and megadrought during the last millennium. Science 328, 486-489.

Crausbay, S.D., 2000. A high-resoution record of climate and lowland vegetation over the past millennium in East Java. MS. thesis, Dept. of Ecology, University of Minnesota. Minneapolis, MN, pp. 123.

Crausbay, S.D., Russell, J.M., Schnurrenberger, D.W., 2006. A ca. 800-year lithological record of drought from sub-annually laminated lake sediment, East Java. J. Paleolimnol. 35, 641-659.

D'Arrigo, R., Wilson, R., Palmer, J., Krusic, P., Curtis, A., Sakulich, J., Bijaksana, S., Zulaikah, S., Ngkoimani, L.O., Tudhope, A., 2006. The reconstructed Indonesian warm pool sea surface temperatures from tree rings and corals: Linkages to Asian monsoon drought and El Niño-Southern Oscillation. Paleoceanography 21, PA3005, doi:10.1029/2005PA001256.

Duan, K.,Yao, T., Thompson, L.G., 2004. Low-frequency of southern Asian monsoon variability using a 295-year record from the Dasuopu ice core in the central Himalayas. Geophys. Res. Lett. 31, L16209, doi:10.1029/2004GL020015.

Dunbar, R.B., Wellington, G.M., Colgan, M.W., Glynn, P.W., 1994. Eastern Pacific sea surface temperature since 1600 A.D.: The $\delta^{18}O$ record of climate variability in Galápagos corals. Paleoceanogr. 9, 291-315.

Edwards, R.L., Chen, J.H., Wasserburg, G.J., 1987. ^{238}U-^{234}U-^{230}Th-^{232}Th systematics and the precise measurement of time over the past 500,000 years. Earth Plan. Sci. Lett. 81, 175-192.

Fleitmann, D., Burns, S.J., Neff, U., Mudelsee, M., Mangini, A., Matter, A., 2004. Palaeoclimatic interpretation of high-resolution oxygen isotope profiles derived from annually laminated speleothems from Southern Oman. Quat. Sci. Rev. 23, 935-945.

Garcia-Herrera, R., Diaz, H.F., Garcia, R.R., Prieto, M.R., Barriopedro, D., Moyano, R., Hernández, E., 2008. A chronology of El Niño events from primary documentary sources in northern Peru. J. Climate 21, 1948-1962.

Gergis, J., Garden, D., Fenby, C., 2010. The influence of climate on the first European settlement of Australia: A comparison of weather journals, documentary data and palaeoclimate records, 1788-1793. Env. Hist. 15, 485-507.

Goldsmith, J.R. and Graf, D.L., 1958. Relation between lattice constants and composition of the Ca-Mg carbonates. Am. Mineral. 43, 84-101.

Green, J., Corbet, S.A., Watts, E., Lan, O.B., 1976. Ecological studies on Indonesian lakes. Overturn and restratification of Lake Lamongan. J. Zool. 180, 315-354.

Griffiths, M.L., Drysdale, R.N., Gagan, M.K., Zhao, J.-x., Ayliffe, L.K., Hellstrom, J.C., Hantoro, W.S., Frisia, S., Feng, Y.-x., Cartwright, I., St. Pierre, E., Fischer, M.J., Suwargadi, B.W., 2009. Increasing Australian-Indonesian monsoon rainfall linked to early Holocene sea-level rise. Nat. Geosci. 2, 636-639.

Grove, R.H., 1998. Global impact of the 1789-93 El Niño. Nature 393, 318-319.

Grove, R.H., 2007. The Great El Niño of 1789-1793 and its global consequences: Reconstructing an extreme climate event in world environmental history. The Medieval History Journal 10, DOI: 10.1177/097194580701000203.

Heegaard, E., Birks, H.J.B., Telford, R.J., 2005. Relationships between calibrated ages and depth in stratigraphical sequences: an estimation procedure by mixed-effect regression. The Holocene 15, 612-618.

Hendon, H.H., 2003. Indonesian Rainfall Variability: Impacts of ENSO and local air-sea interaction. J. Climate 16, 1775-1790.

Kelts, K., Hsü, K.J., 1978. Freshwater carbonate sedimentation. In: Lerman A ed. Lakes: Chemistry, Physics, Geology. Springer-Verlag, New York, pp. 295-323.

Konecky, B.L., Russell, J.M., Rodysill, J.R., Vuille, M., Bijaksana, S., Huang, Y., 2013. Intensification of southwestern Indonesian rainfall over the past millennium. Geophys. Res. Lett., 40, doi:10.1029/2012GL054331.

Lazar, B., Enmar, R., Schossberger, M., Bar-Matthews, M., Halicz, L., and Stein, M., 2004. Diagenetic effects on the distribution of Uranium in live and Holocene corals: Examples from the Gulf of Aqaba. Geochim. Cosmochim. Acta 68, 4583–4593, doi: 10.1016/j.gca.2004.03.029.

Lieberman, V., 2003. Strange Parallels: Southeast Asia in global context, c. 800-1830. Integration on the mainland. Cambridge University Press, Cambridge, 2003.

Mann, M.E., Cane, M.A., Zebiak, S.E., Clement, A., 2005. Volcanic and solar forcing of the tropical Pacific over the past 1000 years. J. Climate 18, 447-456.

Meyers P.A., Lallier-Vergès E., 1999. Lacustrine sedimentary organic matter records of Late Quaternary paleoclimates. J. Paleolimnol. 21, 345-372.

Moy, C.M., Seltzer, G.O., Rodbell, D.T., Anderson, D.M., 2002. Variability of El Niño/Southern Oscillation activity at millennial timescales during the Holocene epoch. Nature 420, 162-165.

Müller, G., Irion, G., Förstner, U., 1972. Formation and diagenesis of inorganic Ca-Mg carbonates in the lacustrine environment. Naturwissenschaften 59, 158-164

Oppo, D.W., Rosenthal, Y., Linsley, B.K., 2009. 2,000-year-long temperature and hydrology reconstructions from the Indo-Pacific warm pool. Nature 460, 1113-1116.

Ortlieb, L., 2000. The documented historical record of El Niño events in Peru: An update of the Quinn record sixteenth through nineteenth centuries. In Henry F. Diaz and Vera Markgraf ((Eds.)) El Niño and the Southern Oscillation: Multiscale variability and global and regional impacts. Cambridge University Press, Cambridge, 2000 pp. 207-295.

Pierrehumbert R.T., 2000. Climate change and the tropical Pacific: The sleeping dragon wakes. Proc. Natl. Acad. Sci. 97, 1355-1358.

Rodysill, J.R., Russell, J.M., Bijaksana, S., Brown, E.T., Safiuddin, L.O., Eggermont, H., 2012. A paleolimnological record of rainfall and drought from East Java, Indonesia during the last 1,400 years. J. Paleolimnol. 47, 125-139.

Sachs, J.P., Sachse, D., Smittenberg, R.H., Zhang, Z., Battisti, D., Golubic, S., 2009. Southward movement of the Pacific intertropical convergence zone AD 1400-1850. Nat. Geosci. 2, 519-525.

Schnurrenberger, D., Russell, J.M., Kelts, K., 2003. Classification of lacustrine sediments based on sedimentary components. J. Paleolimnol. 29, 141-154.

Shapley, M.D., Ito, E., Donovan, J.J., 2005. Authigenic calcium carbonate flux in groundwater-controlled lakes: Implications for lacustrine paleoclimate records. Geochim. Cosmochim. Acta. 69, 2517-2533.

Shapley, M.D., Ito, E., Forester, R.M., 2010. Negative correlations between Mg:Ca and total dissolved solids in lakes: False aridity signals and decoupling mechanisms for paleohydrologic proxies. Geology 38, 427-430.

Stein, M., Goldstein, S.L., 2006. U-Th and radiocarbon chronologies of late Quaternary lacustrine records of the Dead Sea basin: Methods and applications. Geo. Soc. Am. Special Papers 401, 141-154.

Stothers, R.B., 1984. The Great Tambora eruption in 1815 and its aftermath. Science 224, 1191-1198.

Stuiver, M. and Reimer, P.J., 1993. Extended ^{14}C data base and revised Calib 3.0 ^{14}C age calibration program. Radiocarbon 35, 215–230.

Thompson, L.G., Yao, T., Mosley-Thompson, E., Davis, M.E., Henderson, K.A., Lin, P-N., 2000. A high-resolution millennial record of the south Asian monsoon from Himalaya Ice Cores. Science 289, 1916-1919.

Thompson, L.G., Mosley-Thompson, E., Davis, M.E., Lin, P.N., Henderson, K., Mashiotta, T.A., 2003. Tropical glacier and ice core evidence of climate change on annual to millennial timescales. Climatic Change 59, 137-155.

Tierney, J.E., Oppo, D.W., Rosenthal, Y., Russell, J.M., Linsley, B.K., 2010. Coordinated hydrological regimes in the Indo-Pacific region during the past two millennia. Paleoceanography 25, PA1102, doi: 10.1029/2009PA001871.

Tierney, J.E., Smerdon, J.E., Anchukaitis, K.J., Seager, R., 2013. Multidecadal variability in East African hydroclimate controlled by the Indian Ocean. Nature 493, 389-392.

Wolff, C., Haug, G.H., Timmermann, A., Sinninghe Damsté, J.S., Brauer, A., Sigman, D.M., Cane, M.A., Verschuren, D., 2011. Reduced interannual rainfall variability in East Africa during the last ice age. Science 333, 743-747.

Verschuren, D., 1993. A lightweight extruder for accurate sectioning of soft-bottom lake sediment cores in the field. Limnol. Oceanogr. 38, 1796-1802.

Verschuren, D., Laird, K.R., Cumming, B.F., 2000. Rainfall and drought in equatorial East Africa during the past 1,100 years. Nature 403, 410-414.

Sediment depth (cm)	Lab sample code	Dated material	^{14}C age (years BP)	Cal. Age (year CE)	1 Sigma age range 1 (years CE) (probability)	1 Sigma age range 2 (years CE) (probability)	1 Sigma age range 3 (years CE) (probability)
178.4	AA37293	Plant/Wood	236 ± 30	1790	1644:1668 (0.608821)	1782:1797 (0.364274)	1948:1950 (0.026905)
252.2[a]	OS-79520	Bulk Sediment	620 ± 25	1311	1299:1323 (0.40469)	1347:1369 (0.393168)	1380:1392 (0..202124)
326.7	AA37294	Plant/Wood	412 ± 40	1466	1436:1495 (0.861151)	1602:1615 (0.131489)	1509:1510 (0.007361)
371.1	OS-77312	Plant/Wood	690 ± 25	1287	1277:1297 (0.910767)	1373:1377 (0.089233)	
375.6	AA37295	Plant/Wood	692 ± 36	1287	1273:1300 (0.741854)	1368:1381 (0.258146)	
433.2	Beta 228346	Plant/Wood	830 ± 40	1218	1181:1256 (1)		
565.8	OS-77313	Plant/Wood	1190 ± 25	845	810:880 (0.898266)	782:790 (0.101734)	

Table 3.1 AMS ^{14}C ages on Lake Lading samples are listed in order of increasing cumulative depth with the radiocarbon age and measured age uncertainty (years BP), the calibrated age and associated age uncertainty [year in the Common Era (CE)], and one sigma calibrated age ranges in years CE with their associated probabilities.

a Note: This ^{14}C age was excluded from the age model.

Sample ID	**Sample Depth (cm)**	**^{238}U (ppm) (measured)**	**^{232}Th (ppb) (measured)**	**$^{230}Th/^{232}Th$ ($x10^{-6}$)**	**$\delta^{234}U$ (measured)**
A	561.5	6.66 $\pm$ 0.03	1.517 $\pm$ 0.2	27.9 $\pm$ 1.8	49.1 $\pm$ 1.9
B	561.5	8.50 $\pm$ 0.20	13.6 $\pm$ 1.2	24.3 $\pm$ 5.5	46.1 $\pm$ 3.2
Sample ID	**$^{230}Th/^{238}U$ (activity)**	**^{230}Th Date (years CE) (uncorrected)**	**^{230}Th Date (years CE) (corrected)**	**$\delta^{234}U_{initial}$ (corrected)**	
A	0.00256 $\pm$ 0.00015	1732 $\pm$ 16	1774 $\pm$ 26	49.1 $\pm$ 1.9	
B	0.00241 $\pm$ 0.0005	1746 $\pm$ 53	1791 $\pm$ 57	46.1 $\pm$ 3.2	

Table 3.2 U-Th disequilibrium dating measurements on Lake Lamongan aragonite and associated age corrections.

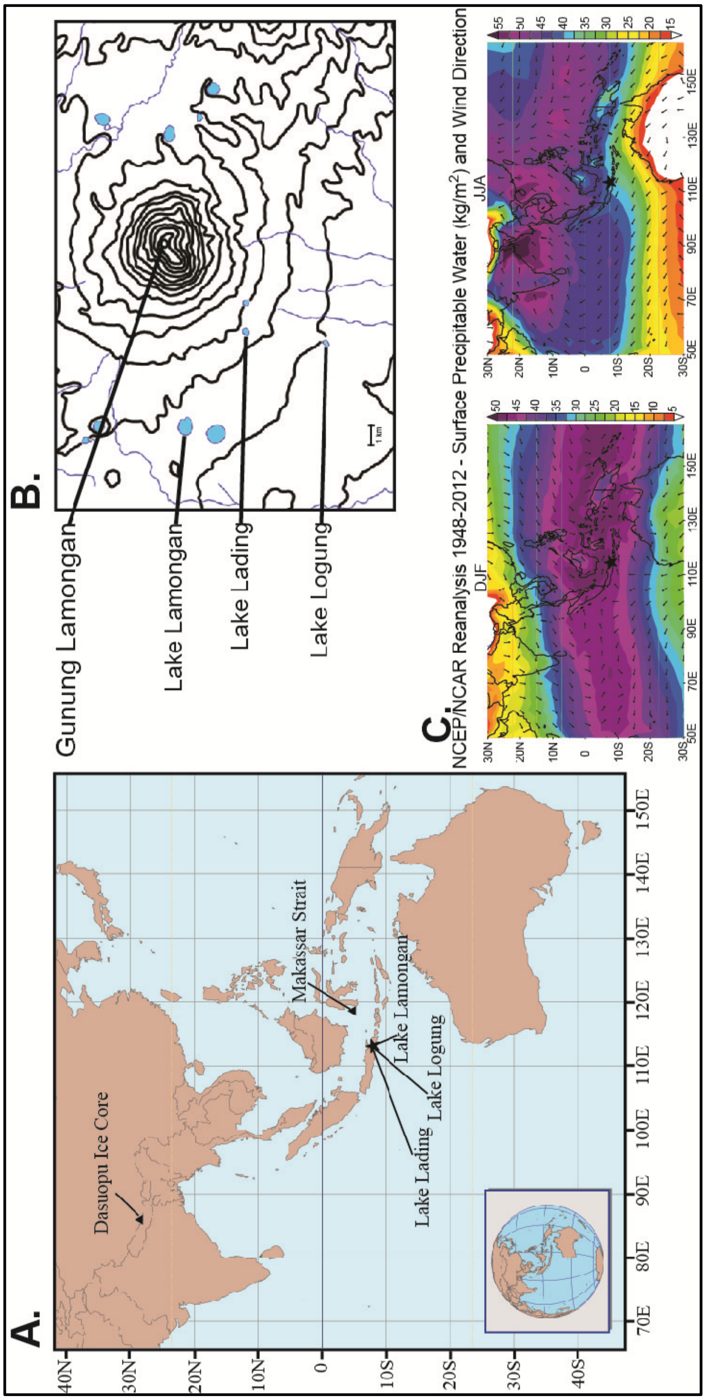

Figure 3.1: Location of our study sites and seasonal precipitation maps. **A**: Regional map highlighting the location of our study sites (star) and the Dasuopu ice core and Makassar Strait SST records mentioned in the discussion section (triangles). **B**: Contour map of Gunung Lamongan volcano in East Java with Lakes Lading, Logung, and Lamongan depicted as light blue circles. Black lines are 100 m contours. **C**: Seasonal precipitable water in kg/m^2 and wind direction at 1000 mb in Java during austral summer (left) and austral winter (right). Cooler colors represent a greater amount of precipitable water.

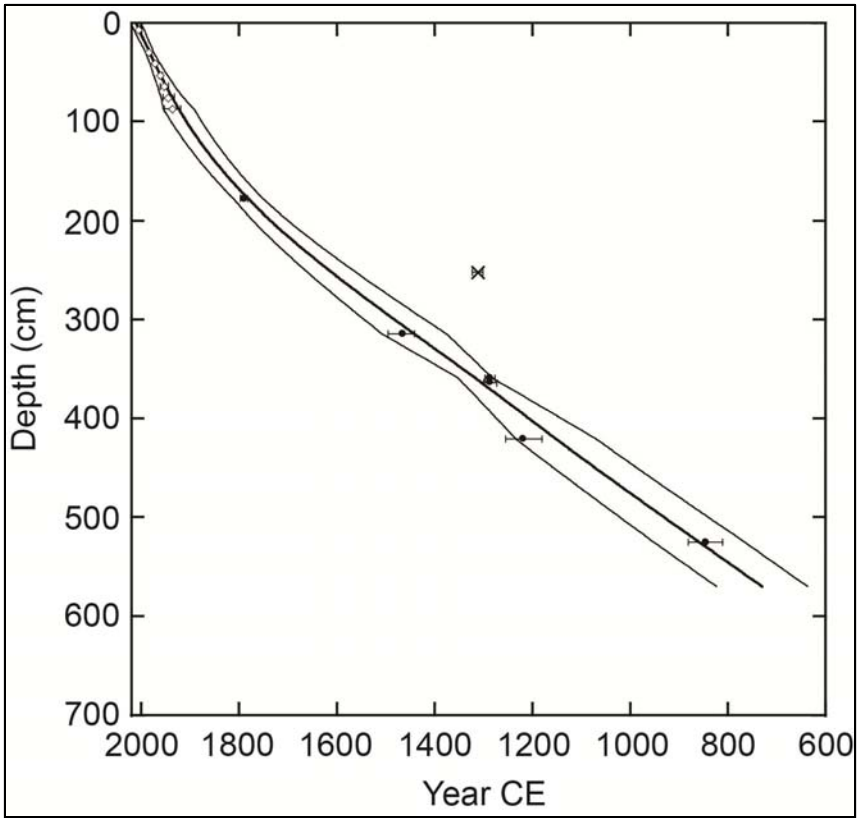

Figure 3.2: The Lake Lading age model. ^{14}C ages are shown as dark circles with error bars indicating their associated 1σ errors and ^{210}Pb dates are shown as open diamonds. The ^{14}C age not included in the age model is depicted with an "x." The thick solid line denotes the age model, derived using methods from Heegaard et al. (2005), and the two thin solid lines represent the uncertainty in the age model. The sedimentation rate increases from 0.4 cm/yr below 2 m to 1.14 cm/yr in the ^{210}Pb-dated portion of the core.

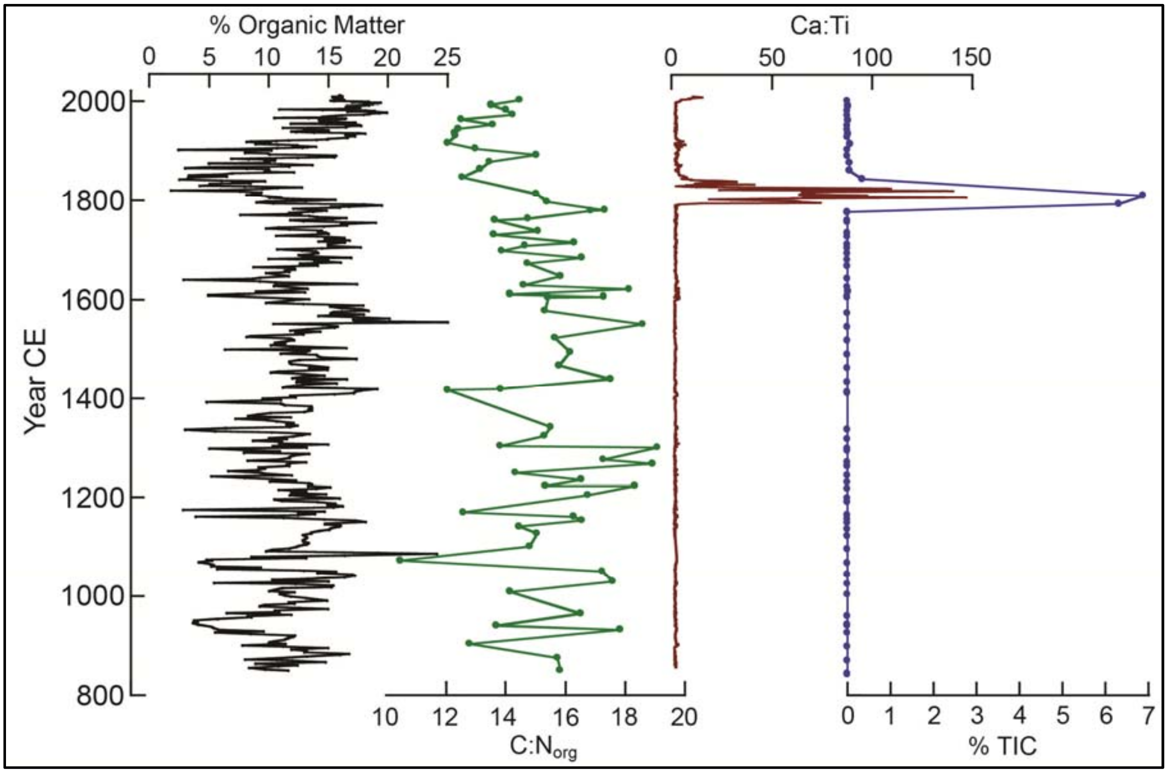

Figure 3.3: Lake Lading sediment geochemistry. The left plot is percent organic content determined by loss on ignition (% Organic matter; black), the left middle plot is the ratio of organic carbon to nitrogen (C:N$_{org}$; green), the right middle plot is Ca:Ti calculated from XRF measurements (maroon), and the right plot is percent inorganic carbon (% TIC; blue). Closed circles are individual data points. These data are plotted on a time axis (on the left).

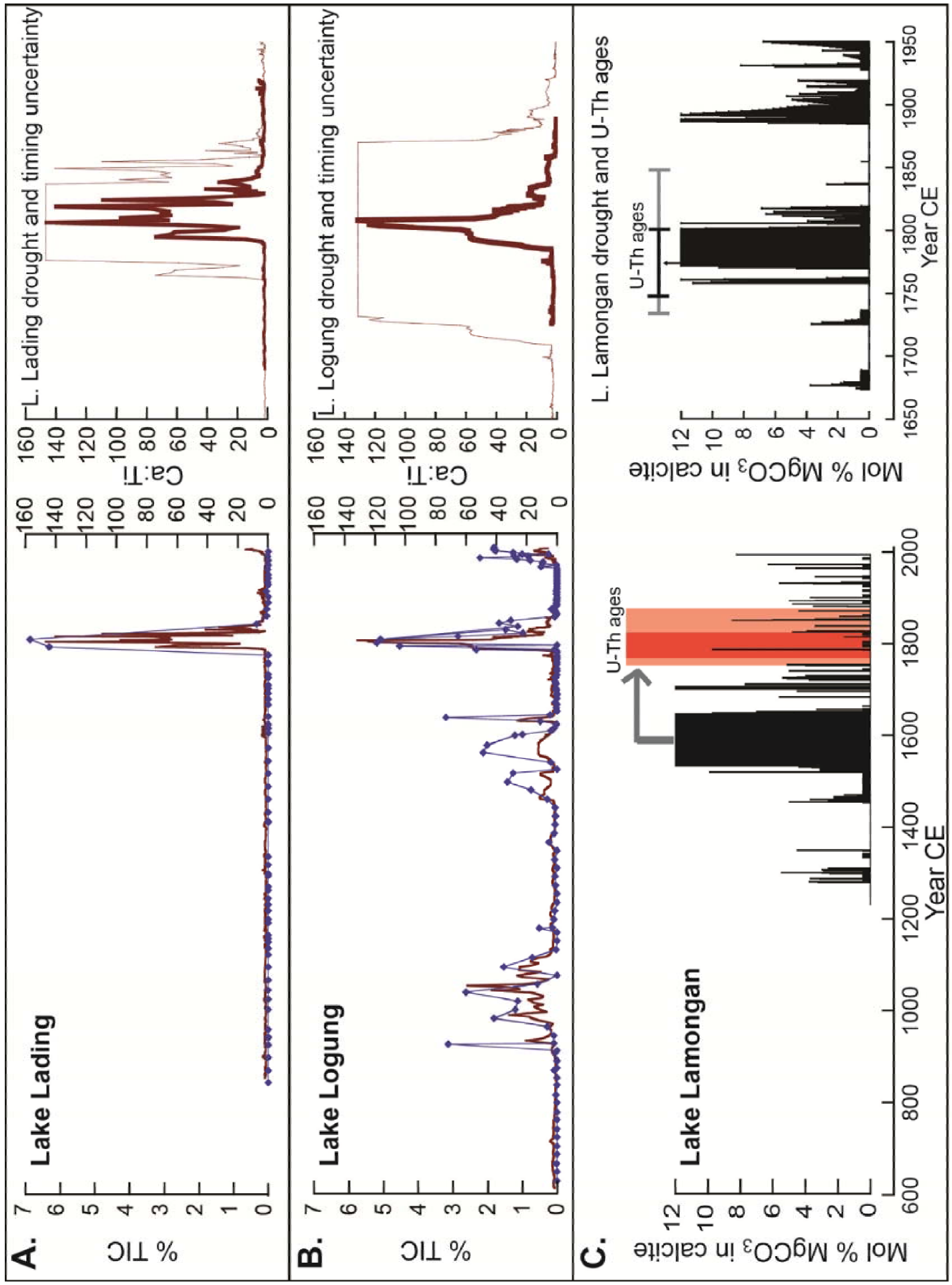
A.
Lake Lading
% TIC
L. Lading drought and timing uncertainty
Ca:Ti
B.
Lake Logung
% TIC
L. Logung drought and timing uncertainty
Ca:Ti
C.
Lake Lamongan
Mol % MgCO3 in calcite
U-Th ages
Year CE
L. Lamongan drought and U-Th ages
U-Th ages
Year CE

Figure 3.4: Drought records from East Java lakes. **A**: On the left, carbonate abundance in Lake Lading is plotted with total inorganic carbon content (% TIC, left axis) displayed in blue circles and Ca:Ti (right axis) displayed in maroon. On the right, Ca:Ti from Lake Lading is plotted in a thick maroon line to show the timing of the late 1700's/early 1800's drought at this site. **B**: On the left, carbonate abundance in Lake Logung (left) is plotted with total inorganic carbon content (% TIC, left axis) displayed in blue circles and Ca:Ti (right axis) displayed in maroon. On the right, Ca:Ti from Lake Logung is plotted in a thick maroon line to show the timing of the late 1700's/early 1800's drought at this site. The earliest onset and latest termination of Ca:Ti in each lake considering maximum age model error is plotted in thin maroon lines to illustrate the maximum age range of the drought. **C**: % $MgCO_3$ in calcite in Lake Lamongan sediments plotted in black on the published age model (left). The arrow points to a dark red rectangle, which represents the U-series age range of Sample A, and a light red rectangle, which represents the U-series age range of Sample B. % $MgCO_3$ in calcite plotted with new ages based upon sedimentation rate between the new U-Th dates (right), shown as black and grey error bars for Sample A and B, respectively, and a core-top age of 1998 CE. The U-Th-dated aragonite lamina is indicated with an arrow.

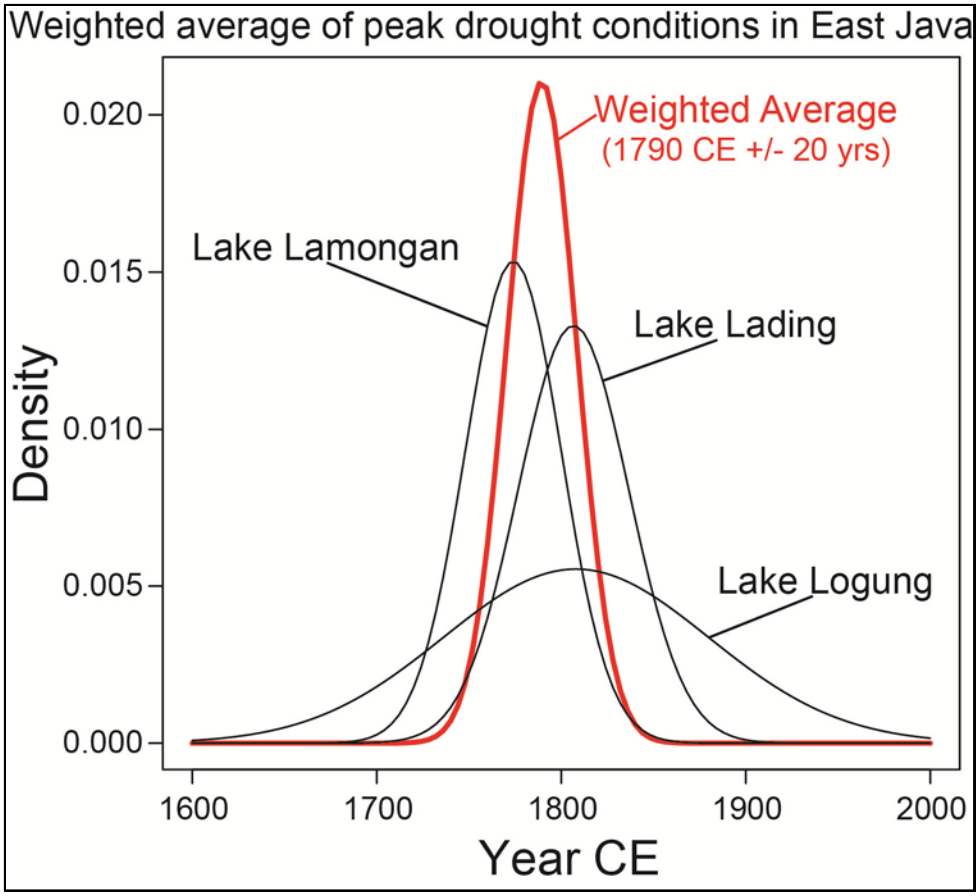

Figure 3.5: The probability density functions of the timing of peak drought in each lake and the weighted average age of East Java drought. The black curve from Lake Lamongan is the probability density function of the U-series age on Sample A, the black curve from Lake Lading is the probability density function of the age and 95% confidence interval from the carbonate abundance maximum occurring at 1806.6 CE +/- 30 yrs, and the black curve from Lake Logung is the probability density function of the age and 95% confidence interval from the carbonate abundance maximum occurring at 1808 +/- 72 yrs. The thick red line is the weighted average age of peak drought conditions in East Java and the variance on the weighted average at the 95% confidence interval.

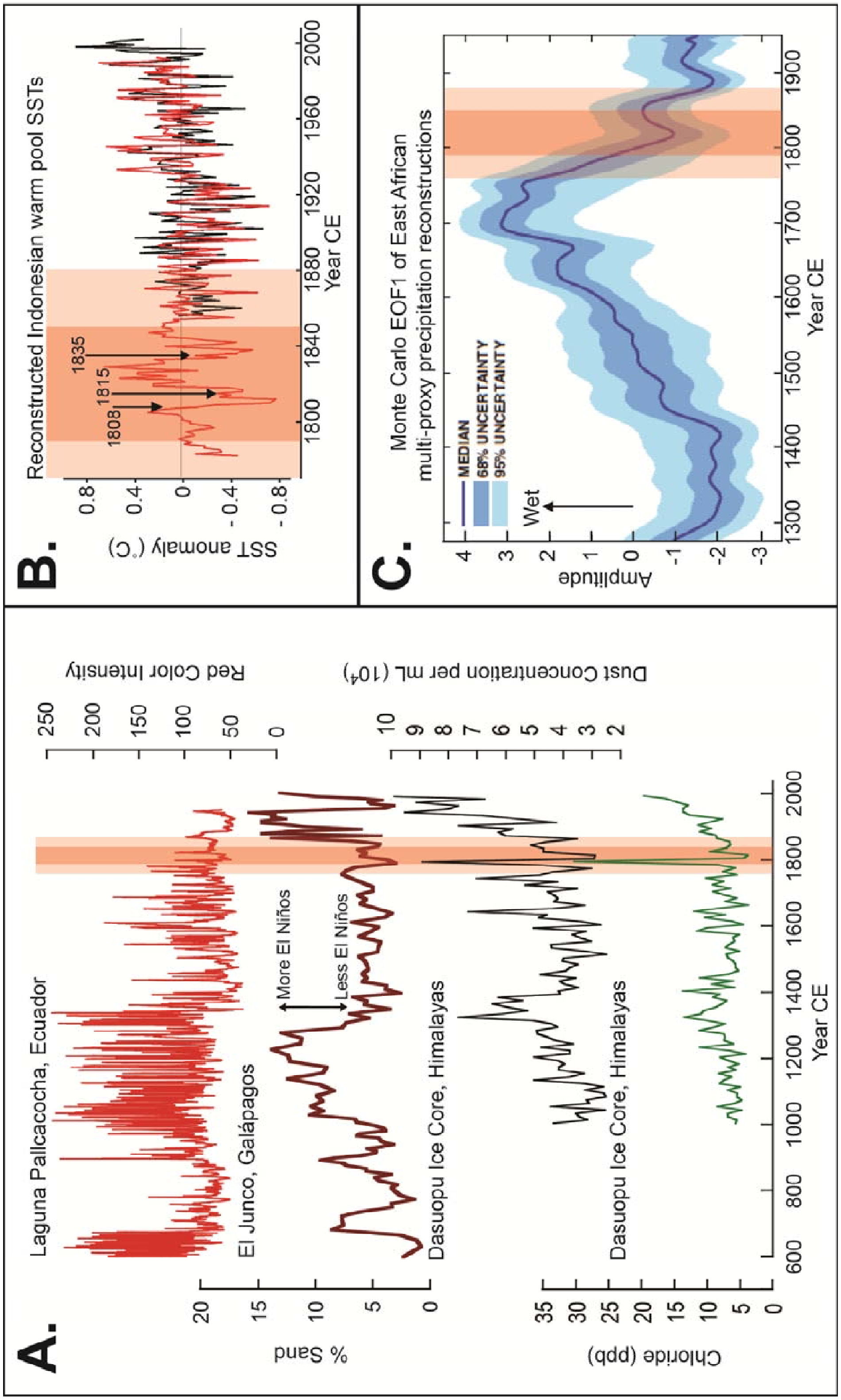
A.
Laguna Pallcacocha, Ecuador
El Junco, Galápagos
Dasuopu Ice Core, Himalayas
Dasuopu Ice Core, Himalayas
More El Niños
Less El Niños
% Sand
Chloride (ppb)
Red Color Intensity
Dust Concentration per mL (10⁴)
Year CE
B.
Reconstructed Indonesian warm pool SSTs
SST anomaly (°C)
1808
1815
1835
Year CE
C.
Monte Carlo EOF1 of East African
multi-proxy precipitation reconstructions
MEDIAN
68% UNCERTAINTY
95% UNCERTAINTY
Wet
Amplitude
Year CE

Figure 3.6: Comparison of Lake Lading drought and relevant paleoclimate records. **Panel A**: From top to bottom the records shown are Laguna Pallcacocha, Ecuador red color intensity (red, Moy et al., 2002), El Junco Lake, Galápagos % sand (maroon, Conroy et al., 2008), and the Dasuopu ice core dust (black) and chloride (green) concentrations (Thompson et al., 2000). Drought in Lake Lading sediments does not occur during any substantial El Niño activity inferred from EEP records, but does begin at the same time as drought inferred from the Himalayan ice core data. The timing of the drought in Lake Lading (1790-1850 CE) is indicated by a dark red rectangle, with the age uncertainty (1760-1790 and 1850-1880 CE) indicated by a light red rectangle. Note that these age ranges are for the Lake Lading drought only, and Lake Lamongan U-Th ages suggest the onset of drought in that basin may have occurred earlier than 1790 (~1775) CE. **Panel B**: Instrumental Indonesian warm pool SSTs are shown in black and reconstructed SSTs, based on tree ring and coral data, is shown as a red line; modified after D'Arrigo et al. (2006). The volcanic eruptions occurring in 1809, 1815, and 1835 are highlighted with arrows. The timing of the drought in Lake Lading (1790-1850 CE) is indicated by a dark red rectangle, with the age uncertainty (1760-1790 and 1850-1880 CE) indicated by a light red rectangle. Anomalously cold SSTs span the decade during which the volcanic eruptions occurred and are concurrent with drought in Lake Lading sediments. **Panel C**: The dark blue thin line is the Monte Carlo EOF1 produced in the study by Tierney et al. (2013) which indicates a prolonged pluvial during the 17th-19th centuries. 68% and 95% age uncertainty in the EOF output are shown as medium and light blue shading. Drought in Lake Lading, illustrated by the darker red rectangle, begins at the tail end of this pluvial, and persists beyond it into the mid-1800's. The lighter red rectangle illustrates the uncertainty in the timing of the drought in Lake Lading.

CHAPTER 4

ENSO-driven flooding events in East Java, Indonesia during the past millennium

Jessica R. Rodysill[1]

James M. Russell[1], Mathias Vuille[2], Brent Lunghino[1], Satria Bijaksana[3]

[1]Department of Geological Sciences, Brown University

[2]Department of Atmospheric and Environmental Sciences, University at Albany

[3]Faculty of Mining and Petroleum Engineering, Institut Teknologi Bandung

For submission to: *Nature Geoscience*

4.1 Abstract

Recent catastrophic flooding in Java, Indonesia has highlighted the importance of understanding the mechanisms that cause extreme precipitation events and their variability in the past. We present the first record of runoff events from lake sediment deposits in East Java, Indonesia spanning the last millennium. Our record reveals significant variations in East Java flooding frequency, with more frequent floods occurring from 850 to ~1400 CE and from ~1800 CE to present. This pattern is also observed in two surface runoff records from the eastern tropical Pacific, implying that on centennial timescales, extreme rainfall events on both sides of the tropical Pacific vary in unison. All three of these records lie in regions that are sensitive to ENSO-driven precipitation anomalies, with flooding in East Java during strong La Niña events and flooding in the eastern Pacific during El Niños. The coherence between flood events in the eastern and western equatorial Pacific suggests that both El Niño and La Niña activity were higher during the Medieval Climate Anomaly and the most recent two centuries, when radiative forcing was high, and that ENSO activity was reduced during the Little Ice Age, when radiative forcing was weak.

4.2 Introduction

Extreme rainfall events in the tropics have enormous societal consequences, destroying crops, drinking water supplies, and homes. As recently as 2013, Indonesia experienced catastrophic flooding that killed 222 people, displaced 300,000 people, and destroyed 27,000 homes (Indonesia National Disaster Management and Mitigation Agency Disaster Bulletin, March 2013). Multiple components of the climate system can cause heavy rainfall in East Java, Indonesia, including variability in the Australian-Indonesian Summer Monsoon (AISM), the El Niño-Southern Oscillation (ENSO), and other local atmospheric convective anomalies associated with Indo-Pacific Warm Pool (IPWP) sea surface temperatures (SSTs). It remains unclear how these patterns varied on long timescales, nor can we predict how they will change in the future.

Lake sediment records of flooding events from the eastern tropical Pacific have provided benchmark records of interannual variability associated with the El Niño-Southern Oscillation (Moy et al., 2002; Conroy et al., 2008), yet these records only capture runoff deposits in one of ENSO's two major centers of action. ENSO events produce rainfall anomalies on both sides of the Pacific, with El Niño events causing heavy rainfall in the eastern tropical Pacific and La Niña events causing heavy rainfall over Indonesia in the west (Ropelewski and Halpert, 1987). Here we present the first reconstruction of runoff events from the Western Pacific Warm Pool based upon a new lake sediment record from East Java, Indonesia to test how patterns of tropical Pacific rainfall varied during the past millennium.

Our record is based on coarse sediment deposits in Lake Lading, a small crater lake in East Java, Indonesia. Extremely high sedimentation rates and laminated sediments preserve individual beds of coarse sediments, giving this millennium-long record a unique sensitivity to short-duration climate events relative to previous paleoclimate records from the region (e.g. Oppo et al., 2009; Tierney et al., 2010; Rodysill et al., 2012; Konecky et al., 2013).

4.2.1 Study site: Modern rainfall patterns and location background

Lake Lading (8˚0.53'S, 113˚18.75'E) is a small, ~200 m diameter, 8.6 m deep maar lake on the southwest side of Gunung Lamongan (Figure 3.1), a volcano associated with the Sunda Arc volcanism (Carn and Pyle, 2001). The lake basin and surrounding catchment in the maar basin are steep sided, and the catchment of Lake Lading is a young volcanic landscape composed of material derived from the mafic-intermediate oceanic crust (Carn and Pyle, 2001). Vegetation in the catchment is open forest, and the crater rim is cultivated (personal observation).

Rainfall stations near Lake Lading average 2560 mm of rainfall per year, most of which occurs between November and April when the AISM strengthens and the Intertropical Convergence Zone (ITCZ) migrates southward over Java (Vose et al., 1992). The dry season in East Java occurs in the Austral winter from, June through September, as the ITCZ migrates northward away from Java. ENSO activity greatly influences interannual rainfall variability in Indonesia; El Niño events delay the onset of the rainy season and cause drought in the June-July-August (JJA) and September-October-November (SON) seasons. La Niña events locally enhance convection and rainfall, causing heavy rainfall during JJA and SON (Hendon, 2003). The IOD also influences convection over Indonesia through reorganizations of Indian Ocean SSTs and atmospheric circulation, sometimes independently from ENSO (Saji et al., 1999; Ashok et al., 2003). Negative dipole events enhance convection in the eastern Indian Ocean and can produce heavy rainfall in East Java.

4.3 Methods

4.3.1 Geochemical and Grain Size data

We measured the magnetic susceptibility (magsusc) and coarse fraction content of the sediments in a composite core from Lake Lading. A detailed description of the core stratigraphy and age model construction is provided in Rodysill et al. (under review). We measured magsusc of the sediments at 1-cm resolution using a point sensor magnetic susceptibility meter on a GeoTek Multi-Sensor Corelogger at Brown University. The sediments were sampled continuously in 1-cm increments for loss-on-ignition and sieving analyses. Loss-on-ignition analyses were used to determine sediment water content and organic matter content following the protocol of Dean (1974). To determine coarse sediment content, each sample was wet sieved at 63 microns after the LOI analysis, dried at 100˚C overnight, cooled to room temperature, weighed, and the dry coarse mass was divided by the bulk dry sediment weight. At nearby Lake Logung, bulk organic N isotopic data were useful for inferring major changes to lake chemistry and ecosystem productivity associated with anthropogenic activity in the catchment after 1860 CE (Rodysill et al., 2012), so we collected the same data from Lake Lading at ~7.5 cm resolution to determine the timing that human activity in the catchment began to have a strong influence on sedimentation. The sub-samples were pretreated to remove inorganic forms of N by soaking in 1 N HCl at room temperature for one hour, rinsed five times with ultra-pure deionized water, and then dried and homogenized for analysis on a

Costech Instruments elemental combustion system coupled to a Delta V Plus isotope ratio mass spectrometer with a Conflo II interface. Precision determined from standards and 10% replication was 0.674%. A subset of samples was measured prior to and after pretreatment to determine the effects of acidification on $\delta^{15}N_{org}$ values, and this test revealed that the isotopic values of both sets of samples were well within our analytical precision with no bias between acidified and unacidified samples.

4.3.2 Construction of runoff records

The magnetic susceptibility and % >63 microns (% sand) datasets from Lake Lading were each filtered with a 12^{th}-order high-pass filter with a cutoff frequency value of 0.1 (10 years) to isolate high-frequency variability. A high-magsusc or coarse deposit anomaly was defined as a value(s) in the high-pass filtered dataset that exceeded 200 SI or 10%, respectively, which defines a coarse deposit as being coarser than 80% of the data. We tested a range of values between 5 and 25% in the high-pass filtered % sand ($COARSE_{high\text{-}pass}$) dataset to determine whether our selections of threshold value influenced long-term trends defined runoff events and determined that the multi-centennial trends are the same for all values (See section 4.4.2). We tested a range of filtering methods to test whether the filtered data trends are sensitive to the type of filtering used.

4.3.3 Instrumental Data

All instrumental precipitation data were measured at the Randuagung weather station in East Java (8.07˚S, 113.3˚E), located ~15 km SE from our study site. These data were made available by the Global Historical Climatology Network and cover Jan. 1927 to Dec. 2011 (Vose et al., 1992). We calculated standardized seasonal precipitation anomalies for December-January-February (DJF), March-April-May (MAM), June-July-August (JJA), and September-October-November (SON). These were compared to the Southern Oscillation Index (SOI) from 1866-2011 (Ropelewski and Jones, 1987) and the SST-based Dipole Mode Index (DMI) from 1856-2007 (Saji et al., 1999) calculated from the Kaplan et al. (1998) dataset.

4.4 Results

4.4.1 Core Stratigraphy and Age Model

The core generally consists of thin beds of diatom oozes alternating with thin beds of silts and sands (Figure 4.1). Authigenic carbonate is uncommon in this sediment core with the exception of a 35 cm thick bed that marks severe drought ca. 1790 CE (Rodysill et al., under review). The sediments are very thinly bedded from 570 cm to 90 cm depth, where the structure of the sediments becomes thickly-bedded to massive to the core top. Two tephra beds at 940 and 1600 CE were removed from the composite stratigraphy prior to application of the age model and are not included in the grain size or magsusc data. Sedimentation rates range from 0.4 cm/yr in the lower 4 meters to 1.14 cm/yr in the upper ^{210}Pb-dated meter of sediment (Figure 4.2). Each 1-cm sample represents just under 3 years in the lower 2.5 meters of the core, ~2 years per sample between 1 and 3 meters depth, and ~1 year per sample in the upper meter of sediment.

4.4.2 Sediment geochemistry and grain size data

Magsusc averages 280 SI and ranges between 1 and 1767 SI (Figure 4.3A). The sand content of the sediments averages 13%, ranging between 0.1 and 88% (Figure 4.3A). Magsusc and % sand are significantly correlated with a Pearson's r value of 0.55, which is likely an underestimation of the strength of the correlation as the magnetic susceptibility sensor integrates measurements over slightly more than 1 cm, a wider signal than the grain size data. High magsusc values in the highpass-filtered dataset align with 92% of the coarse anomalies in the highpass-filtered coarse anomaly dataset ($COARSE_{high\text{-}pass}$), so we determined that magsusc and coarse fraction anomalies are essentially recording the same processes and only utilize the coarse sediment dataset for our discussion.

We defined the cutoff value for an event in the $COARSE_{high\text{-}pass}$ dataset as 10%, which isolates the upper 20% of the probability distribution function of the dataset. Varying the cutoff value between 5 and 25%, which isolate the upper 0.2 through 33% of the probability distribution function of the dataset, does not change the centennial-scale trends of the dataset (Figure 4.4). $COARSE_{high\text{-}pass}$ isolated 36 coarse events throughout the record, 5 of which occur during the historical period (1866 – 2010; Figure 4.3B). Coarse events are common prior to 1350 CE, become less frequent after 1350 CE, and are more frequent again starting in the early 1800s (Figure 4.3B). Event frequency was highest between 950 and 1000 CE, where there were 4 events per 50 years, and was lowest from 1550 to 1600 CE and 1700 to 1750 CE, where there were 0 events per 50 years (Figure 4.3C). Between 1000 and 1350 CE and from 1800 CE to present, event frequency ranged between 1 and 3 events per 50 years, and between 1350 and 1800 CE, event frequency ranged between 0 and 2 events per 50 years. These centennial-scale trends in the filtered dataset are the same for multiple filtering methods (e.g. high-pass, first difference), so we determined the variations in event frequency are insensitive to the type of filter used.

$\delta^{15}N_{org}$ values averaged 0.45‰ throughout the record with a stepwise increase from an average of 0.08‰ before 1840 CE to an average value of 1.69‰ between 1860 CE and the present (Figure 4.5). Between 1900 and 2010 there is a noticeable depletion in isotopic values from ~4‰ to 1‰, but present-day values still remain enriched by ~1‰ relative to the majority of the record prior to the mid 1800s.

4.5 Discussion

4.5.1 Evidence for runoff from proxy data

Lake Lading occupies a relatively steep-sided maar crater composed largely of volcanic tuffs from nearby Gunung Lamongan, allowing for sediments to be easily mobilized and transported from the catchment into the lake. These materials are rich in iron-bearing minerals including olivine, magnetite and Fe-rich pyroxenes that contribute to the abundance of ferromagnetic minerals in the sediments, which are easily detected by magsusc measurements (Eriksson and Sandgren, 1999; Sandgren and Snowball, 2001). Therefore, we attribute high magsusc in the sediment core to greater terrigenous inputs to the center of the lake basin.

Crausbay et al. (2006) determined that the sediments in nearby Lake Lamongan alternate between light-colored diatom and carbonate-rich beds and dark clastic beds in response to heightened diatom productivity and carbonate precipitation during the dry season (Green et al., 1976) and delivery of terrigenous materials to the sediments during wet season rainfall events. Lake Lading sediments similarly alternate between diatom and clastic deposition, and the sand content presumably reflects changes in the amount of wet season clastic deposition. Heavy rainfall should enhance the delivery of coarse sediments into the lake and to our sediment core, accompanying the high magsusc values.

Other processes can result in deposition of coarse sediment near the center of the lake basin, such as shoreline migration during lake lowstands (Digerfeldt, 1986), changes in the flow of river inputs, or earthquakes. If lake level lowstands were responsible for coarse deposits observed in our cores we would expect that local drought would correspond to periods characterized by coarser sediments in Lake Lading. However, a comparison of drought reconstructions from Lake Lading and nearby Lake Logung reveals that droughts correspond to low coarse content and magsusc (Figure 4.6; Rodysill et al., 2012; Rodysill et al., under review). For instance, the most intense drought in the Lake Lading record occurs during a lull in coarse sediment deposition between 1790 and 1860 CE (Figure 4.6; Rodysill et al., under review). A comparison with a δD dataset from the same core from Lake Lading supports our interpretation that coarse deposits and higher magsusc are associated with wet conditions, as century-scale periods of depleted

δD (wet) centered at 900, 1225, 1325, and 1830 CE occur when broad trends in coarse content and magsusc in Lake Lading indicate runoff was high (Figure 4.6; Konecky et al., 2013). Lake Lading has no river or stream inflows, and instead receives much of its clastic inputs from surface runoff. The coarse beds in Lake Lading sediments lack characteristics that are commonly associated with earthquake-driven deposition, including debris flows and microfaults (Beck et al., 1996). These observations led us to infer that coarse sediments in Lake Lading are deposited as a result of runoff from the landscape rather than lowstands, and that high runoff indicates high rainfall.

It is unlikely that $COARSE_{high\text{-}pass}$ captures individual runoff events, since the sedimentation rates are low enough that two or more coarse deposition events occurring within weeks or even a few months of one another would not be distinguishable in our 1-cm (~1-3 year) sampling resolution. Therefore we interpret the $COARSE_{high\text{-}pass}$ record to reflect sub-decadal periods of intense runoff that represents a combination of individual events and an averaged signal of multiple, closely-spaced runoff events.

4.5.2 Influence of landscape alteration on historical sedimentation

East Java is a heavily populated region where widespread agricultural practices continually alter the landscape and sedimentation in the crater lakes (Rodysill et al., 2012). The catchment of Lake Lading is open forest and is not currently cultivated, but its land-use history is poorly documented, and the crater rim and adjacent areas are cultivated for coffee and other crops (personal observation). Our prior work in a nearby crater lake, Lake Logung, documented a 4‰ enrichment in $\delta^{15}N_{org}$ in 1840 CE that coincides with a major regional intensification of agricultural activity in East Java (Figure 4.5; Rodysill et al., 2012). We observe a similar signal in Lake Lading, indicating changes in nitrogen cycling in Lake Lading during a period of widespread agricultural activity in East Java circa 1840 CE. The rise in sedimentation rates occurs at the same time as $\delta^{15}N_{org}$ enrichment and the transition from thinly to thickly bedded sediments, indicating that recent sedimentation is strongly influenced by human activities. The acceleration in sedimentation rate and the loss of laminae indicate that the historical runoff record from Lake Lading may have a muted response to climate forcing relative to the past millennium. Moreover, the gradual decline in grain size and magnetic susceptibility after 1900 CE are unlikely to reflect a reduction in runoff due to a drying climate, because there has not been a significant drying of the climate between 1927 and present in nearby station rainfall data (Vose et al., 1992). Below, we focus the climate-related discussion of our record to the period prior to 1850 CE to avoid misinterpreting anthropogenically-influenced sedimentation as climate-driven.

4.5.3 Instrumental climate data analysis

We tested the correlation between local station rainfall data and the Southern Oscillation Index (SOI) and the Dipole Mode Index (DMI) by comparing seasonal rainfall standardized anomalies to seasonal SOI and DMI values with a Pearson's R correlation from 1927 to 2012, with seasonal lags from 0 to 1 year. This analysis revealed eight significant correlations between the datasets (p-value <0.05; Table 4.1). The strongest correlations are highly significant (p-value <0.001) and indicate that SOI is positively correlated to rainfall near Lake Lading during JJA and SON (Table 4.1) with the strongest correlations at zero lag. These results are consistent with seasonal composite data indicating positive rainfall anomalies occur in East Java during the Austral winter and spring of La Niña years (Figure 4.7). Much like the SOI, the correlation between DMI and East Java rainfall is highly significant (p-value <0.001) and strongly negative during Austral winter and spring, particularly during SON (Table 4.1). There also appears to be a significant positive correlation (p-value <0.01) between DMI and precipitation in East Java with a >6 month lag that may be indicative of drier than normal dry seasons following a negative IOD event and/or wetter than normal dry seasons following a positive IOD event.

A caveat to these relationships is that the SOI is a measure of the pressure difference between Tahiti and Darwin, Australia, and IOD events influence atmospheric pressure at Darwin without influencing the atmospheric pressure in Tahiti. The SOI index therefore potentially indicates changes in IOD in addition to ENSO (Behera and Yamagata, 2001). It is unclear based on these correlations how much of the relationship between SOI and East Java rainfall is attributable solely to ENSO versus the IOD.

4.5.4 Comparison of historical proxies with instrumental data

To test whether runoff deposits in Lake Lading are associated with La Niña and negative IOD events, we compared the $COARSE_{high\text{-}pass}$ dataset from Lake Lading with the SOI in the JJA and SON seasons and DMI in the SON season, when each index was most strongly correlated to East Java rainfall. Event beds in our record are deposited more rapidly than the fine-grained sediments; we use ages determined at the base of each coarse bed, which is likely most representative of the event's true age, as the timing of onset of a runoff event. Of the five coarse deposits between 1866 and 2010, four of the events occurred when the SOI was strongly positive and two occurred when DMI was negative, with both DMI events associated with a positive SOI (Figure 4.8). We suggest, based on the observation that nearly all runoff layers coincide with positive SOI values and fewer than half of the event deposits were associated with negative DMI, that Pacific Ocean dynamics are the main control on heavy rainfall in East Java on sub-decadal timescales. Indeed, the runoff events at 1879, 1908, 1918, and 1950 CE align within a year of severe La Niña events. That said, two La Niña events of equal or greater magnitude did not produce runoff deposits in Lake Lading (Figure 4.8). Large variations in the spatial distribution of rainfall during La Niña events, such as those observed between the 1955 and 1975 events (Figure 4.9), can account for the lack of a one to one relationship between intense La Niña events and flood deposits in the Lake Lading record. Thus, our record cannot be interpreted to capture all ENSO activity and La Niña-driven flooding across Indonesia, but does reflect La Niña-driven flooding in East Java.

4.5.5 Long-term runoff variability 850-1800 CE

Our reconstruction indicates that extreme runoff events were more common between 850 and ~1400 CE and after ~1800 CE. The timing of these changes is remarkably similar to the pattern of temperature changes in the northern hemisphere, namely the warm conditions of the Medieval Climate Anomaly (MCA) prior to 1350 CE, followed by cool conditions during the Little Ice Age (LIA) from 1350-1800. Numerous lines of evidence suggest that the ITCZ migrated northward during the MCA and southward during the LIA in response to these changes in the interhemispheric temperature gradient (Broccoli et al., 2006). This evidence includes records from the western, central, and eastern equatorial Pacific (Sachs et al., 2009), speleothem isotopic records in China (Wang et al., 2005; Zhang et al., 2008), and sedimentological and isotopic reconstructions of climate from Lakes Lading and Logung (Rodysill et al., 2012; Konecky et al., 2013). However, the $COARSE_{high\text{-}pass}$ dataset suggests event-scale rainfall intensity was actually lower during the LIA, and higher prior to and after the LIA, opposite of what we would expect if changes in mean rainfall associated with ITCZ migration drove coarse-fraction sedimentation (Figure 4.3). We conclude that ITCZ dynamics are not directly related to the intense rainfall events in East Java at multi-centennial timescales.

4.5.6 Zonal Pacific runoff relationships

Changes in the strength of the Walker Circulation can influence rainfall amount on multiple timescales on both sides of the tropical Pacific Ocean. A 'stronger Walker' should, all other things equal, enhance rainfall over Indonesia while reducing it in the region of atmospheric subsidence over the eastern tropical Pacific. As noted above, prior work has developed runoff event records from the eastern tropical Pacific, namely a red color intensity-based runoff record in Ecuador and a % sand-based runoff record in the Galápagos (Figure 4.10A-D; Moy et al., 2002; Conroy et al., 2008). We compare our

COARSE$_{high\text{-}pass}$ reconstruction to examine, for the first time, whether extreme precipitation events recorded in the two centers of action of the Walker circulation covary during the last millennium.

The % sand record from the Galápagos and the red color intensity record from Ecuador both indicate a step-wise decrease in runoff in the eastern tropical Pacific from high runoff between 1000 CE and the early-mid 1300s to low runoff from the mid-1300s to 1800 CE (Figure 4.10C and D; Moy et al., 2002; Conroy et al., 2008). We observe a higher frequency of runoff events in East Java from 850 CE to the late 1300s followed by lower runoff event frequency between the late 1300s and the early 1800s. Following the LIA, the frequency of runoff events in East Java increased again in the early 1800s for about a century, similar to an increase in runoff in the Galápagos. These data thus suggest that both the east and west sides of the tropical Pacific Ocean underwent a major shift from more intense to less intense rainfall events during the 1300s, and that rainfall event intensity increased again on both sides of the Pacific after 1800 CE.

Runoff deposits in the Galápagos and Ecuador have previously been interpreted to reflect heavy rainfall during El Niño events (Moy et al., 2002; Conroy et al., 2008), although other interpretations are possible. If runoff deposits at these sites are associated with heavy rainfall during El Niño events, and if the majority of the high-frequency runoff deposits in Lake Lading are associated with heavy rainfall during La Niña events, then the shift from frequent runoff events during the MCA to less frequent events during the LIA observed on both sides of the Pacific implies that El Niño and La Niña activity co-varied on multi-centennial timescales during the last millennium. This, in essence, implies an intensification of ENSO activity during the MCA, and a weakening during the

LIA, as has been suggested by Makou et al. (2010) based on biomarker concentrations in sediments from the Peru Margin.

Many La Niña events in the historical record are not represented by runoff deposits in Lake Lading, and there is well-documented evidence for very strong El Niño events during the late 1700s that are not clearly documented in the sediment-based reconstructions from the eastern tropical Pacific (Moy et al., 2002; Conroy et al., 2008). The spatial heterogeneity in precipitation anomalies associated with ENSO could explain the difference between the Eastern Pacific runoff records between 1800 CE and the present, and might also help to explain slight differences between the eastern Pacific and Lake Lading records. The spatial variability of precipitation anomalies in the tropics amongst ENSO events implies that caution needs to be taken when interpreting the trends in any of these spatially stationary runoff reconstructions as variations in overall ENSO activity. That said, the in-phase behavior between these two centers of action strongly suggests that ENSO activity was enhanced from 1000-1300 and ~1800 CE.

Enhanced ENSO activity during the MCA would appear to contradict the ocean dynamical thermostat hypothesis, which predicts that during periods of enhanced radiative forcing such as the MCA, SSTs in the western Pacific should increase relative to the east due to differential heating (Clement et al., 1996; Cane 2005; Karnauskas et al., 2009). This, in turn, strengthens trade winds and Walker circulation, reinforcing the SST gradient, and suppresses westerly winds that are key to ENSO activity. Proxy records document warm SSTs in the western equatorial Pacific during the MCA (Oppo et al., 2009), yet we lack high-resolution proxy records of eastern equatorial SSTs to test this prediction. Higher ENSO activity during the MCA relative to the LIA could occur if the

SSTs in the eastern tropical Pacific were also warmer during the MCA than the LIA by a minimum of 2˚C to offset the warming observed in the west. This scenario is supported by centennial-resolution isotopic records from the Indo-Pacific Warm Pool region that indicate the MCA (LIA) was dry (wet) in the western Pacific when runoff was high (low) in the east, which is characteristic of an El Niño-like (La Niña-like) mean state climate (Tierney et al., 2010; Rodysill et al., 2012; Konecky et al., 2013).

On the other hand, historical runoff in the eastern and western sites is attributed principally to the stronger ENSO events, suggesting that the decreased frequency of runoff deposits during the LIA records reduced ENSO intensity, rather than ENSO event frequency. Reduced ENSO intensity during the LIA relative to the MCA would not contradict the ocean dynamical thermostat mechanism and could imply that greater radiative forcing and a stronger zonal SST gradient increased the intensity of both El Niño and La Niña events during the MCA relative to the LIA, which is suggested in models (Emile-Geay et al., 2007). The recent increase in runoff on both sides of the tropical Pacific Ocean circa 1800 could either reflect an increase in strong ENSO events in response to positive radiative forcing, similar to the MCA, or an increase in the frequency of ENSO-driven precipitation events in response to a CO_2-induced weakening of the Walker Circulation (Vecchi et al., 2006).

4.6 Conclusions

We present a new record of runoff deposits over the last 1,200 years in lake sediments from East Java, Indonesia. We isolated the high frequency component of the record to investigate the long-term trends in periods of intense rainfall in East Java, finding that the frequency of heavy rainfall events decreased between 1400 and 1800 relative to the MCA and the last two centuries. Comparison of our record with instrumental data shows that historical runoff deposits occur during strong La Niña years, but several La Niña events do not produce runoff deposits in our record; we conclude that ENSO activity plays a strong role in influencing heavy rainfall events in East Java, but our reconstruction does not capture the full spectrum of La Niña activity.

Multi-centennial variations in runoff at our site are identical to runoff patterns reconstructed from two eastern tropical Pacific sites. The relationship between eastern and western Pacific runoff over the past millennium suggests that El Niño and La Niña activity co-vary on centennial timescales, with greater ENSO activity occurring between 850 and 1350-1400 CE and from 1800 CE to present and reduced ENSO activity occurring between 1350-1400 and 1800 CE. Based on these reconstructions, greater (reduced) ENSO activity coincides with increased (reduced) radiative forcing, but the mechanism controlling multi-centennial ENSO variability remains unclear.

4.7 Acknowledgments:

We thank the Government of Indonesia and Indonesian Ministry of Research and Technology (RISTEK) for permission and assistance in conducting field research. We thank Kevin Anchukaitis and Baylor Fox-Kempler for helpful discussions and improving the quality of this work. This research was supported by a NOAA-CCDD grant to J. Russell and M. Vuille.

4.8 References

Appleby, P.G., 1997. Sediment records of fallout radionuclides and their application to studies of sediment-water interactions. Water Air Soil Pollut. 99, 573-586.

Appleby, P.G. and Oldfield, F., 1978. The calculation of ^{210}Pb dates assuming a constant rate of supply of unsupported ^{210}Pb to the sediment. Catena 5, 1-8.

Ashok, K., Guan, Z., Yamagata, T., 2003. A look at the relationship between the ENSO and the Indian Ocean Dipole. J. Meteor. Soc. Japan 81, 41-56.

Beck, C., Manalt, F., Chapron, E., van Rensbergen, P., de Batist, M., 1996. Enhanced seismicity in the early post-glacial period: evidence from the post-Würm sediments of Lake Annecy, northwestern Alps. J. Geodyn. 22, 155-171.

Behera, S.K., Yamagata, T., 2001. Subtropical SST dipole events in the southern Indian Ocean. Geophys. Res. Lett. 28, 327-330.

Broccoli, A.J., Dahl, K.A., Stouffer, R.J. 2006. Response of the ITCZ to Northern Hemispheric cooling. Geophys Res Lett 33, L01702, doi: 10.1029/2005GL024546.

Cane, M.A. 2005. The evolution of El Niño, past and future. Earth Plan. Sci. Lett. 230, 227-240.

Carn, S.A. and Pyle, D.M., 2001. Petrology and geochemistry of the Lamongan Volcanic Field, East Java, Indonesia: primitive Sunda Arc magmas in an extensional tectonic setting? J. Petrology 42, 1643-1683.

Clement, A.C., Seager, R., Cane, M.A., Zebiak, S.E. 1996. An ocean dynamical thermostat. J. Climate 9, 2190-2196.

Conroy, J.L., Overpeck, J.T., Cole, J.E., Shanahan, T.M., Steinitz-Kannan, M. (2008) Holocene changes in eastern tropical Pacific climate inferred from a Galápagos lake sediment record. Quat Sci Rev 27, 1166-1180.

Crausbay, S.D., Russell, J.M., Schnurrenberger, D.W., 2006. A ca. 800-year lithological record of drought from sub-annually laminated lake sediment, East Java. J. Paleolimnol. 35, 641-659.

Dean, W.E., 1974. Determination of carbonate and organic matter in calcareous sediments and sedimentary rocks by loss on ignition: comparison with other methods. J. Sed. Petrol. 44, 242-248.

Digerfeldt, G. 1986. Studies on past lake-level fluctuations. In: Berglund BE (ed.) Handbook of Holocene Palaeoecology and Palaeohydrology. Wiley, Chichester, pp. 127-142.

Emile-Geay, J., Cane, M., Seager, R., Kaplan, A., Almasi, P., 2007. El Niño as a mediator of the solar influence on climate. Paleoceanography. 22, doi:10.1029/2006PA001304.

Eriksson, M.G. and Sandgren, P. 1999. Mineral magnetic analyses of sediment cores recording recent soil erosion history in central Tanzania. Palaeogr. Palaeoclim. Palaeoecol. 152: 365-383.

Green, J., Corbet, S.A., Watts, E., Lan, O.B., 1976. Ecological studies on Indonesian lakes. Overturn and restratification of Lake Lamongan. J. Zool. 180, 315-354.

Heegaard, E., Birks, H.J.B., Telford, R.J., 2005. Relationships between calibrated ages and depth in stratigraphical sequences: an estimation procedure by mixed-effect regression. The Holocene 15, 612-618.

Hendon, H.H., 2003. Indonesian rainfall variability: Impacts of ENSO and local air-sea interaction. J. Climate 16, 1775-1790.

Indonesia National Disaster Management and Mitigation Agency Disaster Bulletin, March, 2013. <http://www.bnpb.go.id/>.

Kaplan, A., Cane, M.A., Kushnir, Y., Clement, A.C., Blumenthal, M.B., Rajagopalan, B., 1998. Analyses of global sea surface temperature 1856-1991. J. Geophys. Res. 103, 18567-18589.

Karnouskas, K.B., Seager, R., Kaplan, A., Kushnir, Y., Cane, M.A., 2009. Observed strengthening of the zonal sea surface temperature gradient across the equatorial Pacific Ocean. J. Climate 22, 4316-4321.

Konecky, B.L., Russell, J.M., Rodysill, J.R., Vuille, M., Bijaksana, S., Huang, Y., 2013. Intensification of southwestern Indonesian rainfall over the past millennium. Geophys. Res. Lett. 40, 386-391.

Makou, M.C., Eglinton, T.I., Oppo, D.W., Hughen, K.A. 2010. Postglacial changes in El Niño and La Niña behavior. Geology 38, 43-46.

Moy, C.M., Seltzer, G.O., Rodbell, D.T., Anderson, D.M., 2002. Variability of El Niño/Southern Oscillation activity at millennial timescales during the Holocene epoch. Nature 420, 162-165.

Lang, S., Lindsey, R. “Flooding and Landslides in Indonesia.” *Natural Hazards: Floods.* National Atmospheric and Space Administration Earth Observatory. 2008. Web. 26 June 2013. <http://earthobservatory.nasa.gov/NaturalHazards/ >

Madden, R.A., Julian, P.R., 1972. Description of global-scale circulation cells in the tropics with a 40-50 day period. J. Atmos. Sci. 29, 1109-1123.

National Ocean and Atmospheric Administration. National Climatic Data Center. Global Historical Climatology Network Monthly. 7 Sept 2012. 20 Sept 2012. <http://www.ncdc.noaa.gov/ghcnm/>

Newton, A., Thunell, R. Stott, L., 2006. Climate and hydrographic variability in the Indo-Pacific Warm Pool during the last millennium. Geophys. Res. Lett. 33, L19710, doi:10.1029/2006GL0273234.

Oppo, D.W., Rosenthal, Y., Linsley, B.K. 2009. 2,000-year-long temperature and hydrology reconstructions from the Indo-Pacific warm pool. Nature 460, 1113-1116.

Poesponegoro, M.D., Notosusanto, N., 1984. Sejarah Nasional Indonesia (Indonesian National History) Book IV. PN Balai Pustaka

Rodysill, J.R., Russell, J.M., Bijaksana, S., Brown, E.T., Safiuddin, L.O., Eggermont, H., 2012. A paleolimnological record of rainfall and drought from East Java, Indonesia during the last 1,400 years. J. Paleolimnol. 47, 125-139.

Rodysill, J.R., Russell, J.M., Crausbay, S.D., Bijaksana, S., Vuille, M., Edwards, R.L., Cheng, H. (Under Review). A severe drought during the last millennium in East Java, Indonesia. *Submitted to Quaternary Science Reviews.*

Ropelewski, C.F., Halpert, M.S., 1987. Global and regional scale precipitation patterns associated with the El Niño/Southern Oscillation. Mon. Wea. Rev., 115, 1606-1626.

Ropelewski, C.F., Jones, P.D., 1987. An extension of the Tahiti-Darwin Southern Oscillation Index. Mon. Wea. Rev., 115, 2161–2165.

Sachs, J.P., Sachse, D., Smittenberg, R.H., Zhang, Z., Battisti, D., Golubic, S. 2009. Southward movement of the Pacific intertropical convergence zone AD 1400-1850. Nat Geosci 2, 519-525.

Saji, N.H., Goswami, B.N., Vinayachandran, P.N., Yamagata, T., 1999. A dipole mode in the tropical Indian Ocean. Nature 401, 360-363.

Sandgren, P. and Snowball, I. 2001. Application of mineral magnetic techniques to paleolimnology. In Last, W.M. and Smol, J.P. (eds.) Tracking environmental change using lake sediments. Vol. 2, Physical and Geochemical Methods. Pp. 217-237.

Schnurrenberger, D., Russell, J.M., Kelts, K., 2003. Classification of lacustrine sediments based on sedimentary components. J. Paleolimnol. 29, 141-154.

Stuiver, M. and Reimer, P.J., 1993. Extended ^{14}C data base and revised Calib 3.0 ^{14}C age calibration program. Radiocarbon 35, 215–230.

Talbot, M.R., 2001. Nitrogen Isotopes in Palaeolimnology. In: Last, W.M., Smol, J.P. (eds.) Tracking Environmental Change Using Lake Sediments. Vol. 2., Kluwer Academic Publishers, Dordrecht, The Netherlands, pp. 401-439.

Tierney, J.E., Oppo, D.W., Rosenthal, Y., Russell, J.M., Linsley, B.K., 2010. Coordinated hydrological regimes in the Indo-Pacific region during the past two millennia. Paleoceanography 25, PA1102, doi: 10.1029/2009PA001871.

Trenberth, K.E., Hoar, T.J., 1996. The 1990-1995 El Niño-Southern Oscillation event: Longest on record. Geophys. Res. Lett. 23, 57-60.

Wang, Y., Cheng, H., Edwards, R.L., He, Y., Kong, X., An, Z., Wu, J., Kelly, M.J., Dykoski, C.A., Li, X. 2005. The Holocene Asian monsoon: Links to solar changes and North Atlantic climate. Science 308, 854-857.

Wheeler, M.C., Hendon, H.H., 2004. An all-season real-time multivariate MJO index: Development of an index for monitoring and prediction. Mon. Wea. Rev. 132, 1917-1932.

Vecchi, G.A., Soden, B.J., Wittenberg, A.T., Held, I.A., Leetmaa, A., Harrison, M.J., 2006. Weakening of the tropical Pacific atmospheric circulation due to anthropogenic forcing. Nature. 441, 73-76.

Verschuren, D., 1993. A lightweight extruder for accurate sectioning of soft-bottom lake sediment cores in the field. Limnol. Oceanogr. 38, 1796-1802.

Vose, R.S., Schmoyer, R.L., Steurer, P.M., Peterson, T.C., Heim, R., Karl, T.R., Eischeid, J., 1992. The Global Historical Climatology Network: Long-term monthly temperature, precipitation, sea level pressure, and station pressure data. ORNL/CDIAC-53, NDP-041. Carbon Dioxide Information Analysis Center, Oak Ridge National Laboratory, Oak Ridge, Tennessee.

Zhang, P., Cheng, H., Edwards, R.L., Chen, F., Wang, Y., Yang, X., Liu, J., Tan, M., Wang, X., Liu, J., An, C., Dai, Z., Zhou, J., Zhang, D., Jia, J., Jin, L., Johnson, K.R. 2008. A test of climate, sun, and culture relationships from an 1810-yr Chinese cave record. Science 322, 940-942.

Correlation Table: East Java Precipitation vs. Southern Oscillation and Dipole Mode Indices									
East Java Precipitation									
Indices		Year 0				Year +1			
		DJF	MAM	JJA	SON	DJF	MAM	JJA	SON
SOI	DJF	-0.055	-0.154	-0.039	-0.301	-0.129			
	MAM		0.039	0.173	0.146	-0.281	-0.180		
	JJA			**0.451**	**0.518**	-0.168	-0.284	-0.046	
	SON				**0.613**	-0.156	-0.220	-0.083	-0.255
DMI	DJF	0.017	-0.015	0.167	-0.124	0.127			
	MAM		0.096	0.065	-0.168	0.052	0.202		
	JJA			-0.174	**-0.365**	0.0730	**0.346**	0.126	
	SON				**-0.601**	0.164	**0.407**	**0.317**	**0.466**

Table 4.1: Correlations between East Java rainfall and the SOI and DMI are listed in this table. Each index was correlated to rainfall in the same season and each following season in the rainfall dataset for one full year. Correlations significant at least at the 95% level are underlined, and correlations significant at least at the 99.9% level are in bold.

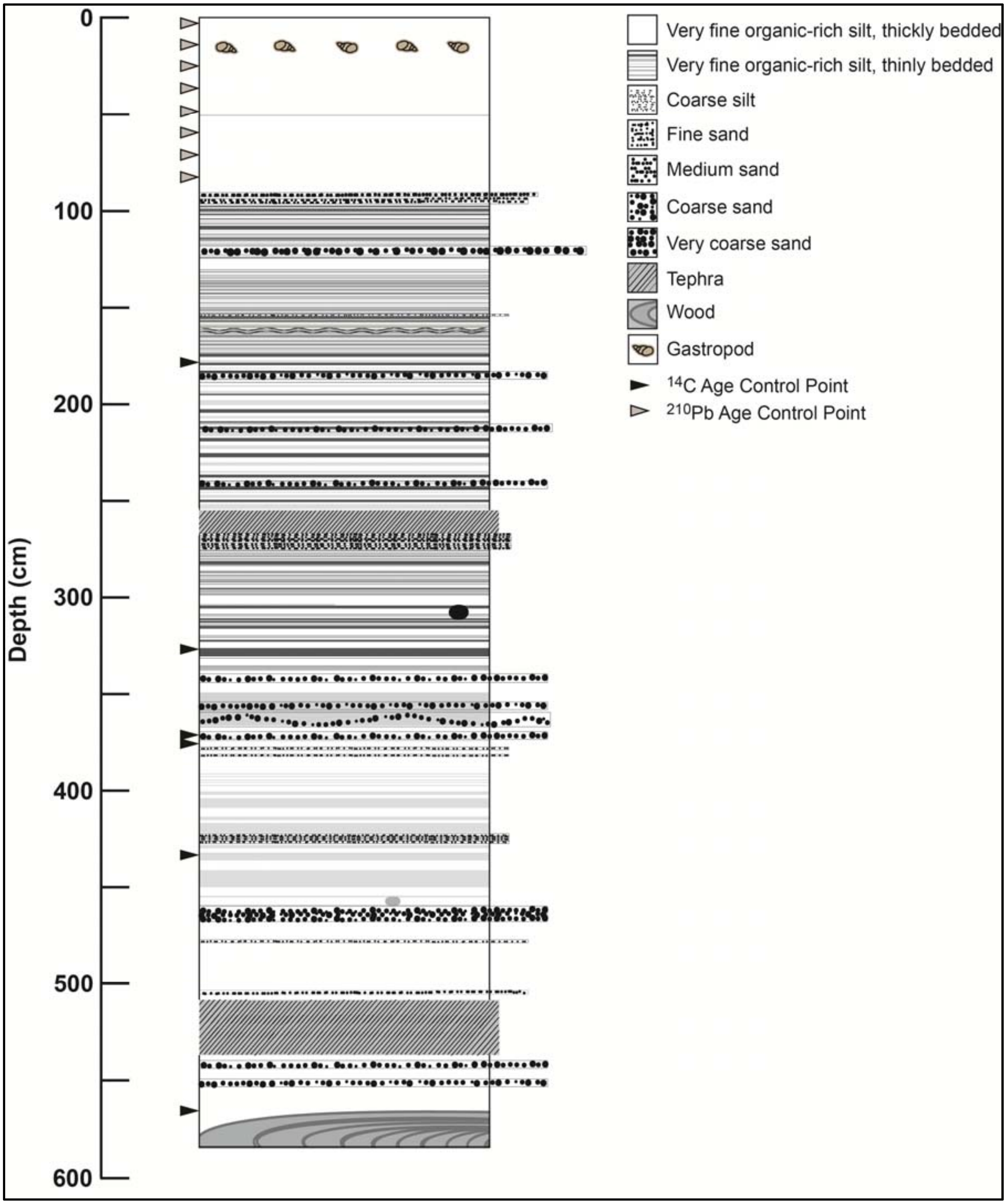

Figure 4.1: Stratigraphic column of Lake Lading sediment core on a depth scale. Various lithologies are plotted with coarser sediments corresponding to longer bed width in the column. Age control points are indicated with triangles along the left side of the stratigraphic column.

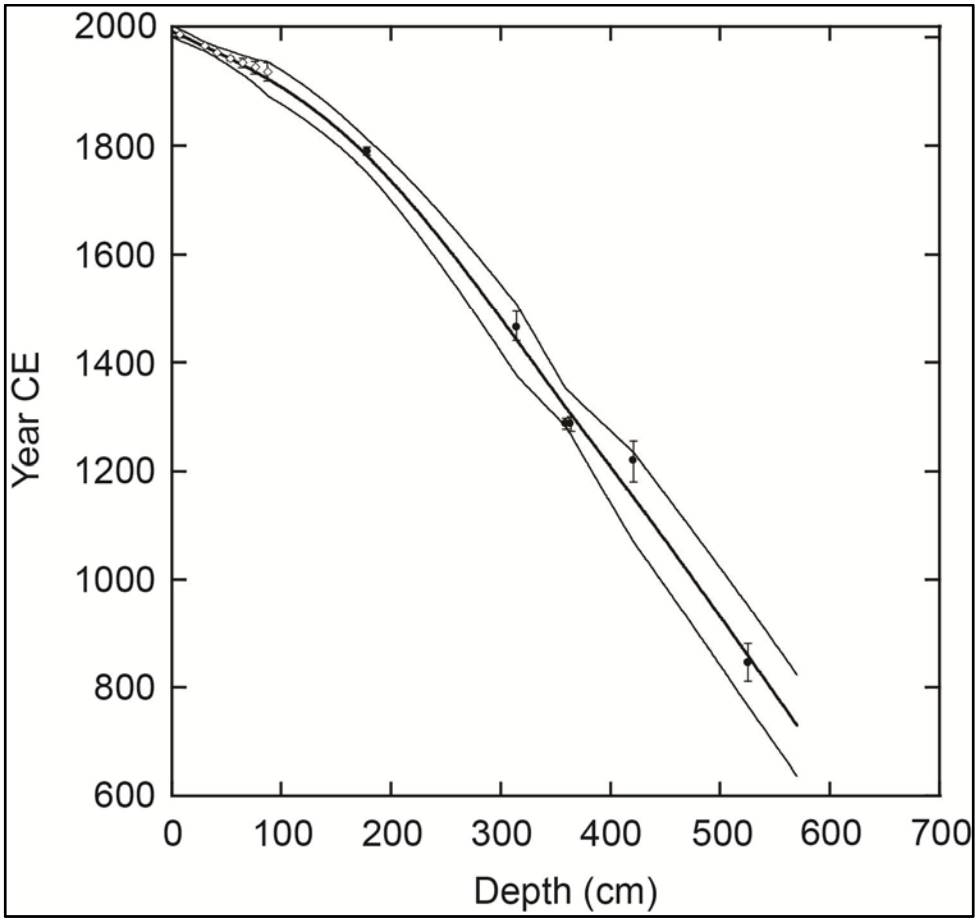

Figure 4.2: Age Model for Lake Lading. ^{14}C ages are displayed as black circles and ^{210}Pb ages are displayed as open diamonds. The uncertainty on each age is shown with error bars. The thick solid line is the age-depth relationship used to construct the age model, and the two thin solid lines are the uncertainty in the age model determined using the mixed-effect regression methods of Heegaard et al. (2005).

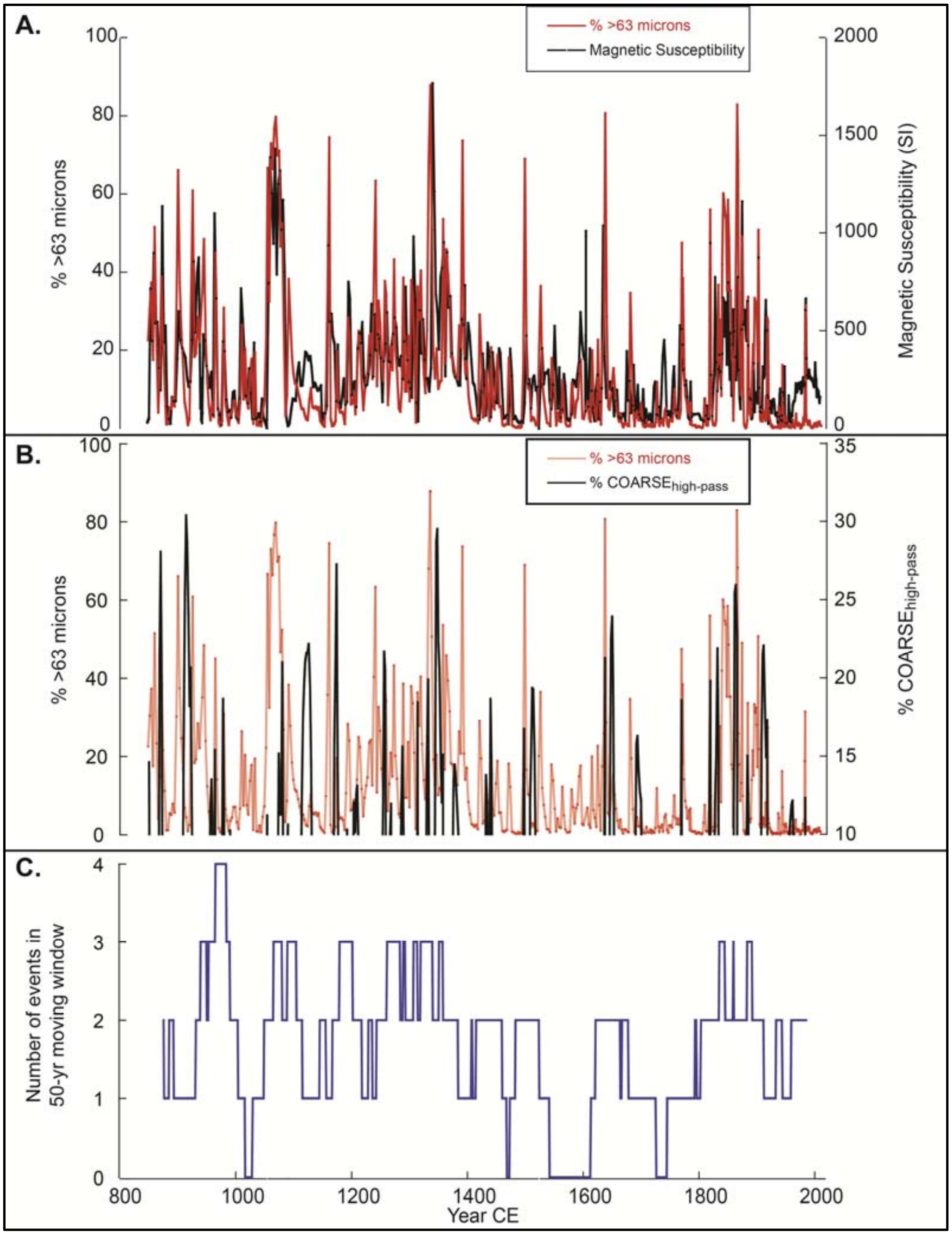

Figure 4.3: A: Magnetic susceptibility (black) and % >63 microns (red) datasets from Lake Lading sediments (this study). The axis for magnetic susceptibility is on the right and for % >63 microns is on the left. B: %COARSE$_{high-pass}$ dataset from Lake Lading sediments (black; this study) is plotted using a cutoff value of 10%. C: The number of runoff events in a 50-yr sliding window from the %COARSE$_{high-pass}$ dataset from Lake Lading (blue; this study).

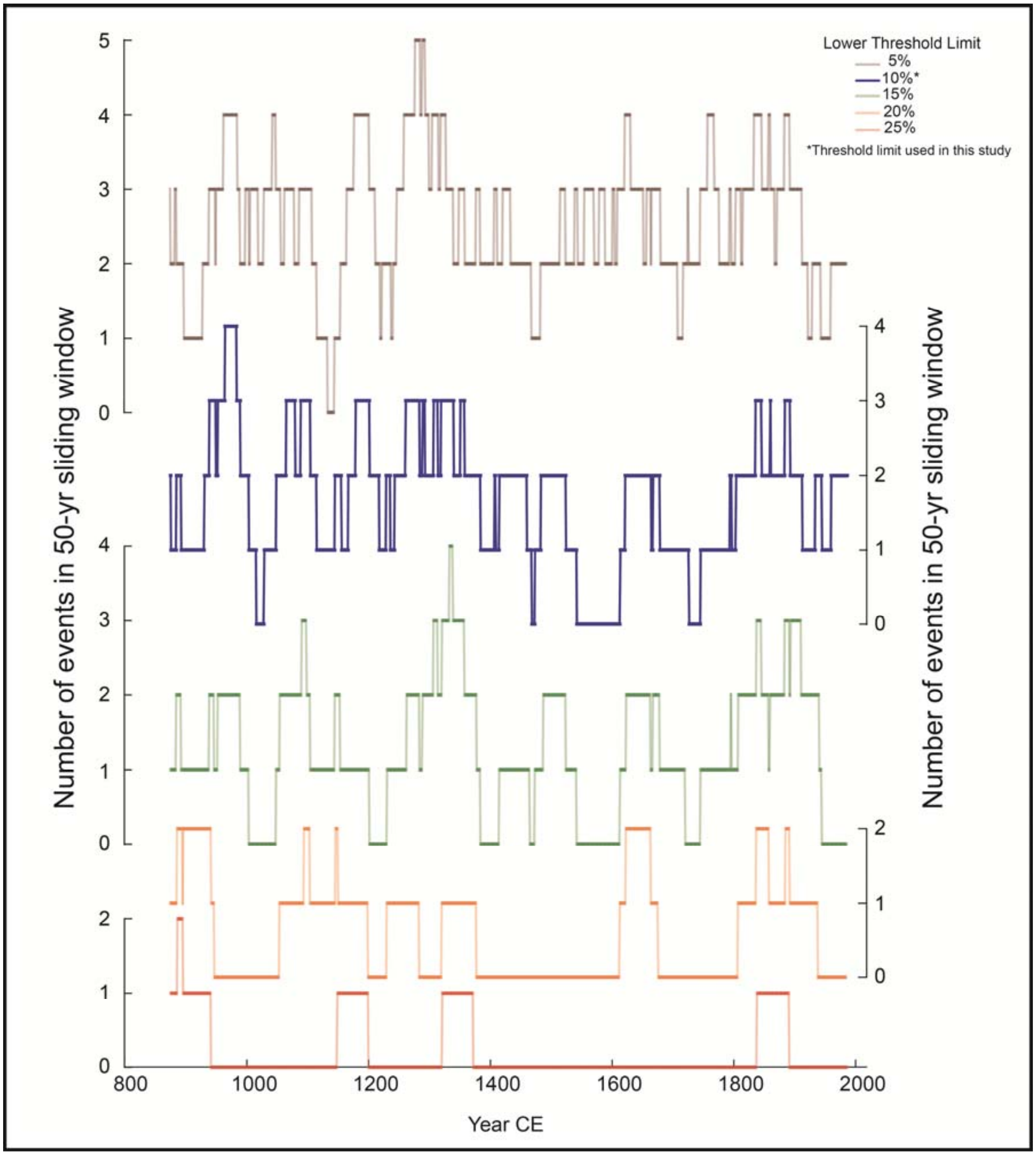

Figure 4.4: Number of runoff events in a 50-yr sliding window from the highpass-filtered % sand dataset from Lake Lading. Each timeseries uses one of five different % coarse cutoff values, used as the lower threshold for defining a runoff event in the highpass-filtered dataset. From top to bottom, the timeseries correspond to cutoff values of 5% (grey), 10% (blue), 15% (green), 20% (orange), and 25% (red).

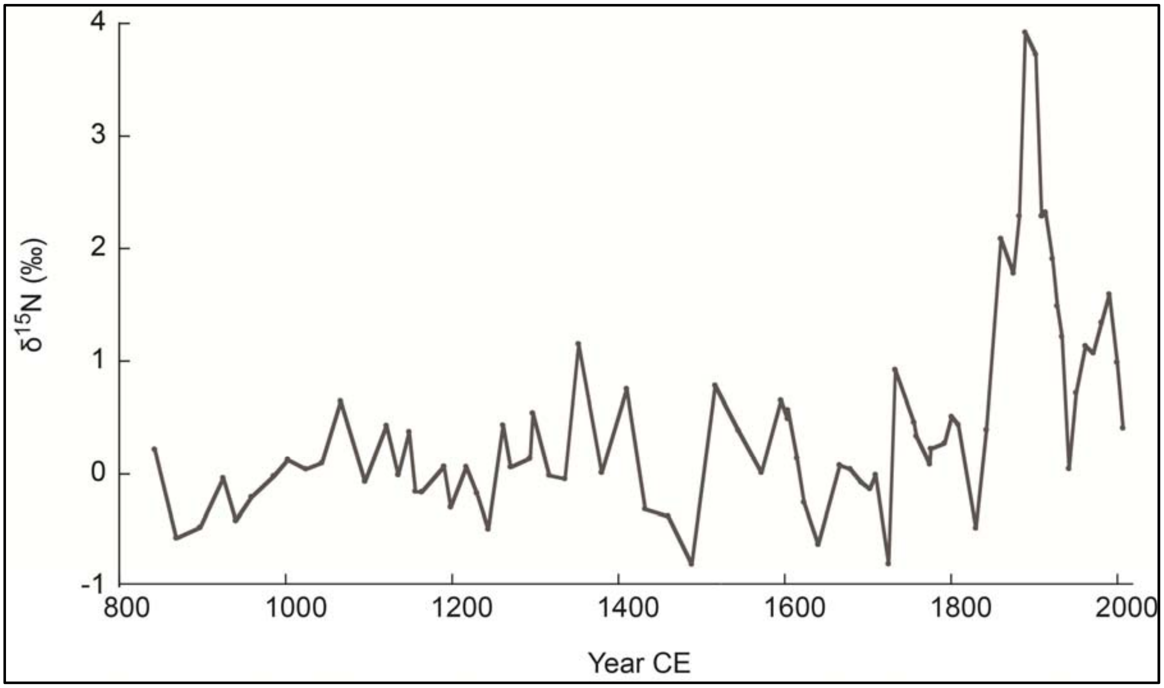

Figure 4.5: Bulk organic nitrogen isotopic data from Lake Lading sediments plotted versus Year CE. Values are reported relative to atmospheric $\delta^{15}N$ in per mille units.

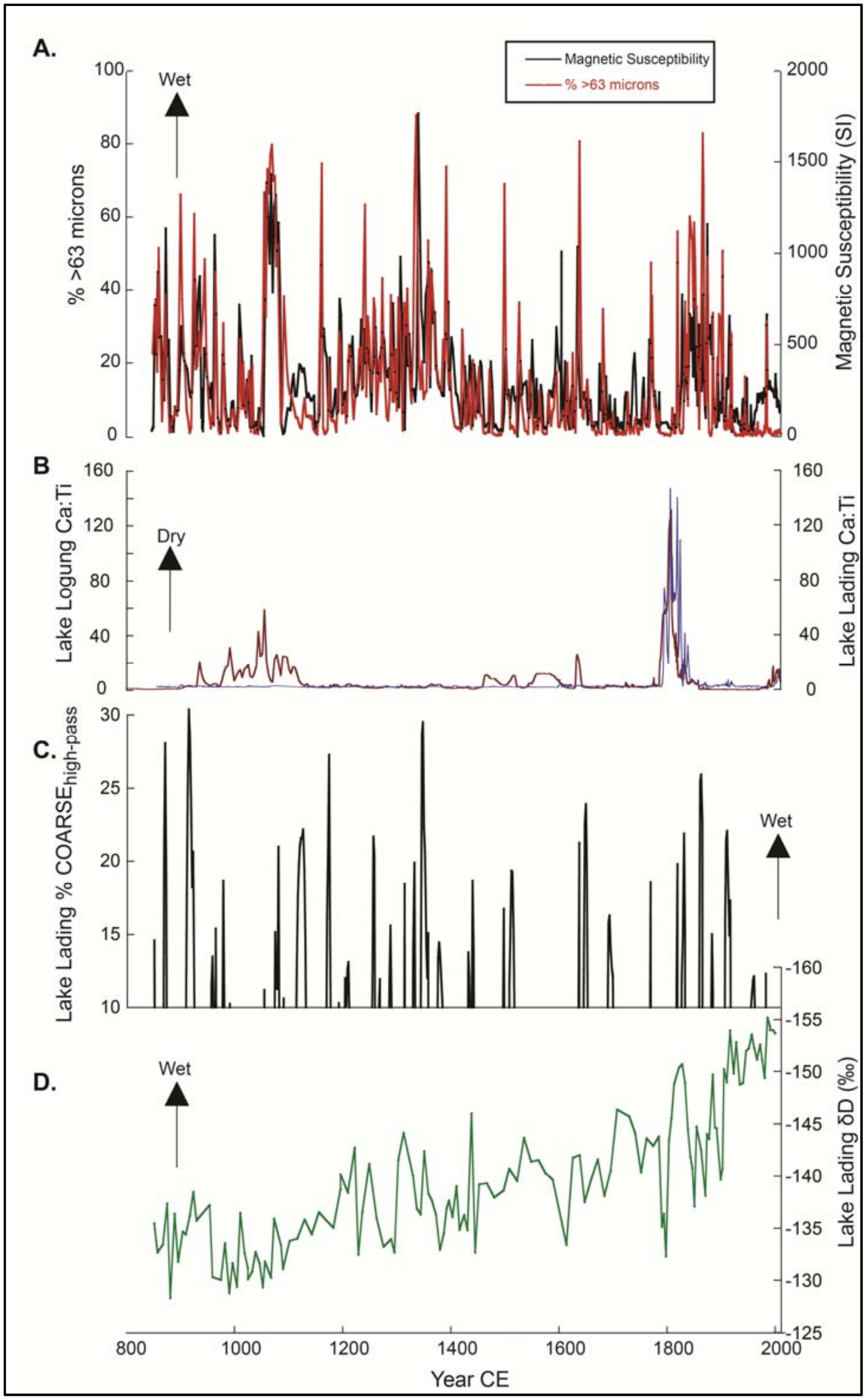

A.
Magnetic Susceptibility
% >63 microns
Wet
% >63 microns
Magnetic Susceptibility (SI)
B
Lake Logung Ca:Ti
Dry
Lake Lading Ca:Ti
C.
Lake Lading % COARSE$_{high-pass}$
Wet
D.
Wet
Lake Lading δD (‰)
Year CE

Figure 4.6: Lake Lading datasets. A: Magnetic susceptibility (black) and % >63 microns (red) datasets from Lake Lading sediments (this study). The axis for magnetic susceptibility is on the right and for % >63 microns is on the left. B: Ca:Ti-based carbonate abundance records from lakes Lading (blue; Rodysill et al., In Prep) and Logung (maroon; Rodysill et al., 2012), plotted such that higher carbonate, interpreted as drought, is up. Lake Lading carbonate abundance axis is on the right, and Lake Logung carbonate abundance axis is on the left. C: $\%COARSE_{high\text{-}pass}$ dataset from Lake Lading sediments (black; this study). D: δD from Lake Lading sediments is plotted in per mille with more depleted values (wet) up (green; Konecky et al., 2013). All datasets are plotted versus Year CE.

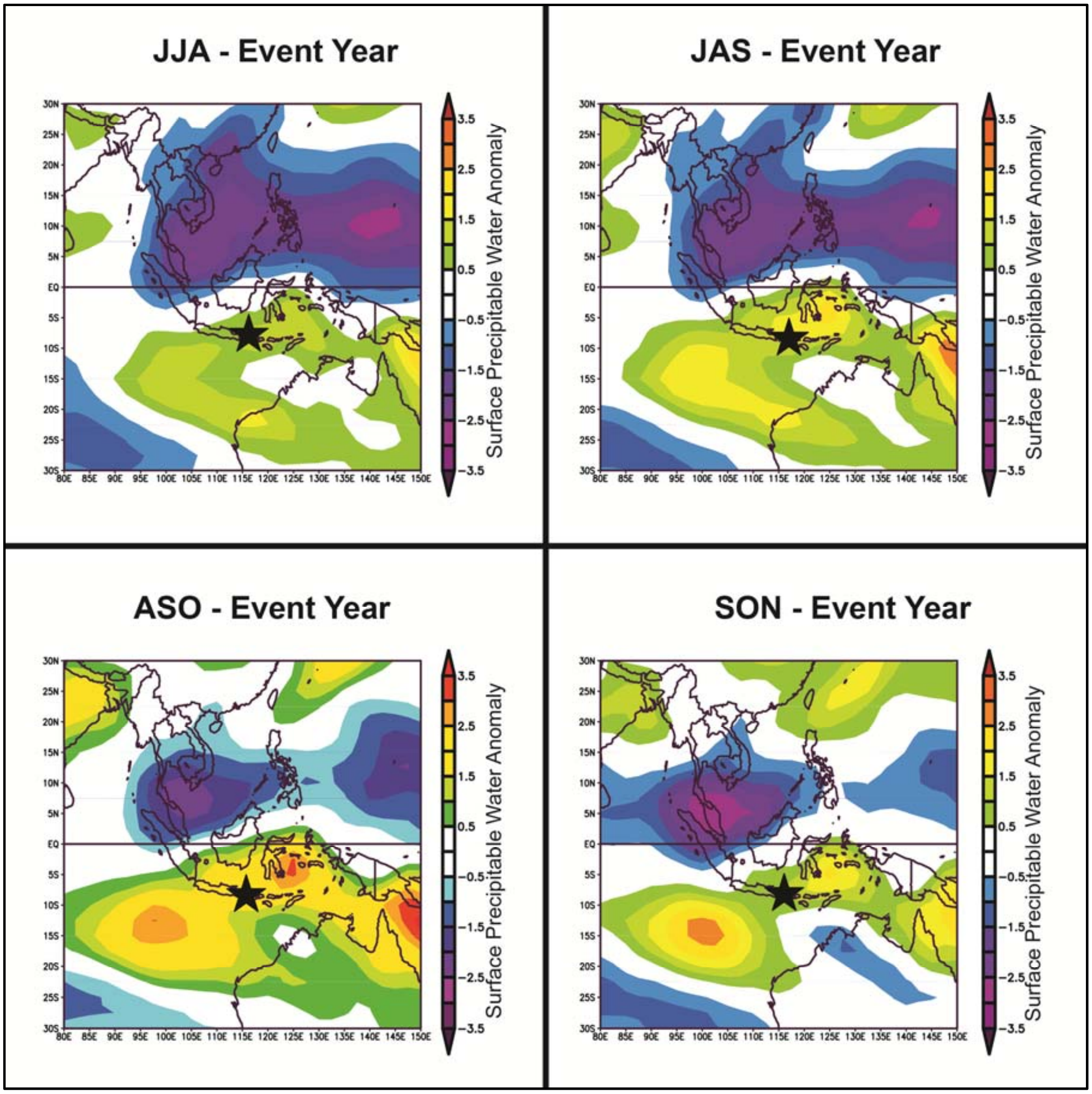

Figure 4.7: Precipitation anomalies for the IPWP region during La Niña years defined as positive anomalies in the 3-month averaged SST dataset from the Niño3.4 region of greater than 0.5˚C for at least five consecutive months, occurring in 1950, 1954, 1955, 1956, 1962, 1964, 1967, 1970, 1971, 1973, 1974, 1975, 1984, 1988, 1995, 1998, 1999, and 2007. Each panel is the NCEP-NCAR reanalysis precipitable water anomaly in kg m^{-2} averaged over three months relative to the average value from 1981-2010. Top left is June-July-August (JJA), top right is July-August-September (JAS), bottom left is August-September-October (ASO), and bottom right is September-October-November (SON).

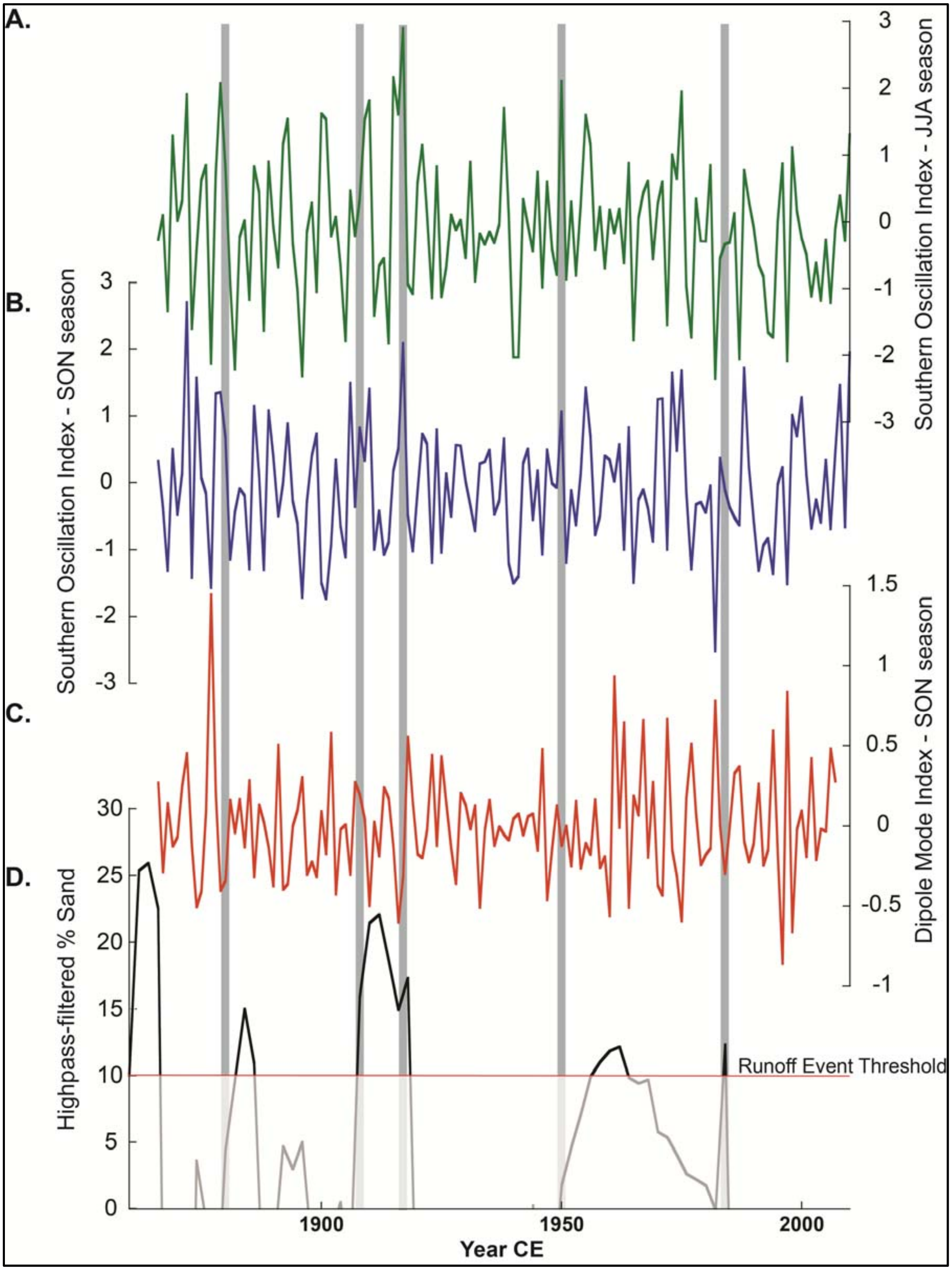
A.
B.
C.
D.
Southern Oscillation Index - JJA season
Southern Oscillation Index - SON season
Dipole Mode Index - SON season
Highpass-filtered % Sand
Runoff Event Threshold
Year CE
1900
1950
2000

Figure 4.8: Comparison of historical highpass-filtered % sand dataset from Lake Lading with SOI and DMI from 1860 to 2010. A: The SOI for the June-July-August (JJA) season is plotted in green. B: The SOI for the September-October-November (SON) season is plotted in blue. C: The DMI for the SON season is plotted in orange. D: The highpass-filtered % sand dataset is displayed with the y-axis cut off at 0% to highlight only the positive anomalies. The horizontal red line at 10% indicates the cutoff value, above which are the % sand values that are characterized as "runoff deposits." Gray bars highlight the start of each of the runoff deposits to visually display the timing of onset of each event. All datasets are plotted versus Year CE.

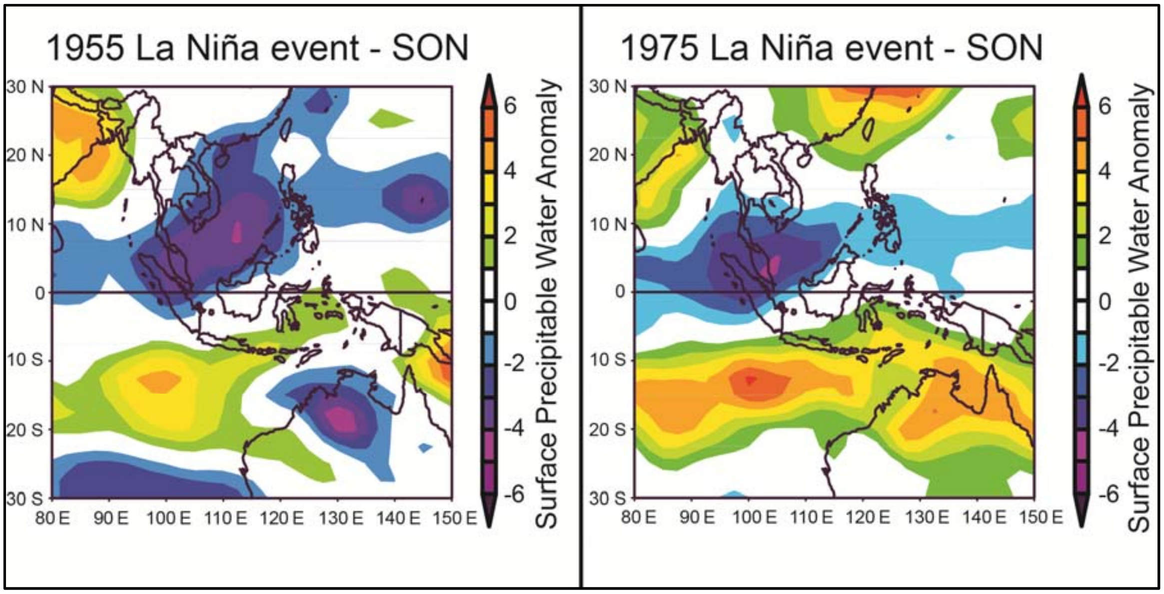

Figure 4.9: Precipitation anomalies for the IPWP region during the 1955 (left) and 1975 (right) La Niña years. Each panel is the NCEP-NCAR reanalysis precipitable water anomaly in kg m^{-2} averaged over September-October-November (SON) relative to the average value from 1981-2010.

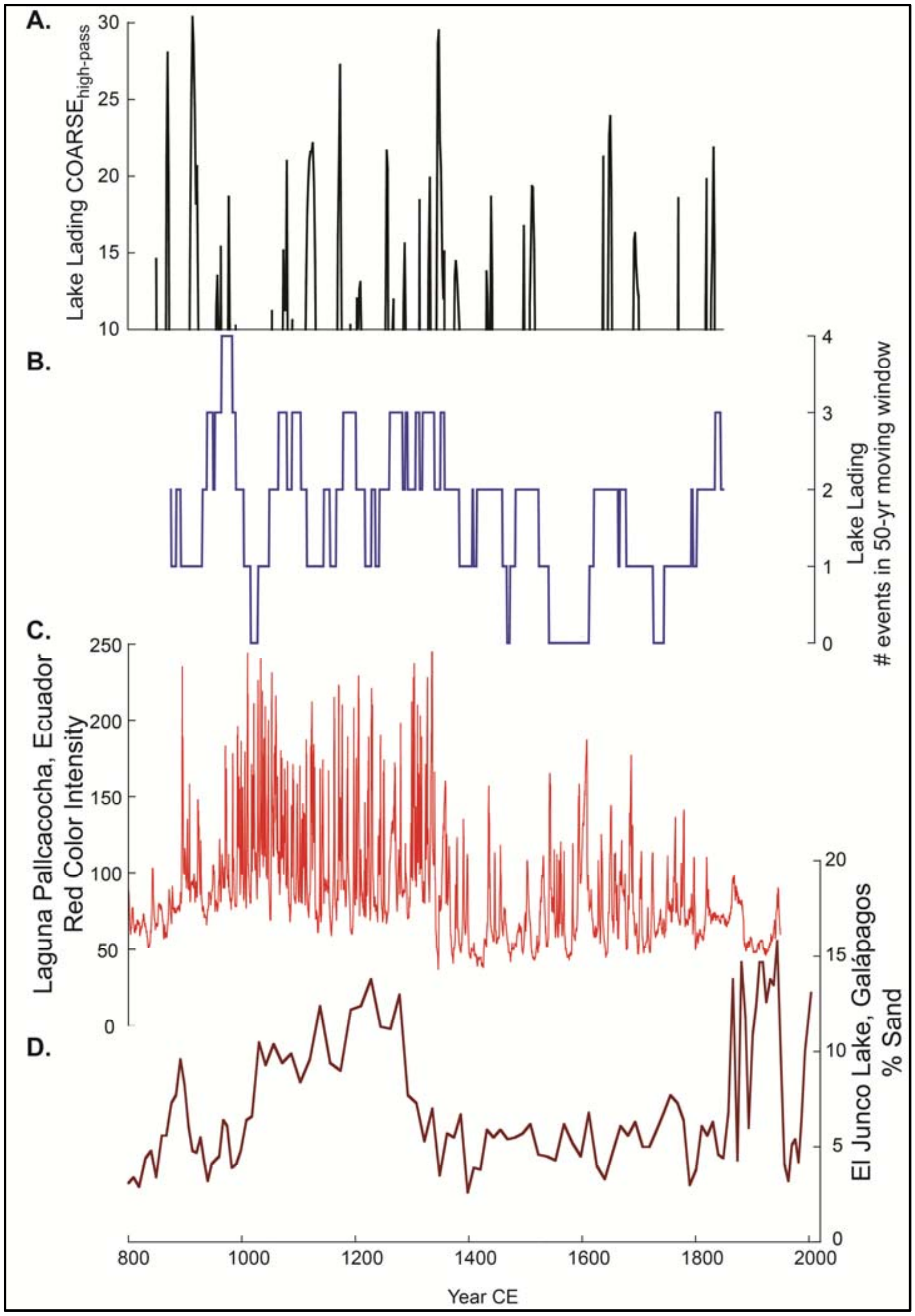

Figure 4.10: Comparison of Lake Lading runoff record with Eastern Equatorial Pacific runoff records are plotted versus Years CE. A: Lake Lading %COARSE$_{high-pass}$ (black; this study) is cut off from 1850 CE to present, when human activity began influencing sedimentation. B: The number of runoff events in a 50-yr sliding window from the %COARSE$_{high-pass}$ dataset from Lake Lading (blue; this study) is cut off from 1850 CE to present. C: Red color intensity in Laguna Pallcacocha sediments in Ecuador (red; Moy et al., 2002). D: % sand in El Junco Lake in the Galápagos (maroon; Conroy et al., 2008).

CHAPTER 5

Northern Gulf of Mexico tropical cyclone activity over the past 4500 years from sediment archives

Jessica R. Rodysill[1]

Jeffrey P. Donnelly[2], Lane, D.P.[2], Richard Sullivan[2], Michael Toomey[2], Dana MacDonald[2]

[1]Department of Geological Sciences, Brown University

[2]Geology and Geophysics, Woods Hole Oceanographic Institution

5.1 Abstract

Intense tropical cyclones pose a considerable threat to the rapidly developing coastline along the northern Gulf of Mexico. Previous work toward understanding long-term past variability in Gulf of Mexico storm climatology from an extremely limited number of sites has revealed major complexities in the spatial patterns of storms and how they relate to forcing mechanisms. We present a new record of intense tropical cyclone activity based on coarse anomaly event detection in sediment cores from Basin Bayou in northwest Florida. We identified periods of heightened storm frequency from 2800 to 2300 B.P., 2000 to 1900 B.P., 1700 to 1600 B.P., and 1100 to 600 B.P. Periods of relatively low storm frequency occurred from 2300 to 2000 B.P., 1600 to 1100 B.P., and 600 to 135 B.P. Our record is remarkably similar to intense storm reconstructions from the northern gulf coast 200 km east of our study site (Lane et al., 2011; Brandon et al., 2013). Together, these records demonstrate that periods of heightened intense hurricane activity in the northern Gulf of Mexico coincide with warmer Atlantic sea surface temperatures, greater thermocline depth associated with the Loop Current, and increased El Niño activity inferred from a runoff record in Ecuador (Moy et al., 2002).

5.2 Introduction

Tropical cyclones are a serious threat for densely populated coastal communities, where the growing concentration of people and properties is resulting in a steady increase in damage costs and loss of life from hurricane landfalls (Pielke et al., 2008). The frequency and intensity of tropical cyclones have varied substantially over the past several decades (IPCC, 2007; Knapp et al., 2010) and are thought to be controlled by sea surface temperature (SST) variations, wind shear, and upper tropospheric temperatures (DeMaria, 1996; Emanuel, 1999; Emanuel, 2003; Jaggar and Elsner, 2006; Mann et al., 2009). The manner in which SSTs, winds, and atmospheric temperatures collectively control storm patterns is less certain, and how future changes in the mean climate state and radiative forcing will influence storm climatology is unclear. Theory, modeling, and analyses of the short historical hurricane record have led to contradicting hypotheses on whether Atlantic tropical cyclone activity will increase, decrease, or remain unchanged in the near future (Henderson-Sellers et al., 1998; Goldenberg et al., 2001; Emanuel, 2005; IPCC, 2007; Grinsted et al., 2013; Holland and Bruyère, 2013). A modeling study by Henderson-Sellers et al. (1998), based on the strong relationship between tropical cyclone genesis and atmospheric parameters (e.g. wind shear, vorticity), predicts that Atlantic tropical cyclone variability will not change significantly in response to future greenhouse gas concentration increases (Henderson-Sellers et al., 1998). On the other hand, Goldenberg et al. (2001) place more weight on the strong relationship between intense historical tropical cyclone frequency and Atlantic SSTs and argue for major multi-decadal variability in accordance with north Atlantic SST trends. Other studies that relate tropical cyclone intensity to SSTs and surface temperatures predict an increase in the proportion of high intensity hurricanes in the Atlantic Ocean basin during the next century in response to increased radiative forcing (e.g. Emanuel, 2005; Webster et al., 2005; IPCC, 2007; Grinsted et al., 2013). The historical record of storms is too short to accurately assess the relationship between the patterns of hurricane frequency and intensity and climate on multi-decadal to millennial-scales, emphasizing the need for storm reconstructions that extend the histories of these events. Developing a network of tropical cyclone histories across the Atlantic basin across several millennia will provide us with a stronger understanding of how tropical cyclone activity has varied across multiple climate states.

Previously published tropical cyclone reconstructions from the northern Gulf of Mexico leave an unclear picture of prehistoric trends in regional hurricane activity (e.g. Liu and Fearn 1993; 2000; Lambert et al., 2008; Lane et al., 2011). Liu and Fearn (1993; 2000) suggest there were frequent intense, Category 4 or 5 storms on the Saffir-Simpson Hurricane Scale based on the identification of overwash deposits in lake sediment cores between 3200 and 700 B.P. at Lake Shelby in Alabama and between 3400 and 1000 B.P. at Western Lake in northwest Florida, but few strong storms were recorded after 700 B.P. A more recent geochemistry-based storm reconstruction from Lake Shelby identified several additional storm deposits after 700 B.P. (Lambert et al., 2008).

More recent reconstructions of intense hurricanes based on overwash deposits in sediment cores from Mullet Pond and Spring Creek Pond in northwest Florida, on the other hand, identify active intervals from 2800 to 2300 B.P. and 1500 to 600 B.P. with quiescent periods from 1900 to 1600 B.P. and from 400 B.P. to the present (Lane et al., 2011; Brandon et al., 2013). These findings are in conflict with the Western Lake reconstruction (Liu and Fearn 2000); the earlier quiescent interval in the Mullet and Spring Creek Pond reconstructions (Lane et al., 2011; Brandon et al., 2013) occurs during heightened activity in the Western Lake record, and heightened intense hurricane activity documented in Mullet and Spring Creek Pond sediments persisted four centuries longer into the last millennium than was inferred from Western Lake sediments.

Additional storm reconstructions are needed to elucidate the trends in tropical cyclone activity that are common to multiple sites and thus represent gulf-wide hurricane activity. We present a new record of tropical cyclone activity over the last 4500 years based on coarse sediment deposition in a bayou in northwest Florida that enhances our understanding of northern Gulf of Mexico intense hurricane activity. This study adds a new paleostorm reconstruction to the growing network of records to piece together a clearer history of basin-wide hurricane activity along the northern coast of the Gulf of Mexico. Periods of heightened tropical cyclone activity in northwestern Florida have been ascribed to variations in surface currents in the Gulf of Mexico (Lane, 2011; Brandon et al., 2013), which can be further supported by our record if it shares the same relationship between heightened storm activity and surface currents in the gulf. Our study site is uniquely in close proximity to Western Lake such that the level of consistency between the long term trends at both sites can be used to test whether the differences between Western Lake and Mullet Pond are due to differences in local hurricane climatology between the two sites or other factors, including poorly supported data interpretations or chronological issues.

5.2.1 Study site

Our study site is Basin Bayou, located on the northeast side of Choctawhatchee Bay, a 45 km-long and 8 km-wide bay in northwest Florida (Figure 5.1). Basin Bayou is approximately 1.5 m deep and is 1.6 km long and 0.6 km wide. The bayou is surrounded by unconsolidated Pleistocene and Holocene-aged siliciclastic sand and clays (Scott et al., 2001). Basin Creek is a small stream with a relatively small watershed (117.5 km^2), representing 3% of the Choctawhatchee Bay watershed area, which drains into the north end of Basin Bayou (EPA, 2013). On the south end of the bayou, a baymouth barrier separates the bayou from Choctawhatchee Bay. A narrow channel cuts through the barrier and is a conduit for tidal water flow between the bayou and the bay. The width of the barrier varies between 250 and 400 m, and its elevation is roughly 1 m, reaching up to 1.5 meters above sea level (m.a.s.l.) on the bay side (Figure 5.1; DOC et al., 2007). Tidal range within Choctawhatchee Bay is minimal, averaging 0.15 m (Ruth and Handley, 2006).

Between 1851 and 2011, 105 tropical cyclones have landed within a 100 nautical mile radius of the opening of Choctawhatchee Bay on the Gulf of Mexico coast (Knapp et al., 2010). Of these storms, sixty-three were tropical depressions or tropical storms, twenty were Category 1, nine were Category 2, and thirteen were Category 3 at landfall (Figure 5.2). No historical Category 4 or 5 storms have made landfall within 100 nautical miles of Basin Bayou. The storms that are more likely to produce diagnostic overwash deposits in Basin Bayou are those that make landfall to the west of our site, where the winds are mainly in the onshore direction such that the storm surge propagates from the Gulf of Mexico into Choctawhatchee Bay through the opening on the southwest side of the bay and then eastward within the bay, storms that have tracked to the north side of Choctawhatchee Bay, driving strong westerly winds that produce large-amplitude waves within Choctawhatchee Bay and propagate eastward across the bay, those that make landfall directly over our site such that the maximum wind velocities pass directly over the bayou, producing waves that overtop the baymouth barrier and transport sand from Choctawhatchee Bay into Basin Bayou, and those that are high intensity at the time of landfall; these storms are highlighted in Table 5.1.

5.3 Methods

5.3.1 Sediment core collection

Our storm reconstruction is based upon lithologic changes in sediment cores from Basin Bayou. We collected three vibracores in July, 2012 that are aligned along the long axis of Basin Bayou, oriented roughly perpendicular to Choctawhatchee Bay (Figure 5.1). We collected these cores in a transect with increasing distance from Choctawhatchee Bay to test whether the coarse deposits we identify are spatially extensive and decrease in thickness and grain size with increasing distance from the bay, as would be expected of bay-source coarse deposits. Each vibracore has a companion overlapping surface drive that was collected with a piston corer to better preserve the less consolidated upper meter of sediments. The surface drive and vibracore from each location were combined into a composite core by matching visually distinctive bedding and trends in geochemical data. The four cores we collected from Basin Bayou, in order of increasing distance from Choctawhatchee Bay, are BaBy6 (30.49033˚N, 86.24995˚W; 6.20 m sediment length; 1.6 m water depth), BaBy1 (30.489733˚N, 86.246317˚W; 1.68 m sediment length; 1.45 m water depth), BaBy4 (30.49213˚N, 86.24368˚W; 7.06 m sediment length; 1.7 m water depth), and BaBy9 (30.50044˚N, 86.24126˚W; 4.64 m sediment length; 0.6 m water depth). BaBy9 was collected with to determine whether Basin Creek supplies significant amounts of coarse sediments into the bayou during periods of heavy rainfall that may not necessarily represent tropical cyclone occurrence. BaBy1 is a surface drive without a companion vibracore. The cores were split and described using the classification method from Schnurrenberger et al. (2003).

5.3.2 Surface sample collection

We collected three sediment samples from various depths in Choctawhatchee Bay, five soil samples from the landscape surrounding Basin Bayou, and one surface sediment sample from Basin Creek to characterize the sediment chemistry in the bay and differentiate that from the sediment chemistry of the sediments on the landscape surrounding Basin Bayou that are transported into the bayou from Basin Creek (Figure 5.1).

5.3.3 Sediment chemistry and grain size

All cores were scanned on an ITRAX Corescanner at Woods Hole Oceanographic Institution at 200 micron increments with a 0.4 s dwell time to obtain radiographic images and at 1 mm increments with a 10 s dwell time to obtain elemental abundance data. Surface samples were analyzed for elemental abundances using an INNOV-X systems Alpha 4000 handheld XRF analyzer with a 90 s dwell time. The clay-rich sediments in Basin Bayou became too hard to sieve after the drying and loss-on-ignition procedures that are often performed on sediment samples for removal of coarse organic material prior to sieving (e.g. Lane et al., 2011). We obtained grain size data in Basin Bayou sediments by sampling at continuous 1 cm increments and separating the samples into two parts; one part was weighed and then dried overnight in a convection oven at 100˚C to determine the water content, and the other part was weighed and wet-sieved at 32 microns to remove the clay particles that solidify when the samples are dried. The fraction of water determined on the subset of samples that were dried in the oven was used to approximate the bulk dry mass of the samples that were sieved. The sieved samples were combusted in a muffle furnace at 550˚C for four hours to remove all organic material and were wet-sieved again at 32 microns post-combustion, dried, and weighed (Dean, 1974). The mass of dried sediment remaining after the sieving and combustion processes was divided by the bulk dry mass of that sample, approximated using the water fraction from the subset of samples that were dried in the oven immediately after sampling, to determine the percent of sediments that is greater than 32 microns in diameter relative to the bulk dry mass. These samples were then wet-sieved at 63 microns to determine the percent of the dry bulk sediments that is sand sized and greater, which we will refer to as %sand.

5.3.4 Age control

The Basin Bayou age models are from a combination of ^{14}C ages on intact bivalve halves using the Continuous-Flow Accelerated Mass Spectrometer (CFAMS) method at the National Ocean Sciences AMS facility (Roberts et al., 2011) and organic ^{14}C ages on plant macrofossils that were strategically sampled near major density transitions detected in the radiographic images obtained from the cores to maximize age control at major sedimentological transitions (Table 5.2). Three plant macrofossils were dated from BaBy6, two plant macrofossils and one bivalve were dated from BaBy1, three plant macrofossils and four bivalves were dated from BaBy4, and one plant macrofossil was dated from BaBy9. The ages derived from bivalves in BaBy1 and BaBy4 had very large age uncertainties, exceeding several centuries, so only the ages obtained from organic carbon were used in the development of the core chronologies. The ages from bivalves did, however, increase with increasing depth and were in agreement with the age-depth relationship defined by the organic carbon dates within age uncertainties, supporting our organic ^{14}C age-based models. All ^{14}C ages were calibrated using the IntCal09 model from Calib6.0 (Stuiver and Reimer, 1993; Stuiver et al., 2005) to years before present (B.P.) where “present” is defined as the year 1950 C.E.

The upper 40 cm of sediments in BaBy4 and BaBy1 were sampled every 3 cm, dried overnight in a convection oven at 100˚C, and homogenized with a mortar and pestle for gamma counting to obtain ^{210}Pb and ^{137}Cs activities. Unsupported ^{210}Pb activity values were determined by subtracting the background activity, assumed to be the average of the activities below the depth where ^{210}Pb activity no longer decreased with increasing depth, from each ^{210}Pb activity measurement. The unsupported ^{210}Pb activities were used to construct a constant rate of supply model for the upper sediments in each core (Figure 5.3; Appleby and Oldfield, 1978; Appleby, 1997).

5.3.5 Historical and spatial data

Historical tropical cyclone data for our study sites are from the International Best Track Archive for Climate Stewardship (IBTrACS) dataset provided by the National Ocean and Atmospheric Administration Coastal Services Center (Knapp et al., 2010). Elevation data used in this study were obtained from light detection and ranging (Lidar) data collected in 2006 at 1 cm per pixel resolution with an elevation uncertainty of 13 cm (DOC et al., 2007).

5.4 Results

5.4.1 Core stratigraphies

The sediments in all of the vibracores from Basin Bayou gradually transition from medium grey silty clay in the lower several meters to dark brown very fine organic-rich silt in the upper 1.5 to 2 m of each core (Figure 5.4). The base of BaBy6, below the grey clay, is very coarse quartz sand that gradually transitions upward to medium grey clay by 3.5 m depth. Several 0.2 to 3 cm-thick beds composed of coarse-grained sediments occur throughout each core; in the base of the cores these beds are composed of quartz sand with broken pieces of carbonate shells and in some cases very coarse terrestrial plant material, and in the upper 1.5 to 2.5 m of all of the cores, the beds do not contain carbonate shell pieces. The coarse beds correspond to higher density layers in the radiographic images (Figure 5.4). The sand beds in BaBy6 are thicker than those observed in BaBy1, BaBy4, and BaBy9, and range between 1 and 5 cm in thickness. A few intact bivalve halves were observed in BaBy1 and BaBy4.

5.4.2 Coarse sediment anomalies

The sand content in BaBy6 varied considerably over the last 4500 years, decreasing by 50% between 4500 and 4000 B.P., increasing by 65% from 4000 to 3000 B.P., then declining from 80% to approximately 5% by 2000 B.P. (Figure 5.5). Sand content in BaBy6 increased again by roughly 40% from 1800 to 1000 B.P., then declined through the present. Superimposed on the long-term trend in sand in BaBy6 are several short-lived increases in sand content varying in magnitude between 20 and 65%. The baseline sand content in BaBy4 and BaBy9 was low between 4500 and 1500 B.P., with several short-lived, 10-55% increases in sand. Few sand beds occurred in BaBy4 and BaBy9 between 2000 and 1000 B.P.; sand beds became more frequent again in these cores between 1000 B.P. and the present. BaBy1 contains several sand beds, particularly after 900 B.P. The magnitude of the increase in sand content within the coarse deposits was greater in BaBy4 than it was in BaBy9, and was greater in BaBy1 than in BaBy4 and BaBy9 for the last 1300 years. The proportion of coarse silt in each sample is constant throughout each core and does not change when sand content changes.

5.4.3 Age models

We constructed the age models for each core by linearly interpolating between ^{14}C ages, which increase linearly with increasing depth in all cores with R^2 values of 0.9994 in BaBy6, 1 in BaBy1 (there are only two ^{14}C ages), 0.9897 in BaBy4, and 1 in BaBy9 (between the single ^{14}C age and the surface; Figure 5.6). The work we present from Basin Bayou is focused on the upper ~3 meters of each long core, where the core chronologies are well constrained with ^{14}C ages on plant macrofossils. Surface sedimentation rates determined from ^{210}Pb ages in BaBy1 and BaBy4 averaged 0.2 cm/yr for the upper 25 cm of sediment accumulation (Figure 5.3A, B). The peak in ^{137}Cs activity in both of these cores is assumed to represent the maximum concentration of ^{137}Cs in the atmosphere, which peaked in 1963 as a result of heightened nuclear weapons testing. In BaBy1, ^{137}Cs activity reached a maximum between 12 and 13 cm, which results in a sedimentation rate of 0.25 $\pm$ 0.2 cm/yr, comparable to the sedimentation rate determined from ^{210}Pb activities (Figure 5.3C). In BaBy4, ^{137}Cs activity peaked between 10 and 15 cm, which results in a sedimentation rate of 0.25 $\pm$ 0.6 cm/yr, in relatively good agreement with the ^{210}Pb-determined sedimentation rate (Figure 5.3D). Basin Bayou sedimentation rates in the deeper sediments, determined from ^{14}C ages, are 0.1, 0.12, 0.07, and 0.07 cm/yr in BaBy6, BaBy1, BaBy4, and BaBy9, respectively, resulting in an average basin-wide sedimentation rate of ~0.1 cm/yr (Figure 5.6). An abrupt geochemical and lithological transition in BaBy6 at 69 cm led us to infer a depositional hiatus (Figure 5.5; 5.6). We assumed the sedimentation rate between 0 and 69 cm was the same as the ^{14}C sedimentation rate below the hiatus and that 0 cm depth represents 2012 CE (Figure 5.6).

5.4.4 Radiograph and XRF data

We used the differences in elemental abundances between surface sediment samples from these various environments to test whether it is possible to chemically differentiate the sediments in the Basin Bayou cores that came from the bay, Basin Creek, or the surrounding landscape. The relative elemental abundances of the surface sediment samples collected at various depths in the bay, the soil samples, and the sample collected from Basin Creek are shown in Table 5.3. All samples are high in Fe, Ti, Ca, K, and Cl relative to Mn, Co, Zn, Rb, Sr, Zr, and Mo. However, the bay samples have higher counts of Fe, Ti, and K relative to the terrestrial soil and river samples. In addition, the bay samples contain high amounts of S and Cr, which are not present above the detection limits in the terrestrial and river samples with the handheld XRF analyzer (Table 5.3).

We selected the elements with distinguishable differences in relative abundances between the bay sediments and those surrounding Basin Bayou, Fe, Ti, K, S, and Cr, to reconstruct the long-term trends in Basin Bayou sediment sources (Figure 5.7A). In BaBy4, all of the selected diagnostic elements remained fairly constant from 5000 to 3000 B.P., gradually declined between 3000 and 2000 B.P., increased from 2000 to 1400 B.P., then decreased rapidly beginning circa 800 B.P. Brief peaks in Ca were more frequent in all cores until 3300 B.P. in BaBy6, 800 B.P. in BaBy1, and 2500 B.P. in BaBy4 (Figure 5.7B) and BaBy9. These high values occur when the ITRAX core scanner directly measures carbonate shells or beds containing pieces of carbonate shells. In BaBy6, all of these diagnostic elements gradually declined between 3000 and 2000 B.P. (Figure 5.7C). While Cr remained low in BaBy6 from 2000 B.P. to the present, Fe, Ti, K, and S increased in abundance between 1700 and 500 B.P. In BaBy1, Fe, Ti, K, and Cr were high from 1300 to 400 B.P., then gradually declined toward the present. The decline in S occurred later, beginning around 200 B.P. In Baby9, the selected elements declined between 3000 and 2000 B.P., and at 800 B.P., Fe, Ti, K, and S increased for approximately 300 years before declining into the present (Figure 5.7D).

5.5 Discussion

5.5.1 Coarse sediment source

Modern sediment deposition throughout Basin Bayou is characterized by very fine, organic-rich silt in a quiescent environment. Sand is deposited in the bayou only when it is transported into the basin from an external source. Possible sources of sand are Choctawhatchee Bay, during storms with surges that exceed the elevation of the baymouth barrier or small surges and/or energetic waves that transport sediment through the inlet, and flooding in the Basin Creek drainage and the catchment surrounding the bayou due to runoff during heavy rainfall. The catchment is an unlikely source of sediments to the center of the bayou, because the landscape surrounding the bayou is extremely flat (< 1m/km) and unlikely to contribute cm-scale, thick sheets of sand across the bayou. Basin Creek has a very small drainage basin (Ruth and Handley, 2006), and probably does not transport enough sand to produce cm-scale, thick sand deposits across the entire basin. The average sand content in the bayou cores decreases with increasing distance from the bay, and with increasing proximity to Basin Creek. Sand content averaged over the last 4500 years in BaBy6, BaBy4, and BaBy9 is 35%, 9%, and 6%, respectively (Figure 5.8). The amplitude of the increase in sand content in individual beds and the frequency of sand beds identified in each core also decrease with increasing distance from Choctawhatchee Bay (Figure 5.7). We expect that a greater amount of sand is deposited closest to its source, implying that the sand beds in Basin Bayou are derived from the transport of sediment by large waves that overtop the baymouth barrier from Choctawhatchee Bay, at the south end of the bayou.

5.5.2 Historical hurricanes in the Basin Bayou record

Cores BaBy4 and BaBy1 have the best chronological control in the historical period from ^{210}Pb and ^{137}Cs ages, and the BaBy4 record extends back to 4500 B.P. Given its distal location from the baymouth barrier and inlet, BaBy4 is likely to be a more complete record and is less likely to receive sediment that is transported through the inlet during non-stormy conditions, so we focus on the BaBy4 core for comparison between historical coarse deposits and local historical hurricane landfalls and for the prehistoric paleostorm reconstruction. Small variations in sand content, while potentially meaningful for understanding storm-driven variations in sedimentation in Basin Bayou, can be difficult to discern from background sedimentation. In order to distinguish event deposits from minor variations in sand content in BaBy4, we defined a single event deposit as a peak in sand content that exceeds the value separating the finer 80% from the coarser 20% of the data in the probability density function of the dataset, which in this case is 9% sand (Figure 5.9).

There are two sand beds in the ^{210}Pb-dated portion of the core, occurring from 1825 to 1873 CE and 1917 to 1937 CE (Figure 5.9, dark grey bars). Age uncertainties in these portions of the ^{210}Pb age model are 13 and 8 years, respectively (Figure 5.9, light grey bars). The first of these beds has a very large age error, but does overlap with Category 3 hurricanes in 1851 and 1877 that made landfall 91.5 km and 177 km to the east of the opening between Choctawhatchee Bay and the Gulf of Mexico, respectively. In 1882, a Category 3 hurricane made landfall directly over Choctawhatchee Bay, which is also within age model error of the sand bed. We simulated the storm surges in Choctawhatchee Bay and Basin Bayou for each of these storms using the Sea, Land, and Overland Surges from Hurricanes (SLOSH) model; the 1851 and 1877 storms produced surge levels of 0.3 m and 0.03 m, respectively, at Basin Bayou, which is not enough to overtop the modern barrier (1 to1.5 m), whereas the 1882 storm produced a surge level of 1.5 m (Figure 5.10). We therefore attribute the first sand layer in the historical period to overwash that occurred during the 1882 hurricane.

In 1917, a Category 3 hurricane made landfall directly over Choctawhatchee Bay, and in 1926 a Category 3 hurricane came onshore 155 km west of the bay. The SLOSH model simulated a surge of 1.1 m for the directly land-falling 1917 storm and 0.9 m for the 1926 storm (Figure 5.10). These surge heights are very similar and it is possible that wind-driven waves could overtop the barrier during the 1926 storm despite the fact that the still water surge height was below the elevation of the barrier. The single bed may therefore represent either or both of these events. The hurricane in 1917 was more proximal to our site, which more likely caused greater local wind velocities that produce larger wave heights than the more distal 1926 storm and might suggest that the layer more likely records the 1917 event. The double sand peaks in the recent historical event layer between 1917 and 1937 could be indicative that the strong hurricanes occurring in 1917 and 1926 both contributed sand to the bayou, but since the variations in sand content within this sand bed are < 2%, within error of the LOI analysis (Heiri et al., 2001), we can only confidently identify one single event bed. We therefore attribute the two sand layers in the historical portion of our record to the direct land-falling Category 3 hurricanes in 1882 and 1917.

Seven other Category 3 hurricanes have passed within 185 km of Choctawhatchee Bay documented in the Best Track dataset that do not correspond to sand beds in BaBy4 (Figure 5.2; Knapp et al., 2010). These storms occurred in 1894, 1916, 1975 (Eloise), 1985 (Elena), 1995 (Opal), 2004 (Ivan), and 2005 (Dennis). The three closest are Eloise (1975), Opal (1995), and Dennis (2005), which produced simulated surge heights in SLOSH of 0.8 m, 0.9 m, and 0.7 m, respectively. Each of these surge heights are below the modern barrier elevation and are therefore unlikely to have formed coarse deposits in Basin Bayou, consistent with the lack of sand beds at these times. These data suggest the storms that produce coarse deposits in Basin Bayou are Category 3 or stronger and make landfall within 75 km of our site. We do not limit our interpretation of the presence of coarse deposits as representing only Category 3 and stronger hurricanes, as a proximal storm that is less intense may still be capable of producing wind-driven surges within Choctawhatchee Bay and/or wind-driven waves that overtop the barrier.

5.5.3 Coarse deposit preservation potential

Several factors influence preservation potential of storm-induced coarse deposits, including the rate of sedimentation, sediment transport processes within the depositional basin (Woodruff et al., 2008), and post-depositional mixing of the sediments (Hippensteel, 2008; Hippensteel, 2010). The modern sedimentation rate is not high enough to resolve individual event layers occurring within approximately a decade of one another given that the observed sand bed thicknesses range between 0.1 and 3 cm. We assume the sand beds are deposited instantaneously, but background, non-event sedimentation between 0.1 and 3 cm corresponds to approximately 0.5-15 years. There may be several event beds in our record that actually represent two or more storms that occurred within a decade or two of one another. Event deposits in Basin Bayou have the potential to be eroded and reworked during subsequent storms and eliminated from the record, particularly in near-shore shallow core sites, reducing the number of event deposits relative to the number of true events. Some of the sand layers in our record may therefore reflect multiple storm deposits that were reworked and combined into a single sand bed. Sediment reworking and low sedimentation rates reduce the number of event deposits in our record relative to the true number of strong storms that impacted our study site.

Conversely, energetic waves during weaker tropical cyclones that do not form an overwash deposit at BaBy4 may deliver reworked coarse sediment from elsewhere in the bayou, producing a sand bed that is not necessarily indicative of a high intensity hurricane. Given the fetch of Basin Bayou (1.66 km), wind velocities associated with Category 5 hurricanes can produce wave heights on the order 1.4 m (Shore Protection Manual, 1984), which is approximately the depth of the bayou at the BaBy4 core site.

While Category 5 storms can potentially rework sediments within Basin Bayou, winds associated with weaker hurricanes or winter storms are not capable of producing coarse beds at the BaBy4 site in the absence of a storm surge that overtops the barrier.

Event deposits, particularly thin beds, may be reworked due to surface bioturbation, resulting in more vertical integration and dilution of coarse grains in the sediment column that reduce the magnitude of the coarse anomaly (Hippensteel, 2008; 2010). In some cases, the dilution that occurs from this process can reduce the coarse anomaly to below our detection threshold, causing a reduction in the number of events preserved in our record. We see no evidence for extensive bioturbation of the sediments in the core stratigraphy; all event deposits have sharp contacts with the sediment above and below. The uppermost ^{210}Pb activity is lower than the three measurements below it (Figure 5.3), which could indicate that there is reworking in the upper few centimeters or it may be that the supply of ^{210}Pb to the sediments was not constant. However, the ^{210}Pb activity in upper sediments of BaBy1 does not increase with increasing depth (Figure 5.3), which may suggest our assumption that the ^{210}Pb supply has been constant is valid. We can not rule out bioturbation in the upper few centimeters as a threat to sand bed preservation.

The number of event beds in our record is unlikely to represent the exact number of intense storms that made landfall near Basin Bayou due to the potential reduction in preserved event deposits relative to the number of tropical cyclones from bioturbation and the low sedimentation rate, and the inferred long-term trends in storm frequency in our record may be influenced by factors other than the frequency of intense storms in northwest Florida. However, agreement between intense historical hurricanes and recent sand beds in our record adds confidence to our interpretation that coarse anomalies in Basin Bayou sediments are mainly representative of local intense hurricanes.

5.5.4 Late Holocene site sensitivity

Storm-induced deposition in our record occurs when surge heights exceed the elevation of the barrier and when there is substantial transport energy capable of delivering sand >700 m from the barrier to the core site. Basin Bayou is currently closed off from Choctawhatchee Bay by a baymouth barrier that sets the minimum storm surge capable of delivering sand from the bay into the bayou between 1 and 1.5 m (Figure 5.1), which historically limits storm deposition in Basin Bayou to storms that make landfall within 75 km of our site and are approximately Category 3 strength or higher. Choctawhatchee Bay is separated from the Gulf of Mexico by a ~500 to 1000 m-wide barrier on the southwest edge with a 600 m-wide opening through which storm surges can propagate (Figure 5.1). Barriers are transient landforms that are sensitive to sediment availability and changes in current direction and strength (Donnelly and Webb, 2004); the existence, length, and/or elevation of these barriers may have been different during the last 4500 years and influenced the susceptibility of Basin Bayou to bay-sourced storm-induced sand deposits. Sea-level rise throughout the late Holocene also likely contributed to the sensitivity of Basin Bayou to storm-induced deposition. Lower than modern sea level circa 4500 B.P. (-4 m; Törnqvist et al., 2006) may have influenced the elevation of the barriers separating Basin Bayou from Choctawhatchee Bay and the bay from the Gulf of Mexico, and would also have increased the distance of our site from the northern gulf coast across which storm surges propagate, potentially reducing the sensitivity of the bayou to storm deposition relative to today.

Variations in the elevation and length of either of these barriers during the past 4500 years would affect the sensitivity of Basin Bayou to storm-induced overwash deposition. If the baymouth barrier were non-existent or shorter in length, then wind-derived wave energy in Choctawhatchee Bay could more easily deliver coarse sediments into Basin Bayou in the absence of a storm surge, which would increase the frequency of coarse storm deposits without necessitating a change in storm frequency or intensity. If the barrier between Choctawhatchee Bay and the Gulf of Mexico were smaller or non-existent, surge heights within the bay could have been larger than today during identical storm conditions and more easily overtopped the baymouth barrier into Basin Bayou. Conversely if either of these barriers were higher, Basin Bayou may have been more sheltered from storm-induced deposition and fewer storm deposits would have been preserved without a change in storm climatology. During the mid-Holocene when sea level was ~4 m lower than present, the steep slope of the Florida shelf near our study site would have resulted in 500-600 additional meters between the gulf coast and Basin Bayou (USGS, 2013), requiring larger surges and wave energy to form sand layers at our study site relative to today. This configuration could have inhibited the formation of coarse deposits in the mid-Holocene during storm conditions that are analogous to those that create coarse deposits in the historical period.

We evaluated the sensitivity of Basin Bayou to overwash deposits during the past 4500 years in response to baymouth barrier evolution by identifying geochemical indicators of Choctawhatchee Bay sediments in the cores from the bayou. We utilized the difference in elemental abundances between modern bay sediments and the geochemistry of the Basin Creek and soil samples immediately surrounding the bayou to characterize the bulk chemistry of sediments that are derived from the bay (Table 5.3). We interpret relatively higher abundances of Fe, Ti, K, S, and Cr in the Basin Bayou cores as indicating a greater portion of bay-derived sediments, which we infer is an increase in the exchange of water and sediments between the bayou and the bay due either to a shorter baymouth barrier or a wider opening at the south end of the bayou.

The coarse-grained sediments in the study region are dominantly pure quartz, whereas the fine-grained silty-clay sediments derived from the bay and bayou are more chemically diverse with relatively higher abundances of Fe, Ti, K, S, and Cr compared to the pure sand (Table 5.3; Scott et al., 2001). Increases in the quartz sand content in the sediment cores dilute the signatures of these elements due to a relative increase in quartz-dominated sediments. Variations in relative abundances of the selected elements are likely to reflect variations in the input of coarse quartz sand and/or varying inputs of relatively more chemically-diverse fine-grained sediments. When the trends in elemental abundances are negatively correlated to grain size we interpret those changes as dilution or concentration of chemically-diverse sediments, whereas elemental abundance trends that do not correlate to grain size are representative of bay-derived sediment inputs due to more open low-energy exchange between Basin Bayou and Choctawhatchee Bay. If more coarse sediments were delivered to Basin Bayou from Choctawhatchee Bay due to an opening in or a lower elevation of the baymouth barrier, then we might expect grain size and these elemental abundances to be positively correlated. The broad, centennial-scale and longer chemical trends in BaBy6 and after 2000 B.P. in BaBy4 and BaBy9 are negatively correlated to grain size, so we interpret variations in Fe, Ti, K, S, and Cr in these intervals as changing influx of coarse sand that is unrelated to barrier dynamics (Figure 5.7A, C, D).

A gradual decline in Fe, Ti, K, S, and Cr occurs in BaBy4 and BaBy9 between 3000 and 2000 B.P. and is not correlated to grain size variations, so we interpret this trend as a decline in the low-energy input of sediments from Choctawhatchee Bay starting circa 3000 B.P. (Figure 5.7A, D). This chemical transition accompanies the transition from grey clay in these cores prior to 3000 B.P., which is macroscopically identical to the surface sediment samples from Choctawhatchee Bay, to very fine organic-rich silt by 2000 B.P. Fragments of carbonate shells, which are observed throughout the surface sediment samples from Choctawhatchee Bay, are present in the thin coarse sediment beds in Basin Bayou until ~2500 B.P. in BaBy4 and BaBy9 (Figure 5.7B), another indication that bay-derived sediment deposition in the bayou decreased between 3000 and 2000 B.P. We conclude based on these observations that between 4500 and 3000 B.P. the connection between the bayou and Choctawhatchee Bay was more open, similar to the two embayments to the east of Basin Bayou (Figure 5.1), increasing the likelihood that coarse grained sediments from the bay were transported to our site during tropical cyclones. Between 3000 and 2000 B.P., Basin Bayou became less susceptible to receiving coarse sediments from Choctawhatchee Bay, and the mechanism producing event deposits in the bayou changed from dominantly high wave energy to high wave energy paired with overwash deposition from storm surges that exceed the barrier height.

Over the last 4500 years, changes in bay currents and sediment transport in response to sea-level rise may have resulted in the construction of the barrier through increased sediment supply (Davidson-Arnott, 2010), reducing the sensitivity of our site over the course of our record. Geochemical data from Choctawhatchee Bay sediment cores suggests the bay was more openly connected to the Gulf of Mexico prior to 3000 B.P., gradually became separated by the barrier between 3000 and 1000 B.P., and was abruptly reconnected with the gulf circa 1000 B.P. (Ranasinghe et al., 2012). A high magnitude coarse deposit in Basin Bayou at 1190 (Figure 5.11), which may represent a very intense hurricane, marks the rise in event frequency in Basin Bayou and is approximately when Ranasinghe et al. (2012) suggest that the East Pass opened in the barrier between Choctawhatchee Bay and the Gulf of Mexico. This large magnitude storm may have been responsible for opening the barrier, allowing for the propagation of storm surges throughout the bay and increasing the likelihood that a given hurricane would deposit coarse sediments in Basin Bayou.

All of these geochemical data suggest that Basin Bayou was more susceptible to storm-induced coarse sediment deposition prior to 3000 B.P. followed by a gradual decrease in site sensitivity until at least 1000 B.P. After 1000 B.P., Basin Bayou may have received greater surge heights due to more open exchange between Choctawhatchee Bay and the Gulf of Mexico, but may have been less sensitive to overwash due to the presence of the baymouth barrier. On the other hand, sea-level rise over the last few millennia could have caused Basin Bayou to be increasingly more susceptible to storm-induced deposition due to decreasing site-to-sea distance through the construction of the baymouth barrier during the late Holocene, which should result in an increase in the frequency of event deposits throughout the last 4500 years in pace with the rate of sea-level rise (Törnqvist et al., 2006).

During the last two millennia, the Basin Bayou record should only contain sand deposits from higher intensity events that produced a storm surge greater than the elevation of the baymouth barrier and enough wave energy to transport sand sized particles into the bayou. Prior to 3000 B.P., while the coarse sediment deposition during tropical cyclones required less significant surge heights to mobilize and transport sand to the core site relative to the most recent two millennia, it would still have taken a high intensity storm to provide the wind-driven transport energy necessary to deliver sand between 1200 and 1300 m laterally to BaBy4. Decreasing wave energy diminishes the grain size that is transported; Woodruff et al. (2008) demonstrated with an advective settling model that sand-sized grains can be transported ~200 m under Category 5 storm strength at Laguna Playa Grande, Puerto Rico. While this model is not directly applicable to our site, we can infer based on the fact that our modern core location is 3.5 times the distance from the barrier as the one used in the model, that intense storms are also necessary to deliver sand 700 m into Basin Bayou. These data suggest coarse deposits in Basin Bayou represent intense hurricanes throughout the last 4500 years despite the changing barrier configuration and sea level rise.

5.5.5 Storm reconstruction from 4500 B.P. to present

Based on the detection threshold of 9%, described in Section 5.5.2, there have been 36 events in the BaBy4 record during the last 4500 years (Figure 5.11). Event deposits are present in our reconstruction at 3880, 3720, 3680, 3440, 3400, 3350, 3230, 3110, 2940, 2820, 2740, 2700, 2580, 2500, 2360, and 2300 B.P. followed by three closely-spaced events at 2020, 1960, 1910 and four closely-spaced events at 1710, 1670, 1640, and 1580 B.P. After four centuries without coarse deposits, a large magnitude event occurred in BaBy4 in 1190 B.P., corresponding to a rise from 3 to 70% sand. This major coarse event was followed by a cluster of several closely-spaced events at 1080, 920, 880, 800, 760, 700, 630, and 570 B.P. The coarse deposits between 1190 and 880 and at 570 B.P. are thicker and have higher sand content than those between 800 and 600 B.P. , suggesting they may represent much stronger storms. A single event in the Basin Bayou record between 570 to 135 B.P., occurring at 310 B.P., implies there was a lack of intense hurricane activity during these five centuries. Three recent events in BaBy4 occurred at 135, 95, and 20 B.P.

Average event frequency increased from 0.22 events/century between 4500 and 3000 B.P. to 0.25 events/century between 3000 and 2000 B.P., to 0.53 events/century between 2000 B.P. and the present despite decreasing sensitivity to overwash deposition. Between 4500 and 3000 B.P., Basin Bayou was open to Choctawhatchee Bay and the Gulf of Mexico, requiring less of a storm surge for coarse sediment deposition in the bayou. Site sensitivity decreased as the barriers separating the bay from the gulf and the bayou developed between 3000 and 2000 B.P., and we expect that Basin Bayou was the least sensitive to coarse sediment deposition from 2000 B.P. to the present due to the presence of the baymouth barrier.

The increasing storm frequency over the course of the last 4500 years could be attributed to rising sea level and a decreasing site-to-sea distance. However, sea-level rose steadily over the last few millennia (Törnqvist et al., 2006) while storm deposition in Basin Bayou sediments occurred in pulses, and the rate of sea-level rise gradually decreased whereas event frequency in our record more than doubled during the last two millennia relative to the previous millennium. The pulses of coarse sediment deposition appear to be controlled by factors other than barrier evolution and sea-level rise. We attribute the punctuated increases in event frequency to multi-centennial variations and an overall increase in the frequency of intense storms at our study site during the last 4500 years.

The average storm frequency in our reconstruction over the last 500 years was 0.008 events per century, ~40% lower than between 500 and 1200 B.P. Given that Basin Bayou likely records higher intensity hurricanes, and if sand bed thickness in our record relates to paleostorm intensity, these data suggest intense hurricanes were more common at times during the past few millennia than we have observed in the historical period.

5.5.6 Northern Gulf of Mexico tropical cyclone activity over the past 4500 years

Western Lake is located 20 km southeast of Basin Bayou; nearly every storm to make landfall in the area should pass over both sites nearly simultaneously (Figure 5.1; Liu and Fearn, 2000). The intense hurricane reconstructions from both sites should therefore be similar, assuming accurate chronologies and constant site sensitivities over the duration of the records. The Western Lake record lacks historical coarse deposits and the strongest historical storms to make landfall near this site were Category 3, so the authors assume all coarse deposits in the prehistoric record represent Category 4 and 5 storms (Liu and Fearn, 2000). This record is then expected to have fewer overwash deposits than our reconstruction of ~Category 3 and greater storms. Prior to 2500 B.P., the Western Lake record is very similar to the Basin Bayou record. While Western Lake contains fewer events overall, the events that exist align fairly well with events at our site (Figure 5.11). After 2500 B.P., the agreement between these two sites diminishes. The active interval in the Western Lake record occurs during the longest quiescent period in the Basin Bayou record, between 1600 and 1100 B.P., and only a single overwash event is documented in the Western Lake record after 1200 B.P. while event frequency in Basin Bayou is highest relative to the past 4500 years.

Otvos (2002) challenged the interpretation that the Western Lake reconstruction can only record $\geq$ Category 4 hurricanes by pointing out existing inlet channels and dips in the barrier dune elevation through which sediments could have been channeled into the lake during weaker storms. These inferences are supported by the presence of buried inlets along the coast near Western Lake, suggesting there has previously been a period of active inlets that have subsequently been buried by the barrier dune (Otvos, 2002). Further, Otvos (2002) brought up a number of poorly-supported inferences that Liu and Fearn (2000) made about the Western Lake record, including the inference that sand layers are all representative of storms, the size of the deposit is directly related to storm intensity, and the stability of the depositional environment has remained unchanged through time. The dissimilarity between the Western Lake record and that of Basin Bayou further suggests that Western Lake sediments may not have recorded only very intense hurricanes during the last 5000 years, and that the site sensitivity may have varied through time. Prior to 2500 B.P., when the two sites are in agreement, Basin Bayou was more open to Choctawhatchee Bay and the Gulf of Mexico, so these two sites likely had similar sensitivities to storm deposition during the period when the two records are in good agreement with one another. If Western Lake was more sensitive to overwash deposits due to decreased dune elevation or the presence of inlets prior to 2500 B.P. than after 1200 B.P., then the discrepancy between the two sites can be explained in terms of deposit formation and preservation rather than storm climatology, which should be similar for these sites given their close proximity.

Alternatively, if there is a radiocarbon reservoir effect in Western Lake similar in magnitude to the those identified in Lake Shelby (Lambert et al., 2008) and Eastern Lake (Das et al., 2013), the timings of the events could be shifted significantly. As a simple test, we applied a 985-year reservoir age correction to the bulk organic ^{14}C ages from the Western Lake record, which is the value used for bulk organic ^{14}C ages in Eastern Lake (Das et al., 2013), 5.6 km east of Western Lake. The updated chronology shifts the active intervals in Western Lake to between 2700 and 2300 B.P., 1900 and 1700 B.P., and 1000 B.P. to present (Figure 5.11). We are not necessarily suggesting the Western Lake chronology is in need of a 985-yr reservoir correction, but this test revealed that a reservoir correction identical to the one used in adjacent sites brings the events from that record into better alignment with events recorded in Basin Bayou. A slightly less aggressive reservoir correction could bring the Western Lake record into even better alignment with the Basin Bayou reconstruction.

The original storm reconstruction form Lake Shelby, 140 km west of Basin Bayou, has a similar active interval of intense ($\geq$ Category 4) hurricanes to that observed in Western Lake, with five events spanning 3200 to 700 B.P. (Figure 5.11; Liu and

Fearn, 1993). More recent work with an updated chronology has shown that the upper 62 cm in the Lake Shelby reconstruction, a sapropel unit, spans only the last 700 years after applying nearly 1000-year reservoir corrections to the ^{14}C dates (Lambert et al., 2008) as opposed to >2000 years (Liu and Fearn, 1993). Lambert et al. (2008) developed a geochemical approach to identifying hurricane deposits in the upper sapropel unit in the Lake Shelby sediment core following the assumption that seawater flooding in the lake provides the nutrients that induce heightened productivity, which alters carbon and nitrogen isotopic values in the sediments. They identified eleven storm events in the upper sapropel unit and shifted the timing of the most recent sand bed from 700 B.P. to 245 B.P., placing that event within 12 years of a known historical hurricane that made landfall and caused extensive damage near Mobile, AL in 1717 CE. The Lambert et al. (2008) approach relies on seawater spilling into Lake Shelby during storms, which requires less energy than sand transport and implies their reconstruction may also be recording weaker storms than the sand bed-based approach by Liu and Fearn (1993). The two different methods used to reconstruct paleostorms in Lake Shelby sediments may therefore cause these two records to reflect very different ranges of storm intensities. Lambert et al. (2008) identified 11 storms over the last 700 years including one that occurred within 45 years of the 310 B.P. event in our Basin Bayou record (Figure 5.11). The three most recent events in the revised Lake Shelby reconstruction align within 15 years of the three most recent events in our reconstruction (Lambert et al., 2008). Based on this comparison, the last 700 years of storm histories for Lake Shelby and Basin Bayou agree remarkably well for two sites that are separated geographically such that they are not expected to have identical storm deposition patterns.

The Basin Bayou storm reconstruction is in good agreement with a record of high magnitude storms in the northern Gulf of Mexico that is based on overwash deposits in Mullet Pond (Lane et al., 2011). Mullet Pond, which is 200 km east of Basin Bayou, is far enough from our site that it is generally not influenced by the same storms; only the hurricane in 1926 coincides with historical overwash deposits in both sites (Lane et al., 2011). Similarities between these records are therefore likely to reflect trends in intense hurricane occurrence across the northern gulf coast, in addition to local storm histories. A new ~2500-year-long reconstruction from Spring Creek Pond (Brandon et al., 2013), located 20 km north of Mullet Pond, shares several characteristics with the Mullet Pond and Basin Bayou reconstructions. These records together indicate that intense storms were more common between 2800 and 2300 B.P. and 1100 to 600 B.P. and were less common from 600 B.P. to 150 B.P. (Figure 5.11). Prior to 3000 B.P., storms frequencies in both the Mullet Pond and Basin Bayou records were neither active nor quiet. The two main periods where our reconstruction differs from the Mullet Pond and Spring Creek Pond records is between 2300 and 1600 B.P., when the Mullet Pond and Spring Creek Pond sediments record a relatively prolonged quiescent interval for intense hurricanes and from 1600 to 1100 B.P., when the record from Basin Bayou has a relatively reduced number of events during a period of heightened activity in the other two reconstructions. These differences may be attributed to either varying intense storm climatologies between the sites, where Basin Bayou was impacted by more intense hurricanes than Mullet Pond and Spring Creed Pond, or by the varying sensitivity of Basin Bayou to overwash. Between 2300 and 1600 B.P. the barrier separating Choctawhatchee Bay and the Gulf of Mexico and the baymouth barrier at the south end of Basin Bayou had both likely developed and reduced site sensitivity relative to 4500 to 3000 B.P. It is more reasonable, then, that the difference can be explained by a higher number of intense hurricanes that were directed toward Basin Bayou than Mullet and Spring Creek Ponds between 2300 and 1600 B.P. Between 1600 and 1100 B.P. event frequency increased in the Mullet and Spring Creek Pond records, but there are no events in the Basin Bayou record. It is possible either that intense storms were more commonly directed toward Mullet and Spring Creek Ponds than Basin Bayou during these five centuries, with the possibility that event frequency of lower intensity storms incapable of producing overwash deposits at Basin Bayou remained unchanged, or that the site sensitivity was lower due to the development of barriers separating Basin Bayou from Choctawhatchee Bay and the Gulf of Mexico. The active and inactive intervals detected in both of these records simultaneously are likely representative of northern Gulf of Mexico intense storm activity.

The generally good agreement between the overwash record from Mullet Pond (Lane et al., 2011) and Spring Creek Pond (Brandon et al., 2013) and the inconsistency between the Western Lake (Liu and Fearn, 2000) reconstruction and the Basin Bayou reconstruction may either indicate that the Western Lake reconstruction reflects variations in site sensitivity as suggested by Otvos (2002), or that storm climatology between our study site and the Mullet Pond region differs significantly during the last few millennia, which implies that our reconstruction from Basin Bayou is altered by chronological or site sensitivity uncertainties such that it is out of sync with the Western Lake record. We find it unlikely that errors in the chronology or co-varying site sensitivities at Basin Bayou, Mullet Pond, and Spring Creek Pond caused the periods of heightened and reduced hurricane activity in these three records to coincide by chance, so we favor the first explanation, that either an inaccurate chronology or variations in the sensitivity of Western Lake to storm deposition has changed during the last few millennia. Alternatively, it is possible that some of the difference between the Basin Bayou and Western Lake records can be explained by differing mechanisms depositing coarse sediment during hurricane landfalls. A storm that washes over the barrier between the Gulf of Mexico and Western Lake may not also produce a storm surge that propagates through Choctawhatchee Bay and over the barrier into Basin Bayou, or it may not have the wave energy necessary to mobilize and transport bay sediment into the center of the bayou. Conversely, a storm that has little surge on the Gulf Coast, with the dominant wind direction lining up with the maximum fetch of Choctawhatchee Bay, may produce large waves that overtop the baymouth barrier and transport sand in Basin Bayou without producing surge-induced deposits in Western Lake. While different deposition mechanisms can account for a fraction of the disagreement between the Western Lake and Basin Bayou reconstructions, the opposing trends during the last 1200 years are more likely the result of chronological inaccuracies.

5.5.7 Controls on Gulf of Mexico tropical cyclone activity

Intense tropical cyclone variability in the Gulf of Mexico is likely controlled by variations in the overall number of hurricanes that form in the Atlantic Ocean, factors that drive storms into the Gulf of Mexico as opposed to up the eastern seaboard or away from North America, and factors that prolong and intensify storms in the Atlantic Ocean and within the Gulf of Mexico. The location of cyclogenesis historically correlates to the landfall location, with more Gulf Coast landfalls occurring from storms that formed in the deep tropics and on the western half of the Atlantic Ocean (Kossin et al., 2010). The number of historical tropical cyclones in the Atlantic basin, particularly strong hurricanes, correlates with Atlantic SSTs (Goldenberg et al., 2001; Emanuel, 2005; Webster at al., 2005), with warmer SSTs corresponding to a higher number of intense hurricanes. The active interval between ~1200 and ~500 B.P., where the Basin Bayou, Mullet Pond, and Spring Creek Pond records all agree (highlighted with a grey bar in Figure 5.12) corresponds with a period of warmer SSTs in a high-resolution reconstruction from the eastern tropical Atlantic (deMenocal et al., 2000). The period of warmer SSTs began a few centuries before hurricane activity picked up in the Basin Bayou record, and it overlaps with the active period that is present in the Mullet and Spring Creek Pond reconstructions. Frequent overwash deposits in the Basin Bayou and Mullet Pond records between 2800 and 2300 B.P. also correspond to higher reconstructed Atlantic SSTs (Figure 5.12). Atlantic SSTs cooled during the Little Ice Age (LIA; ~600-150 B.P.), which corresponds to a decrease in Gulf hurricane frequency in the Basin Bayou, Mullet Pond, and Spring Creek Pond sediment records. The three recent overwash deposits in the Basin Bayou reconstruction occur when Atlantic SSTs warmed following the LIA (highlighted with a brown bar in Figure 5.12). The agreement between Gulf of Mexico cyclone activity and reconstructed Atlantic SSTs implies a relationship between cyclogenesis in the Atlantic basin and intense tropical cyclones making landfall in the Gulf of Mexico. The relationship between Atlantic SSTs and storminess in the Basin Bayou reconstruction is not perfect; SSTs off the west African coast between 4500 and 3500 B.P. were equivalent to those during the Medieval Climate Anomaly (MCA; ~1000-700 B.P.), when activity was high in the Gulf of Mexico storm reconstructions, yet 4500 to 3500 B.P. is a rather inactive period in both the Basin Bayou and Mullet Pond records. The high frequency of overwash deposits in the Basin Bayou reconstruction circa 2000 B.P. occurs when Atlantic SSTs are cool. From this, we hypothesize other factors partially control the frequency of intense storms in the Gulf.

Model and proxy comparisons demonstrate there was a period of heightened Atlantic tropical cyclone activity possible attributable to warm tropical Atlantic SSTs and the La Niña-like state during the during the MCA relative to the LIA (Chapter 4; Mann et al., 2009). Our data and the Mullet Pond data agree with these trends quite well, with heightened Gulf of Mexico hurricane activity during the MCA and persisting through 700-600 B.P., followed by reduced hurricane activity at both sites during the LIA. A reduction in upper atmospheric wind shear due to the mean La Niña-like state and/or warm tropical Atlantic SSTs during the MCA could have increased the overall frequency of storms in the Atlantic basin. Within the Gulf of Mexico, hurricanes may have been strengthened by the stronger ocean-to-atmosphere temperature gradient during strong El Niño events (Jaggar and Elsner, 2006), which may have been more frequent during the MCA (Moy et al., 2002; Chapter 4).

Upon arrival in the Gulf of Mexico, storms during the MCA may have been fueled by warmer SSTs in the Gulf and/or a thicker warm surface mixed layer due to Loop Current activity (Richey et al., 2007), increasing their intensities. Tropical cyclone formation and maintenance rely on the presence of a steep temperature gradient between the cold atmosphere and warm sea surface temperatures as well as a deep warm surface ocean layer to maintain the temperature gradient long enough to continually fuel the cyclone. A shallow thermocline allows for deeper, colder water to be incorporated into the mixed layer during high energy storm conditions, reducing the surface water to lower troposphere temperature gradient and weakening the tropical cyclone (Emanuel, 1986; Lane, 2011). A deeper, warmer surface layer in the Gulf of Mexico associated with more Loop Current penetration therefore produces more favorable conditions for maintaining tropical cyclone strength (Lane, 2011). The Loop Current flows into northern Gulf of Mexico during boreal summer, deepening the thermocline during summer and early fall (Richey et al., 2007). The *G. sacculifer*-based reconstruction from the Pigmy Basin suggests Loop Current penetration was greater from 1400 to 600 B.P. than from 600 B.P. to present and the Mg/Ca-based SST reconstruction from the same location suggests local SSTs were warmer between 1400 and 1000 B.P. (Richey et al., 2007). The more recent active interval in the Mullet Pond, Spring Creek Pond, and Basin Bayou records, from 1100 to 600 B.P., occurs when the *G. sacculifer* abundance-based reconstruction of the Loop Current suggests that the warm surface current was penetrating deeper into the Gulf of Mexico (Figure 5.12) and during the last century of a period characterized by warmer SSTs (Richey et al., 2007; Brandon et al., 2013). While the Basin Bayou reconstruction suggests intense hurricane activity was minimal when local SSTs were warm between 1400 and 1100 B.P., the Mullet and Spring Creek Pond records both suggest higher intense hurricane activity at this time, supporting local SSTs as a driving factor in intense hurricane variability.

In addition to a thicker warm surface layer, tropical cyclone strength in the Gulf of Mexico can also be enhanced when the thermal gradient between the water surface and the atmosphere is strengthened due to a cooling of the lower stratosphere, as occurs during El Niño events (Jaggar and Elsner, 2006). We compared the Mullet Pond and Basin Bayou storm reconstructions with a red color intensity record of runoff from Laguna Pallcacocha in Ecuador, a region that experiences heavy rainfall during El Niño events (Figure 5.12; Moy et al., 2002). Runoff in Ecuador was high during the period of intense tropical cyclone activity in the Mullet Pond and Basin Bayou records, indicating the frequency of moderate to strong El Niño events was high (Moy et al., 2002; Chapter 4). These observations suggest that the deepening of the thermocline in the Gulf of Mexico due to enhanced Loop Current penetration and cooling of the lower stratosphere during periods of high runoff in Ecuador, which may reflect periods of increased El Niño activity, sustained a thermal gradient that was necessary to support strong tropical cyclones in the Gulf of Mexico and may drive centennial-scale intense storm variability over the last two millennia.

Atlantic SSTs are projected to rise over the next century in response to greenhouse gas forcing (IPCC, 2007), which may increase the number of intense storms in the Atlantic basin and the Gulf of Mexico. If the future climate state is analogous to the MCA, we might expect more frequent and more intense hurricanes in the Gulf of Mexico than has been observed historically. Global temperatures are also expected to rise over the coming century (IPCC, 2007), which tends to draw the Intertropical Convergence Zone (ITCZ) northward due to a greater interhemispheric temperature gradient (Broccoli et al., 2006). A more northerly ITCZ tends to enhance Loop Current penetration in the Gulf of Mexico (Poore et al., 2004), which could also add to the intensity of storms in the coming century.

5.6 Conclusions

We reconstructed a new record of hurricane landfalls in northwest Florida based on the identification of coarse deposits identified in sediment cores from Basin Bayou. Given the modern configuration of the bayou, storm-induced deposition at our coring location only occurs during intense hurricanes that make landfall in very close proximity to the site. Geochemical data suggest that Basin Bayou more openly exchanged water and sediments with Choctawhatchee Bay and the Gulf of Mexico more frequently between 4500 and 3000 B.P. than from 2000 B.P. to the present. These data suggest a higher sensitivity to storm-induced deposition prior to 2000 B.P., limiting our confidence in the reconstruction of intense hurricanes to 2000 B.P. to present. Prior to 2000 B.P., our record may represent only intense storms to do lower sea level or may incorporate sand deposits from smaller, weaker storms due to the absence of the protecting barrier. Despite the transition in site sensitivity during the late Holocene, the average number of events per century after 2000 B.P. was greater than the average number of events per century when the basin was more openly exchanging fine-grained sediments with Choctawhatchee Bay and the increase in frequency was punctuated and became increasingly more frequent than the gradual and slowing local sea level rise rates, so there has clearly been an increase in the frequency of intense storms at Basin Bayou over the last 4500 years. Heightened storm activity in the Basin Bayou storm reconstruction occurred from 2800 to 2300 B.P., 2000 to 1900 B.P., 1700 to 1600 B.P., and 1100 to 600 B.P. (Figure 5.11). Quiescent intervals in the Basin Bayou record occurred from 2300 to

2000 B.P., 1600 to 1100 B.P., and 600 to 135 B.P. (Figure 5.11). The active periods at Basin Bayou correlate with active intervals from other northern Gulf of Mexico reconstruction of intense storms from Mullet Pond (Lane at al., 2011) and Spring Creek Pond (Brandon et al., 2013). These sites together suggest the occurrence of intense northern Gulf of Mexico storms during the last two millennia is related to the influence of Atlantic SSTs, the Loop Current, and El Niño activity on creating a higher number of storms in the Atlantic basin and a stronger ocean surface to lower stratosphere temperature gradient and provides a deeper layer of warm surface water within the Gulf of Mexico that maintains storm strength. Warming Atlantic SSTs and increased Loop Current penetration over the coming century could produce a greater number of intense hurricanes in the Gulf of Mexico.

5.7 Acknowledgements

We thank Trevor Harrison and Lance Croft for field assistance and Stephanie Madsen for laboratory assistance. Funding for this project was provided by the Strategic Environmental Research and Development Program (SERDP) grant awarded to Jeffrey Donnelly, Rob Evans, and Andrew Ashton and grants from NOAA and NSF (P2C2), number P2C2-OCE-0903020 awarded to Jeffrey Donnelly.

5.8 References

Appleby, P.G., 1997. Sediment records of fallout radionuclides and their application to studies of sediment-water interactions. Water Air Soil Pollut. 99, 573-586.

Appleby, P.G. and Oldfield, F., 1978. The calculation of ^{210}Pb dates assuming a constant rate of supply of unsupported ^{210}Pb to the sediment. Catena 5, 1-8.

Brandon, C.M., Woodruff, J.D., Lane, D.P., Donnelly, J.P., 2013. Tropical cyclone wind speed constraints from resultant storm surge deposition: A 2500 year reconstruction of hurricane activity from St. Marks, FL. Geochem., Geophys., Geosys. 14, doi:10.1002/ggge.20217.

Broccoli, A.J., Dahl, K.A., Stouffer, R.J., 2006. Response of the ITCZ to Northern Hemispheric cooling. Geophys. Res. Lett. 33, L01702, doi: 10.1029/2005GL024546.

Das, O., Wang, Y., Donoghue, J., Xu, X., Coor, J., Elsner, J., Xu, Y., 2013. Reconstruction of paleostorms and paleoenvironment using geochemical proxies archived in the sediments of two coastal lakes in northwest Florida. Quat. Sci. Rev. 68, 142-153.

Davidson-Arnott, R., 2010. An introduction to coastal processes and geomorphology. Cambridge: University Press.

Dean, W.E., 1974. Determination of carbonate and organic matter in calcareous sediments and sedimentary rocks by loss on ignition: comparison with other methods. J. Sed. Petrol. 44, 242-248.

deMenocal, P., Ortiz, J., Guilderson, T., Sarnthein, M., 2000. Coherent high- and low-latitude climate variability during the Holocene Warm Period. Science 288, 2198-2202.

Department of Commerce (DOC), National Oceanic and Atmospheric Administration (NOAA), National Ocean Service (NOS), Coastal Services Center (CSC), 2007. 2006 Florida Lidar: Escambia, Santa Rosa and Walton Counties. <http://www.csc.noaa.gov/digitalcoast>

DeMaria, M., 1996. The effect of vertical shear on tropical cyclone intensity change. J. Atmos. Sci. 53, 2076-2087.

Donnelly, J.P., Webb III, T., 2004. Backbarrier sedimentary records of intense hurricane landfalls in the northeastern United States. In: Murnane, R. and Liu, K. (eds.), Hurricanes and Typhoons: Past Present and Potential, New York: Columbia Press, pp. 58-96.

Emanuel, K.A., 1986. An air-sea interaction theory for tropical cyclones: Part I: Steady-state maintenance. J. Atmos. Sci. 43, 585-604.

Emanuel, K.A., 1999. Thermodynamic control of hurricane intensity. Nature. 401, 665-669.

Emanuel, K.A., 2003. Tropical Cyclones. Annu. Rev. Earth Planet. Sci. 31, 75-104.

Emanuel, K., 2005. Increasing destructiveness of tropical cyclones over the past 30 years. Nature 436, 686-688.

Environmental Protection Agency (EPA). "Watershed assessment, tracking and environmental results." 7 July 2013. Web. 7 July 2013. < http://epadev.induscorp.com/epadevdb_tmdl_web/attains_watershed.control?p_huc=03130005&p_state=GA&p_cycle=1998&p_report_type=T>

Goldenberg, S.B., Landsea, C.W., Mestas-Nuñez, A.M., Gray, W.M., 2001. The recent increase in Atlantic hurricane activity: Causes and implications. Science 293, 474-479.

Grinsted, A., Moore, J.C., Jevrejeva, S., 2013. Projected Atlantic hurricane surge threat from rising temperatures. PNAS. 110, 5369-5373.

Heiri, O., Lotter, A.F., Lemcke, G., 2001. Loss on ignition as a method for estimating organic and carbonate content in sediments: reproducibility and comparability of results. J. Paleolim. 25, 101-100.

Henderson-Sellers, A., Zhang, H., Berz, G., Emanuel, K., Gray, W., Landsea, C., Holland, G., Lighthill, J., Shieh, S-L., Webster, P., McGuffie, K., 1998. Tropical cyclones and global climate change: A post-IPCC assessment. Bull. Am. Meteor. Soc. 79, 19-38.

Hippensteel, S.P., 2008. Preservation Potential of Storm Deposits in South Carolina Back-Barrier Marshes. J. Coast. Res. 24, 594-601.

Hippensteel, S.P., 2010. Paleotempestology and the pursuit of the perfect paleostorm proxy. GSA Today. 20, 52-53.

Holland, G., Bruyère, C.L., 2013. Recent intense hurricane response to global climate change. Clim Dyn.

IPCC (Intergovnermental Panel on Climate Change). Contribution of Working Group I to the Fourth Assessment Report of the Intergovernmental Panel on Climate Change, 2007. Solomon, S., D. Qin, M. Manning, Z. Chen, M. Marquis, K.B. Averyt, M. Tignor and H.L. Miller (eds.) Cambridge University Press, Cambridge, United Kingdom and New York, NY, USA.

Jaggar, T.H., Elsner, J.B., 2006. Climatology models for extreme hurricane winds near the United States. J. Clim. 19, 3220-3236.

Kossin, J.P., Camargo, S.J., Sitkowski, M., 2010. Climate modulation of North Atlantic hurricane tracks. J. Clim. 23, 3057-3076.

Knapp, K.R., Kruk, M.C., Levinson, D.H., Diamond, H.J., Neumann, C.J., 2010. The International Best Track Archive for Climate Stewardship (IBTrACS): Unifying tropical cyclone best track data. Bull. Amer. Meteor. Soc. 91, 363-376.

Mann, M.E., Woodruff, J.D., Donnelly, J.P., Zhang, Z., 2009. Atlantic hurricanes and climate over the past 1,500 years. Nature. 460, 880-885.

Lambert, J.W., Aharon, P., Rodriguez, A.B., 2008. Catastrophic hurricane history revealed by organic geochemical proxies in a coastal lake sediments: a case study of Lake Shelby, Alabama (USA). J. Paleolimnol. 39, 117-131.

Lane, D.P., 2011. Late Holocene Hurricane Activity and Climate Variability in the Northeastern Gulf of Mexico. Ph.D. Thesis. MIT/WHOI Joint Program in Oceanography/Applied Ocean Science and Engineering. Massachusetts Institute of Technology. Boston, MA.

Lane, P., Donnelly, J.P., Woodruff, J.D., Hawkes, A.D., 2011. A decadally-resolved paleohurricane record archived in the late Holocene sediments of a Florida sinkhole. Mar. Geo. 287, 14-30.

Liu, K., Fearn, M.L., 1993. Lake-sediment record of late Holocene hurricane activities from coastal Alabama. Geology 21, 793-796.

Liu, K., Fearn, M.L., 2000. Reconstruction of prehistoric landfall frequencies of catastrophic hurricanes in northwestern Florida from lake sediment records. Quat. Res. 54, 238-245.

Moy, C.M., Seltzer, G.O., Rodbell, D.T., Anderson, D.M. 2002. Variability of El Niño/Southern Oscillation activity at millennial timescales during the Holocene epoch. Nature 420, 162-165.

Otvos, E.G., 2002. Discussion of “Prehistoric landfall frequencies of catastrophic hurricanes…” (Liu and Fearn, 2000). Letter to the Editor. Quat. Res. 57, 425-428.

Pielke Jr., R.A., Gratz, J., Landsea, C.W., Collins, D., Saunders, M.A., Musulin, R., 2008. Normalized hurricane damage in the United States: 1900-2005. Nat. Haz. Rev. 9, 29-42.

Ranasinghe, P.N., Donnelly, J.P., Evans, R.L., van Hengstum, P.J., Ashton, A.D., 2012. “Changes in hurricane activity in northeastern Gulf of Mexico during last 8500 yrs. – A hurricane record from Choctawhatchee Bay, Destin FL.” American Geophysical Union Fall Meeting, San Fransisco, CA, 3-7 Dec. OS31A-1699. Poster Presentation.

Richey, J.N., Poore, R.Z., Flower, B.P., Quinn, T.M., 2007. 1400 yr multiproxy record of climate variability from the northern Gulf of Mexico. Geology. 35, 423-236.

Roberts, M.L., von Reden, K.F., Burton, J.R., McIntyre, C.P., Beaupré, S.R., 2011. A gas-accepting ion source for Accelerator Mass Spectrometry: Progress and applications. Nuclear Instruments and Methods in Physics Research Section B: Beam Interactions with Materials and Atoms. 294, 296-299.

Ruth, B., Handley, L.R., 2006. Choctawhatchee Bay. Seagrass status and trends in the northern Gulf of Mexico 1940-2002. 143-153.

Schnurrenberger, D., Russell, J.M., Kelts, K., 2003. Classification of lacustrine sediments based on sedimentary components. J. Paleolimnol. 29, 141-154.

Scott, T.M., Campbell, K.M., Rupert, F.R., Arthur, J.D., Green, R.C., Means, G.H., Missimer, T.M., Lloyd, J.M., Yon, J.W., Duncan, J.G., 2001. Geologic map of the state of Florida. Florida Geological Survey and Department of Environmental Protection.

Shore Protection Manual, 1984. 4th ed. Department of the Army, Waterways Experiment Station, Coastal Engineering Research Center.

Stuiver, M. and Reimer, P.J., 1993. Extended ^{14}C data base and revised Calib 3.0 ^{14}C age calibration program. Radiocarbon 35, 215–230.

Stuiver, M., Reimer, P.J., Reimer, R., 2005. CALIB 5.0.2 [WWW program and documentation]. www.calib.org: Unknown Publisher.

Törnqvist, T.E., Bick, S.J., van der Borg, K., de Jong, A.F.M., 2006. How stable is the Mississippi Delta? Geology. 34, 697-700.

United States Geological Survey (USGS). St. Petersburg Coastal and Marine Science Center. “Response of Florida Shelf Ecosystems to Climate Change.” 6 May 2013. Web. 8 July 2013. <http://coastal.er.usgs.gov/flash/bathy-entireFLSH.html>

Wagner, A.J., Guilderson, T.P., Slowey, N.C., Cole, J.E., 2011. Pre-bomb surface water radiocarbon of the Gulf of Mexico and Caribbean as recorded in Hermatypic corals. Radiocarbon 51, 947-954.

Webster, P.J., Holland, G.J., Curry, J.A., Chang, H.-R., 2005. Changes in tropical cyclone number, duration, and intensity in a warming environment. Science. 309, 1844-1846.

Woodruff, J.D., Donnelly, J.P., Mohrig, D., Geyer, W.R., 2008. Reconstructing relative flooding intensities responsible for hurricane induced deposits from Laguna Playa Grande, Vieques, Puerto Rico. Geology. 36, 391-194.

Category	Landfall west of Choctawhatchee Bay opening		Category	Direct Landfall (within 20 nautical miles of Choctawhatchee Bay opening)
3	1916		3	1882
3	1995 (Opal)		3	1917
3	2004 (Ivan)		3	1975 (Eloise)
3	2005 (Dennis)			
2	1926		2	1896
1	1859		1	1877
1	1911		1	1887
1	1932		1	1936
1	1950 (Baker)		1	1956 (Flossy)
1	1995 (Erin)			
1	1997 (Danny)			
Trop. Storm	1889		Trop. Storm	1879
Trop. Storm	1894		Trop. Storm	1880
Trop. Storm	1902		Trop. Storm	1901
Trop. Storm	1919		Trop. Storm	1904
Trop. Storm	1939		Trop. Storm	1957 (Debbie)
Trop. Storm	1959 (Irene)		Trop. Storm	1994 (Alberto)
Trop. Storm	1985 (Juan)		Trop. Storm	2000 (Helene)
Trop. Storm	2005 (Arlene)		Trop. Storm	2001 (Barry)
Trop. Storm	2009 (Ida)			
			Subtrop. Storm	1969
Trop. Depression	1977		Trop. Depression	1987
			Trop. Depression	2007 (Ten)

Table 5.1: Historical tropical cyclones from the IBTrACS dataset listed in order of decreasing intensity at landfall. Left: Cyclones that made landfall within 50 nautical miles to the west of the connection between Choctawhatchee Bay and the Gulf of Mexico. Right: Cyclones that made landfall directly over the connection between the bay and the gulf, within 20 nautical miles.

Sed. depth (cm)	Lab sample code	Dated material	^{14}C age (years B.P.)	Cal. Age (year B.P.)	2 Sigma range 1 (years B.P.) (probability)	2 Sigma range 2 (years B.P.) (probability)	2 Sigma range 3 (years B.P.) (probability)	2 Sigma range 4 (years B.P.) (probability)
Basin Bayou – BaBy6								
71.9*	OS-102190	Plant Macrofossil	1920 +/- 25	1862	1820:1904 (0.921)	1906:1925 (0.394793)		
98.65*	OS-102403	Plant Macrofossil	2190 +/- 30	2219	2125:2313 (1)			
290.4*	OS-102390	Plant Macrofossil	3870 +/- 120	4272.5	3956:4589 (0.975262)	3923:3954 (0.010627)	4591:4615 (0.007287)	4765:4784 (0.006823)
Basin Bayou – BaBy1								
48.25*	OS-98130	Plant Macrofossil	365 +/- 25	355	424:499 (0.564332)	318:392 (0.435668)		
122.3	*OS-96543*	*Bivalve*	*1430 +/- 100*	*1358*	*1168:1548 (0.987234)*	*1140:1161 (0.009985)*	*1096:1102 (0.00278)*	
165.3*	OS-98279	Plant Macrofossil	1370 +/- 25	1293.5	1268:1319 (0.976754)	1322:1331 (0.023246)		
Basin Bayou – BaBy4								
85*	OS-102814	Plant Macrofossil	1190 +/- 35	833.5	767:900 (0.874869)	918:962 (0.072296	714:745 (0.052835)	
153.5*	OS-102380	Plant Macrofossil	2140 +/- 65	2157	1987:2327 (0.996349)	1953:1957 (0.003651)		
166.5	*109732*	*Bivalve*	*3118 +/- 156*	*3285*	*2922:3648 (0.979441)*	*3653:3688 (0.014186)*	*2888:2906 (0.006373)*	
176.5	*109733*	*Bivalve*	*3086 +/- 266*	*3343.5*	*2705:3982 (0.997503)*	*2618:2633 (0.002139)*	*2552:2555 (0.000358)*	
251	*109734*	*Bivalve*	*3502 +/- 266*	*3832.5*	*3141:4524 (0.997282)*	*3081:3092 (0.001543)*	*3115:3122 (0.001175)*	
340*	OS-102189	Plant Macrofossil	4040 +/- 30	4502	4423:4581 (0.970656)	4769:4781 (0.02397)	4603:4606 (0.005373)	
501.5	*109735*	*Bivalve*	*5380 +/- 269*	*6167*	*5588:6746 (1)*			
Basin Bayou – BaBy9								
161.5*	OS-102404	Plant Macrofossil	2270 +/- 30	2205	2158:2252 (0.5093)	2299:2347 (0.4907)		

Table 5.2: Radiocarbon dating sample information for each core is listed by cumulative depth with 2-sigma calibrated age ranges in years before 1950. CFAMS-dated samples are italicized. Samples included in the final age model for each core are marked with an asterisk next to the cumulative depth.

Elemental abundance (counts)	Bay-2.1 m	Bay-4.1 m	Bay-5.9 m	Basin Creek	
S	0	3007	2667	0	
Cl	7477	7281	10360	3163	
K	1757	1742	1289	558	
Ca	353	621	357	0	
Ti	1920	1390	1023	394	
Cr	38	51	43	0	
Mn	116	280	142	0	
Fe	9014	27822	19038	3166	
Co	0	225	211	50	
Elemental abundance (counts)	**Terrestrial 1**	**Terrestrial 2**	**Terrestrial 3**	**Terrestrial 4**	**Terrestrial 5**
S	0	0	0	0	0
Cl	5355	3887	4790	3606	9467
K	502	362	590	774	467
Ca	0	112	3605	8275	1362
Ti	508	167	413	333	369
Cr	0	0	0	0	0
Mn	26	0	55	94	31
Fe	808	1136	768	1289	759
Co	0	0	0	0	0

Table 5.3: XRF-derived elemental abundances of three Choctawhatchee Bay surface sediment samples, a surface sediment sample from Basin Creek, and five surface soil samples. Units are counts.

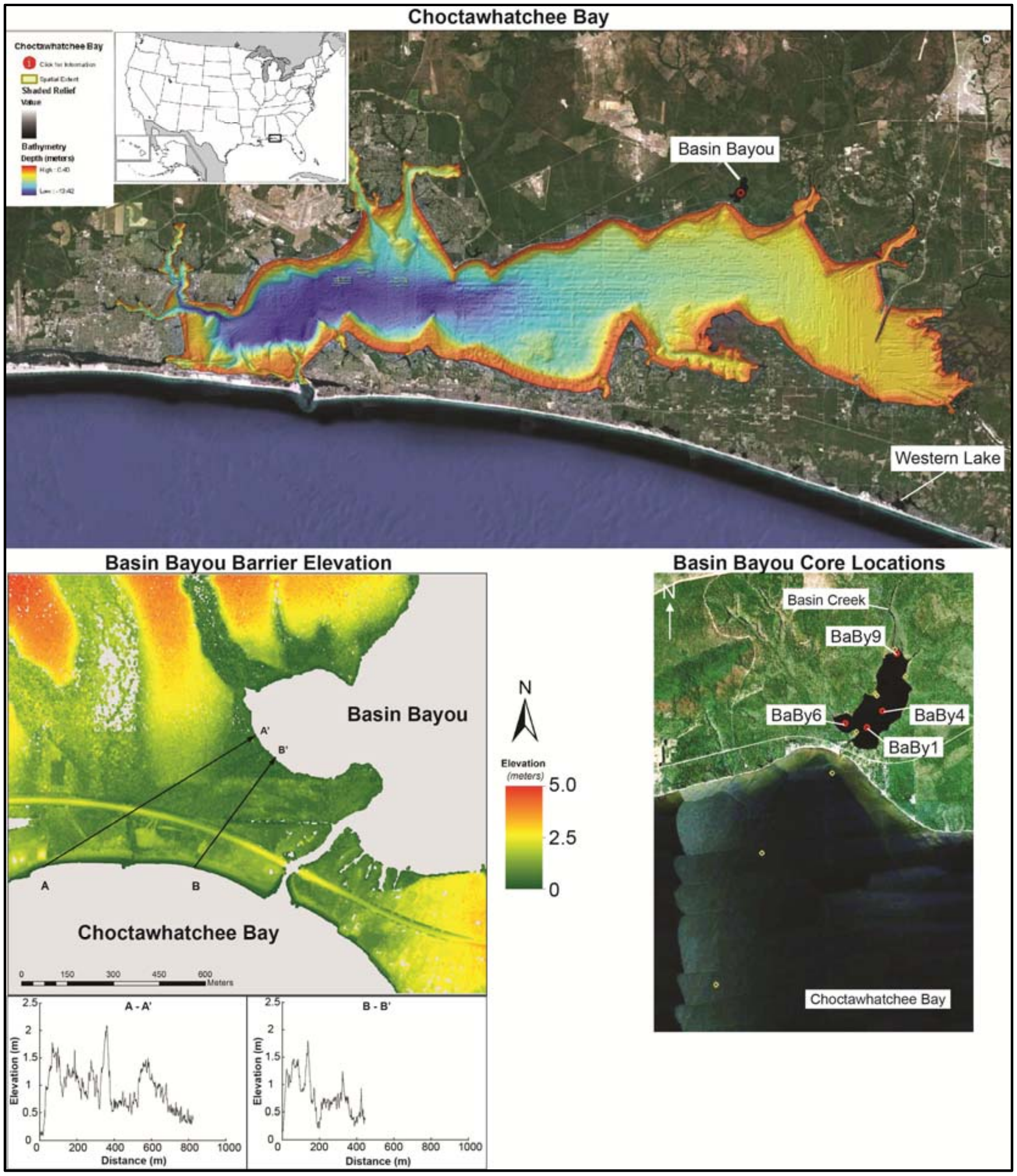

Figure 5.1: Site location maps. Top: Color bathymetry map of Choctawhatchee Bay in Google Earth provided by the National Oceanic and Atmospheric Administration, with shallower depths displayed as warmer colors. Basin Bayou (this study) and Western Lake (Liu and Fearn, 2000) are labeled, with a red target symbol marking the coring location in Basin Bayou. Bottom Left: Lidar elevation map of the baymouth barrier separating Basin Bayou (top right corner of image) from Choctawhatchee Bay (bottom left corner of image). Elevation is in meters with warmer colors indicating higher elevations. Two elevation profiles are shown on the bottom to display the elevation variations along transects A to A' and B to B'. Bottom Right: Core locations in Basin Bayou are displayed as red target symbols, and surface samples included in this study are displayed as open yellow diamonds.

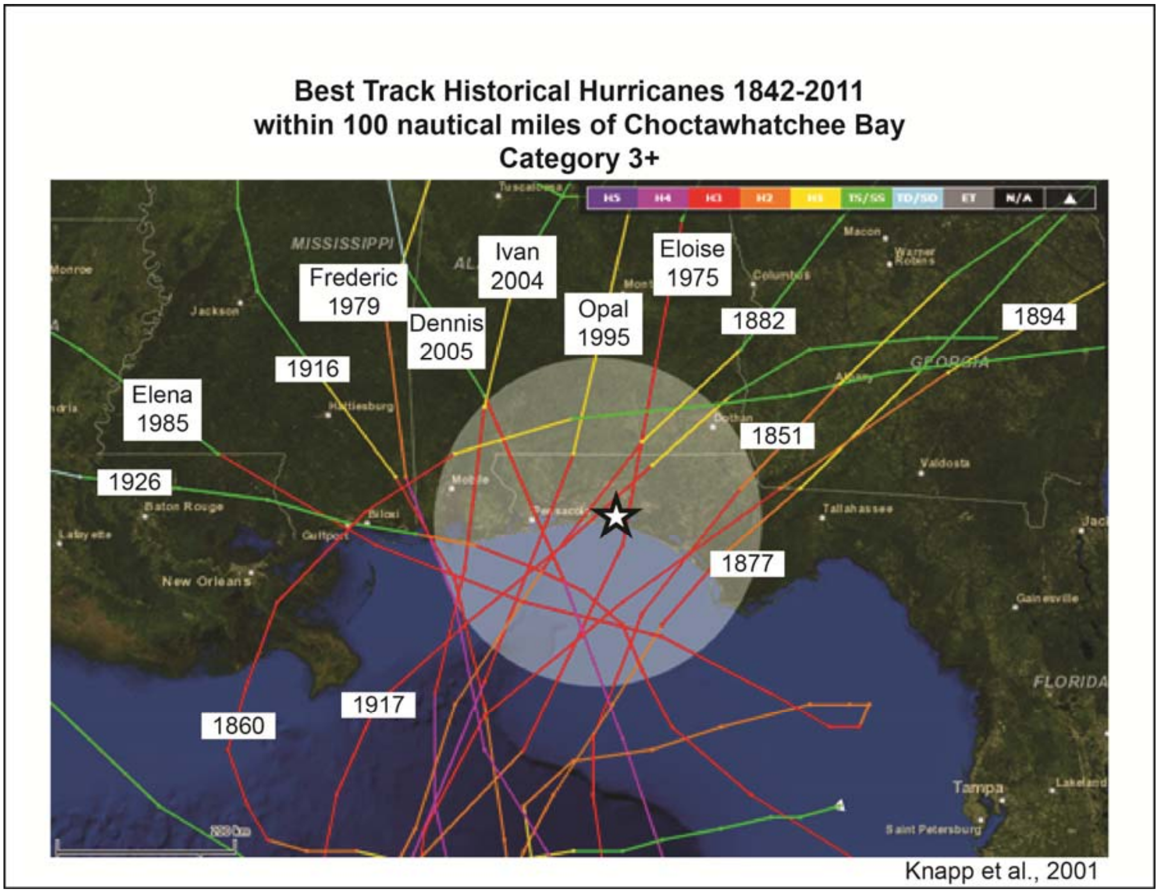

Figure 5.2: Storm tracks for all historical cyclones in the IBTrACS dataset that passed within 100 nautical miles of the connection between Choctawhatchee Bay and the Gulf of Mexico. The year and name, if applicable, of each storm is labeled with a white box overlaying the storm track. Our study site is indicated with a white star.

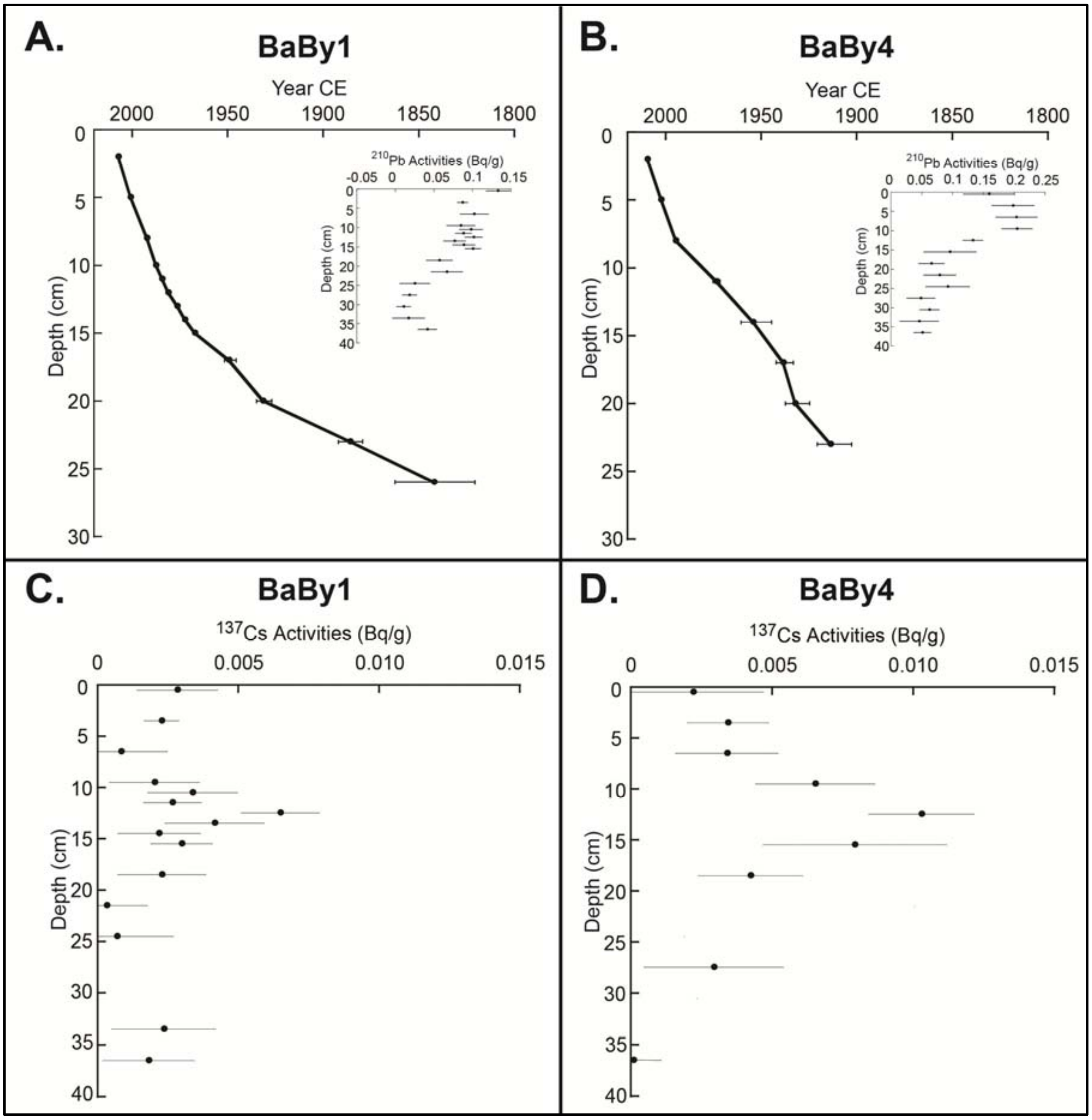

Figure 5.3: A: ^{210}Pb age vs. depth profile for BaBy1 is plotted with ^{210}Pb age uncertainties indicated with error bars. B: ^{210}Pb age vs. depth profile for BaBy4 is plotted with ^{210}Pb age uncertainties indicated with error bars. Insets in A. and B. are ^{210}Pb activity vs. depth profiles for each core. C: ^{137}Cs vs. depth profile for BaBy1. D: ^{137}Cs vs. depth profile for BaBy4. Horizontal lines indicated analytical uncertainty in each activity measurement.

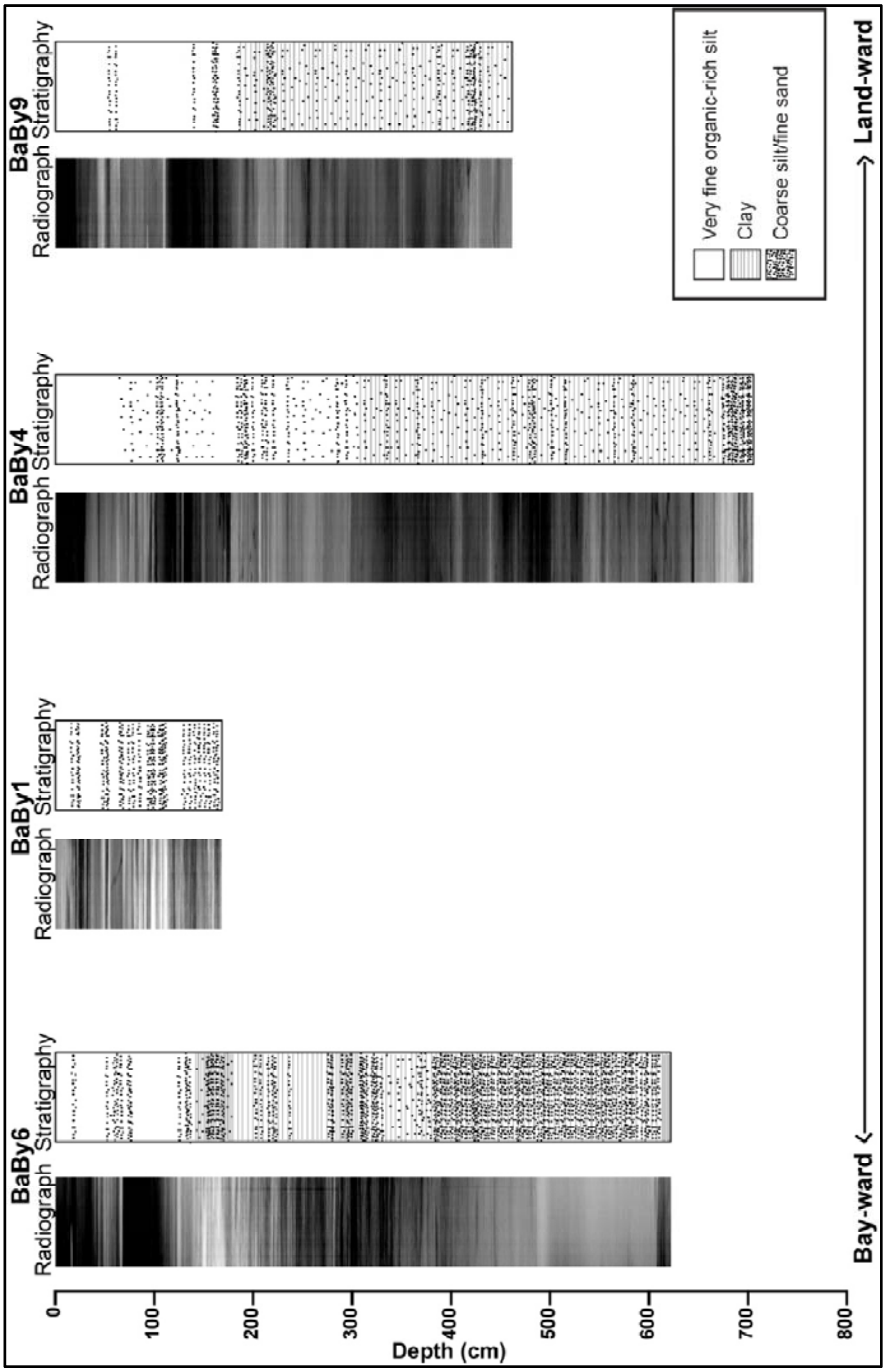

Figure 5.4: Radiographic images and stratigraphic columns of Basin Bayou cores on a depth scale. Cores are displayed with increasing distance from the bay from left to right. Grey-scale colors on radiographic images are inverted such that white indicates high density and black indicates low density.

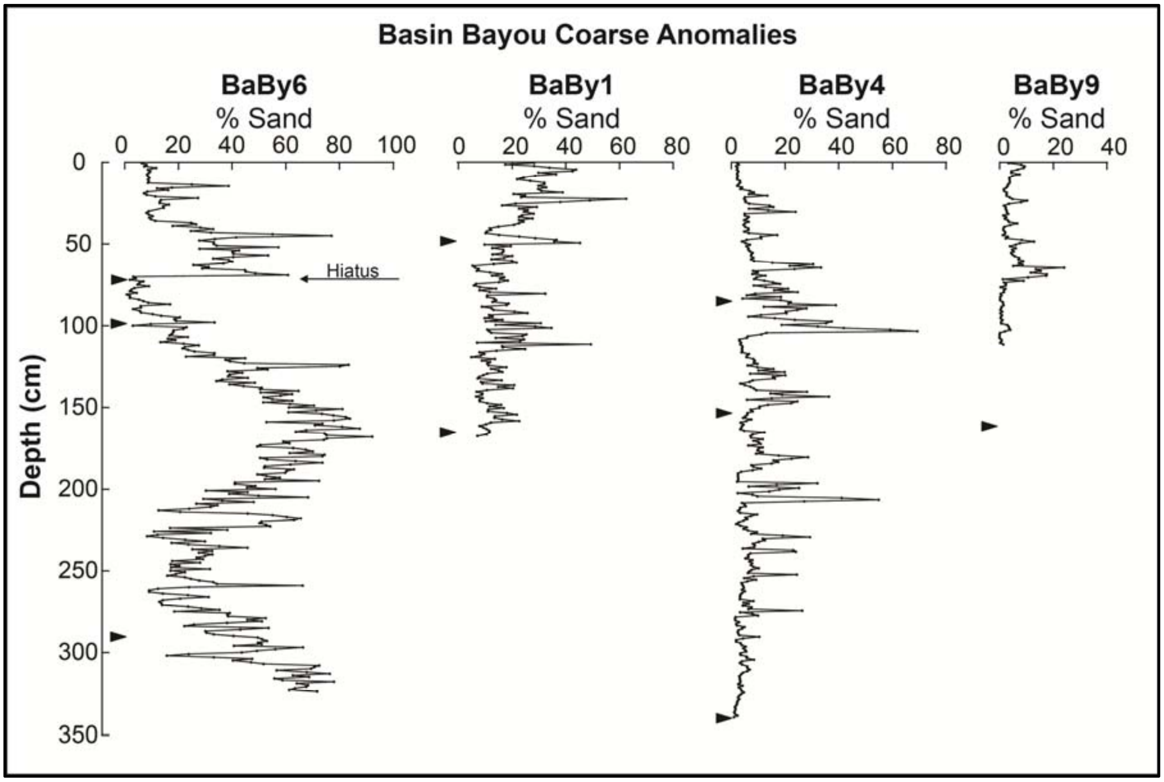

Figure 5.5: Percent sand for BaBy6, BaBy1, BaBy4 and BaBy9 are plotted from left to right in black. Each circle represents an individual measurement. All data are plotted vs depth. Black triangles indicate ^{14}C age control points.

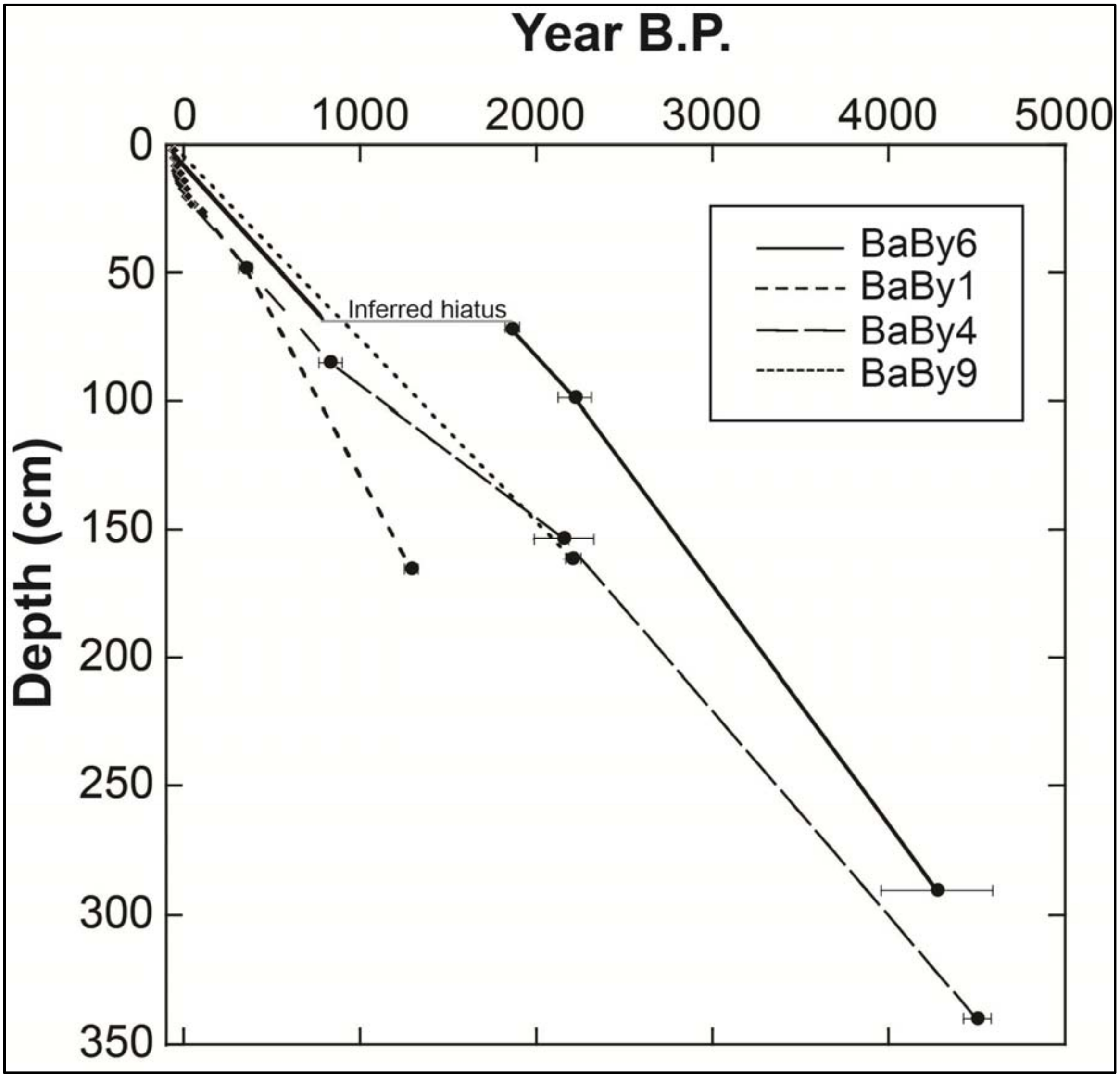

Figure 5.6: Age vs. depth profiles for BaBy6, BaBy1, BaBy4, and BaBy9. Circles represent ^{14}C ages and diamonds represent ^{210}Pb ages. Age uncertainties are indicated with error bars.

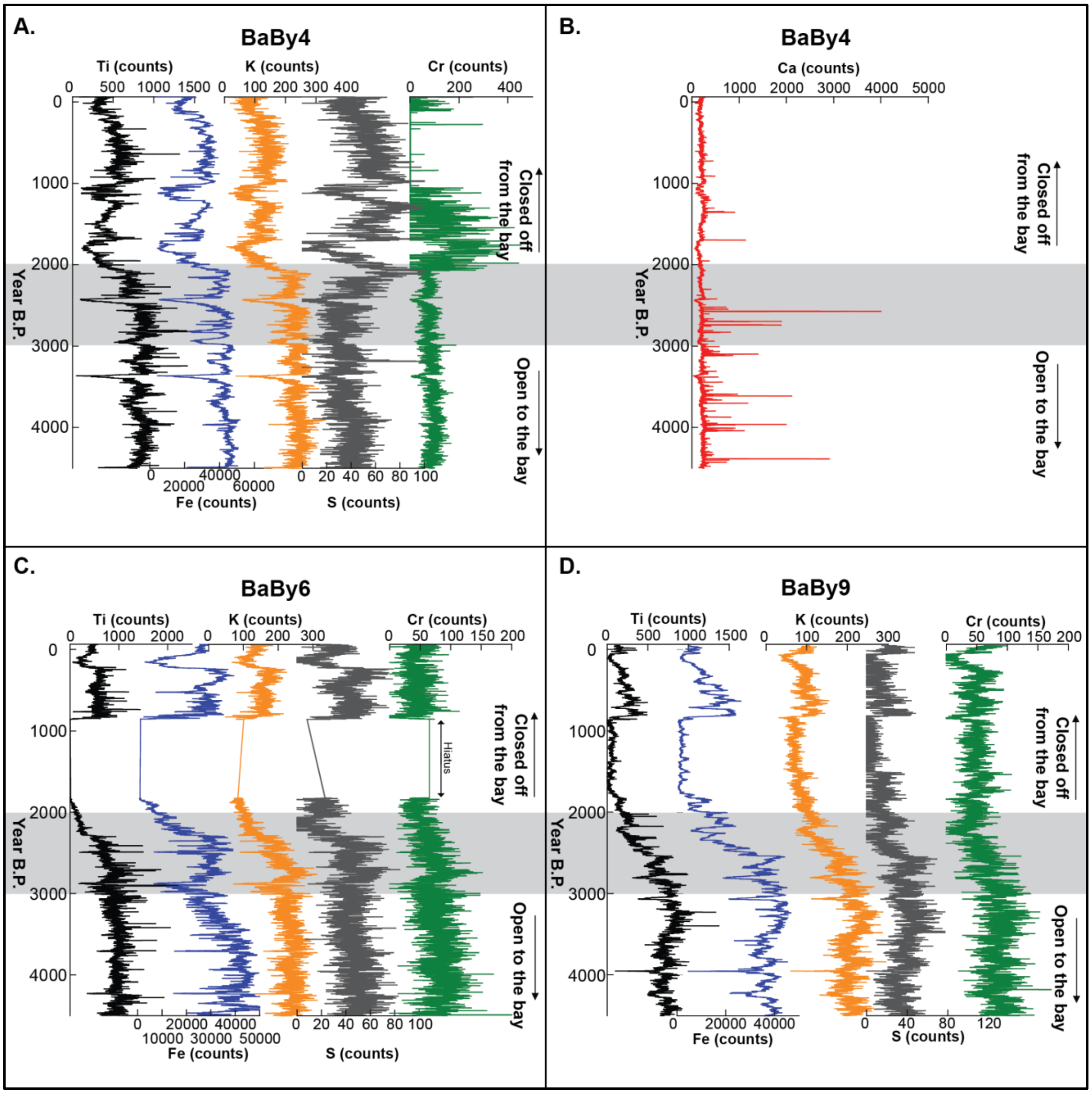

Figure 5.7: XRF-derived elemental abundances for selected elements are displayed in units "counts" and plotted vs. years before 1950. Elements plotted in panels A, C, and D from left to right are Ti (black), Fe (blue), K (orange), S (grey), and Cr (green). The horizontal grey bar highlights the transition in elemental abundances observed in all cores between 3000 and 2000 B.P. Arrows on either side of the grey bar label our interpretation of whether the bayou was more open to the bay (below grey bar) or closed to the bay (above grey bar). A: Selected elemental abundances from BaBy4. B: XRF-derived Ca counts from the BaBy4 core are plotted in red. C: Selected elemental abundances from BaBy6. D: Selected elemental abundances from BaBy9.

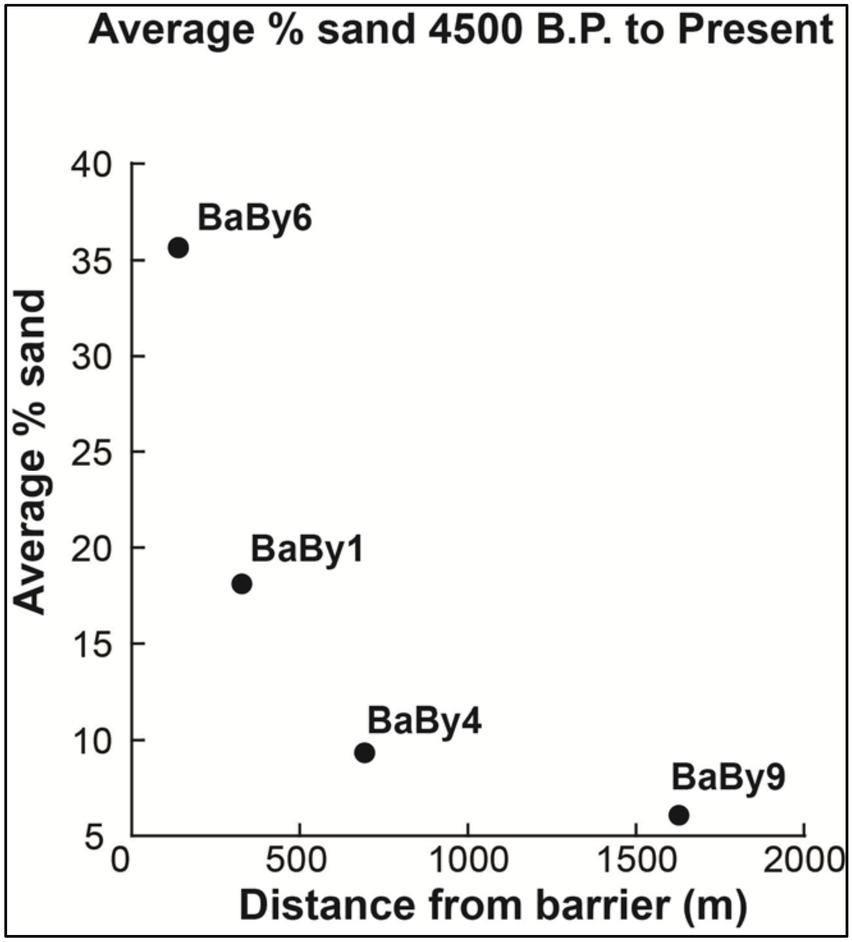

Figure 5.8: The % sand value for each core, averaged across the interval 4500 B.P. to present, are plotted relative to distance from the baymouth barrier at the south end of Basin Bayou.

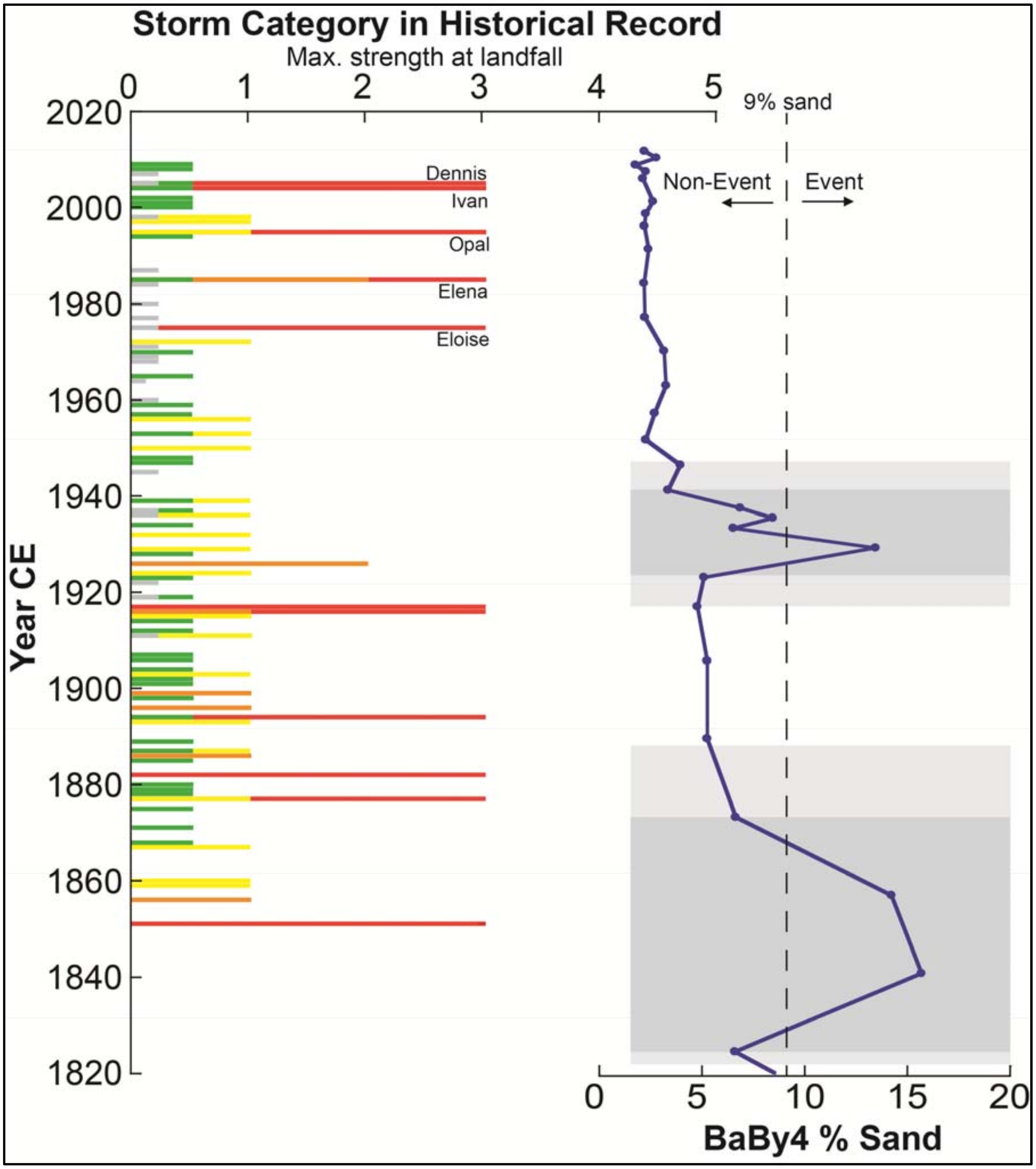

Figure 5.9: Left: All historical cyclones from the IBTrACS dataset to pass within 100 nautical miles of Basin Bayou are plotted such that the longer bars and warmer colors correspond to increasingly higher hurricane intensities. Grey bars are tropical depressions, green are tropical storms, yellow are Category 1, orange are Category 2, and red are Category 3. Right: ^{210}Pb-dated portion of the BaBy4 % sand dataset is plotted in blue. Each circle represents an individual measurement. Dark grey bars across the two beds with increased sand content relative to the rest of the record highlight the duration of each event. Light grey bars represent the age uncertainty in that portion of the age model.

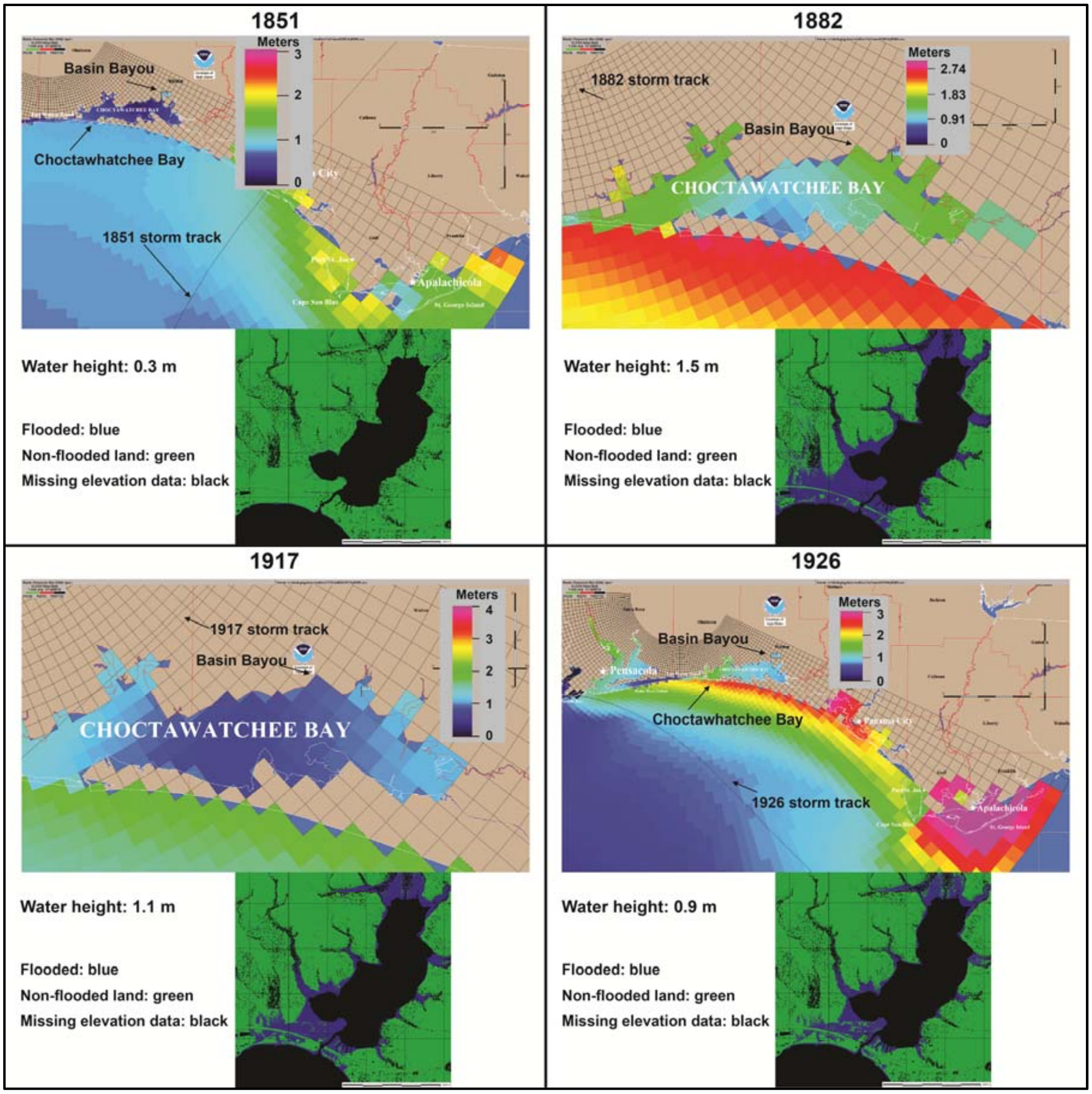

Figure 5.10: SLOSH simulations of storm surge heights for historical storms occurring in 1851, 1882, 1917, and 1926. Each panel displays a map on the top from the SLOSH simulation extracted when surge levels were highest at Basin Bayou. Below each SLOSH simulation map is an elevation map of Basin Bayou and the baymouth barrier displaying the level of flooding (blue) for the maximum surge level during each event.

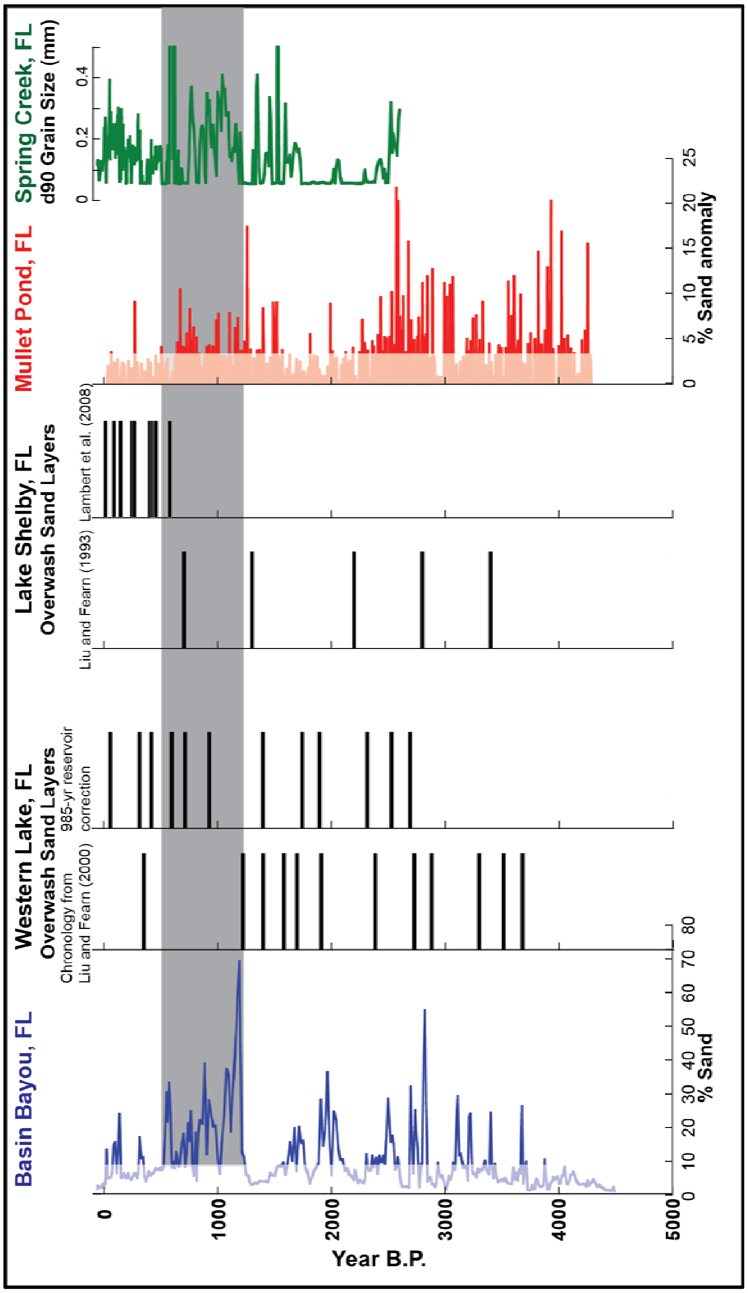

Figure 5.11: Comparison of Gulf of Mexico paleostorm reconstructions. From left to right the records displayed are: the Basin Bayou storm reconstruction from this study, which is % sand in BaBy4 (blue), overwash event record from Western Lake, FL as published in Liu and Fearn (2000) and with 985-yr reservoir correction as discussed in text (black bars represent individual events), overwash event record from Lake Shelby, as published in Liu and Fearn (1993) and in Lambert et al. (2008), the coarse anomaly overwash record from Mullet Pond, FL (red, Lane et al., 2011), and the coarse anomaly overwash record from Spring Creek, FL (green, Brandon et al., 2013). All % sand values in the Basin Bayou and Mullet Pond records that are not characterized as event deposits are faded such that the events visually stand out.

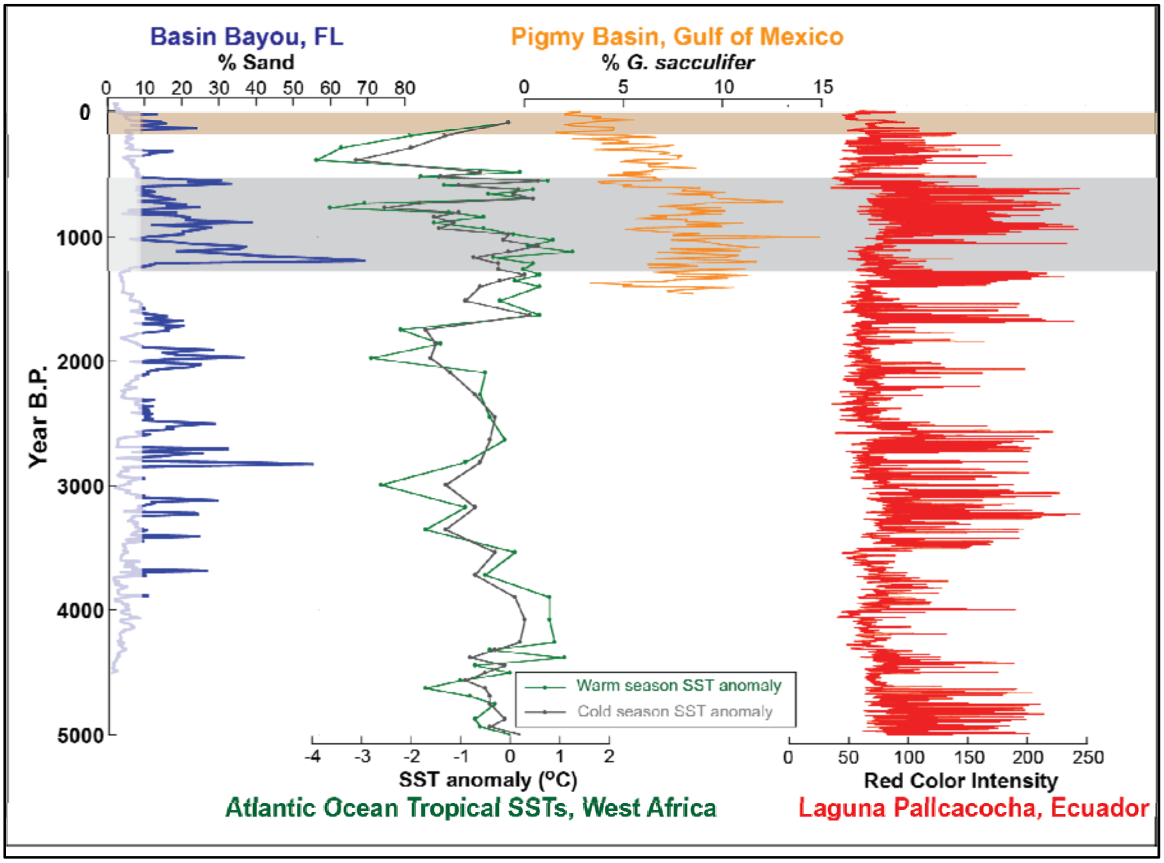

Figure 5.12: The Basin Bayou storm reconstruction, which is % sand in BaBy4, is plotted in blue (left). All % sand values that are not characterized as event deposits are faded such that the events in our record visually stand out. To the right of the Basin Bayou record are cold (grey) and warm (green) season sea surface temperature anomalies in degrees Celsius in the tropical Atlantic Ocean off the coast of West Africa (deMenocal et al., 2000). To the right of the Atlantic SST reconstructions is the *G. sacculifer* abundance record from the Pigmy Basin (orange), a proxy for the Loop Current in the northern Gulf of Mexico (Richey et al., 2007). On the far right is the red color intensity record of runoff from Laguna Pallcacocha in Ecuador (red; Moy et al., 2002). All data are plotted vs years before 1950. The horizontal grey bar highlights the most active interval in Basin Bayou over the last 4500 years that coincides with a greater number of high-threshold events in the Mullet Pond reconstruction, anomalously higher SSTs near West Africa, a greater relative abundance of *G. sacculifer* (more Loop Current penetration), and high red color intensity in the Laguna Pallcacocha runoff record. The horizontal brown bar highlights a secondary active interval that coincides with anomalously warm SSTs near West Africa and little Loop Current penetration and runoff in Ecuador.

CHAPTER 6

Extreme floods and millennial-scale paleohydrologic variations during the Holocene preserved in floodplain lake sediments

Jessica R. Rodysill[1]

Jeffrey P. Donnelly[2], Michael Toomey[2], Richard Sullivan[2]

[1]Department of Geological Sciences, Brown University

[2]Geology and Geophysics, Woods Hole Oceanographic Institution

For submission to: *Quaternary Science Reviews*

6.1 Abstract

Recent river flooding along the northern Gulf of Mexico coast has frequently forced the evacuation of entire communities and repeatedly destroyed homes and infrastructure, calling attention to the need to better predict and prepare for these events. Expanding flood records beyond the historical period is necessary to understand the mechanisms that drive decadal-scale and longer trends in flood occurrence throughout a range of mean climate states. Riverine flood reconstructions are complicated by the dynamic nature of the river floodplain environment, which results in the erosion of the paleoflood record (e.g. Knox, 1983; 2000) and the erosion and re-deposition of plant macrofossils that are commonly used for obtaining flood chronologies (e.g. Knox, 1993; Goman and Leigh, 2003). We present a new record of riverine flood deposits from northwest Florida during the Holocene in lake sediment archives from Red Bug and Henry Lee ponds. Our record is based on the identification of event deposits in sediment cores from two sites that continually accumulated sediment during the past 9000 years and have dependable ^{14}C chronologies. We identified twenty-five high-magnitude floods, four of which were intense enough to form coarse sediment deposits in Henry Lee Pond, which is insensitive to historical flooding relative to Red Bug Pond. Flood deposits are concentrated between 9000 and 7000 years ago and from 2200 years ago to present, with reduced flood frequency between 5000 and 2200 years ago. Extreme flooding during the Holocene appears to be closely related to climate and sea level-driven changes in regional water table depth, suggesting that the water table depth plays a

significant role in determining whether heavy rainfall will quickly be absorbed into the subsurface or will produce a major flood, consistent with historical relationships between flooding, water balance, and heavy rainfall.

6.2 Introduction

The Gulf of Mexico coast is a densely populated area that is commonly impacted by extreme climate events, in particular hurricanes, floods, and drought. Interannual floods in the Choctawhatchee River floodplain in northwest Florida destroy homes, businesses, and infrastructure despite the presence of engineered levee systems along portions of the river (Advanced Hydrological Prediction Service). Heavy rainfall causes major floods in the wide floodplain of the Choctawhatchee River, often spanning several miles on either side of the river and destroying farm land, homes, and businesses (Walton County Flood Information Reference Guide). Recent floods exceeding three meters above minor flood stage have led the federal government to purchase homes and land in small communities near the river to prevent destruction of property and loss of life, particularly after the devastating flood that was induced by heavy rainfall during Hurricane Alberto in 1994 (Washington County History). The instrumental records of flood history and climate variations are too short to gauge how the frequency of floods varies on decadal and longer timescales or to clearly identify the mechanisms that drive flooding throughout a variety of environmental and climatic conditions. Reconstructing long climate records beyond the instrumental record is essential to our understanding of the cause and timing of such events.

In this study, we reconstructed flooding in the Choctawhatchee River valley in northwest Florida during the Holocene through the identification of flood deposits in sediment cores from two sinkhole lakes in the floodplain (Figure 6.1). Our work is designed to overcome common challenges of flood reconstructions, namely erosive removal of flood deposits from the floodplain and chronology problems caused by erosion and re-deposition of old sediment during floods, by benefiting from sediment preservation in lake basins. We examine two sites in our study, Red Bug Pond and Henry Lee Pond, that are located in the Choctawhatchee River floodplain and have different sensitivities to flooding, to not only construct a history of flooding in northwest Florida, but also to approximate relative flood intensities of the events that we reconstruct.

6.3 Background

6.3.1 Regional climate

Our study site receives 1700 mm of rainfall annually on average, with a wet season from June to September and a secondary wet season in February and March (Table 6.1; Figure 6.2; Vose et al., 1992). Local evaporation rates are highest in the late spring and summer months, exceeding precipitation values in April, May, June, and October (Table 6.1; Figure 6.2; Farnsworth and Thompson, 1982). The average annual precipitation to evaporation ratio (P:E) for our study site is net positive (1.27) and varies significantly depending on the season (Figure 6.2). During the summer wet season, the high evaporation rates roughly balance the moisture delivered from rainfall, and during the spring and fall dry seasons, evaporation exceeds rainfall and causes a net negative moisture flux into the ground. In the winter and early spring secondary wet season, however, precipitation flux is nearly twice the evaporation rate, and the net moisture flux into the ground is positive.

Summer rainfall in northwest Florida is controlled by the delivery of warm, moist air from the Gulf of Mexico when the Intertropical Convergence Zone (ITCZ) migrates north of the equator, and the northeasterly winds shift to southeasterly across the Gulf of Mexico (Climate Prediction Center; Watts and Hansen, 1994; Poore, 2008). The amount of rainfall delivered to our study site during the summer months is affected by Gulf of Mexico sea surface temperatures (SSTs), which are influenced by the Loop Current, a warm surface current that penetrates northward into the Gulf during the summer (Climate Prediction Center; Watts and Hansen, 1994; Poore, 2008). Warmer SSTs correspond to a greater amount of moisture in the atmosphere and higher rainfall amounts in northern Florida (Climate Prediction Center). Tropical storms and hurricanes bring rainfall to our study site, typically from June through November. Winter rainfall in northwest Florida is typically reduced relative to summer rainfall due to a southward shift in the ITCZ, the shift in wind direction from southeasterly to northeasterly, cooler Gulf of Mexico SSTs, less influence of the Loop Current, and decreased convection over the cooler land surface (Climate Prediction Center; Poore, 2008). Anomalous rainfall during late winter and spring occurs as a result of the phase of the El Niño-Southern Oscillation (ENSO), where El Niño events tend cause excess rainfall and La Niña events tend to cause drought between January and March (Climate Prediction Center). Extreme rainfall events capable of inducing flooding in northwest Florida occur during afternoon and evening thunderstorms in the summer, tropical cyclones in the late summer and fall, and winter storm fronts during the late winter and spring (Watts and Hansen, 1994; Walton County Flood Information Reference Guide).

Monthly rainfall averages for our study site were calculated from historical precipitation data from the De Funiak Springs weather station (30.74˚N, 86.07˚W), station number 74778001 in the Global Historical Climate Network, located 30 km northwest of Red Bug Pond (Table 6.1; Vose et al., 1992). The data span 1900 to 2005 with sporadic missing values. Monthly evaporation averages for our study site are derived from a combination of pan evaporation test data and estimated values based upon meteorological data using the Penman equation (Farnsworth and Thompson, 1982). The evaporation rates used in this study are the average of monthly evaporation rates from the three locations that are within 250 km of Red Bug and Henry Lee Ponds: Fairhope, AL; Mobile, AL; and Tallahassee, FL (Table 6.1). The monthly evaporation rates from Fairhope, AL (30.53˚N, 87.92˚W), located 200 km west of our study site, are based on 45 years of pan evaporation measurements (Farnsworth and Thompson, 1982). This station is near the Mobile, AL airport weather station (30.67˚N, 88.25˚W), 230 km west of our study site, where evaporation rates were estimated using the Penman equation based on 15 years of weather data. The third station we used to calculate the average regional evaporation at our study site is located at the Tallahassee, FL airport (30.37˚N, 84.37˚W), 145 km east of our study site, where evaporation was estimated using the Penman equation based on 15 years of weather data.

6.3.2 Local flood history

Historical flood data for this region are from the Bruce-Ebro USGS monitoring station (30.450833°N, 85.898333°W), located 9.5 km downstream from our study sites, where the river elevation is 2 m below that near Red Bug and Henry Lee Ponds. We assumed that flood stages at our study sites are equivalent to two meters above the elevation of the flood stage recorded at the monitoring station, which is consistent with real time river stage data that demonstrate that the differences in river stages between monitoring stations are equivalent to the difference in elevation between those stations (Advanced Hydrologic Prediction Service).

Since 1929, the Choctawhatchee River at the USGS Bruce-Ebro monitoring station has risen above Action Stage (3.05 m above sea level) 85 times (Table 6.2). Of these events, 4 floods crested between 3.96 and 4.27 meters above sea level (m.a.s.l.; Minor Flood Stage), 39 floods crested between 4.27 and 5.03 m.a.s.l. (Moderate Flood Stage), and the water rose above 5.03 m (Major Flood Stage) 32 times (Advanced Hydrological Prediction Service). Historical flooding took place year-round, but the majority (88%) of floods happened between December and May (Figure 6.2). The majority of major floods (81%), those that exceed 5.03 m at the monitoring station, also happened between December and May.

Historical flooding in the Choctawhatchee River valley has resulted from heavy rainfall during a wide range of climate conditions, making floods difficult to predict. Of the 35 tropical cyclones that passed within 100 nautical miles of the study site, four resulted in rainfall that induced flooding, accounting for 4 of the 85 floods that have occurred in the Choctawhatchee River valley since 1929 (Table 6.2; Advanced Hydrological Prediction Service; Tropical Prediction Center). Every El Niño event in the Niño3.4 SST dataset and the Southern Oscillation Index between 1929 and 2010 is associated with at least one flood, and in some cases as many as four flood crests occurred during the winter and spring months of individual El Niño years, accounting for 32 of the 85 floods (38%) in the instrumental flood record (Table 6.2; Advanced Hydrological Prediction Service). Taking into account that El Niño years only occur during 28% of the years between 1929 and 2010, and 38% of the floods occurred during El Niño years, floods are 1.4 times more likely to occur during an El Niño year than a non-El Niño year. However, it should be noted that 22 floods (26%) occurred during La Niña years, which typically cause drier than normal spring and summer seasons in northwest Florida and account for 26% of the years between 1929 and 2010. 30 floods (35%) occurred during "normal" conditions in the tropical Pacific and in the absence of hurricane strikes; these conditions represent 45% of the years between 1929 and 2010 (Table 6.2). Hurricanes and El Niño events together account for 34 of the 85 historically documented floods (40%), yet 60% of the historical floods are not associated with hurricanes or El Niño conditions; other factors in addition to extreme rainfall contribute to flooding. While multiple mechanisms can produce heavy rainfall in northwest Florida and induce river flooding, the infiltration of rainfall during intense precipitation events could play an important role in flood occurrence, where poor infiltration due to a shallower water table and higher soil moisture may reduce the percolation of heavy rainfall into the groundwater and induce flooding. Subsurface moisture balance as the dominant control on the frequency of flooding is supported by the observation that the greatest proportion of historical floods occurs during the winter and early spring months, when precipitation exceeds evaporation and groundwater is likely higher than during the summer and fall seasons, rather than occurring during the summer months when the highest rainfall occurs (Figure 6.2).

6.3.3 Study sites

Our study sites are located on either side of Holmes Creek, a small branch of the Choctawhatchee River that represents 8.5% of the Choctawhatchee River watershed (Figure 6.1; Florida Water Science Center). The drainage area at this point along the Choctawhatchee River system is 11,350 km^2 (Pride, 1958). Red Bug Pond and Henry Lee Pond are likely cover-collapse sinkholes, the most common sinkhole type in northwest Florida, and are separated from the limestone bedrock by greater than 200 meters of siliciclastic sediment (Sinclair and Stewart 1985). Maximum water depths in Red Bug Pond and Henry Lee Pond were 4.4 and 3.7 m, respectively, in 2011.

6.4 Methods

6.4.1 Core collection

We collected two long vibracores from the eastern basin of Red Bug Pond in 3" diameter aluminum barrels. Each core overlaps with a surface drive collected with a piston corer in 3" polycarbonate tubes for better preserved core-top sediments than is accomplished with vibracoring techniques. Core 1 from Red Bug Pond (RBP-Core 1; 30.536150°N, 85.870367°W) was collected in 4.4 m water depth and is 5.2 m in length, and RBP-Core 2 (30.535233°N, 85.870017°W) was collected in 4.1 m water depth and is 5.57 m long (Figure 6.1). We collected a single core from Henry Lee Pond (HLP-Core 1; 30.525150°N, 85.855480°W) using a piston corer and recovered 1.68 m of sediment from 3.7 m water depth (Figure 6.1). The cores were split and macroscopically described following the methods outlined by Schnurrenberger et al. (2003) and are kept in cold storage at the Woods Hole Oceanographic Institution (WHOI).

6.4.2 Surface sample collection

Seventeen surface sediment samples from the sediment-water interface were collected with an Ekman Dredge to characterize sediment properties in Red Bug Pond during normal, non-flood conditions (Figure 6.1). The bulk composition, grain size, and grain shape of these samples were compared with nine terrestrial sediment samples from within 100 m of the lake basin that were collected with a spoon from the surface soil layer just below the leaf litter to differentiate between the sediments derived from typical sedimentation processes to those washed in during periods of high runoff (Figure 6.1). River sediment samples were collected from the shore, shallow water, and mid-channel depths in both the Choctawhatchee River and Holmes Creek upstream from our study sites for the purpose of determining whether the riverine sediments differed in bulk composition, grain size, and grain shape from local catchment sediments to aid in characterizing flood deposits in Red Bug and Henry Lee Ponds.

6.4.3 Age control

The upper 50 cm of the sediment core from Henry Lee Pond and from each surface drive from Red Bug Pond were sampled, dried overnight in a drying oven at 100˚C, and homogenized using a mortar and pestle for gamma counting to obtain ^{210}Pb and ^{137}Cs activities. Sampling resolution for HLP-Core 1, RBP-Core 1, and RBP-Core 2 activity measurements were one, 1 cm-thick sample every 2 cm, 6 cm, and 3 cm, respectively. Ages from ^{210}Pb activities were determined using a linear regression model by calculating the mass accumulation rate of unsupported ^{210}Pb in the sediments and assuming that the sedimentation rate and ^{210}Pb deposition were constant. This approach more accurately predicted the peak in ^{137}Cs to be near its expected age (1963 CE) in both lakes than the constant rate of supply model, for which a more precise measurement of background ^{210}Pb is necessary to accurately determine ages (Figure 6.3; Appleby and Oldfield, 1978; Appleby, 1997). Unsupported ^{210}Pb was calculated by assuming background ^{210}Pb levels were achieved below the depth at which the activity measurements were identical, within error, of all activities below that depth. All activities below this depth were averaged to calculate the background ^{210}Pb activity, which was subtracted from each measurement above to determine the amount of unsupported ^{210}Pb in each measurement.

Radiocarbon ages were obtained at the Woods Hole Oceanographic Institution National Ocean Sciences AMS facility (NOSAMS) on nine plant macrofossils in RBP-Core 1, three plant macrofossils from RBP-Core 2, and five plant macrofossils from the

Henry Lee Pond core (Table 6.3). Plant macrofossils were rinsed and sonicated with filtered deionized water to clean sediment from each sample and were pretreated at NOSAMS. All radiocarbon ages were calibrated using the IntCal09 model in the Calib 6.0 program (Stuiver and Reimer, 1993; Stuiver et al., 2005) to years before present (B.P.) where "present" is defined as the year 1950 C.E.

6.4.4 Laboratory analyses

All cores were imaged on a GeoTek corescanner at Brown University and analyzed for elemental abundances and radiographic images on an Itrax corescanner at WHOI. Cores were scanned on the Itrax at 1 mm increments with a 10 s dwell time and radiographic images were obtained at 200 micron increments with a 0.4 s dwell time. Each core was sampled at continuous 1 cm increments; samples were dried overnight in a drying oven and burned at 550˚C in a muffle furnace for 4 hours to determine the mass lost on ignition (LOI; Dean, 1974). All burned samples were wet-sieved at 32 and 63 microns to determine the portion of dry bulk sediment that was larger than coarse silt and fine sand, respectively. Surface samples were analyzed in the same manner to determine % LOI, % >32 microns (coarse silt and sand), and % >63 microns (% sand). Elemental abundances for each surface sample were measured using an INNOV-X systems Alpha 4000 handheld XRF analyzer with a 90 s dwell time.

6.4.5 Spatial analyses and instrumental data

Elevation data used to compare site elevations and the surrounding topography were obtained using a combination of orthoimagery collected in 2004 at 50 cm pixel resolution and light detection and ranging (Lidar) elevation data collected in 2007 at 10 cm resolution provided by the United States Geological Survey (DOC et al., 2006; NWFWMD, 2013). The elevation uncertainty for the 2007 Lidar dataset is 13 cm. Elevation profiles at the point of entry of flood waters to each pond, defined as the lowest elevation pathway between the river channel and each lake, were extracted from the datasets using ArcMap 10.

6.5 Results

6.5.1 Age models

Surface sedimentation rates determined by the ^{210}Pb models in RBP-Core 1 and 2 were 0.47 and 0.40 cm/yr, respectively (Figure 6.3). These sedimentation rates align well with the expected timing of the peak in ^{137}Cs (Figure 6.3), which should correspond to the maximum atmospheric ^{137}Cs concentration during heightened nuclear weapons testing in 1963 CE. No clear peak in ^{137}Cs is observable in Core 2, likely due to diffusion of ^{137}Cs in the sediments, however the ^{210}Pb-based sedimentation rate approximates that 1963 CE occurred at 18.9 cm, which falls within the cluster of the highest activities observed in the ^{137}Cs profile and adds confidence to our ^{210}Pb-based age prediction (Figure 6.3). The independent sedimentation rates in Core 1 and Core 2 are nearly identical, so we argue that the ^{210}Pb-based sedimentation rates credible. In Henry Lee

Pond, the surface sedimentation rate determined from the ^{210}Pb model is 0.3 cm/year, slightly lower but very similar to the modern Red Bug Pond sedimentation rate. This rate predicts that the 1963 CE should occur at 14 cm depth, which aligns well with the peak in ^{137}Cs activity (Figure 6.3).

Age control extending from the instrumental period through the early Holocene for the records from both sites is based on linear interpolation between ^{14}C ages in each core (Figure 6.4). The ^{14}C age at 105 cm depth in RBP-Core 1 was ~100 years older than the age at 150 cm depth. Since it is much more likely that old plant material was deposited amongst younger sediments at 105 cm depth than for young material to be reworked through ~ 1 m of sediment, we have excluded the exceptionally older ^{14}C age at 105 cm in RBP-Core 1 from the age model. The sedimentation rate changes considerably in RBP-Core 1, from 0.04 cm/yr across a coarse-rich section (see below) to 0.01 cm/yr after a transition from sandy to organic-rich sediments. After 2100 B.P., the sedimentation rate gradually increases through time, reaching 0.47 cm/yr in the last century. In RBP-Core 2, the basal age is >48,000 years B.P., and the first sample that provided a ^{14}C age occurred during the early Holocene at 1.6 m. The sedimentation rate from 1.6 to 0.7 m was 0.03 cm/yr and rose abruptly to 0.4 cm/yr from 0.51 m to the core top, revealing a considerable age gap in the upper meter of the core. In Henry Lee Pond, the sedimentation rate gradually increases through time from 0.02 cm/yr to 0.3 cm/yr.

6.5.2 Surface sample analyses

The samples collected from the Red Bug Pond catchment are low in organic matter, with LOI values averaging 8.6 +/- 6.8%, and very coarse, averaging 58.8 +/- 31.4% sand (Figure 6.5). Samples collected from the sediment-water interface in Red Bug Pond are much higher in organic matter, with LOI values averaging 62.6 +/- 17.5%, and much lower in coarse content, averaging 8.2 +/- 17.5% sand. One sediment-water interface sample had a very high sand content much like the catchment values; this sample was collected 20 m from shore on the northeast side of the pond near a gravel road on private property. We did not detect distinctive differences in elemental abundances, grain shape, or lithology between the catchment sand and the river sand samples; each of these samples consisted of sub-rounded quartz grains. Based on our analyses, there is no clear way to chemically or physically differentiate sand deposits from a river source versus a very local catchment source.

6.5.3 Sediment core descriptions and relative proportions of major components

The cores from Red Bug and Henry Lee Ponds exhibit substantial changes in sediment type, with similar sequences at both study sites. The base of RBP-Core 1is dominated by peat with macroscopic roots, stems and leaves (Figure 6.6). The peat bed is 75% organic material, based on LOI values (Dean, 1974), and is punctuated by eight 1- to 7-cm-thick sand beds containing between two- and five-fold increases in the proportion of sand, which occur at 8740, 8700, 7990, 7880, 7710, 7680, 7650, and 7580 B.P. (Figure 6.7). The peat in RBP-Core 1 is truncated by an abrupt transition to a greater than 1-m-thick section of very coarse inorganic sediment at 7500 B.P., marked by a transition in the sand content from 2% to 77% (Figures 6.6; 6.7). The sand content varies markedly for 2500 years, reaching broad minima from 7100 to 6770 B.P. and from 6200 to 5540 B.P. Above the sand beds is a gradational transition to very fine organic-rich silt that extends to the core-top, which is dominated by very fine organic-rich silt, with 58% average organic content between 4000 and 2000 B.P. followed by a step-wise increase to about 67% organic matter at 2000 B.P. This upper sapropel-dominated section contains eight prominent 0.25-cm- to 2-cm-thick beds characterized by abrupt, temporary decreases in organic content, and increases in coarse silt and sand content of between 8% and 40%, occurring at approximately 4890, 2180, 1420, 900, 480, 440, 25 and 12 B.P. Additionally, this core contains several smaller amplitude abrupt, temporary rises in sand content. We do not see evidence for hiatuses in the core stratigraphy of RBP-Core 1 (e.g. erosional lithologic contacts, oxidation of the sediments, sharp sedimentation rate changes), suggesting that the RBP-Core 1 location was subaqueous throughout the entire Holocene (Figures 6.6; 6.7).

In Core 2 from Red Bug Pond (RBP-Core 2) the basal sediments are 14.7% organic matter and contain a relatively high amount of sand compared to the base of RBP-Core 1 (18.6%; Figure 6.7). Below a sharp erosional contact at 302 cm, the basal sediments in RBP-Core 2 gradually transition from mainly peat to dominantly very coarse inorganic clayey sand. Above 302 cm, the sediments abruptly transition to pure, very coarse quartz sand (Figures 6.6; 6.7). The sharp nature of the erosional contact suggests that there is a depositional hiatus associated with the facies change. Below 302 cm depth, a sample at the base of the core is too old to be dated with ^{14}C techniques (Table 6.3); we interpret the age information and lithological relationships as indicating that all sediments in the core deeper than 302 cm were deposited before the Holocene. A ^{14}C age ranging from 8389 to 8542 B.P. was sampled from peat-dominated sediment characterized by 80% organic matter above the pure sand bed at 158.2 cm. The lack of evidence for a depositional hiatus above 302 cm (e.g. sharp transition in sediment lithology, chemistry, sedimentation rate) led us to interpret that the upper three meters of sediment in RBP-Core 2 were deposited continuously, so we extrapolated the sedimentation rate from the two ^{14}C ages in the organic-rich portion of the core back through 302 cm (Figure 6.4). At 5600 B.P., the organic-rich, peaty sediments transition to a bed with less organic matter (55%) and a 20% increase in the sand content. Just above this transition, there are nearly 5000 yrs missing between the uppermost ^{14}C date and the lowermost ^{210}Pb date, which are only 20 cm apart (Figure 6.4). The upper ^{210}Pb-dated section of the core is dominated by very fine organic-rich silt with slightly lower organic content (66%). In this section there are eight event beds characterized by a rise in sand content between 3 and 7% higher than the value below it centered at 1922, 1928, 1936, 1942, 1944, 1966, 1975, 1985 and 2004 CE (Figure 6.9). Two of these events overlap in timing with rises in sand content in RBP-Core 1, centered at 1925 and 1937 CE.

The Henry Lee Pond stratigraphy is similar to the cores from Red Bug Pond (Figure 6.6). The bottom of the core (7700 to 5000 B.P.) is dominantly peat with 93% organic matter, with the exception of a 3 cm-thick sand bed at 5470 B.P. reaching 19% sand (Figure 6.7). The peat is truncated by a roughly 60 cm-thick sand bed averaging 27% sand at 5000 B.P., which gradually transitions back to peat by 2200 B.P. The peat gradually transitions to very fine organic-rich silt by 66 B.P. (1884 CE) and is characterized by 53% organic matter with sand composing less than 0.5% of the sediments. There are no beds characterized by higher sand in the recent century like those observed in the Red Bug Pond cores.

6.6 Discussion

6.6.1 Holocene lake history

The coarse sediments prior to 9800 years B.P. in the core from Red Bug Pond that was collected in shallower water (RBP-Core 2) indicate that location was a high energy environment during the early Holocene, possibly associated with shoreline wave action (Figure 6.6; Dearing, 1997). These data suggest lake level was lower between 13,000 and 9800 B.P. than at present (Dearing, 1997). Between 9800 and 8900 B.P., sediments in RBP-Core 2 gradually transitioned to fine-grained, organic-rich sediments, suggesting that lake level rose relative to 13,000 B.P.

The core collected from deeper water (RBP-Core 1) was dominated by peat made up of coarse roots, stems and leaves between 8700 and 7500 B.P., which is indicative of an environment with little turbidity where plenty of sunlight reached the sediments and allowed for widespread growth of macrophytes. RBP-Core 1 lacks widespread rooted plant growth today, which could indicate that the lake was shallower than today to allow sufficient sunlight to reach the bottom and support plant growth, or it could imply that the water was clearer and light penetration was deeper in the early to mid-Holocene than it is currently. The latter explanation is supported by regional pollen data indicating that cypress swamps and evergreen shrub bogs known to contribute to brown water in lakes became significantly more abundant during the late Holocene (Watts, 1971), though no local pollen reconstructions exist near enough to our site to verify that the regional vegetation changes are also expressed locally. The lack of coarse sediment in RBP-Core 1 between 8700 and 7500 B.P., implying this site was far enough from the sand-rich shoreline that it accumulated very little sand or coarse silt, and the introduction of cypress swamps and bogs in the late Holocene at the expense of dry oak forests and prairies support the first explanation - that local moisture increased throughout the Holocene (Watts, 1969; Watts, 1971; Watts, 1975; Grimm et al., 1993; Watts and Hansen, 1994).

The Red Bug Pond and Henry Lee Pond core stratigraphies suggest there have been multiple pulses of sinkhole activity in the early- to mid-Holocene followed by lake level fluctuations in the mid- to late-Holocene in northwest Florida throughout the Holocene. High sand content in RBP-Core 1 from 7400 to 5600 B.P. occurred while the coarse fraction in RBP-Core 2 and HLP-Core 1 remained near 3% and 1.3%, respectively. RBP-Core 2 is in slightly shallower water than RBP-Core 1, so if a decrease in lake level and an approaching shoreline increased the wave energy and caused sand deposition in RBP-Core 1 during the early Holocene, we expect sedimentation at RBP-Core 2 would be affected at the same time if not slightly earlier. Multiple sinkholes have been recently active within 7 km of Red Bug Pond (Sinkholes of Washington County Map, 2008), so it is possible that major grain size variations in Red Bug Pond sediments between 7400 and 5600 B.P. could be attributed to sinkhole activity in the vicinity rather than water table changes. In this scenario, the sand deposition in RBP-Core 1 was caused by slope failure due to a catastrophic sinkhole collapse, which is common in this region (Sinclair and Stewart, 1985), causing a sudden steepening and destabilization of the basin walls and delivering large amounts of unconsolidated sediment from the catchment into the center of the basin. Slumping of unconsolidated sand into lake basins during sinkhole collapse has been documented in several northern Florida lakes (Kindinger et al., 2001). Following the initial sinkhole collapse, sand may continuously be transported from the basin walls to the basin center for a period of time resulting from the steep gradient of the newly deepened basin. Based on the lithologic data from RBP-Core 1, there may have been several episodes of sinkhole activity in Red Bug Pond during the early- to mid-Holocene.

It is unlikely that major slope failure and sand deposition occurring at RBP-Core 1, raising sand content in the core by 80% during the first event and 40% during the second, does not coincide with a sedimentation change at RBP-Core 2, which is just 100 m away. If the north and south ends of Red Bug Pond were isolated from one another in the early Holocene such that RBP-Core 1 and RBP-Core 2 were separated into two different sub-basins, then the two sites may respond differently to environmental changes. Basin isolation could explain why sediment deposition in RBP-Core 2 was unaffected by sinkhole activity and continued to support an aquatic plant-rich environment until at least 5600 B.P. Sinkhole collapses within lake basins that only impact a portion of the lake basin, isolating smaller basins within the larger lake basin have been documented in northern Florida lakes (Kindinger et al., 2001). The sub-basins in Red Bug Pond are currently connected by surface water, implying that the water table was lower between 7400 and 5600 B.P. than it is today such that the north and south ends of the lake were not connected by surface water. The water table depth variations may have been driven by sea level rise; sea level was between 11 and 4 meters below modern sea level during the early and mid-Holocene (Törnqvist et al., 2004).

Red Bug Pond and Henry Lee Pond sediments are indicative of a shallow water environment beginning circa 5600 B.P., suggesting northwest Florida was drier than today during the mid-Holocene. At 5600 B.P., sand content in both cores from Red Bug Pond increased simultaneously and culminated in a depositional hiatus in RBP-Core 2 at 5400 B.P. Sand content in the Henry Lee Pond core began increasing around 5000 B.P. The sand content in both lakes during the mid-Holocene was between 3 and 7 times higher than in the core-top sediments despite the abundance of sand on the modern landscape, and the core-top sediments contain high amounts of very fine-grained organic matter that can only be deposited under low energy conditions (Dearing, 1997). We interpret the rise in sand content in both lakes as decreases in lake level resulting in greater influence of wave base energy that ultimately resulted in erosion at RBP-Core 2 (Digerfeldt, 1986; Dearing, 1997). The later rise in sand content in HLP-Core 1 indicates either that the core location was in deeper water and further from the shoreline than the cores in Red Bug Pond, or that Henry Lee Pond is less sensitive to moisture balance changes than Red Bug Pond.

Alternatively, the same 5000 yr-long hiatus in RBP-Core 2 could have occurred in the absence of a lake level decline in the mid-Holocene if sediments were deposited continually at both core locations and subsequently eroded away at the RBP-Core 2 site by a large erosive flood or a severe decline in lake level (Digerfeldt, 1986) during the early 20th century. There is no evidence in local precipitation data for such a severe drought during the early 20th century (Vose et al., 1992), and lithologic data from RBP-

Core 1 and HLP-Core 1 lack evidence for a recent lowstand. The greatest historical flood in 1929 CE (21 B.P.) could have removed 5000 years of the sediment record, however we find it unlikely that 1.5 m of sediment could be eroded from the RBP-Core 2 site without influencing sedimentation at the RBP-Core 1 site just 100 m away. The peat below the hiatus is reddish brown and appears more oxidized than the dark brown peat identified elsewhere in the Red Bug Pond cores, suggesting that the peat was sub-aerially exposed and supporting our inference that this hiatus was caused by a mid-Holocene lake lowstand. The mid-Holocene decreases in Red Bug Pond and Henry Lee Pond lake levels occurred despite continuous sea-level rise (Törnqvist et al., 2004), which should have raised the water table and corresponded to a rise in lake level in the absence of a climatic influence, indicating that a drying of the local climate likely contributed to the lake-level changes during the mid-Holocene. Sinkhole activity can be initiated in response to declining groundwater levels (Kindinger et al., 2001; Southwest Florida Water Management District), which could suggest that the climate in northwest Florida began drying during the early- to mid-Holocene prior to the inferred lake level decline at 5000 B.P.

We assume sedimentation at the RBP-Core 1site was continuous through the drought and into the late Holocene from the lack of evidence for a depositional hiatus. The transition from sand-rich to peat-rich to very fine grained organic-rich silt in RBP-Core 1after 5000 B.P. and in HLP-Core 1 after 4500 B.P. is characteristic of increasing water depth (Figure 6.7), as deeper water reduces the influence of wave energy and allows for deposition of finer sediments. Increasing lake levels in the late Holocene may relate to a transition to a wetter climate and/or a rising water table related to sea–level rise. We conclude based on these observations that the lake level in Red Bug Pond is currently deeper than it was during the mid-Holocene.

The deep water table between 7400 and 5600 B.P. and the lower lake levels and drier climate after 5000 B.P. inferred from our reconstructions from both Red Bug and Henry Lee Ponds, followed by higher lake-levels from the late-Holocene into the present, is consistent with previous moisture reconstructions that are based upon pollen studies in Florida and southern Georgia and Alabama (Watts, 1969; Watts, 1971; Watts, 1975; Grimm et al., 1993; Watts and Hansen, 1994). Many sites included in these studies (e.g. Lake Louise and Mud Lake) exhibit a hiatus in the very early Holocene and do not begin deposition until after 8500 B.P., suggesting the Pleistocene-Holocene transition was either climatically drier than today, the water table was significantly lower due to a lower relative sea level, or a combination of the two (Watts, 1969; 1971). Moisture gradually increased during the Early Holocene, raising water levels to the point where deposition began at these sites (Watts, 1969; 1971). These observations are consistent with our interpretation that the Red Bug Pond lake level was significantly lower than today before 9800 B.P. and rose over the next millennium based on transition from high sand content or fine-grained organic-rich silt in RBP-Core 2.

The southeastern U.S. pollen reconstructions showed a high abundance of Quercus pollen along with pollen from grasses until the mid-Holocene, suggesting that the vegetation on the landscape was dominantly a dry oak forest with prairie openings due to either a drier climate than today that lasted until the mid-Holocene, or due to a deeper water table resulting from lower sea level. The inferred basin isolation within Red Bug Pond between 7400 and 5600 B.P. supports these pollen data that suggest the water table was lower. Our record also provides new evidence for climatic controls on mid-Holocene dryness in northern Florida, since lake level in both Red Bug Pond and Henry Lee Pond declined during the mid-Holocene and resulted in a depositional hiatus in RBP-Core 2 while sea level was rising (Törnqvist et al., 2004). The pollen records indicate that the southeastern U.S. transitioned to a pine forest with the introduction of cypress swamps and bayheads after 5000 B.P. (uncalibrated ^{14}C years; Watts, 1971), indicative of a shoaling water table either due to sea-level rise following the collapse of the Laurentide Ice Sheet (LIS), a transition to a wetter climate, or a combination of the two. Our interpretation that the lake level in Red Bug Pond and Henry Lee Pond increased circa 4500 B.P. and gradually increased through the late Holocene is consistent with these observations, though this evidence for lake-level rise occurs ~1000 years after the onset of pine forestation.

A transition to a wetter climate in the early Holocene followed by mid-Holocene drought, inferred from lake level reconstructions and pollen-based vegetation changes, has also been observed in the northeast United States (Shuman et al., 2001; Newby et al., 2000; Shuman et al., 2005; Shuman and Donnelly, 2006; Shuman et al., 2009). Shuman et al. (2002) hypothesized that the early Holocene increase in moisture in both the northeast and southeast United States may have been driven by the combined effects of insolation and changes in the size and position of the Laurentide Ice Sheet (LIS). While higher insolation during the early Holocene would have resulted in higher temperatures, increasing evapotranspiration in northwest Florida during the summer season, the presence of the LIS would have weakened the effects of the rising temperature on strengthening the land-sea temperature gradient due to its high albedo and the anticyclone along its southern edge. The presence of the LIS would have dampened the strength of the summer monsoon, which is vital for delivering moisture from the Gulf of Mexico to the continental interior, resulting in a net negative moisture balance during the early Holocene. Following the collapse of the LIS circa 8200 B.P., the diminishing anticyclone would have allowed the summer monsoon to strengthen in response to the increased heating of the continental interior that would follow the drop in albedo and the increased influence of the Bermuda High. The stronger summer monsoon would have drawn moisture from the Gulf of Mexico northward to the continental interior, bringing moisture to both the southeast and northeast United States after 8000 B.P. We hypothesize that this scenario could have caused the lake level rise between 9800 and 8900 B.P. that we inferred in our Red Bug Pond paleohydrology reconstruction.

Shuman and Donnelly (2006) proposed a scenario that could explain mid-Holocene drought in the northeastern United States involving precipitation seasonality changes. As summer insolation waned in the mid-Holocene, the Bermuda subtropical high would have weakened, reducing northward transport of subtropical moisture during the summer relative to just after the collapse of the LIS circa 8000 B.P. This would result in drier conditions not only in the northeast, but also in the southeast United States where modern summer moisture is sourced from the Gulf of Mexico during the summer monsoon. Shuman and Donnelly (2006) suggest one explanation for increasing moisture circa 3000 B.P. in the northeast United States could be the increasing influence of winter precipitation, as winter insolation increased during the late Holocene, likely increasing temperature and precipitation as well. While this is only one possible scenario for explaining moisture trends in the northeast United States, the trends in our paleohydrology reconstruction are consistent with the mechanisms suggested for the Holocene moisture trends.

6.6.2 Historical flood records

6.6.2.1 Evidence for anthropogenic influence on sedimentation and flood susceptibility

In order to accurately assess how floods of various magnitudes are represented in the sediment cores based on the comparison of historical floods to the lake sediment records, it is necessary to consider the effects of drastic changes to the landscape, such as land clearance, on sedimentation in the lakes. We examined the history of land clearance and road construction adjacent to our sites and compared that to geochemical data corresponding to known anthropogenic activities to assess whether the character of flood deposits may have been altered in the recent portion of the sedimentary record.

Aerial photos of the area reveal that the gravel road trending southwest-northeast ~40 m of the southeast shore Red Bug Pond and the gravel road running southwest-northeast ~35 m on the northwest edge of Henry Lee Pond were constructed between April 9, 1951 and May 31, 1966. Land to the north of Red Bug Pond was cleared in the time interval between these photographs, and additional clearing took place along its north and west shores between May 31, 1966 and January 23, 1976. The land clearance and road construction around Red Bug Pond in the 1950s, 1960s and 1970s coincides with a sharp rise in terrestrial input in the sediment cores as suggested by XRF-derived

Fe and Ti abundances in RBP-Core 1 (Figure 6.8), a measurement commonly used to approximate clastic inputs (e.g. Peterson et al., 2000). The relationship between Ti and Fe and known landscape activities suggests these elements are good indicators of terrigenous inputs at this site and can be used to infer periods of land disturbance in the catchment when aerial imagery is not available. The gravel brought in for road maintenance and periodic grading of the road on the unstable, artificial slope on which the road was built may result in the delivery of inorganic material to both coring locations in Red Bug Pond. In RBP-Core 2, which is proximal to the gravel road, sand content is low during initial landscape clearance and road construction but rises in the last two decades when Ti and Fe data suggest landscape alterations intensified. The rise in sand content does not occur in RBP-Core 1, which is distal from the road, making it unlikely that during non-flood, low energy conditions, sand from the southeast corner of the lake would be reworked and deposited at that site. Runoff of road material during heavy rainfall or road maintenance is the likely source of the sand in the upper portion of RBP-Core 2. High Fe and Ti counts in RBP-Core 1 could indicate that very fine inorganic sediment from the road is occasionally delivered to that core site, which is more easily transported than large sand grains.

Prior to the 1950s, average Fe and Ti counts in Red Bug Pond remained low for several centuries, suggesting the catchment landscape was relatively stable and landscape alteration was minimal (Figure 6.8). The earliest available aerial photo from March 1, 1947 indicates the land surrounding Henry Lee Pond was deforested prior to this time, but the exact date of land clearance in uncertain. Since documentation of human-induced land clearance around Henry Lee Pond is scarce, we use the same elemental indicators that we used in Red Bug Pond to approximate catchment land stability and determined that the land surrounding the lake was cleared in the late 1890's when both Fe and Ti rise markedly relative to the previous 7600 years (Figure 6.8). Our inference that land clearance occurred in the late 1800's aligns in timing with widespread deforestation that occurred elsewhere in Washington County, when the timber industry expanded following the construction of the railroad in 1881 (Washington County History). We expect that landscape alterations influence how sediment is transported within the catchment during floods, both through destabilizing the landscape during deforestation and agricultural practices and by unnaturally stabilizing the landscape through planting of crop vegetation. Therefore, we characterized flood deposits in our sediment cores for our paleoflood reconstruction by more closely examining the historical flood record prior to 1950 and compared that with sedimentation in the Red Bug Pond sediment cores.

6.6.2.2 Modern susceptibility of sites to flooding

We used Lidar elevation data to identify the lowest elevation pathway between Holmes Creek and our study sites to estimate the elevation of the minimum flood stage that could affect sedimentation at our study sites. Red Bug Pond is situated at 7.05 m.a.s.l., and is separated from the river by higher elevation that reaches 15.5 m.a.s.l. on the northwest side of the lake (D.O.C., 2006; Figure 6.1). The southeast corner of Red Bug Pond is connected to Holmes Creek by a sub-aerial channel that gradually increases in elevation from the river to the lake until it reaches 9.3 m.a.s.l. (Figure 6.1; D.O.C., 2006). Given the current elevation of Holmes Creek, 4.23 m.a.s.l., a flood stage would need to exceed 5.07 m from its average stage, corresponding to a flood stage of 8.07 m at the Bruce-Ebro USGS monitoring station, for flood waters from Holmes Creek containing suspended sediment to reach Red Bug Pond. Two floods of this magnitude happened historically, occurring in 1929 and 1994 (Table 6.2; Advanced Hydrological Prediction Service). The elevation across this valley was artificially raised during the construction of the gravel road, which elevated the barrier between Holmes Creek and Red Bug Pond to its current elevation of 9.3 m and likely made this site less sensitive to flood impacts during the last 60 years. To approximate the flood stage needed to reach the elevation of Red Bug Pond prior to road construction, we estimated the elevation of the channel prior to the road construction using Lidar data collected between Red Bug Pond and Holmes Creek based on our visual field observations that the road was artificially elevated ~2 m above a relatively flat area. We assumed that the elevation plateau averaging 7.09 m.a.s.l. in the Lidar-based elevation profile shown in Figure 6.1 is the natural barrier separating Red Bug Pond from Holmes Creek, and the steep-sided topographic high rising 2.21 m above this elevation plateau is an artificial addition to the elevation across the valley (Figure 6.1; NWFWMD, 2013). Prior to road construction in the mid 20th century, floodwaters needed to exceed only 2.86 m above the normal stage to reach Red Bug Pond in the absence of the steeply-sloping mound on which the road was constructed. Based upon flood crest data from the nearby monitoring station, at least eleven floods have exceeded 2.86 m from normal stage since 1929, corresponding to a flood stage of 5.86 m at the Bruce-Ebro USGS monitoring station (Table 6.2; Advanced Hydrological Prediction Service).

Henry Lee Pond is situated at an elevation of 5 m.a.s.l. and is connected to Holmes Creek by a small channel that increases in elevation from the river to the west side of the lake until it reaches 8.3 m.a.s.l., about 4.07 m above the river elevation (DOC et al., 2006; Figure 6.1). Based on our elevation data, the flood stage must exceed at least 4.07 m above Holmes Creek, corresponding to 7.07 m at the Bruce-Ebro USGS monitoring station, in order for flood waters to reach Henry Lee Pond. Flood stages reaching this elevation occurred during the same two floods that were high enough to reach Red Bug Pond in 1929 and 1994 (Table 6.2; Advanced Hydrological Prediction Service). The road constructed in the channel between the Holmes Creek and Henry Lee Pond may have added up to 0.5 m of elevation; using the same reasoning as for Red Bug Pond, the natural barrier separating the lake from Holmes Creek is at an elevation of just under 8 m.a.s.l., which is consistent with our field observations that the road at this site was not as elevated from the natural land surface as at Red Bug Pond (Figure 6.1). Two floods in addition to the 1929 and 1994 events exceeded 3.57 m above Holmes Creek, which corresponds to a stage of 6.89 m at the Bruce-Ebro USGS monitoring station, occurring in 1990 and 1998. Both of these events occurred after the road was constructed, and therefore we do not expect that they were large enough to impact sedimentation in Henry Lee Pond.

6.6.2.3 Flood signature in the Red Bug Pond sedimentary record

The modern sedimentation rate in Red Bug Pond is not high enough to resolve multiple floods occurring in the same year or interannually, given that event deposits are between 0.25 and 2 cm thick, yet only 0.4 cm of sediment accumulates over the course of an entire year on average. Single sand beds in Red Bug Pond sediments may therefore represent either one or several floods. For example, major historical floods occurred in 1937 and 1939 CE in the Holmes Creek valley and should have been large enough to form flood deposits in Red Bug Pond, but these two floods only coincide with a single sand bed in RBP-Core 1 that spans ~1935-1940 CE. For this reason, our flood reconstruction is likely missing some of the events that were large enough to deposit sand at our site, underestimating the true number of major floods over the Holocene. Eleven historical flood stages that were high enough to reach Red Bug Pond and potentially influence sedimentation in the lake occurred in 1929, 1937, 1939, 1960, 1975, 1978, 1990, 1994, twice in 1998, and 2009 (Figure 6.9). The floods occurring in 1929, 1937, and 1939 are associated with increases in the coarse silt and sand contents and a decrease in the percent organic matter in RBP-Core 1 within the ^{210}Pb age uncertainty (Figure 6.9). For each of these events, the fraction of sand relative to silt decreases throughout the event, indicating a fining upward trend for each deposit. This relationship is based only on 2-3 data points but could suggest a decrease in depositional energy throughout each deposit that is characteristic of the energy dissipation from high sand transport during peak flood intensity to fine-grained deposition in a still lake environment. The 1960 flood is associated with a minor increase in sand content that is not confidently distinguishable from background noise. Minor increases in Ti abundance accompany the grain size anomalies, but these variations are less than 50 counts and are not distinctly above background variations. No change in Fe content is observed in these event layers.

Historical flooding before 1950 resulted in increases in sand content and decreases in organic matter of twice the magnitude in Core 2 as was observed in Core 1 (Figure 6.9). This evidence could also suggest that the source of the flood deposits is the channel at the southeast corner of Red Bug Pond that we identified using the Lidar elevation data, which is closer to the Core 2 location (Figure 6.1). Sand pulses caused by land clearance would more likely happen on the northern edge of the lake, where the satellite imagery indicates most of the land clearance has occurred, which would result in greater sand content in the more proximal Core 1 than in Core 2. Sand could be deposited at both sites as a result of lake lowstands rather than flooding, but the coarse deposits we identified between 1929 and 1960 actually occurred during years with exceedingly higher than normal rainfall (Vose et al., 1992), so we assume these deposits are diagnostic of flooding.

We infer based on elevation data and satellite imagery that Red Bug Pond became significantly less susceptible to river floods after the 1950s-1960s following the construction of the road. After the 1950s the signature of flood deposits in the sediments is muted. Five floods after the 1950s were between 0.5 and 2 m higher and in some cases had higher flow velocities than the late 1930s floods that produced diagnostic flood deposits in Red Bug Pond sediment cores, yet these later events are not associated with changes in grain size in RBP-Core 1 (Figure 6.9). For example, the recent flood in April, 2009 reached an elevation of 6.25 m and had a maximum discharge of 77,100 cubic feet per second but is not associated with a sand bed in our sediment core, while a comparable flood occurring in August, 1939 reached an elevation of 6.28 m with a maximum discharge of 69,000 cubic feet per second coincides with a sand bed in RBP-Core 1

(Figure 6.9; Pride, 1958; Advanced Hydrological Prediction Service). While individual floods are not distinguishable in the grain size data after 1950, the substantially higher sand content in RBP-Core 2 and the higher Ti and Fe in RBP-Core 1 after the mid 1980s could be associated with the high number of floods in the late 1980s and the 1990s. The broad peaks in Ti and Fe in these upper sediments in RBP-Core 1 were measured at 10 times the resolution of the grain size data, suggesting that the sampling resolution was not so low that the signal of individual floods blended into broad, decadal-scale increases in the grain size data, rather bioturbation in the surface sediments likely smeared the flood signal across several centimeters in the upper sediments. Alternatively, as suggested by the elevation data, flooding did not affect deposition in Red Bug Pond after the road was constructed, and the higher sand content in Core 2 and increased Ti and Fe in Core 1 are were caused by a different process, such as maintenance of the gravel road on the southeast corner of the lake.

6.6.2.4 Comparison between Red Bug and Henry Lee Ponds

Including two sites in our study provides a unique opportunity to utilize the different sensitivities of these sites to flooding as an indicator of flood magnitude in the past. Neither historical flood that exceeded the elevation of Henry Lee Pond, occurring in 1994 and 1929, resulted in a change in sand content or organic matter content in the sediment core (HLP-Core 1; Figure 6.9). Clearly, Henry Lee Pond is less sensitive to flooding than Red Bug Pond, and the lack of a flood signature in this site during major historical flooding suggests there are factors other than the additional meter of elevation that make this site less sensitive to flooding.

The Henry Lee Pond core does not have diagnostic changes in lithology during the historical floods that we expect should impact sedimentation at that study site. The most likely reasons for this are that water velocity is too low to transport sand into either lake during floods, water discharge during extreme flooding is not energetic enough to transport sediment only at the Henry Lee Pond site, or the sediment availability differs between the two sites. It is possible that even when the flood stage is high enough to reach the elevation of our study sites, the water velocity is too low to mobilize and transport sand into the lakes, meaning that flooding does not impact sedimentation at either Red Bug or Henry Lee Ponds. Additionally, floods documented at the USGS monitoring station in the Choctawhatchee River just downstream from our study sites do not necessarily correspond to flooding in Holmes Creek at our study sites, especially if the flood is a result of heavy rainfall in southern Alabama, outside of the Holmes Creek watershed. Our study sites are close to the confluence of the massive Choctawhatchee River and Holmes Creek, thus we anticipate that floods in the Choctawhatchee River valley caused by heavy rainfall outside of the Holmes Creek watershed can affect our study sites by backing up the drainage of Holmes Creek at the confluence of the two rivers, less than 1 km south of our study sites. However, it may be the case that flooding documented at the Bruce-Ebro USGS monitoring station does not impact sedimentation at either study site. The deposits we observe in Red Bug Pond sediments at the same time as extremely high historical floods would then need to be caused by a process that is unrelated to river discharge. Heavy rainfall may produce excessive runoff in the Red

Bug Pond catchment that transports coarse sediments into the center of the basin while also increasing surface flow and causing flooding in the Choctawhatchee River valley, but very low relief of this region is unfavorable for transporting coarse sediment. Furthermore, if these deposits are due to rainfall-driven runoff rather than river water transportation, then we expect that coarse-grained deposits should occur in the nearby Henry Lee Pond as well. The slope of the catchment at Henry Lee Pond is slightly steeper than at Red Bug Pond, so coarse runoff deposits are more likely to occur at this site than at Red Bug Pond and should be present in HLP-Core 1 if they are present in RBP-Core 1 (Figure 6.1).

A more likely explanation for the absence of historical sand deposits in Henry Lee Pond is that the surface morphology impacts the geometry of currents and flow velocities during flooding in Holmes Creek, allowing for mobilization of sediments into the Red Bug Pond basin but limiting flow velocities adjacent to Henry Lee Pond such that they are not energetic enough to mobilize sediments at that site. To speculate further, the topography between Red Bug Pond and Holmes Creek has little change in relief, whereas at Henry Lee Pond there are multiple variations in relief between it and Holmes Creek, which could reduce the velocity of the floodwaters before they enter Henry Lee Pond (Figure 6.1). Another factor that could conceivably result in an absence of deposits in Henry Lee Pond during flooding is a difference in sediment availability between the two sites, which depends on the surface geology of the region. Red Bug Pond is situated in the Miocene Alum Bluff Group that consists of unconsolidated sands and clays, while Henry Lee Pond is on the border between the Alum Bluff Group and the Pliocene-aged Citronelle Formation that consists of unconsolidated gravel, sand, silt, and clay (Scott et al., 2001). Both of these formations should contain abundant coarse sediment for high velocity floodwaters to mobilize and transport into both basins, but heterogeneity within these units and their surface exposures could result in more sand availability at Red Bug Pond but more clay or gravel exposed in the Henry Lee Pond catchment. Gravel would potentially be too coarse for flood velocities to mobilize and clays would not affect the grain size in flood deposits in Henry Lee Pond. Clay inputs during flooding at Henry Lee Pond might affect the sediment chemistry without changing the grain size, potentially explaining broad increases in Fe and Ti during historical floods (Figure 6.9). Bioturbation in the sediments could smooth the chemical signal of these potentially flood-derived deposits across several centimeters, which translates to decadal-scale variations in Fe and Ti given the sedimentation rate, comparable to our observations (Figure 6.9).

We conclude from our observations that Henry Lee Pond is less susceptible to receiving sand deposits during flooding than Red Bug Pond. The best available evidence implicates sediment availability and contrasting river flow velocities between the sites as the most likely reasons why Red Bug Pond is more susceptible to sand deposition during flooding in the Choctawhatchee River valley. Sedimentation in Henry Lee Pond has not been affected by any major historical floods; floods that are large enough to overcome any elevation barrier between Holmes Creek and Henry Lee Pond are likely of greater magnitude than any of those in the historical period, assuming the site has remained insensitive to flooding consistently throughout the Holocene. Given that sinkhole activity would only lower the elevation of the land surrounding Henry Lee Pond, and that sea level has been rising throughout the Holocene, the assumption that this site has not become less susceptible to flooding is well-supported. The lack historical flood deposits in Henry Lee Pond then sets the lower limit on flood stage for deposits observed at this site to greater than the largest flood in the instrumental record, which was 10.9 meters at this part of the Choctawhatchee River. Intense floods that are unprecedented in the historical period may be more turbulent and capable of eroding and transporting sand locally, or they may transport coarse sediment from outside the Henry Lee Pond catchment into the lake basin. Alternatively, paleoflood deposits in Henry Lee Pond sediments may represent higher-velocity conditions associated with rapid, shorter-duration floods (i.e. flash floods) that are capable of transporting coarse sediment relative to large, relatively slower-moving floods. Coarse beds in Henry Lee Pond thus represent either more massive floods or short-duration and high-velocity floods, both of which are unprecedented in the historical record.

6.6.3 Holocene flood reconstruction

We expect that the signature of floods preserved in the sediment cores over the last several millennia should be similar to the event deposits that align with historical floods between 1929-1950: a greater proportion of coarse-grained sediment that is paired with a decrease in organic content. In order to distinguish flood deposits from minor background variations in sand content, we set a threshold above which all peaks in % sand are identified as coarse event deposits. The threshold value for Red Bug Pond, 3.6 % sand, was chosen because it is the value separating the upper 20% of the % sand data from the lower 80% in the probability distribution function of the dataset, excluding the data between 7500 and 5000 B.P. where the sand variations are likely related to sinkhole activity and lake level changes. In Henry Lee Pond, the threshold value that separates the upper 20% of the data in the probability distribution function for that dataset, excluding 5000 to 2200 B.P. where sand variations are likely related to lake level changes, is 7.6% sand. Based on these criteria, we identified twenty-two event deposits in the Red Bug Pond record in addition to the two historic events beds, indicating major flooding greater than 5 m.a.s.l. in Holmes Creek prior to the start of the instrumental flood record occurred in 440, 480, 560, 900, 1420, 2000, 2180, 2410, 2610, 3300, 4440, 4720, 4890, 7580, 7650, 7680, 7710, 7880, 7990, 8540, 8700, and 8740 B.P. (Figure 6.10). Each of these deposits occurs within very fine-grained organic-rich sediments; in each coarse bed the proportion of sand relative to silt decreased throughout the event deposit, similar to the historic event beds. The decrease in the sand fraction of each pre-historical coarse deposit is only based on 2 to 3 measurements per event, but it may be indicative of decreasing depositional energy that is characteristic of a flood deposit. The base of each flood deposit should represent the highest depositional energy as the flood stage reached the elevation threshold for deposition in Red Bug Pond, presumably also increasing river discharge and flow velocity, resulting in coarse sand deposition. As each flood dissipated and the river velocity slowed, the transport energy would have decreased below the threshold of sand transport and would deposit more silt than sand. Finally, as the flood stage dropped below the elevation of Red Bug Pond during each flood, the transport energy within the lake should have diminished, and the end result would be a fining upward sequence. There are several other brief increases in sand content superimposed on the coarse-grained portion of the core between 7500 and 5000 B.P. that may represent floods, but it is unclear whether flooding caused these variations or if they represent sediment reworking where sand availability was higher due to sinkhole activity. For this reason we limit our flood reconstruction to between 9000 and 7500 B.P. and from 5000 B.P. to present.

The long-term record from Henry Lee Pond contains only one clear event bed at 5470 B.P. and a broad increase in sand content between 400 and 350 B.P. (Figure 6.10), which may represent one or several flood deposits. These are interpreted to be large-magnitude floods that are unprecedented in the historical period. The recent rise in sand content in HLP-Core 1 beginning at 400 B.P. occurs in close timing with two events in the Red Bug Pond record, suggesting there may have been an exceptionally large event around 400 B.P. that was large enough to deliver coarse sediments into Henry Lee Pond. The magnitude of this event in the Red Bug Pond record is the largest of all flood deposits in that record between 5000 B.P. and the present, which is consistent with our interpretation that the magnitude of this flood was unprecedented in the historical period. This event in HLP-Core 1 does occur within age model uncertainty of event beds with relatively higher sand content compared to the majority of event beds that are present in both cores from Red Bug Pond at 5540 B.P., but this is during the interval with exceptionally large sand content variations that are likely due to processes unrelated to river flooding. It is possible that the rise in sand content in RBP-Core 1 at 5540 B.P. may represent a single large flood deposit rather than declining lake level, which would imply that regional drought did not occur until a few centuries later, when we observe a depositional hiatus in RBP-Core 2 and a broad increase in sand content in Henry Lee Pond. We do not include the period from 5000 to 2200 B.P. in our flood reconstruction from Henry Lee Pond to avoid misinterpreting sand content variability due to greater coarse sediment availability as flood indicators when they could actually represent other processes such as facies migration during subtle variations in lake level or easier sediment reworking in shallower water (Digerfeldt, 1986).

The Red Bug Pond reconstruction indicates that major floods in the Choctawhatchee River valley were common from 2200 B.P. to present and between 9000 and 7500 B.P., but were less common from 5000 to 2200 B.P. Extremely large floods that formed sand beds in Henry Lee Pond that are unprecedented in the instrumental flood record occurred circa 400 and 5500 B.P. Flooding capable of depositing sand in Henry Lee Pond did not occur during the instrumental period, so the mechanism that produces floods of such extraordinary magnitude is unknown.

6.6.4 The role of climate on Holocene flooding

Of the 85 historical floods, 32 of which exceeded Major Flood Stage, our reconstruction only documents the four most extreme historic events, excluding those extreme events that occurred post-landscape alteration and did not result in sand beds in Red Bug Pond (Figure 6.9). Our reconstruction therefore only represents approximately 5% of the total number of historical floods and 12.5% of the major floods. A record like this one is most useful for understanding how broad trends in major flood frequency differ during past mean climate states that may be analogous to future climate scenarios, periods where ENSO event frequency was higher or lower than today, and periods when hurricane climatology was different than today. These reconstructed relationships are useful to more accurately predict broad trends in climate extremes.

In order for flooding to occur, substantial amounts of rain must fall over a short period of time such that it flows on the surface before it can be absorbed into the groundwater through the surface sediments. Flooding in the Choctawhatchee River valley may be driven by intense rainfall events during hurricanes, winter storms associated with ENSO teleconnections, high rainfall due to warmer Gulf of Mexico SSTs, and/or heavy precipitation that is simply due to random atmospheric circulation variability and convective activity. The occurrence of flooding is also likely controlled by how well the rainfall is infiltrated into the subsurface, based on the greater occurrence of historical floods during late winter/early spring, when the water table is higher, relative to during the summer, when rainfall amount is higher but the water table is lower.

The majority of historical floods occurred during winter and spring months, when precipitation anomalies in Florida are correlated to ENSO (Figure 6.2; Climate Prediction Center). We assessed the role of ENSO on the long-term history of major floods by comparing our reconstruction with a record of runoff based on red color intensity of a sediment core from Ecuador (Moy et al., 2002), a region which commonly experiences heavy rainfall during El Niño events (Figure 6.11). This comparison assumes that heavy rainfall in Ecuador corresponded to heavy rainfall in Florida via ENSO teleconnections consistently throughout the Holocene. The runoff reconstruction from Laguna Pallcacocha, Ecuador is a Holocene-length record indicating that the frequency of El Niño-driven runoff deposits increased during the Holocene until 1200 B.P., then decreased into the present (Figure 6.11; Moy et al., 2002). Sixteen paleofloods in our reconstruction occurred from 9000 to 7500 B.P. and after 1200 B.P. (~5.8 floods per 1000 years) contrasted with the nine floods that occurred between 5000 B.P. and 1200 B.P. (~2.3 floods per 1000 years; Figure 6.11). While mechanisms other than El Niño events are certainly capable of producing heavy rainfall that causes runoff into Laguna Pallcacocha, the overall trend in this record, if at all representative of ENSO variability, would suggest that the long-term variability in El Niño activity is not the dominant influence on the patterns of major flooding in Florida. Mechanisms other than ENSO variability likely controlled the history of Choctawhatchee River flooding during the Holocene, but we do not discount the possibility that El Niño-driven rainfall in northwest Florida contributed to flooding in our reconstruction.

Given the weak relationship between broad trends in ENSO-driven rainfall in Ecuador and flood frequency, it may be the case that the mechanisms driving rainfall anomalies during the fall and summer months (i.e. hurricanes and Gulf of Mexico SSTs) were more important in causing river floods during the early and mid-Holocene than they are today. Local tropical cyclone reconstructions that extend back to the start of the Holocene are lacking, limiting our ability to test whether hurricanes induced flooding in the Choctawhatchee River valley during the last 10,000 years. We tested the role of mid- to late-Holocene hurricane climatology on major flood frequency trends by comparing our flood reconstruction a new record of tropical cyclone activity from Basin Bayou (Chapter 5) located 35 km southwest of Red Bug Pond as well as with a 4500 year-long hurricane record that is based on overwash deposits in sediments from Mullet Pond, located 160 km east of our study sites in northern Florida (Lane et al., 2011; Figure 6.12). Comparison of our flood reconstruction with the Basin Bayou record allows us to assess whether strong tropical cyclones striking the Red Bug Pond region induced flooding at the event scale before the historical period, and comparison with trends shared by the Basin Bayou and Mullet Pond records may elucidate a broader relationship between centennial-scale tropical cyclone variability in the Gulf of Mexico and long-term flooding trends in Florida.

Ten of the thirteen floods occurring between 4500 B.P. and present coincide within the ~80-year age uncertainties of overwash deposits in Basin Bayou (Figure 6.12; Chapter 5), implying that hurricane-driven rainfall may partially control on late Holocene flooding in northwest Florida as is the case in the historical period. A single event deposit in the Basin Bayou record at 310 B.P. may correspond to the extremely large flood documented in both Red Bug and Henry Lee Ponds at 400 B.P., suggesting that hurricanes played a role in causing the floods that are unprecedented in the historical record. Three floods do not correspond to an overwash deposit in Basin Bayou, which could mean that those events were driven by rainfall induced by a different mechanism, or that weaker tropical cyclones made landfall and induced riverine flooding without being energetic enough to transport sand to the center of Basin Bayou (Chapter 5). There are numerous overwash deposits in the Basin Bayou record that do not correspond to riverine flood deposits, suggesting that the rainfall amount during these strong storms was not great enough to cause flooding. Storm intensity does not tend to correspond to rainfall amount (National Hurricane Center, 2013), so we do not necessarily expect intense storm frequency in the Gulf of Mexico to relate directly to flooding in Florida. Flooding can result from low intensity tropical cyclones that pass slowly across our study region, delivering excess rainfall, and these storms would not be reflected in the high intensity storm reconstruction from Basin Bayou or Mullet Pond (National Hurricane Center, 2013).

If the long-term variations in major flood frequency were dominantly controlled by the long-term frequency of intense storms, we might expect that periods characterized by fewer strong storms would correspond to periods characterized by fewer flood deposits in Red Bug Pond. Four of the eight floods in the Red Bug Pond reconstruction between 600 and 4500 B.P. (900, 2000, 2410, and 2610 B.P.) occurred when the Mullet Pond and Basin Bayou storm records suggest Gulf of Mexico intense tropical cyclone activity was high (Figure 6.12). Numerous floods after 600 B.P., however, occurred when both overwash records indicate a quiescent interval characterized by very little intense hurricane activity. The broad trends in the frequency of deposits do not relate directly to centennial-scale variations in strong storms, which could imply that other mechanisms may be modulating the occurrence of floods, perhaps in addition to storm-induced rainfall, or that floods are simply random rare events.

Broad changes in Gulf of Mexico SSTs across decades or millennia likely influence the amount of moisture in the atmosphere that is advected over land, allowing for more intense rainfall during periods characterized by warmer SSTs. A reconstruction of Loop Current activity from the Pigmy Basin in the Gulf of Mexico suggests that centennial-scale variability in Loop Current penetration, and thus rainfall in Florida, may be linked to the migration of the mean position of the ITCZ in response to changes in solar insolation (Poore et al., 2003; Poore et al., 2004). We tested whether warmer SSTs or a stronger Loop Current influence in the northern Gulf of Mexico corresponded to a greater number of major floods in northwest Florida by comparing our reconstruction to a

1400-year record of Mg/Ca-based SSTs and a *G. sacculifer* abundance-based record of Loop Current strength from the Pigmy Basin (Figure 6.12; Richey et al., 2007). These records do not have the age control required to test the relationship between flooding and Gulf of Mexico SSTs and Loop Current strength on the event scale, but we can infer whether mean SSTs or Loop Current activity modulates the long-term variability in flood frequency. The Loop Current influence in the northern Gulf of Mexico was stronger between 1400 and 600 B.P. than in the recent few centuries (Richey et al., 2007), which should correspond to warmer SSTs and broadly higher rainfall in northern Florida. Only one flood occurred in our record between 1400 and 600 B.P. contrasted with five floods between 600 B.P. and present when Loop Current penetration was minimal (Figure 6.12). Poore et al. (2003) identified a millennial-scale relationship during the Holocene between Loop Current penetration into the northern Gulf of Mexico and ITCZ migration, where a more northerly ITCZ during the mid-Holocene thermal maximum corresponded to greater Loop Current penetration, followed by a decrease in Loop Current penetration into the Late Holocene. If the Loop Current were a major control on the millennial-scale trends in major flood frequency in northwest Florida, we expect that the southward migration of the ITCZ during the mid- to late-Holocene should correspond to a decrease in flood frequency; flood deposits increase in frequency after 5000 B.P. in our reconstruction (Figure 6.11). Gulf of Mexico SSTs were cooler between 400 and 150 B.P. relative to 1000 B.P. to 400 B.P. and 150 B.P. to present (Richey et al., 2007; Richey et al., 2011), yet more floods occurred between 400 and 150 B.P. (~8 floods per 1000 years) contrasted with the periods characterized by warmer SSTs (~5 floods per 1000 years; Figure 6.12). From these comparisons we conclude that broad variations in

Gulf of Mexico SSTs have little influence on the centennial-scale flood frequency in northern Florida, consistent with historical relationships. Unlike winter storms during El Niño years and hurricanes, which produce excessive amounts of rainfall in a short period of time, the Gulf of Mexico SST mechanism does not necessarily produce the heavy rainfall events that cause flooding. The floods in our record in 1420, 900, and 440 B.P. do coincide with very brief periods of intensified Loop Current in the northern Gulf of Mexico and the floods at 560, 480, 25, 13 and 11 B.P. coincide with very brief periods of warm reconstructed Gulf of Mexico SSTs, suggesting that while these Gulf temperature and current mechanisms do not appear to influence the long-term flooding variability, they may contribute to the flood-inducing heavy rainfall.

While flooding is likely associated with heavy rainfall during El Niño years, hurricanes, and warm Gulf of Mexico SSTs, there have certainly been periods of heightened El Niño activity, heightened hurricane activity, and periods of warmer SSTs that did not produce major flooding in the Choctawhatchee River valley both historically and throughout the Holocene. Flooding in the Choctawhatchee River valley may be a random phenomenon that cannot be predicted based on variations in climate or environmental conditions. Alternatively, groundwater elevation and soil moisture may have a more dominant role in flood occurrence than mechanisms that produce heavy rainfall.

Although the highest monthly average rainfall in northwest Florida occurs during the summer months, evaporation also peaks at this time and approximately balances precipitation (Figure 6.2). The majority of flooding occurs during winter and spring months when precipitation is nearly twice the regional evaporation and the water table depth is shallow, potentially reducing the capacity of the subsurface to infiltrate rainfall (Figure 6.2). If this mechanism operated across the Holocene to control the long-term history of flooding, we expect that fewer floods occurred when our lake-level reconstruction and regional pollen data suggest the water table was low during the mid-Holocene. In fact, our observations align with this hypothesis quite well: ten floods occurred during the wet early Holocene (~6.7 floods/1000 years) and eleven floods occurred after 2600 B.P. (~4.2 floods/1000 years) while only four floods occurred during the dry mid-Holocene (~1.7 floods/1000 years; Figure 6.10). We limit our comparison of mid-Holocene flood history to the period from 5000 to 3000 B.P., excluding 7400 to 5000 B.P. when sand variations may represent either floods or sand mobilization due to sinkhole activity.

The lack of local Holocene-length climate reconstructions and our inability to provide a precise age control in our flood reconstruction make it difficult to assess the cause the more intense floods that are preserved in Henry Lee Pond sediments. The more recent strong flood that is present in the Henry Lee Pond record at approximately 400 B.P. overlaps, within age model uncertainty, with increased runoff in Ecuador, a period of deeper Loop Current penetration into the northern Gulf of Mexico, and an overwash deposit in the local tropical cyclone reconstruction from Basin Bayou (Figures 6.11, 6.12; Moy et al., 2002; Richey et al., 2007; Chapter 5). This event also takes place during the very late Holocene when sea level was higher than during the previous millennia (Törnqvist et al., 2004) and during a period of inferred higher lake levels based on the Henry Lee Pond and Red Bug Pond stratigraphies (this study). The Loop Current influence and El Niño event precipitation may have resulted in higher rainfall during the year this event took place, contributing excess water to the subsurface such that infiltration of surface water from rainfall into the groundwater was further reduced. A tropical cyclone may have delivered an extraordinary amount of rainfall during an abnormally wet year, causing a massive flood. Based on this single event, we suggest that these more extreme floods occur when several factors that can result in heavy rainfall and prevent infiltration into the subsurface coincide. However, it is important to note that this assessment is purely speculative and based only on a single event.

6.7 Conclusions

We reconstructed the sedimentation histories of two lakes situated in the Choctawhatchee River floodplain in northwest Florida during the Holocene. Reconstructing riverine floods by utilizing lake sediment archives provides a record of well-dated intense flood deposits, eliminating the chronological challenges and discontinuity of floodplain-based reconstructions. Using the same sediment cores, we also reconstructed the history of millennial-scale hydrological changes over the course of our flood reconstruction that is vital for understanding the mechanisms controlling the Holocene flood history. Sinkhole activity complicated the flood reconstruction by adding sand to the sediment record through mechanisms unrelated to flooding, limiting our flood reconstruction to 9000 to 7500 B.P. and 5000 B.P. to present.

Broad changes in sedimentation in Red Bug and Henry Lee Ponds indicate that the regional moisture increased circa 9800 B.P. and remained relatively wet through the early Holocene. A coarsening of the sediments in both lakes between 5600 and 4500

B.P. leading to a hiatus in one of the cores from Red Bug Pond implies regional lake levels declined despite sea-level rise. We conclude, based on these observations, that climate became dry during the mid-Holocene. Our reconstruction indicates a return to a wetter climate began between 5250 and 4400 B.P., continued by a gradual increase in moisture through the late Holocene. Red Bug and Henry Lee Ponds are theoretically susceptible to flooding during some of the most extreme historical floods, based on land and flood elevation data. The Red Bug Pond record contains ~2 cm-thick coarse deposits superimposed on the long-term changes in grain size, which align in timing with historical flooding. We identified prehistoric flood deposits based on flood signatures during the historical period. The Henry Lee Pond record remained unchanged during the historical period despite the susceptibility of that site to historical flooding based on the elevation of the site and historical flood elevations. We utilized the insensitivity of Henry Lee Pond to the historical floods that affected Red Bug Pond to approximate relative differences in extreme flood intensities before the historical period.

The majority of historical floods occurred during the early and late Holocene, when our reconstruction indicates the region was wet relative to the middle Holocene. We conclude that water table depth strongly influences the occurrence of extreme flooding in the Choctawhatchee River valley on long timescales, more so than the long-term variability of the climate phenomena that produce heavy rainfall events (e.g. hurricanes, winter storms during El Niño events). One extreme event that is recorded in both Red Bug and Henry Lee Pond sediments occurred during the mid-Holocene before the water table decline, and another event occurred circa 400 B.P. These extreme events likely occurred when groundwater depth was shallow, such that precipitation did not easily drain into the subsurface, and coincided with warm Gulf of Mexico current and atmospheric patterns that are associated with heavy rainfall in northwest Florida driven by multiple components of regional climate at the same time. As sea level continues to rise in the future, the shoaling water table may result in more frequent intense flooding due to poor infiltration of precipitation during intense rainfall events.

6.8 Acknowledgements

We thank Pete van Hengstum, Kelsey Condon, Aaron Beltzer, Nalaka Ranasinghe, and Dana Macdonald for assistance with field work. We thank Stephanie Madsen and Trish Rodysill for assistance with lab work. Funding for this project was provided by the Strategic Environmental Research and Development Program (SERDP) grant awarded to Jeffrey Donnelly and a student research grant from the Geological Society of America awarded to Jessica Rodysill.

6.9 References

"Advanced Hydrologic Prediction Service." National Oceanic and Atmospheric Administration. 30 May 2013. Web. 30 May 2013. <http://water.weather.gov/ahps/>.

Appleby, P.G., 1997. Sediment records of fallout radionuclides and their application to studies of sediment-water interactions. Water Air Soil Pollut. 99, 573-586.

Appleby, P.G., Oldfield, F., 1978. The calculation of ^{210}Pb dates assuming a constant rate of supply of unsupported ^{210}Pb to the sediment. Catena 5, 1-8.

Climate Prediction Center. National Centers for Environmental Prediction. National Oceanic and Atmospheric Administration. 24 January 2005. Web. 4 July 2013. <http://www.cpc.ncep.noaa.gov/>

Dean, W.E., 1974. Determination of carbonate and organic matter in calcareous sediments and sedimentary rocks by loss on ignition: comparison with other methods. J. Sed. Petrol. 44, 242-248.

Dearing, J.A., 1997. Sedimentary indicators of lake-level changes in the humid temperate zone: a critical review. J. Paleolim. 18, 1-14.

Department of Commerce (DOC), National Oceanic and Atmospheric Administration (NOAA), National Ocean Service (NOS), Coastal Services Center (CSC), 2006. 2004 Florida Greenway ADS40 Orthoimagery and Digital Elevation Model. <http://www.csc.noaa.gov/digitalcoast>

Digerfeldt, G., 1986. Studies on past lake-level fluctuations. In “Handbook of Holocene Palaeoecology and Palaeohydrology.” B. E. Berglund, Ed., pp. 127–142. Wiley, Chichester.

Enfield, D.B., Mestaz-Nuñez, A.M., Trimble, P.J., 2001. The Atlantic Multidecadal Oscillation and its relation to rainfall and river flows in the continental U.S. Geophys. Res. Lett. 28, 2077-2080.

Farnsworth, R.K., Thompson, E.S., 1982. Mean monthly, seasonal, and annual pan evaporation for the United States. NOAA technical report NWS 34.

"Florida Water Science Center." United States Geological Survey (USGS): Water resources of Florida. 10 May 2013. Web. 1 June 2013. <http://fl.water.usgs.gov/>.

Goman, M., Leigh, D.S., 2003. Wet early to middle Holocene conditions on the upper Coastal Plain of North Carolina, USA. Quat. Res. 61, 256-264.

Grimm, E.C., Jacobson, Jr., G.L., Watts, W.A., Hansen, B.C.S., Maasch, K.A., 1993. A 50,000-year record of climate oscillations from Florida and its temporal correlation with the Heinrich Events. Science. 261, 198-200.

Heegaard, E., Birks, H.J.B., Telford, R.J., 2005. Relationships between calibrated ages and depth in stratigraphical sequences: an estimation procedure by mixed-effect regression. The Holocene 15, 612-618.

Kindinger, J.L., Davis, J.B., Flocks, J.G., 2001. High-Resolution Single-Channel Seismic Reflection Surveys of Orange Lake and Other Selected Sites of North Central Florida. United States Geological Survey. Open file report 94-616.

Knox, J.C., 1983. Responses of floods to Holocene climatic change in the upper Mississippi valley. Quat. Res. 23, 287-300.

Knox, J.C., 1993. Large increases in flood magnitude in response to modest changes in climate. Nature 361, 430-432.

Knox, J.C., 2000. Sensitivity of modern and Holocene floods to climate change. Quat. Sci. Rev. 19, 439-457.

Lane, P., 2011. Late Holocene Hurricane Activity and Climate Variability in the Northeastern Gulf of Mexico. Ph.D. Thesis. MIT/WHOI Joint Program in Oceanography/Applied Ocean Science and Engineering. Massachusetts Institute of Technology. Boston, MA.

Lane, P., Donnelly, J.P., Woodruff, J.D., Hawkes, A.D., 2011. A decadally-resolved paleohurricane record archived in the late Holocene sediments of a Florida sinkhole. Mar. Geol. 287, 14-30.

Moy, C.M., Seltzer, G.O., Rodbell, D.T., Anderson, D.M. 2002. Variability of El Niño/Southern Oscillation activity at millennial timescales during the Holocene epoch. Nature 420: 162-165.

National Hurricane Center, 2013. "Hurricane Preparedness-Hazards." National Oceanic and Atmospheric Administration. 5 March 2013. Web. 12 July 2013. <http://www.nhc.noaa.gov/prepare/hazards.php>

Newby, P.E., Killoran, P., Waldorf, M.R., Shuman, B.N., Webb, R.S., Webb III, T., 2000. 14,000 Years of Sediment, Vegetation, and Water-Level Changes at the Makepeace Cedar Swamp, Southeastern Massachusetts. Quat. Res. 53, 352-368.

Northwest Florida Water Management District (NWFWMD), 2013. 2007 Northwest Florida Water Management District (NWFWMD) Lidar: Portions of Bay, Calhoun, Jackson and Washington Counties. Publisher: NOAA's Ocean Service, Coastal Services Center (CSC). <http://www.csc.noaa.gov/Lidar>

Peterson, L.C., Haug, G.H., Hughen, K.A., Röhl, U., 2000. Rapid changes in the hydrologic cycle of the tropical Atlantic during the last glacial. Science 290, 1947-1951.

Poore, R.Z., 2008. Holocene climate and climate variability of the Northern Gulf of Mexico and Adjacent Northern Gulf Coast: A Review. Open Paleont. J. 1, 7-17.

Poore, R.Z., Dowsett, H.J., Verardo, S., Quinn, T.M., 2003. Millennial- to century-scale variability in Gulf of Mexico Holocene climate records. Paleoceanog. 18, doi:10.1029/2002PA000868.

Poore, R.Z., Quinn, T.M., Verardo, S., 2004. Century-scale movement of the Atlantic Intertropical Convergence Zone linked to solar variability. Geophys. Res. Lett., 31, doi:10.1029/2004GL019940.

Pride, R.W., 1958. Floods in Florida, magnitude and frequency. United States Department of the Interior U.S. Geological Survey open file report. pp. 127.

Ramsey, C.B., 2008. Deposition models for chronological records. Quat. Sci. Rev. 27, 42-60.

Richey, J.N., Hollander, D.J., Flower, B.P., Eglinton, T.I., 2011. Merging late Holocene molecular organic and foraminiferal-based geochemical records of sea surface temperature in the Gulf of Mexico. Paleoceanog. 26, doi:10.1029/2010PA002000.

Richey, J.N., Poore, R.Z., Flower, B.P., Quinn, T.M., 2007. 1400 yr multiproxy record of climate variability from the northern Gulf of Mexico. Geology. 35, 423-426.

Schnurrenberger, D., Russell, J.M., Kelts, K., 2003. Classification of lacustrine sediments based on sedimentary components. J. Paleolimnol. 29, 141-154.

Scott, T.M., Campbell, K.M., Rupert, F.R., Arthur, J.D., Green, R.C., Means, G.H., Missimer, T.M., Lloyd, J.M., Yon, J.W., Duncan, J.G., 2001. Geologic map of the state of Florida. Florida Geological Survey and Department of Environmental Protection.

Shuman, B., Bartlein, P., Logar, N., Newby, P., Webb III., T., 2002. Parallel climate and vegetation responses to the early Holocene collapse of the Laurentide Ice Sheet. Quat. Sci. Rev. 21, 1793-1805.

Shuman, B., Bravo, J., Kaye, J., Lynch, J.A., Newby, P., Webb III, T., 2001. Late Quaternary Water-Level Variations and Vegetation History at Crooked Pond, Southeastern Massachusetts. Quat. Res. 56, 401-410.

Shuman, B., Donnelly, J.P., 2006. The influence of seasonal precipitation and temperature regimes on lake levels in the northeastern United States during the Holocene. Quat. Res. 65, 44-56.

Shuman, B.N., Newby, P., Donnelly, J.P., 2009. Abrupt climate change as an important agent of ecological change in the Northeast U.S. throughout the past 15,000 years. Quat. Sci. Rev. 28, 1693-1709.

Shuman, B.N., Newby, P., Donnelly, J.P., Tarbox, A., Webb III, T., 2005. A Record of Late-Quaternary Moisture-Balance Change and Vegetation Response from the White Mountains, New Hampshire. Annals of the Association of American Geographers. 95, 237–248.

Sinclair, W.C., Stewart, J.W., 1985. Sinkhole type, development, and distribution in Florida. USGS. Map Series No. 110. Tallahasee, Florida.

Sinkholes of Washington County, Florida, 2008. Florida Center for Instructional Technology. Sinkholes Map. University of South Florida, Tampa, FL. Web. 12 July 2013. < http://fcit.usf.edu/florida/maps/>

Southwest Florida Water Management District. Sinkholes Brochure. Web. 12 Sept. 2013. < http://www.swfwmd.state.fl.us/hydrology/sinkholes/brochure.pdf>

Stuiver, M., Reimer, P.J., 1993. Extended ^{14}C data base and revised Calib 3.0 ^{14}C age calibration program. Radiocarbon. 35, 215–230.

Stuiver, M., Reimer, P.J., Reimer, R., 2005. CALIB 5.0.2 [WWW program and documentation]. www.calib.org: Unknown Publisher.

Törnqvist, T.E., González, J.L., Newsom, L.A., van der Borg, K., de Jong, A.F.M., Kurnik, C.W., 2004. Deciphering Holocene sea-level history on the U.S. Gulf Coast: A high-resolution record from the Mississippi delta. Geol. Soc. Amer. Bull. 116, 1026-1039.

Vose, R.S., Schmoyer, R.L., Steurer, P.M., Peterson, T.C., Heim, R., Karl, T.R., Eischeid, J., 1992. The Global Historical Climatology Network: Long-term monthly temperature, precipitation, sea level pressure, and station pressure data. ORNL/CDIAC-53, NDP-041. Carbon Dioxide Information Analysis Center, Oak Ridge National Laboratory, Oak Ridge, Tennessee.

Walton County Flood Information Reference Guide. 2010. Walton County Planning and Development Services.

"Washington County History." Washington County. Washington County Computer Department. 28 May 2013. Web. 30 May 2013. <http://www.washingtonfl.com/default.htm>.

Watts, W.A., 1969. A pollen diagram from Mud Lake, Marion County, north-central Florida. Geol. Soc. Amer. Bull. 80, 631-642.

Watts, W.A., 1971. Postglacial and interglacial vegetation history of southern Georgia and central Florida. Ecology. 52, 676-690.

Watts, W.A., 1975. A late Quaternary record of vegetation from Lake Annie, south-central Florida. Geology. 3, 344-346.

Watts, W.A., Hansen, B.C.S., 1994. Pre-Holocene and Holocene pollen records of vegetation history from the Florida peninsula and their climatic implications. Palaeogeog. Palaeoclim. Palaeoecol. 109, 163-176.

Month	Precip. (mm)	Evap. (mm) Fairhope, AL	Evap. (mm) Mobile, AL	Evap. (mm) Tallahassee, FL	Avg. Evap. (mm)	P:E	Floods	Major Floods
Jan.	116.32	50.038	68.58	63.5	60.71	1.92	9	3
Feb.	134.05	62.23	83.312	73.152	72.90	1.84	13	0
Mar.	152.04	98.552	123.444	143.002	121.67	1.25	21	9
Apr.	117.32	127.762	148.336	150.876	142.32	0.82	18	9
May	118.59	159.512	182.626	178.054	173.40	0.68	5	1
June	163.41	164.084	181.864	176.784	174.24	0.94	1	1
July	218.15	153.67	165.1	161.544	160.10	1.36	1	1
Aug.	188.86	142.24	159.766	157.48	153.16	1.23	2	2
Sept.	156.90	115.824	143.764	138.938	132.84	1.18	3	1
Oct.	82.77	96.266	132.08	123.698	117.35	0.71	2	1
Nov.	99.62	59.944	91.694	82.296	77.98	1.28	1	0
Dec.	121.35	44.196	72.898	65.278	60.79	2.00	9	4

Table 6.1: Monthly averaged precipitation values in mm per month from the sources described in the text are listed in the first data columns of Table 1. The second data column is monthly evaporation values determined through pan evaporation experiments in Fairhope, AL. The third and fourth columns are monthly evaporation values estimated from meterological data in Mobile, AL and Tallahassee, FL, respectively. The fifth column is the average of all three monthly evaporation values listed in Columns two through four. The sixth data column is the monthly precipitation value divided by the evaporation value for that same month. The seventh and eighth data columns are the total number of floods and number of major floods that occurred during each month since 1929.

Flood Crest Date	Flood Crest Elevation (feet)	Flood Crest Elevation (meters)	El Niño Year	La Niña Year	Non-ENSO year	Hurricane
3/15/1929	29.19	8.90		X		
11/22/1930	16.44	5.01			X	
1/19/1932	14.49	4.42			X	
4/18/1933	16.59	5.06			X	
3/11/1934	14.77	4.50			X	
3/16/1935	12.17	3.71			X	
1/10/1936	17.9	5.46			X	
9/6/1937	19.98	6.09			X	Unnamed 1937
3/24/1938	15.72	4.79			X	
8/20/1939	20.62	6.28		X		Unnamed 1939
2/23/1940	16.01	4.88	X			
3/27/1941	11.72	3.57	X			
1/6/1942	16.39	5.00	X			
1/27/1943	16.07	4.90	X			
3/30/1944	16.84	5.13			X	
5/5/1945	12.24	3.73			X	
8/11/1946	17.82	5.43			X	
3/12/1947	18.73	5.71	X			
4/4/1948	19.16	5.84			X	
12/4/1948	15.96	4.86			X	
9/5/1950	16.09	4.90		X		
4/5/1951	12.87	3.92		X		
2/22/1952	14.1	4.30	X			
5/11/1953	14.73	4.49			X	
12/12/1953	17.76	5.41			X	
4/21/1955	14.75	4.50		X		
3/19/1956	12.55	3.83		X		
4/12/1957	15.98	4.87	X			
3/15/1958	14.03	4.28	X			
3/11/1959	14.93	4.55			X	
4/9/1960	19.94	6.08			X	
4/20/1961	16.99	5.18			X	
4/5/1962	16.81	5.12			X	
1/27/1963	14.58	4.44		X		
5/2/1964	17.05	5.20		X		
12/20/1964	16.9	5.15		X		
3/7/1966	17.03	5.19	X			
1/9/1967	15.65	4.77			X	
12/17/1967	13.33	4.06		X		
5/25/1969	14.04	4.28	X			

4/6/1970	16	4.88	X			
4/2/1971	15.16	4.62		X		
3/11/1972	12.96	3.95		X		
4/7/1973	16.99	5.18	X			
2/12/1974	16.35	4.98		X		
4/15/1975	21.48	6.55		X		
10/24/1975	15.94	4.86		X		
12/5/1976	16.09	4.90	X			
1/31/1978	19.74	6.02	X			
3/1/1979	18.37	5.60			X	
3/18/1980	16.95	5.17			X	
2/17/1981	15.82	4.82			X	
2/8/1982	16.25	4.95			X	
2/8/1983	15.06	4.59	X			
2/13/1985	15	4.57		X		
2/12/1986	16.07	4.90			X	
3/6/1987	13.48	4.11	X			
6/14/1989	17.65	5.38		X		
3/23/1990	22.88	6.97			X	
3/10/1991	18.45	5.62			X	
2/12/1992	14.46	4.41	X			
12/1/1992	16.6	5.06	X			
7/11/1994	26.76	8.16	X			Alberto
2/17/1995	16.25	4.95	X			
4/5/1996	15.28	4.66		X		
2/21/1997	14.48	4.41			X	
3/10/1998	15.35	4.68	X			
3/13/1998	22.61	6.89	X			
10/4/1998	20.95	6.39		X		
3/27/2000	9.5	2.90		X		
3/19/2001	15.56	4.74		X		
4/15/2002	12.99	3.96	X			
4/14/2003	15.22	4.64	X			
9/23/2004	14.35	4.37	X			Frances
4/4/2005	18.87	5.75	X			
1/8/2006	12.78	3.90			X	
4/23/2007	11.57	3.53	X			
2/26/2008	16.14	4.92		X		
12/18/2008	15.31	4.67			X	
4/2/2009	20.52	6.25			X	
12/8/2009	14.82	4.52	X			
12/21/2009	19.06	5.81	X			
1/25/2010	17.13	5.22	X			
2/20/2010	13	3.96	X			
5/8/2010	13.3	4.05	X			

Table 6.2: Every flood documented at the Bruce-Ebro station since 1929 is listed by date in both feet and meters in this table. Each flood occurring during an El Niño year, a La Niña year, a non-ENSO year, and/or a hurricane are denoted by an “X” in the respective column. Rows highlighted in grey denote Major Floods (>16.5 feet).

Sed. depth (cm)	Lab code	Dated material	^{14}C age (years B.P.)	Cal. Age (years B.P.)	2 Sigma range 1 (years B.P.) (probability)	2 Sigma range 2 (years B.P.) (probability)	2 Sigma range 3 (years B.P.) (probability)	2 Sigma range 4 (years B.P.) (probability)
Red Bug Pond Core 1								
105*	OS-102187	Plant/Wood	1040 +/- 25	951.5 +/- 29.5	922:981 (0.964581)	1035:1047 (0.035419)		
150	OS-98125	Plant/Wood	910 +/- 20	841.5 +/- 71.5	770:913 (1)			
198.5	OS-90495	Plant/Wood	1530 +/- 25	1387.5 +/- 36.5	1351:1424 (0.615286)	1456:1517 (0.335598)	1428:1445 (0.049115)	
254.75	OS-98126	Plant/Wood	1960 +/- 25	1908.5 +/- 43.5	1865:1952 (0.914759)	1958:1987 (0.072563)		
289.5	OS-98127	Plant/Wood	2140 +/- 20	2100.5 +/- 56.5	2044:2157 (0.856491)	2262:2298 (0.143509)		
312.5	OS-102188	Plant/Wood	2870 +/- 25	2999 +/- 76	2923:3075 (0.967241)	2889:2906 (0.032759)		
332	OS-90521	Plant/Wood	4000 +/- 35	4473 +/- 61	4412:4534 (0.979146)	4556:4568 (0.014425)	4542:4548 (0.006429)	
438	OS-103765	Plant/Wood	6610 +/- 55	7502.5 +/- 72.5	7430:7575 (1)			
497.5	OS-90475	Plant/Wood	7520 +/- 55	8343.5 +/- 67.5	8276:8411 (0.767137)	8199:8269 (0.232863)		
Red Bug Pond Core 2								
69.5	OS-101621	Plant/Wood	4850 +/- 35	5616 +/- 37	5579:5653 (0.77536)	5482:5529 (0.22464)		
158.2	OS-86379	Plant/Wood	7660 +/- 45	8465.5 +/- 76.5	8389:8542 (1)			
547	OS-86378	Plant/Wood	> 48000					
Henry Lee Pond Core 1								
46	OS-101619	Plant/Wood	220 +/- 25	168 +/- 20	148:188 (0.441734)	269:306 (0.427578)	-1:13 (0.101895)	198:212 (0.028793)
58.75	OS-101620	Plant/Wood	765 +/- 35	700 +/- 37	663:737 (1)			
74.5	OS-98128	Plant/Wood	3180 +/- 25	3405.5 +/- 41.5	3364:3447 (1)			
120.5	OS-103613	Plant/Wood	4620 +/- 30	5418 +/- 44	5374:5462 (0.69946)	5296:5332 (0.297371)	5349:5351 (0.00317)	
166	OS-98129	Plant/Wood	6860 +/- 35	7689.5 +/- 73.5	7616:7763 (0.974059)	7773:7785 (0.025941)		

Table 6.3: Samples submitted for ^{14}C dating techniques from all three sediment cores are separated by core and then listed by depth in this table with their NOSAMS sample ID, the type of sample that was dated, the age of the sample in radiocarbon years with the analytical uncertainty, the calibrated age and age uncertainty, and the 2-σ age ranges with their associated probabilities in parentheses.

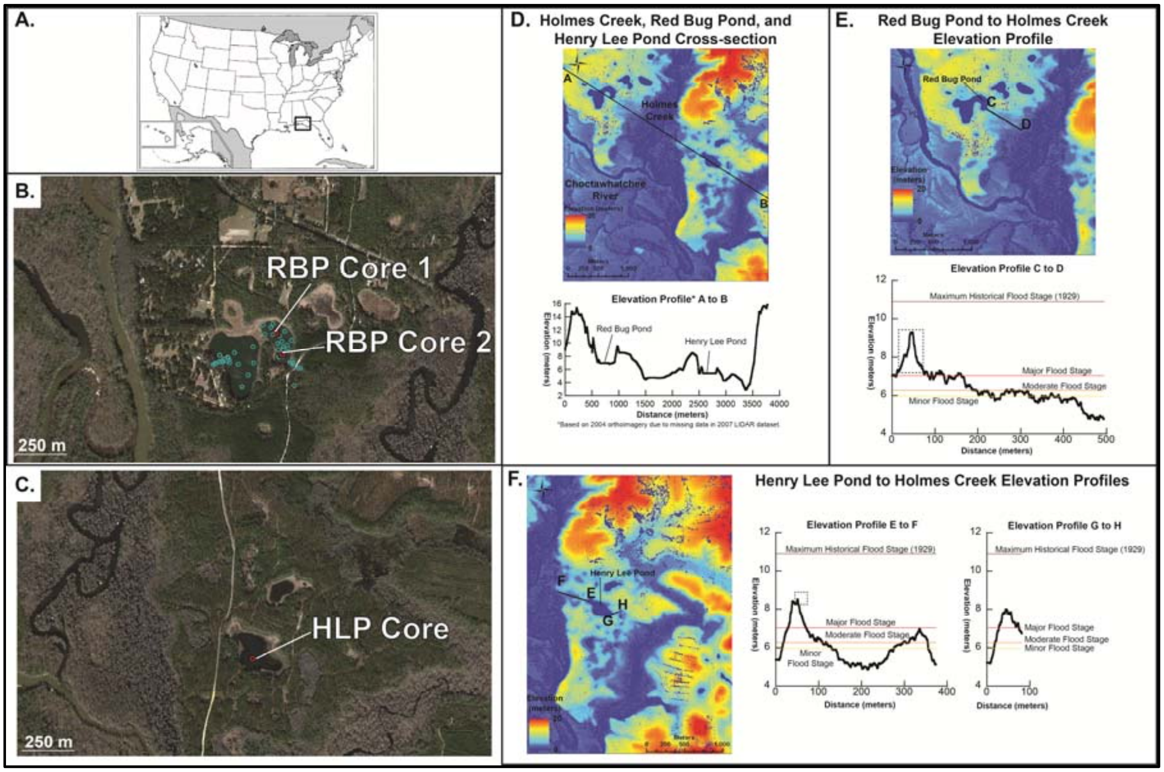

Figure 6.1: Study sites and elevation data. A. Map of the United States. Our study region is outlined with a bold black box. B. Close-up of Red Bug Pond showing core locations (red circles) and surface sample locations (blue circles). C. Close-up of Henry Lee Pond showing core location (red circle). D. Elevation map of Holmes Creek valley. An elevation profile across transect A-B (labeled on map), extending across Red Bug Pond, the Holmes Creek Valley, and Henry Lee Pond, is displayed below the map. The locations of Red Bug Pond and Henry Lee Pond are labeled on the elevation profile. E. Elevation map of Red Bug Pond and Holmes Creek. An elevation profile across transect C-D (labeled on map), extending through the lowest topographic high that separates the lake from the river is displayed below the map. The dashed rectangle outlines the part of the profile we assumed was artificially built up to support the road that was constructed here. Yellow, orange, red, and brown lines indicate the elevations of Minor Flood Stage, Moderate Flood Stage, Major Flood Stage, and the Maximum historical flood stage occurring in 1929, respectively, as defined by the Advanced Hydrologic Prediction Service. F. Same as E. but for Henry Lee Pond. Lidar-based elevation data for the part of the floodplain containing our study sites are displayed in color maps, with warmer colors corresponding to higher elevations. All of the maps are created with a 20 m elevation range, with dark blue corresponding to an elevation of 0 m.a.s.l. or missing data and red representing 20 m.a.s.l.

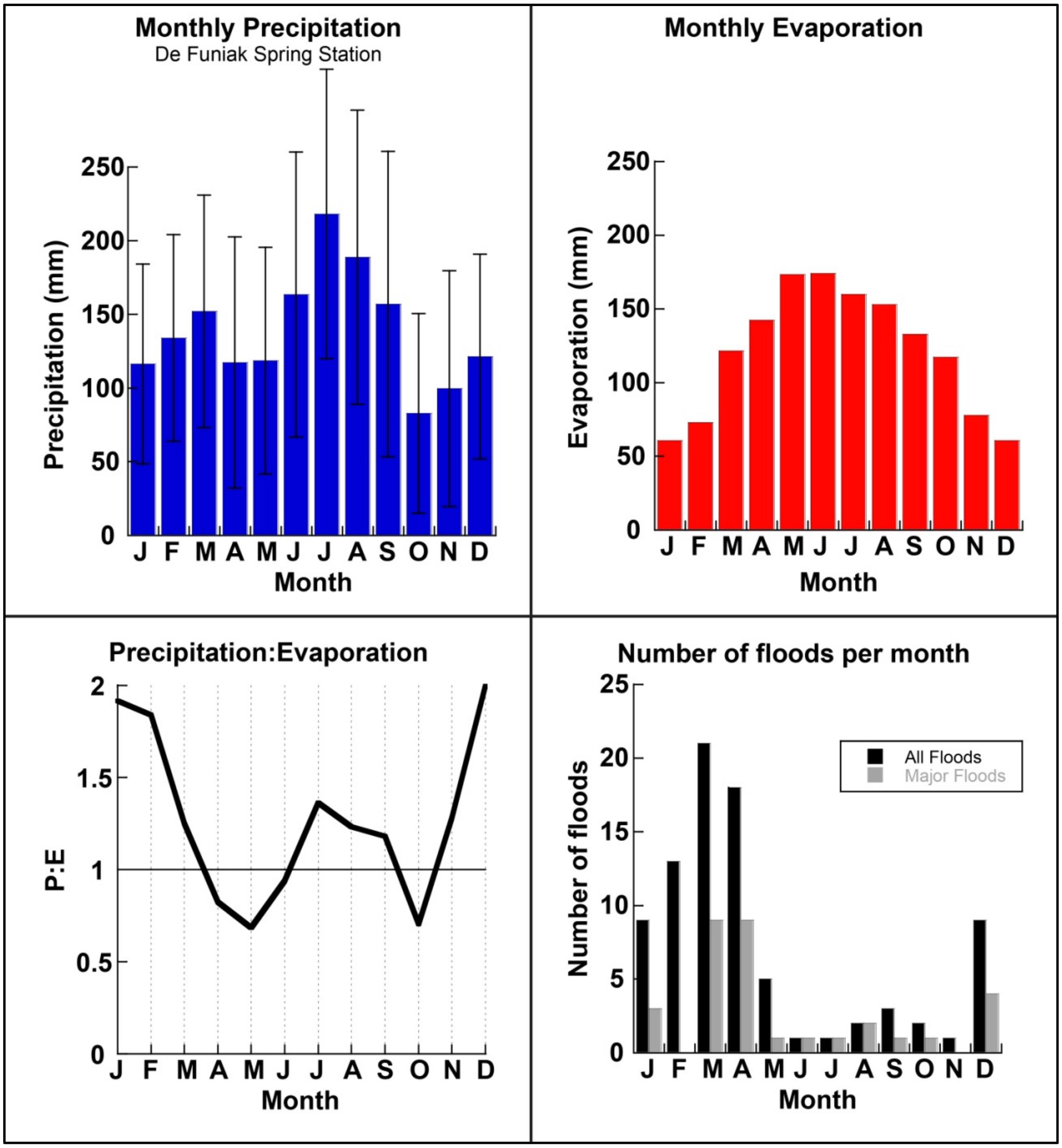

Figure 6.2: Local climatology. Top left: Average monthly precipitation in millimeters calculated from rainfall data from the De Funiak Spring Station between 1900 and 2005 is shown as blue bars. Monthly standard deviations from the mean are indicated with black error bars. Top right: Average monthly evaporation in millimeters estimated from a combination of pan evaporation measurements and approximations based on meterological data from three sites in southern Alabama and northern Florida is shown as red bars. Bottom left: The ratio of average monthly precipitation to average monthly evaporation (P:E) is shown for each month. P:E = 1 indicates precipitation equals evaporation for that data point, P:E <1 indicates more water is evaporated than precipitated, and P:E >1 indicates more water is precipitated than evaporated. Bottom right: The number of floods occurring in each month at the Bruce-Ebro USGS monitoring station is shown as black bars. The same is shown for only those floods exceeding major flood stage (16.5 feet at Bruce-Ebro) as grey bars.

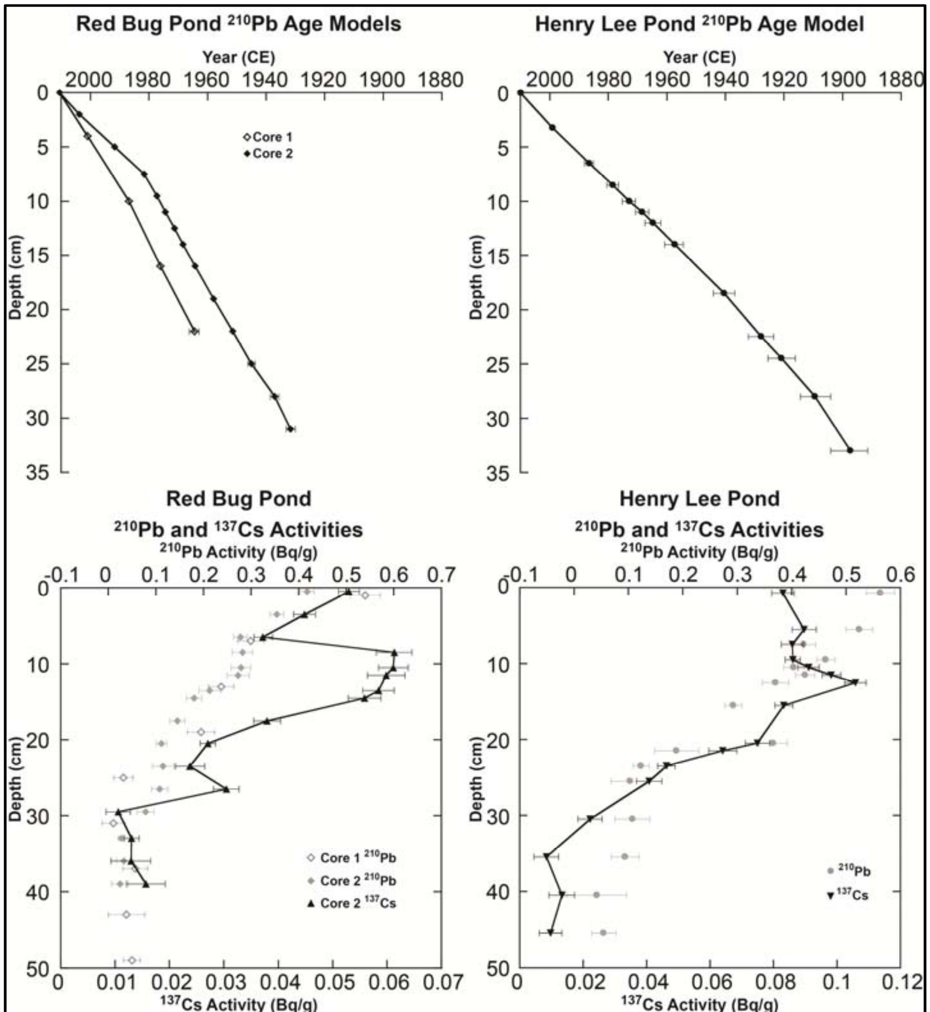

Figure 6.3: ^{210}Pb and ^{137}Cs-based chronologies in the core tops of Red Bug and Henry Lee pond cores. The depth vs. age relationship given by the ^{210}Pb-based age model for Red Bug Pond Core 1 and 2 are shown on the top left. Open diamonds with error bars are the age control points for Core 1 and closed diamonds with error bars are the age control points for Core 2. The depth vs. age relationship given by the ^{210}Pb-based age model for Henry Lee Pond core is on the top right. Circles with error bars are individual age control points. Age control points for both sites were determined from measured ^{210}Pb activities, which are shown on the bottom. Grey open and closed diamonds with error bars on the bottom left are ^{210}Pb activities and analytical uncertainties measured on RBP-Core 1 and RBP-Core 2, respectively. Grey circles and error bars on the bottom right are ^{210}Pb activities and analytical uncertainties measured on HLP-Core 1. ^{210}Pb age model behavior was tested by identifying the 1963 Cesium peak determined from ^{137}Cs activities, which are shown on the bottom two plots. Triangles pointing up with error bars on the bottom left and triangles pointing down with error bars on the bottom right are ^{137}Cs activities and analytical uncertainties for RBP-Core 2 and HLP-Core 1, respectively.

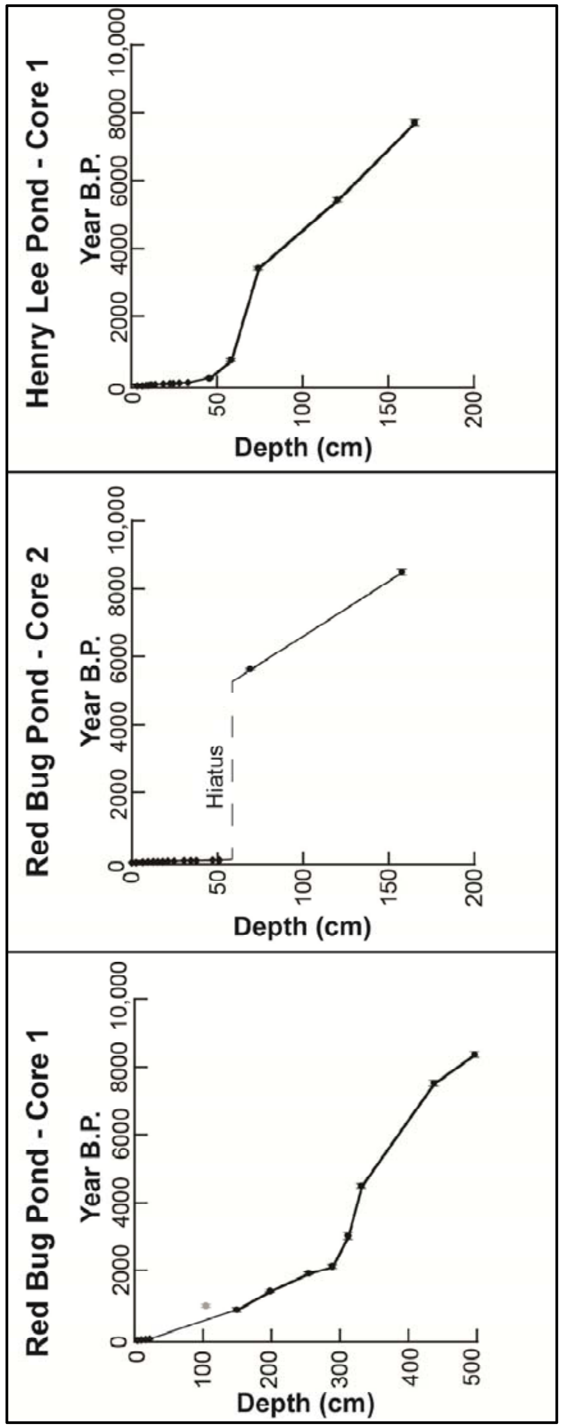

Figure 6.4: ^{210}Pb- and ^{14}C-based depth vs. age relationships for the Red Bug and Henry Lee pond cores. The age model for RBP-Core 1 is on the left, RBP-Core 2 is in the middle, and HLP-Core 1 is on the right. ^{210}Pb age control points are displayed as black diamonds, ^{14}C age control points are displayed as black circles, and the ^{14}C age that was not included in the RBP-Core 1 age model is displayed as a grey circle.

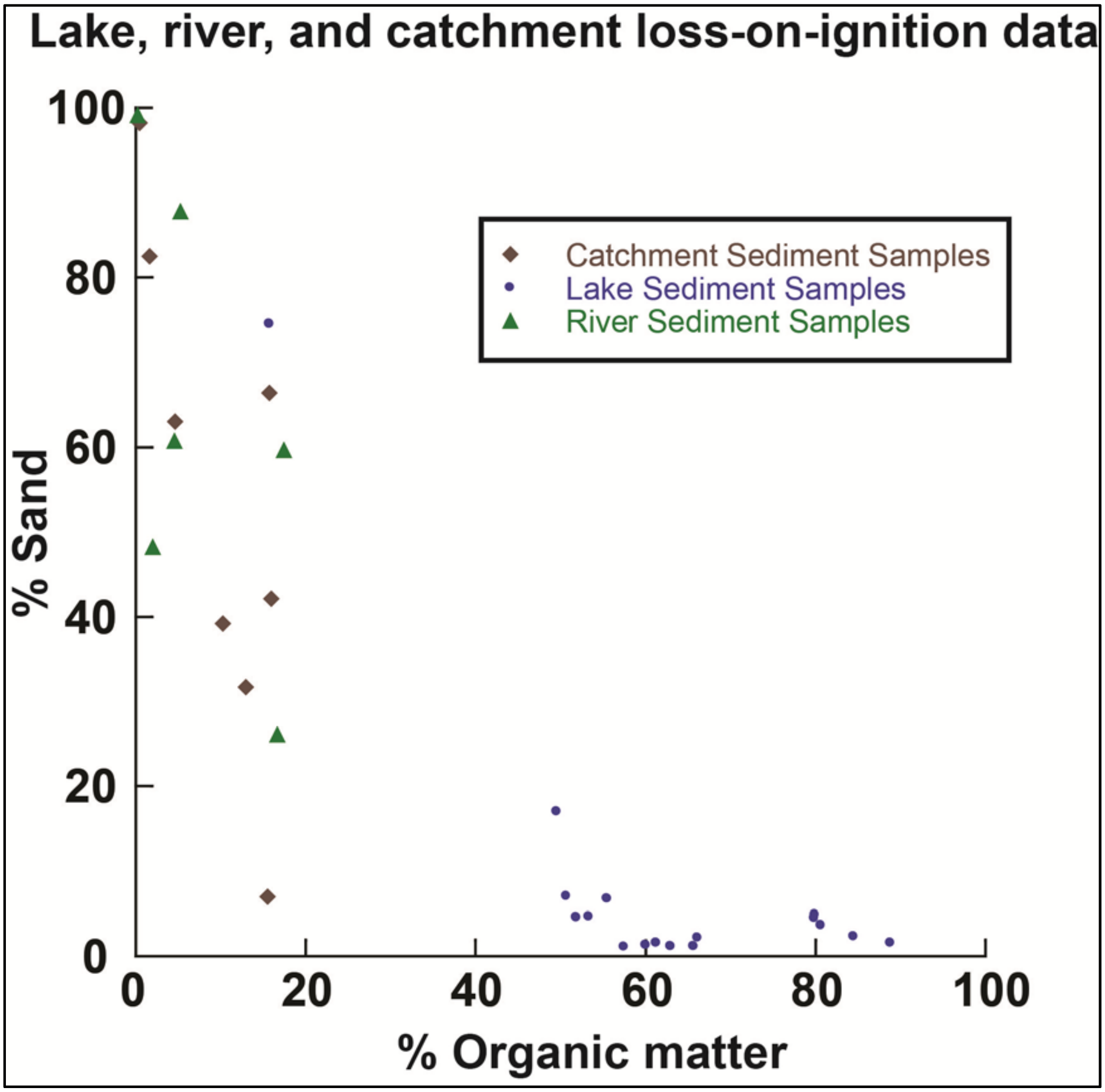

Figure 6.5: Loss-on-ignition data for the sediment-water interface samples, catchment samples, and river samples are displayed as % organic matter on the x-axis versus % >63 microns on the y-axis. Samples from the sediment water interface in Red Bug Pond are blue dots, from the catchment surrounding Red Bug Pond are brown diamonds, and from the rivers are green triangles.

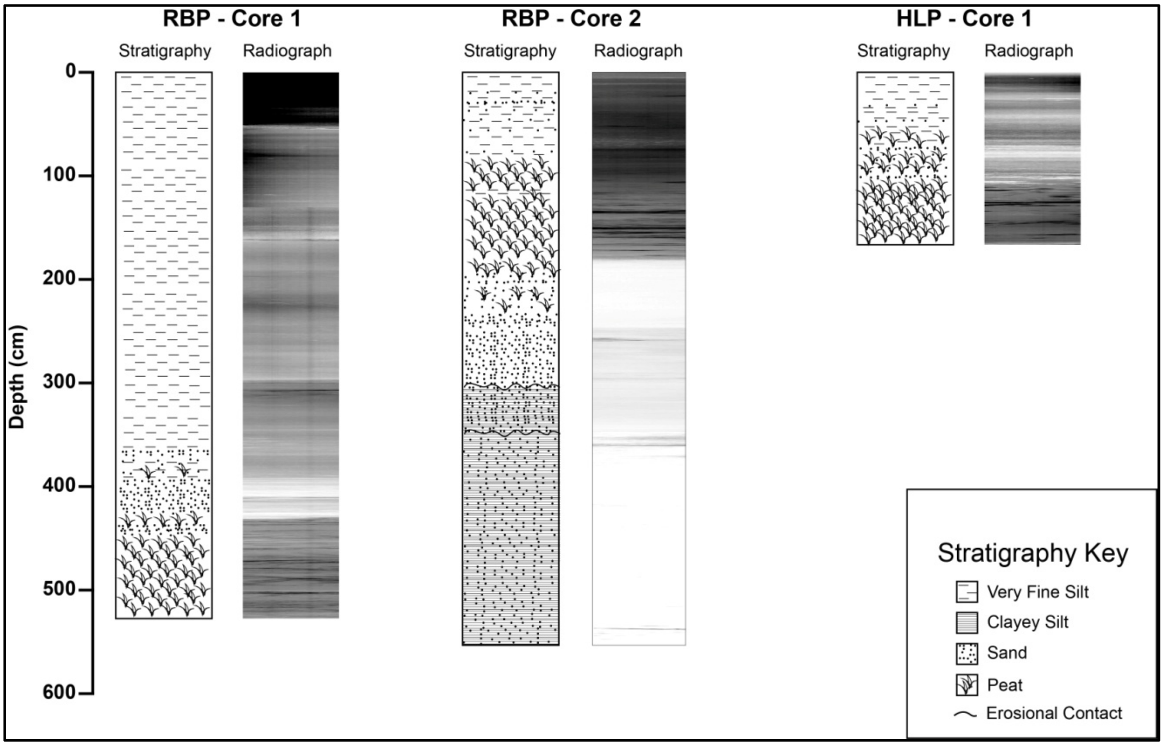

Figure 6.6: Stratigraphic columns and radiographic images for Red Bug and Henry Lee pond cores on a depth scale. RBP-Core 1 is on the left, RBP-Core 2 is in the middle, and HLP-Core 1 is on the right. Each stratigraphic column is displayed to the left of the radiographic image corresponding to that particular core. Radiographic images are inverted such that lighter shades indicate higher density.

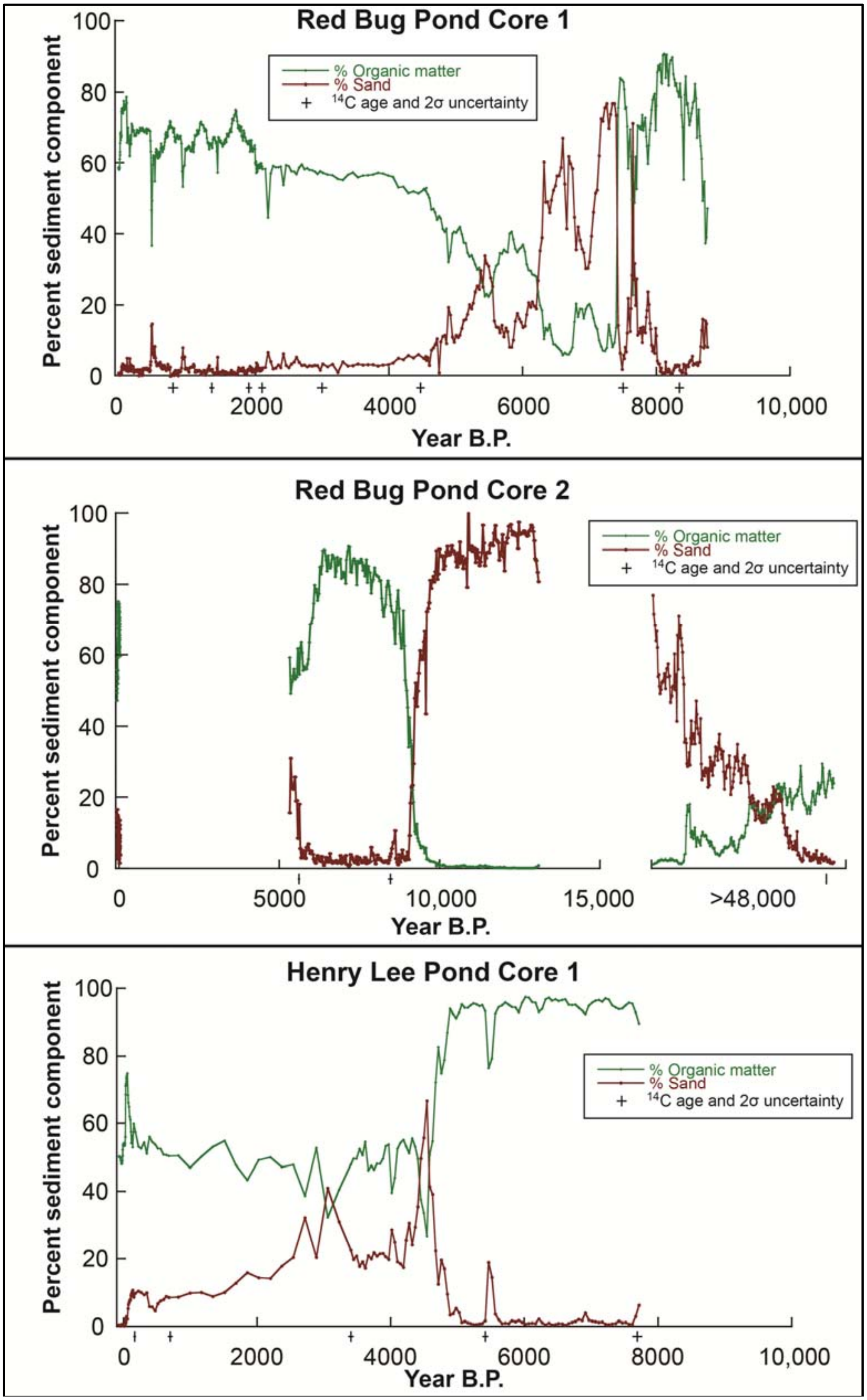

Red Bug Pond Core 1
% Organic matter
% Sand
+ ^{14}C age and 2σ uncertainty
Percent sediment component
0
20
40
60
80
100
0
2000
4000
6000
8000
10,000
Year B.P.
Red Bug Pond Core 2
% Organic matter
% Sand
+ ^{14}C age and 2σ uncertainty
Percent sediment component
0
20
40
60
80
100
0
5000
10,000
15,000
>48,000
Year B.P.
Henry Lee Pond Core 1
% Organic matter
% Sand
+ ^{14}C age and 2σ uncertainty
Percent sediment component
0
20
40
60
80
100
0
2000
4000
6000
8000
10,000
Year B.P.

Figure 6.7: Down-core loss-on-ignition data for the Red Bug and Henry Lee pond cores are shown with RBP-Core 1 on the top, RBP-Core 2 in the middle, and HLP-Core 1 on the bottom. The data are plotted versus years B.P., where "present" is the year 1950 C.E. For each core, % organic matter is displayed in green and % >63 microns is displayed in dark red. Individual measurements are indicated by circles. Age control points for each core are shown as crosses below the x-axis, where the width of the symbol represents the age uncertainty.

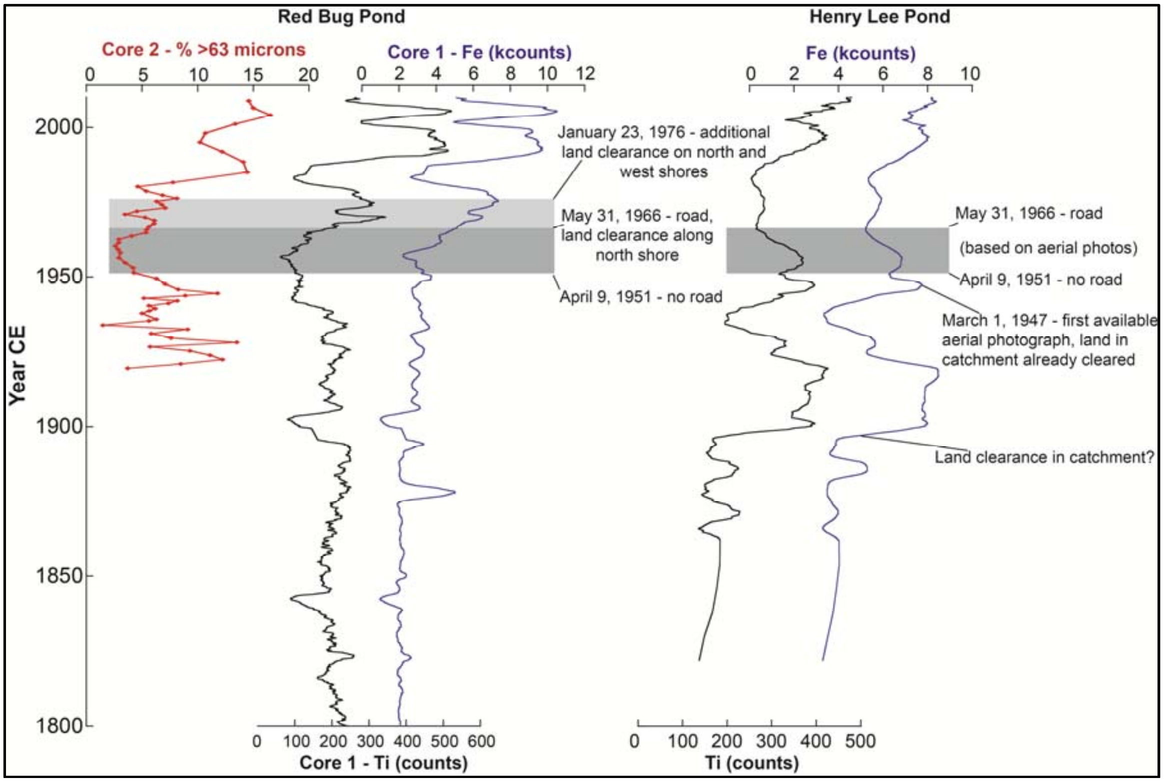

Figure 6.8: Core-top % >63 microns and XRF-derived Fe and Ti abundances in Red Bug Pond sediments are shown on the left, and Fe and Ti abundances in Henry Lee Pond sediments are shown on the right. The grain size data is from RBP-Core 2 and is shown in red, with circles indicating individual measurements. Ti counts (bottom axes) for RBP-Core 1 and HLP-Core 1 are shown in black, and Fe in thousands of counts (top axes) are shown in blue. The data are plotted against years in the Common Era (CE). The dark grey rectangles represent the time between the available aerial photos during which major changes to the landscape near the site occurred. The light grey rectangle across the Red Bug Pond record represents the time between the available aerial photos during which smaller-scale landscape alterations occurred.

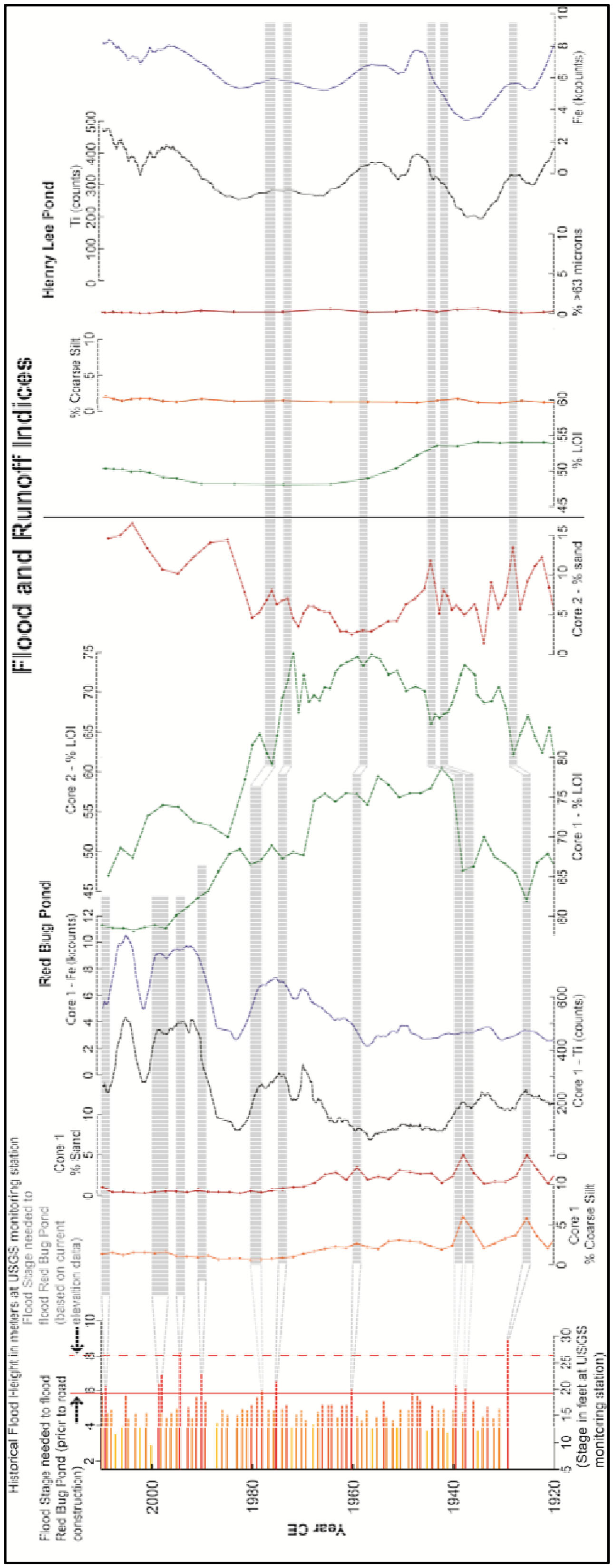
Flood and Runoff Indices
Red Bug Pond
Henry Lee Pond
Historical Flood Height in meters at USGS monitoring station
Year CE
(Stage in feet at USGS monitoring station)
Core 1 % Sand
Core 1 % Coarse Silt
Core 1 - Ti (counts)
Core 1 - Fe (kcounts)
Core 1 - % LOI
Core 2 - % LOI
Core 2 - % sand
% LOI
% Coarse Silt
% >63 microns
Ti (counts)
Fe (kcounts)

Figure 6.9: A comparison of the historical flood record to Red Bug and Henry Lee pond sediment core data. On the far left, all historical floods recorded at the Bruce-Ebro USGS monitoring station are displayed as horizontal bars. The lengths of the bars correspond to the flood crest height at the station, which is displayed in feet on the bottom x-axis and in meters on the top x-axis. The colors of the bars correspond to whether they were categorized as Action Stage (yellow), Minor Flood Stage (orange), Moderate Flood Stage (dark orange), or Major Flood Stage (red). The two vertical lines represent the flood stages necessary for the river water to spill over into Red Bug Pond; the dashed red line is the elevation the river would have to exceed based on the current lidar elevation data and the solid red line is the elevation the river would have to exceed before the road was built across the valley connecting the lake and Holmes Creek. To the right of the historical flood record are grain size and elemental abundance data from Red Bug Pond Cores 1 and 2 and Henry Lee Pond. The data shown are RBP-Core 1 % coarse silt (% of sediment between 32 and 63 microns by mass; orange), % sand (% >63 microns; red), Ti counts (black), Fe thousands of counts (blue), and % organic matter (green). To the right of that are % organic matter (green) and % sand (red) from RBP-Core 2. To the right of the vertical black line are data from Henry Lee Pond sediments, including % organic matter (green), % coarse silt (orange), % sand (red), Ti counts (black), and Fe thousands of counts (blue). All data are plotted against years CE. Circles in the loss-on-ignition data from all three cores represent individual measurements. The grey horizontal bars through the figure highlight the timing of historical floods that are in some cases shifted slightly within age model error to highlight the grain size and organic content changes associated with historic floods.

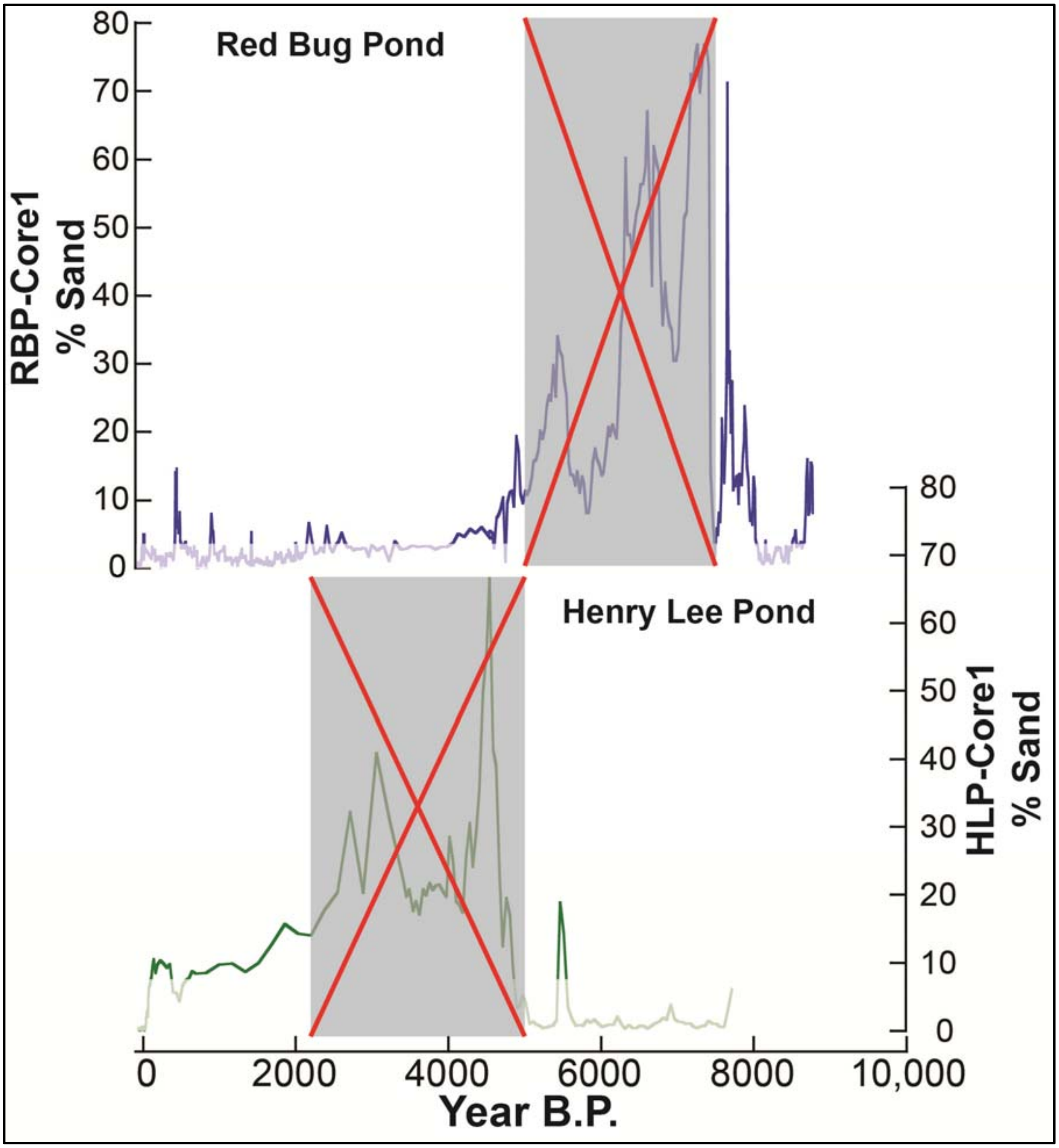

Figure 6.10: Holocene-length flood reconstructions from Red Bug and Henry Lee ponds The Red Bug Pond % sand data are on top in blue and the Henry Lee Pond % sand data are on the bottom in green. The periods 5000 to 7500 B.P. and 2200 to 5000 B.P., which are not included in the flood reconstructions in Red Bug Pond and Henry Lee Pond, respectively (See Section 6.6.3) are covered by a grey box with a red "X." The % sand values below the threshold for event detection are faded out to highlight flood events in these records. The data are plotted against years B.P.

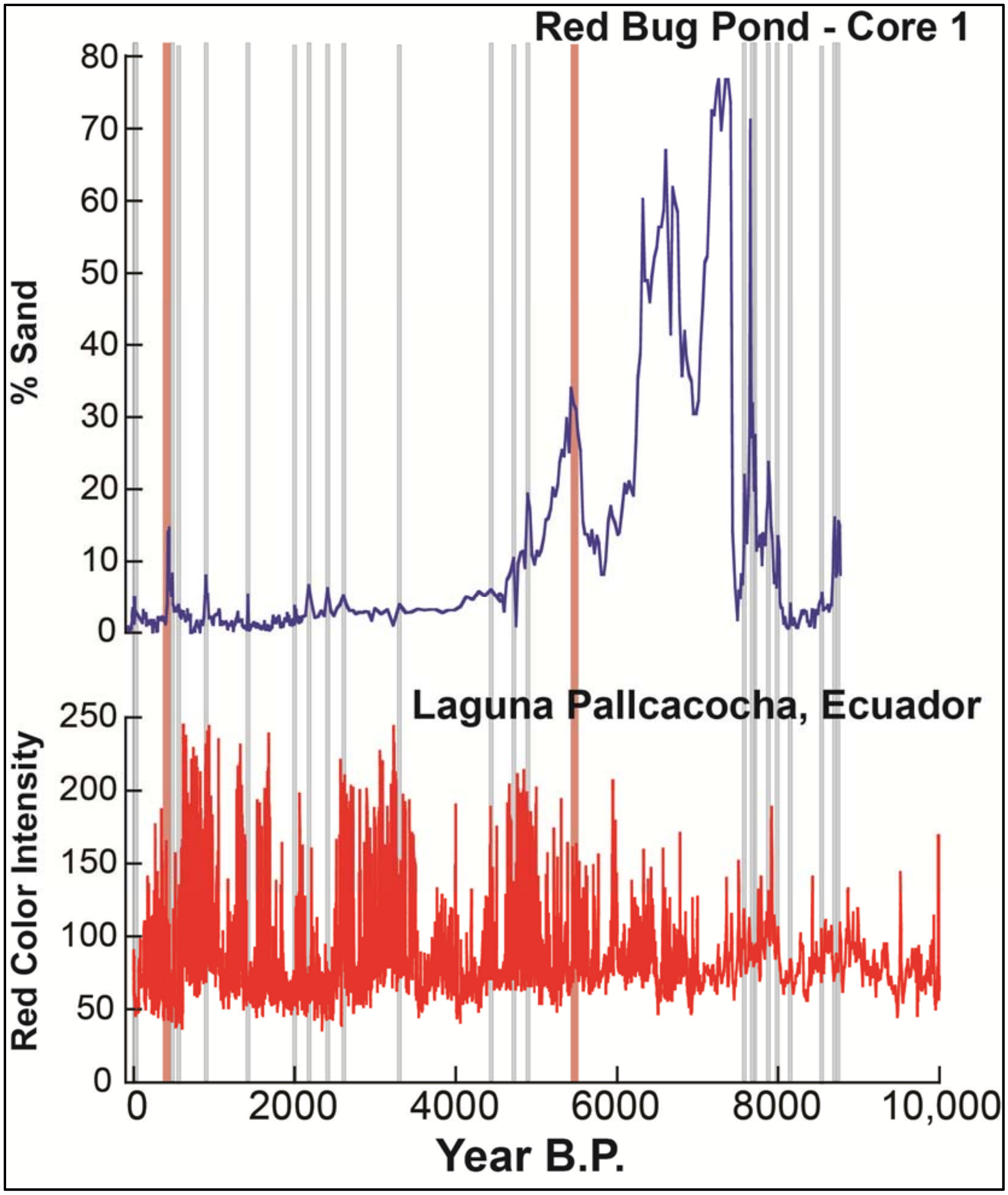

Figure 6.11: A comparison of the Holocene-length flood reconstruction from Red Bug Pond with a red color intensity record from Ecuador (Moy et al., 2002). The Red Bug Pond % sand record is on top in blue and the red color intensity record is displayed on the bottom in red. All dataset are plotted against years B.P. The grey vertical bars highlight floods detected in the Red Bug Pond record, and the red vertical bars highlight the two more extreme floods that are present in the Henry Lee Pond record.

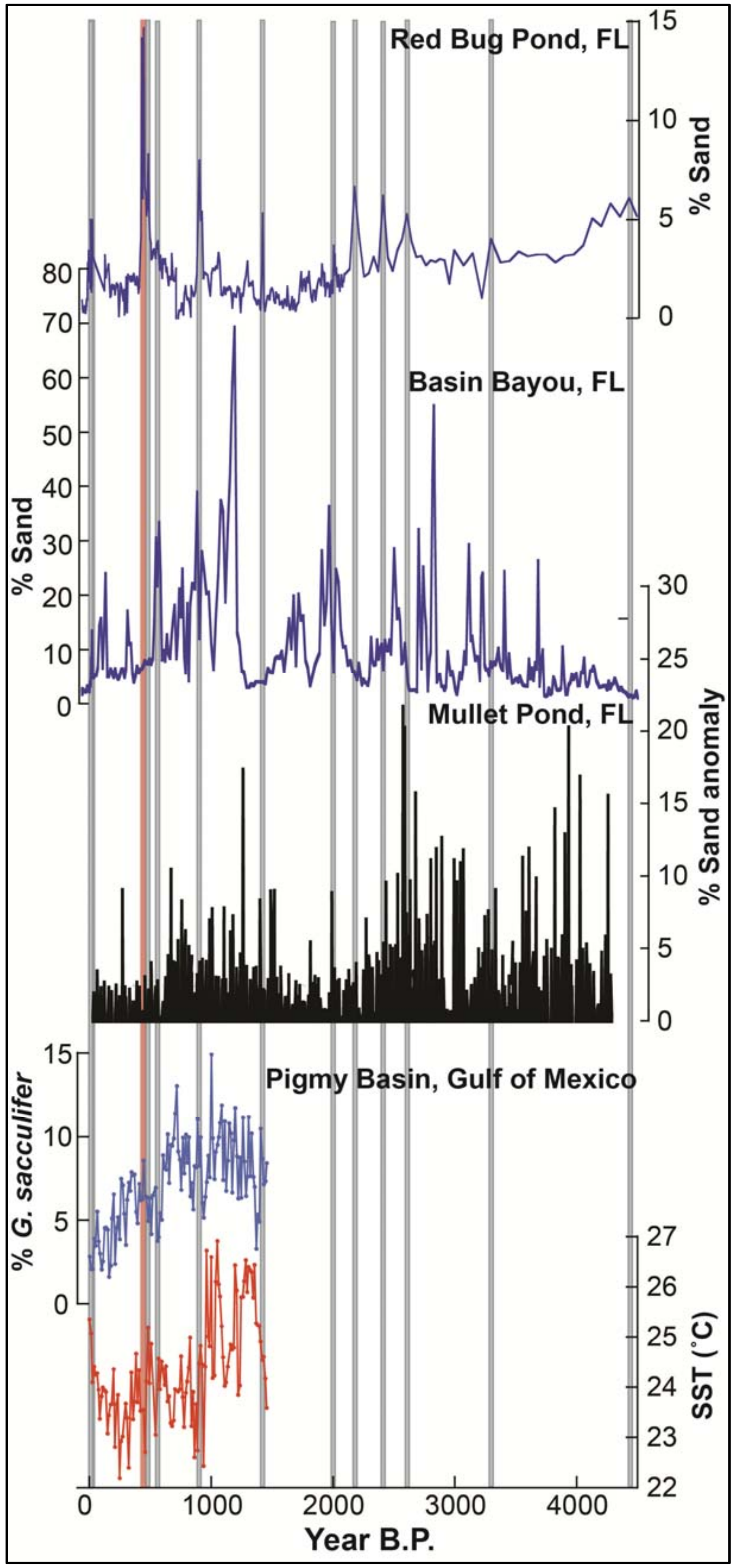
Red Bug Pond, FL
% Sand
Basin Bayou, FL
% Sand
Mullet Pond, FL
% Sand anomaly
Pigmy Basin, Gulf of Mexico
% G. sacculifer
SST (°C)
Year B.P.

Figure 6.12: A comparison of our flood reconstruction from Red Bug Pond (blue) during the past 4500 years with a time series of intense storm deposit reconstructions from Basin Bayou (dark blue; Chapter 5) and Mullet Pond, FL (black; Lane et al., 2011) . Two 1400-year-long records of Loop Current penetration (light blue), inferred from % *G. sacculifer*, and Gulf of Mexico SSTs (orange) from the Pigmy Basin in the Gulf of Mexico (Richey et al., 2007) are plotted against years B.P. The vertical grey bars highlight the floods detected in the Red Bug Pond record after 4500 B.P., and the red vertical bar highlights the more extreme flood that is present in the Henry Lee Pond record.